Morphology and Self-Assembly Behavior of Side Chain Liquid Crystalline Block Copolymers

by

Eric Anton Verploegen

Bachelor of Science in Materials Science and Engineering
Cornell University, Ithaca, New York, 2002

Submitted to the Department of Materials Science and Engineering
In partial fulfillment of the requirements for the degree of
DOCTOR OF PHILOSOPHY IN MATERIALS SCIENCE AND ENGINEERING
at the
MASSACHUSETTS INSTITUTE OF TECHNOLOGY
JUNE 2008

Signature of Author:_____
Department of Materials Science and Engineering
April 29th, 2008

Certified by:_____
Paula T. Hammond
Bayer Chair Professor of Chemical Engineering
Thesis Supervisor

Certified by:_____
Edwin L. Thomas
Morris Cohen Professor of Materials Science and Engineering
Thesis Supervisor

Accepted by:_____
Samuel M. Allen
POSCO Professor of Physical Metallurgy
Chair, Departmental Committee on Graduate Studies

In Memory
Mark Joseph Verploegen

Morphology and Self-Assembly Behavior of Side Chain Liquid Crystalline Block Copolymers

by

Eric Anton Verploegen

Submitted to the Department of Materials Science and Engineering on April 29th, 2008
in partial fulfillment of the requirements for the degree of
Doctor of Philosophy in Chemical Engineering

Abstract

There is significant interest from both the academic and industrial communities for understanding and controlling the self-assembly behavior of complex macromolecular systems and has been an active area of research in recent years. Such systems can be designed to result in a wide range of nanoscale morphologies and greater functionality can be introduced with increasing complexity.

This thesis focuses on the synthesis and characterization of a class of side chain liquid crystalline block copolymers (SCLCBCPs) that are based on a low glass transition temperature (T_g) siloxane backbone. Moieties that self-assemble into smectic liquid crystalline (LC) phases are covalently attached to the polystyrene-polyvinylmethylsiloxane (PS-PVMS) block copolymer backbone. Precise control over the functionalization of the LCs onto the functional siloxane backbone allows for unique control over the self-assembly and the resulting properties of the system. The LC content significantly affects the stability of the smectic mesophase and subsequently the interactions with the inter-material dividing surface (IMDS) with the PS domains. A strong preference for homogenous anchoring of the LC moieties relative to the IMDS is observed, and increasing the LC content intensifies the preference for this arrangement. Utilizing the effects of LC anchoring to alter the self-assembly behavior is a reoccurring theme throughout this work. Additionally, the mechanical properties of these materials can be precisely manipulated over several orders of magnitude through variations in LC content and the block copolymer backbone architecture.

Several methods can be used to manipulate the morphologies of these materials once synthesized including, thermal annealing and mechanical deformation. Thermal annealing provides additional mobility for self-assembly often resulting in morphological rearrangements. Mechanical deformation can be used to orient the self-assembled structures relative to an applied shear flow. Additionally, the self-assembled morphologies of spin cast into thin films were investigated. The presence of the substrate has significant effects upon the orientation of the morphologies; thermal annealing and variations liquid crystal content are shown to be useful tools for achieving a wide range of thin film morphologies.

Thesis Supervisors: Paula T. Hammond,
Bayer Chair Professor of Chemical Engineering

Edwin L. Thomas,
Morris Cohen Professor of Materials Science and Engineering

TABLE OF CONTENTS

List of Figures

List of Tables

Acknowledgements

I would first like to express my deepest gratitude to my advisors Prof. Paula Hammond and Prof. Edwin Thomas who provided me with invaluable direction, guidance, and support without which this work would not be possible. I would also like to thank my thesis committee Prof. Robert Cohen and Prof. Krystyn Van Vliet for their extremely valuable input and support that helped guide me through this process.

I would like to thank all of my colleagues and collaborators that I have worked with over the years. All of the members of the Hammond and Thomas groups that provided me with friendship, help, and advice: Lu, LaRuth, LaShanda, Mike Berg, Nicole, Phuong, Jodie, Kris Wood, Jinhwa, Kris Stokes, Piljin, Greg, Avni, Nathan, Dan Bonner, Shujun, Helen, Amanda, Friederike, Mike Petr, Yong Hoon, Jung-Ah, Byeong-Su, Kevin, Seung Woo, Hyung-il, Mara, Andy, Dan Schmidt, Anita, Renee, Zhiyong, Brian, Henry, Joe Walish, Nick, Woo Soo, Ji-Hyun, Taras, Rafal, Rachel, and Ryan Waletzko. A special thanks to Lu Tian who provided me with an "on the job" education of synthetic chemistry; without his friendship and help I would have never been able to make any materials to study. Mitch Anthematem, Jung-Sheng Wu, Aaron Moment, LaRuth McAfee, Bruce Yu, and Keith Reed who worked on side chain liquid crystalline polymers in the Hammond group and laid the foundation for my work. A special thanks to Piljin Yoo for assistance with AFM, and Phuong for all the late night technical consults. Thanks so much to the guys that introduced me to carbon nanotubes Ben Wang, John Hart, Ryan Bennett, Prof. Cohen, Gary Chia, Andy Miller, and Kyle Yazzie; it has been a great experience working with such an awesome group of people. Thanks to Prof. Caroline Ross and Yeon Sik Jung for their help with tempated self-assembly and etching of thin films and Prof. Gareth McKinley, Sarah Bates, and Johannes Soulages for their help with photo-responsive rheology.

Many thanks to all of the undergrads who have worked for me over the years and made this work possible: Albert Park, Alexandra Tcaciuc, Darren Verploegen (it was great to meet one of the family at MIT!), Derrick Boone, Tejia Zhang, Nick Murlo, Mariel Kozberg, and Kyle Yazzie. A VERY special thanks to Tejia who has been working tirelessly with me for over two years now. Her incredible skill, talent, enthusiasm, and dedication were invaluable. I am looking forward to following her future success with graduate research at Harvard and beyond!

All of the people at the ISN who provided a fun work environment and put up with my antics: Marco Carega, Maureen Caulfield, Abeer Chaudhuri, Kurt Keville, Randy Hill, Marlisha McDaniels, Cathy Byrne, John Joannopoulos, Ned Thomas, Bill Peters, Franklin Hadley, Josh Freedman, Amy Tatem Bannister, the all knowing always helpful Steve Kooi, and all of the students and post-docs thank you! All of the brilliant and fun people at MIT that shared in the grad school experience and inspired me especially: Joe Shuga, Shannan, Angus, Fred, Mauro, Alejandro, Bonna, Ben Wang, RDB, Sharon, Erik Allen, Joe Lowery, the Boston Poker Tour, and the MSE Ultimate team, thanks for all the good times!

I am very grateful for the facilities and funding agencies that made this work possible: The U.S. Army Research Office through the Institute for Soldier Nanotechnologies at MIT under contract number DAAD-19-02-D0002, the MIT Center for Materials Science and Engineering Shared Experimental Facility (National Science Foundation Award Number DMR-9400334), the National Synchrotron Light Source, Brookhaven National Laboratory, supported by the U.S. Department of Energy, Office of Science, Office of Basic Energy Sciences, under contract number DE-AC02-98CH10886, the Cornell High Energy Synchrotron Source (CHESS) which is supported by the National Science Foundation and the National Institutes of Health/National Institute of General Medical Sciences under award DMR-0225180. A special thanks to Arthur Woll at the G line at CHESS, whose support and guidance enabled the pursuit of many interesting and ridiculous X-ray experiments.

I would also like to give thanks to all of my friends from outside of MIT whose friendship I cherish! Everyone from Annapolis, especially: Nick, Greg, James, Alex, Matt, Conor, and Nicole. From Cornell: Josh, Jon, Faraz, Cyrus, Stephanie, Marty Murtagh, Yuanming Zhang, and the rest of the members of the Sass and Wiesner groups. A special thanks to Prof. Ulrich Wiesner for getting me started in polymer science, through both your wonderful classes and your guidance as my research advisor. All of my friends from around Boston: Ricky, Chad, Dan, Kevin, Chris, Courtney, Stevie, TD, Mike G, Tariq, Bonner, Joanna, Meghan, Tim, and Liz who made this last year extra fun! All of the guys down in Providence for so many great weekend getaways: Joe, Laura, Ashley, Susan, Tim, Colin, Kara, Luke, and Matt.

Finally, and most importantly, I would like to thank my amazing family whose love and support makes each day wonderful. My Mom, the most important person in my life, has made me the person I am today. She has been there for me every single day and has always pushed and supported me, both personally and academically, to be my best. By instilling the values of education and hard work in our family, she enabled me to pursue a career in science and made my education possible. My sister Leslie, with whom I share a special bond, will always be one of my very best friends and my favorite person. Tom, who keeps the rest of us grounded with his thoughtfulness and easy-going demeanor. My Dad, who taught me about making something out of nothing and enjoying what you do; your memory will be with me forever.

Chapter 1 Introduction

1.1 Liquid Crystals and Liquid Crystalline Elastomers

Liquid crystals (LC) are molecules that exhibit some degree of order while in a liquid-like state. Liquid crystals attractive for use in many applications including memory devices, sensors, and displays. Molecules that exhibit liquid crystalline behavior typically have a rigid component and some form of molecular anisotropy. The degree of order in these systems can be quantified by defining a director in the direction of orientation, and calculating an order parameter. One description is Hermans orientation parameter, which can be defined for axially oriented systems as:[1,2]

$$f = \frac{1}{2}\left(3\left\langle \cos^2\phi \right\rangle - 1\right) \tag{1}$$

Where ø is the angle between the individual liquid crystal's director and the chosen reference direction. The factor in brackets represents the mean-square cosine of the azimuthal angle, calculated from the following equation:

$$\left\langle \cos^2\phi \right\rangle = \frac{\int_0^{\pi/2} I(\phi)\sin\phi\cos^2\phi\, d\phi}{\int_0^{\pi/2} I(\phi)\sin\phi\, d\phi} \tag{2}$$

This parameter ranges from 1 to -½, with $f = 0$ for a completely random distribution of orientations. When f is 1 or -½ the system is completely aligned parallel or perpendicular, respectively, to the chosen reference direction.

The most common liquid crystalline phases for rod-like LCs are; isotropic, nematic, smectic A, smectic C, and smectic C* (Figure 1-1)[3]. Isotropic phases do not posses any preferential orientation and have the characteristics of a simple liquid. A nematic phase only exhibits orientational order in one dimension, resultant from a preference of the liquid crystals to orient along a common direction. The smectic A phase has orientational order as well as positional order, forming layers that have the molecules preferentially aligned along the direction normal to the layers. Another similar smectic phase is the smectic C, where the director is oriented at some angle θ to the layer normal. If the molecule contains a chiral center a rotation of the director will occur in a helical manner, and this is called a smectic C* phase. The distance over which one full rotation occurs is the pitch.

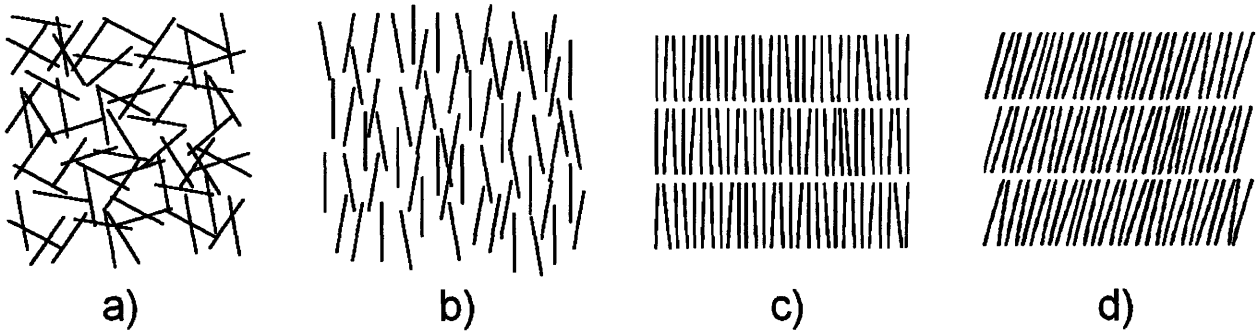

Figure 1-1. Schematic representation of a) isotropic, b) nematic, c) smectic A, and d) smectic C liquid crystalline phases.

Ferroelectricity is the ability of a molecule to display a polarization in the absence of an externally applied field. Spontaneous polarization is when a polarization remains in a material after the application and removal of an electric field. All ferroelectric materials exhibit piezoelectricity; the direct piezoelectric effect occurs when an applied field produces a strain in the material. Conversely, the indirect piezoelectric effect is when an applied strain results in a polarization. Smectic C* liquid crystals exhibit spontaneous polarization, however due to the rotation of the director there is no net polarization. This can be overcome by confining the material between surfaces separated by a distance less than the pitch of the rotation, transforming the smectic C* into a smectic C phase.

Liquid crystalline (LCP) polymers have attracted recent interest due to their ability to combine the properties of small molecule liquid crystals and those of a polymer [4]. LC polymeric materials benefit over their small molecule LC counterparts from the mechanical integrity that the polymer component provides to the system. Additionally, by lightly crosslinking the polymer a liquid crystalline elastomer (LCE) can be created, allowing for the combination of the rubber elasticity of a polymer network with the properties of LC phases. This class of materials can be designed to exhibit a conformational change on the molecular level in response to thermal, electrical or optical stimulation. The molecular conformational change can lead to a macroscopic change in the optical, thermal, or mechanical properties of the materials, making them candidates for electro-mechanical, actuator, and shape memory applications.

The increased viscosity of the liquid crystalline polymer system leads to an increase in the response time of the liquid crystalline phase. This effect can be minimized by using a polymer backbone with a low glass transition temperature (T_g). Siloxane based LCEs present specific advantages associated with the very low T_g of the siloxane backbone, including a nearly

ideal elastometric response, allowing for the materials to retain their properties over a wide temperature range, particularly at very low temperatures[5-7].

Thermotropic liquid crystalline elastomeric actuators have been developed, where a LC phase transition leads to a dimensional change or actuation. The polymer backbone can be forced into a more extended state when the LC is in the nematic state, compared to the isotropic state, as shown in Figure 1-2[6]. Such nematic LCE fibers have been shown to exhibit reversible strains of over 30% when heated and cooled above and below the nematic to isotropic transition temperature (Figure 1-3) [6, 8].

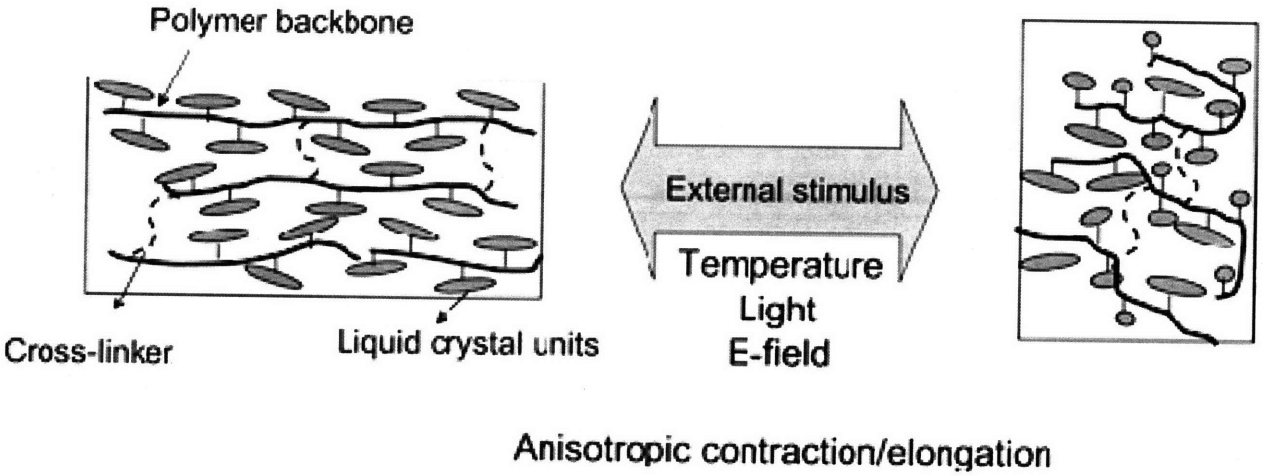

Figure 1-2. Schematic of the liquid crystalline elastomer as an actuator[6].

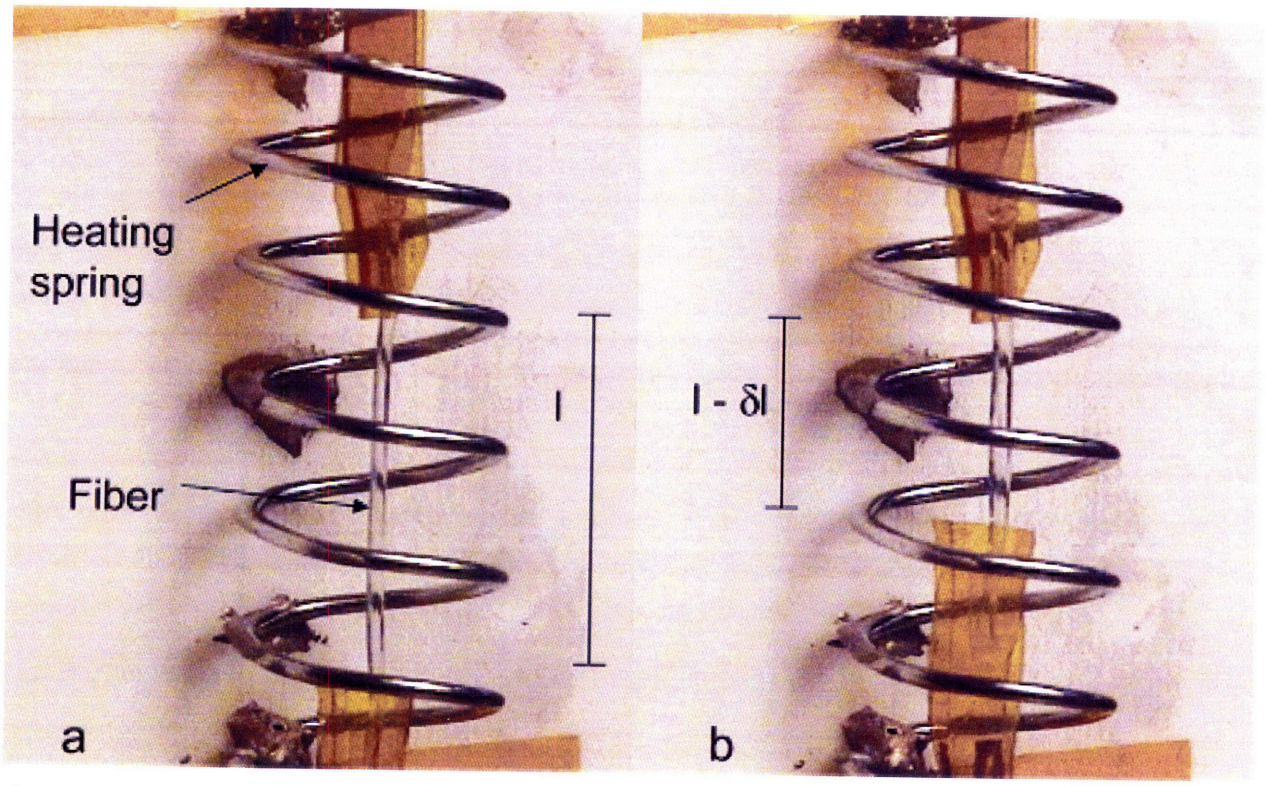

Figure 1-3. Fiber actuation under a load of 0.002 N. The 200 mg weight attached to the bottom end of the fiber is not visible. The fiber is in the extended state in the nematic phase (a) and contracted in the isotropic phase. The fiber regains its original length upon cooling[6].

The electroclinic effect observed in smectic LC phases can be manipulated in order to create materials that act as reversible actuators. In these materials an applied electric field induces a tilt in the director of the smectic moieties, which results in a decrease in the smectic layer thickness, see Figure 1-4. If the smectic layers are uniaxially aligned, the change in smectic layer thickness translates to a net change in the film thickness. Crosslinked siloxane networks with side chain smectic LCs have been well oriented through mechanical deformations, [9, 10] and their electro-mechanical properties studied [11]. These materials have been shown to exhibit electro-mechanical responses with strains up to 4% with applied voltages of 1.5 V/μm [5, 12, 13]. The voltage is significantly less than what is required for other polymeric actuators such as P(VDF-TrFE), ~150 V/μm. The strain achievable is much greater than that of common ceramic piezoelectric actuators, ~0.15%, but is less than what can be achieved by a LC thermotropic actuator[5]. Among the limitations of this actuation mechanism are the maximum strain achievable and the amount of force per unit area that can be generated. An additional processing step of achieving uniaxial aligned smectic layers is required, and it should also be noted that the need for application of an electric field orthogonal to the direction of actuation presents significant limitations for many applications.

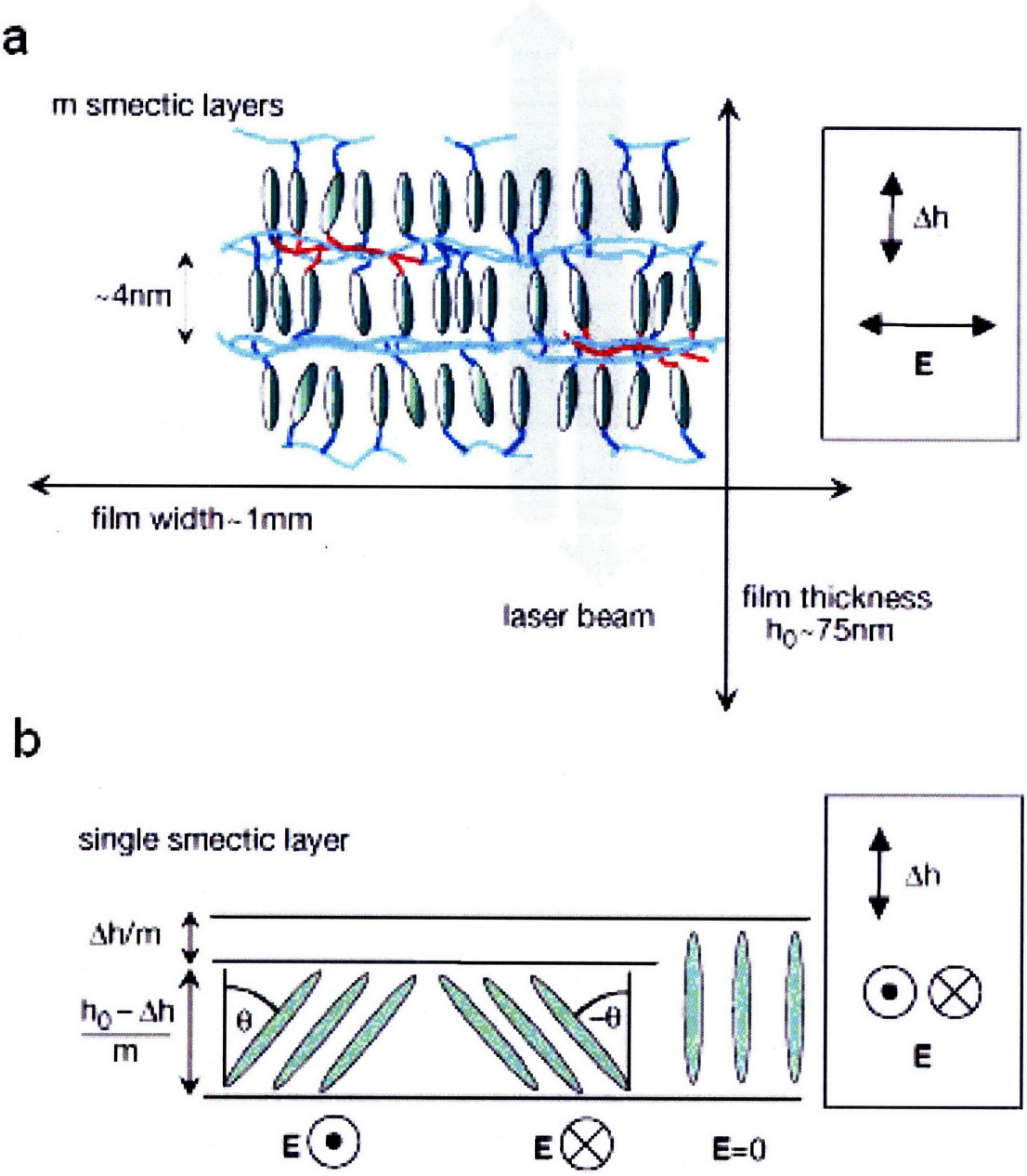

Figure 1-4. a) Schematic of the measurement geometry for electroclinic LCE actuator. A laser beam in the interferometer passes twice through the film to measure the thickness modulation Δh. b) Schematic of the electroclinic effect. Without the electric field, one smectic layer has the thickness h_o. The application of a lateral electric field results in a tilt angle θ proportional to the electric field. Each smectic layer shrinks by Δh, resulting in a net strain of the film in the direction perpendicular to the smectic layer normal[5].

Photo-responsive LCEs present several potential advantages compared with LCEs that rely on thermotropic phase transitions or application of electric field. The utilization of photoisomerization of LC moieties in order to produce actuator materials was first proposed by deGennes[14]. This class of materials can be stimulated by exposure to particular wavelengths of electromagnetic radiation (light), resulting in molecular rearrangements that manifest the desired effects. For example, this class of materials has been used to create photo-responsive shape memory polymers[15]. There are several examples of molecules, including LCs containing azo groups, that have garnered great interest for their abilities to photoisomerize to generate useful properties in polymers [16-18].

Azobenzene moieties undergo a *trans* to *cis* photoisomerization upon exposure to 366nm light. The *trans* state is the equilibrium state and the moiety relaxes to the *trans* state with time. The return to the *trans* state can be accelerated with either heat, or stimulation with light > 540nm. The photoisomerization of liquid crystals containing azo moieties has been shown to disrupt the stability of nematic[19] and smectic[20] LC phases. If properly designed the azobenzene moiety in the *trans* state can be incorporated into a smectic LC phase, with little effect upon its stability. However, upon photoisomerization the azobenzene moiety in the *cis* state has been shown to significantly disrupt the smectic LC phase, leading to a change in the smectic to isotropic transition temperature (T_{iso}) [16, 21, 22]. An isothermal smectic to isotropic transition can be achieved when the T_{iso} is above operating temperature when the azo moiety in the *trans* state and the T_{iso} is lowered below the operating temperature when the azo moiety is switched to the *cis* state. By inducing a smectic to isotropic transition, significant molecular conformational changes can be achieved, leading to a change in the properties of the material (diffusivity, mechanical, and dimensional). It has also been shown that dissolving the azo moieties into the

LC phase can result in switching times up to two orders of magnitude faster than if the azobenzene moiety is covalently attached to the polymer[23]. However, the drawback with such a system is that there is a potential for the depletion of the photo-responsive moiety with time under certain conditions.

Recently, several groups have utilized photoisomerization to create materials that exhibit a bending actuation due to the contraction or expansion of a material that has had one surface exposed to light [23-25]. This contraction of the surface of the material exposed to light results in internal stress in the material that leads to bending of the film (Figures 1-5 and 1-6).

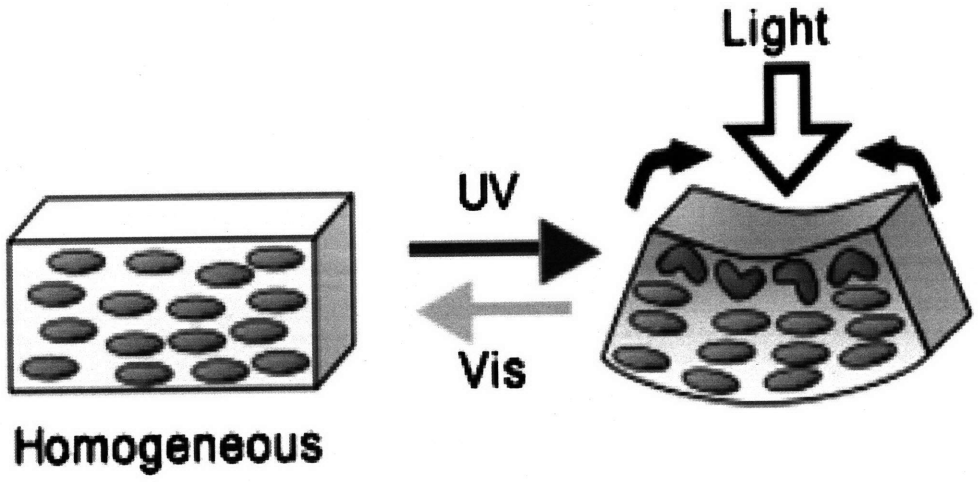

Figure 1-5. A schematic of the bending actuation driven by exposure to UV light (366 nm) and return to upon exposure to visible light (>540 nm)[24].

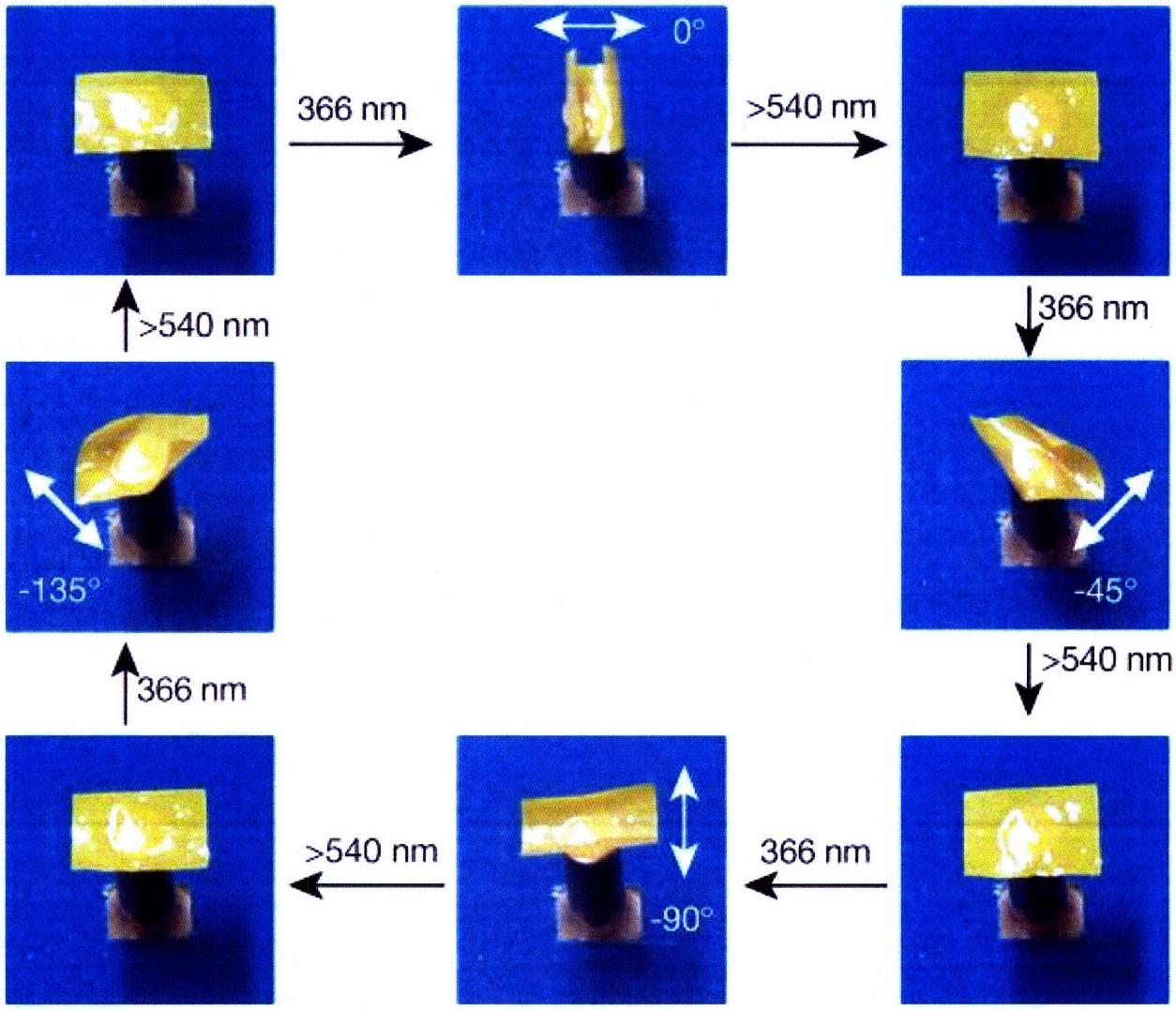

Figure 1-6. An example of a LCE photo-responsive film that utilizes the photoisomerization of an azo moiety to create an actuation effect. Photographic frames of the film bending in different directions in response to irradiation by linearly polarized light of different angles of polarization (white arrows) at 366 nm, and being flattened again by visible light longer than 540 nm. The flat film (4.5 mm × 3 mm × 7 μm) lay on a copper stick fixed to a copper plate; a stage under the plate was set at 85 °C to control the temperature of the film, which was covered by a piece of blue paper[25].

1.2 Block Copolymers

Block copolymers consist of two or more chemically different polymer segments, or blocks, connected by a covalent linkage. At lower temperatures nanophase segregation occurs due to unfavorable enthalpic interactions between the two blocks. The covalent linkage between the two components prevents macrophase separation. However, heating the system can provide the entropic driving force for phase mixing to occur, resulting in a disordered state (Figure 1-7). The temperature where phase mixing occurs is called the order disorder transition temperature (T_{ODT}).

The nanophase segregated block copolymer morphologies that self-assemble under the right conditions have attracted great interest for numerous applications[26]. In bulk a range of morphologies can be formed including lamellae, bicontinuous gyroids, hexagonal packed cylinders, and cubic packed spheres, as shown in Figure 1-8[27]. The phase behavior of bulk A-B block copolymers are determined by three experimentally controllable factors: the overall degree of polymerization, N, the composition, f (overall volume fraction of the A component), and the A-B segment-segment (Flory-Huggins) interaction parameter, χ. Block copolymers are increasingly used as templating materials; thus, the ability to control the formation of specific patterns and structures is of growing interest and applicability.

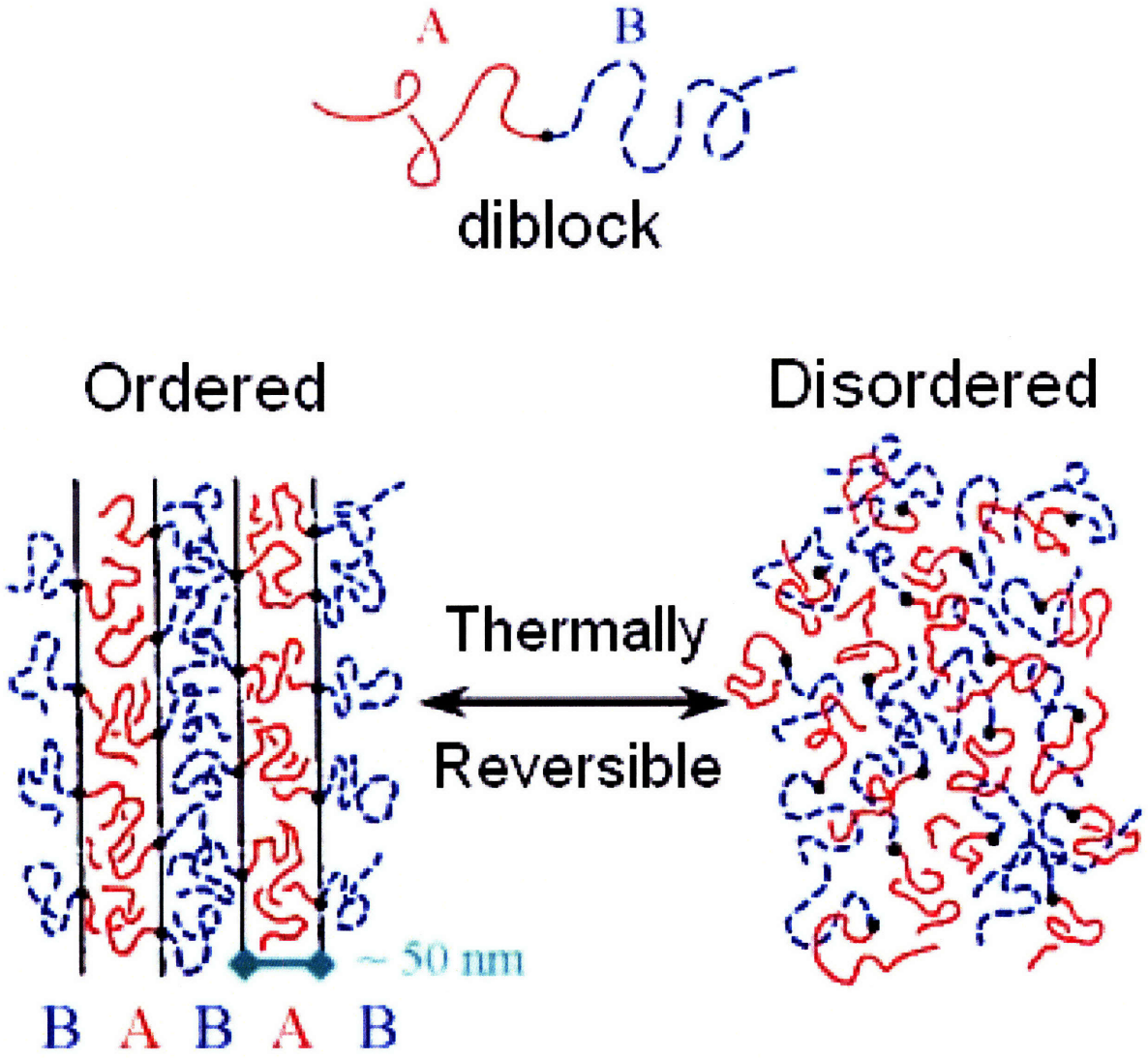

Figure 1-7. Schematic of an A-B diblock copolymer in the disordered and ordered states[26].

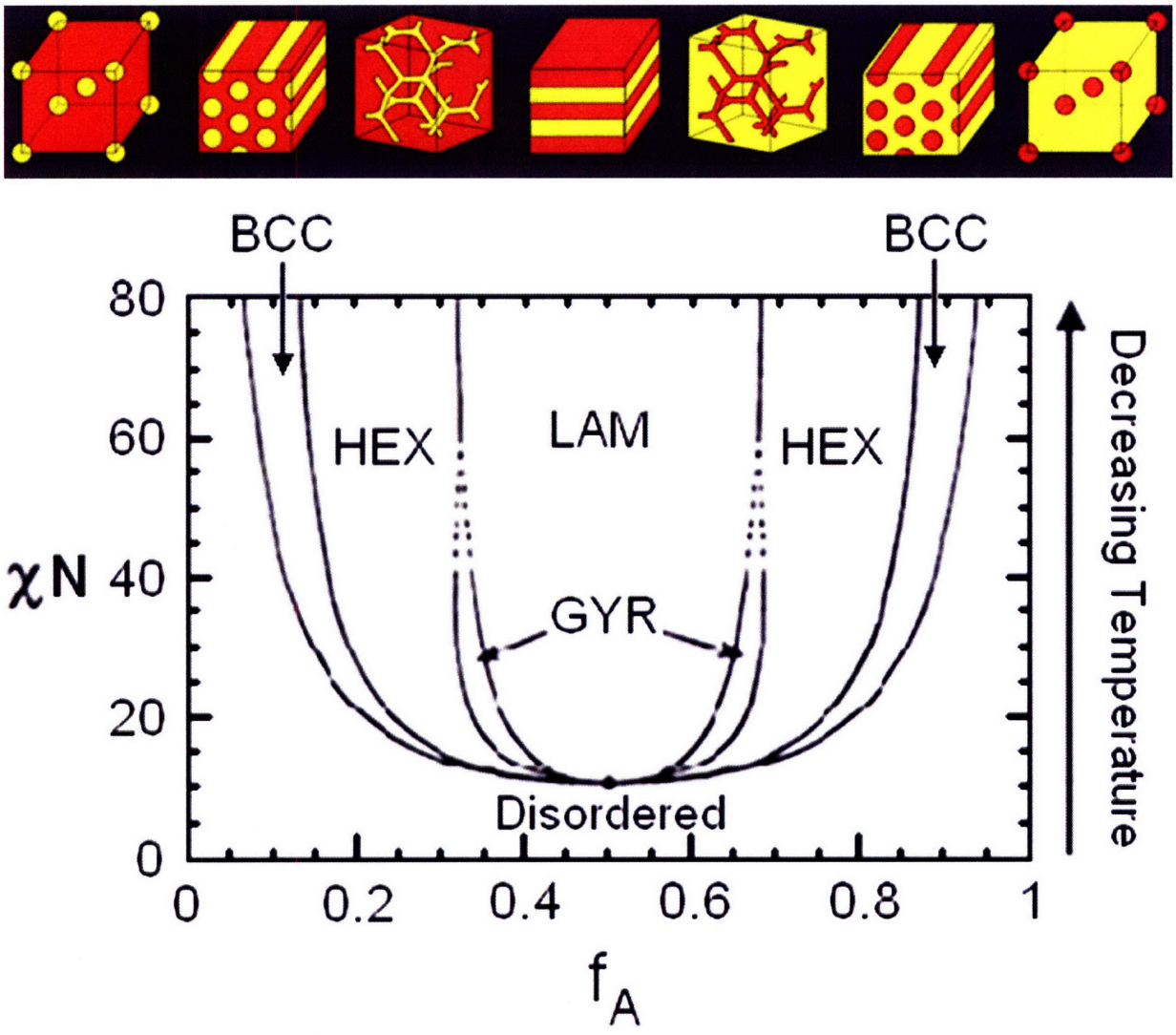

Figure 1-8. Top – From left to right, examples of cubic packed spheres, hexagonal packed cylinders, bicontinuous gyroids, lamellae, inverse bicontinuous gyroids, inverse hexagonal packed cylinders, and inverse cubic packed spheres. Bottom – Theoretical phase diagram of an amorphous-amorphous A-B diblock copolymer[28].

Many more complex block copolymer architectures, useful for a wide range of applications, can be designed and synthesized, including A-B-C and A-B-A triblock copolymers, graft copolymers, star block copolymers, and dendritic block copolymers. One such application for A-B-A triblock copolymers is thermoplastic elastomers, where the outer block has a high T_g (above the operating temperature) and the center block has a larger volume fraction and a T_g below the operating temperature. When phase segregation occurs the hard domains act as physical crosslinks creating an elastomer. The advantage that this type of elastomer has over a conventional chemically crosslinked elastomer is that it can be remolded and processed by raising the temperature above that of the hard block's T_g.

The incorporation of a liquid crystalline component into a block copolymer leads to an interplay between the liquid crystalline mesophase, significantly effecting the bulk self-assembly behavior[29-36]. The presence of a liquid crystalline block has been shown to stabilize certain morphologies, leading to asymmetries in the phase behavior of the block copolymer, as well as stabilization of certain liquid crystalline phases[37]. The inter-material dividing surface (IMDS) of the block copolymer mesophase can be used to orient the liquid crystalline mesophase, as the liquid crystals will preferentially orient with respect to the IMDS due to surface stabilization effects. Furthermore, the block copolymer IMDS can be used to confine a chiral smectic liquid crystalline mesophase, allowing for the helix to be unwound[38], leading to a material that can exhibit a net polarization.

Gaining a more complete understanding of the interactions between the block copolymer and the liquid crystalline mesophases is key for enabling control over the morphologies and thus the properties of these systems. Recent research has increased in the area of LC block copolymers, in order to tailor the desired electro-mechanical or electro-optical properties of the material in it's final form[31, 32, 36, 39-48].

1.3 Controlling the Morphologies of Side Chain Liquid Crystalline Block Copolymers

1.3.1 Mechanical Deformation

It is desired to control the morphology of these side chain liquid crystalline block copolymers (SCLCBCPs), namely to achieve uniform orientation of the block copolymer and the liquid crystalline mesophases.

Alignment of smectic C layers and can be achieved via two uniaxial deformations. The first uniaxial deformation aligns the director of the liquid crystal. However, there are still two possible orientations of the smectic layers, and a second uniaxial deformation is applied the angle ø to the first deformation. The angle ø corresponds to the tilt angle of the liquid crystal director relative to the smectic layer normal, as shown in Figure 1-9.

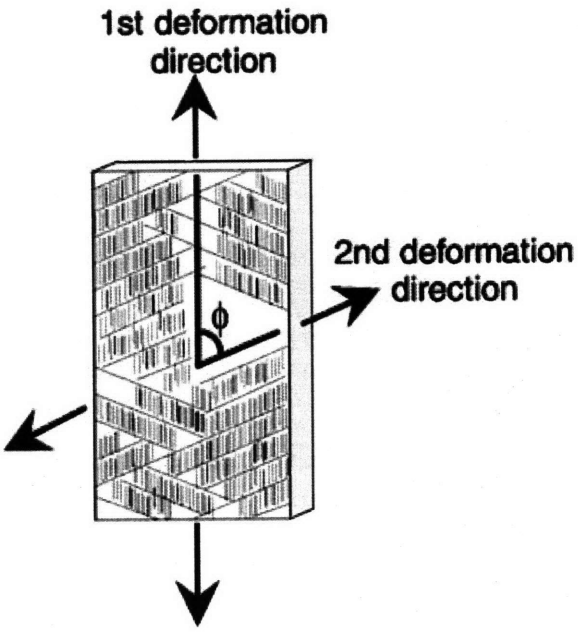

Figure 1-9. Geometry of sample deformation for achieving aligned smectic C layers[11].

Due to kinetic restrictions the typical morphology of a solvent cast block copolymer will be an isotropic multigrain structure. This morphology consists of domains that have a random distribution of orientations. In order to achieve a morphology that has a monodomain structure some type of external field must be applied. Examples of various techniques utilized to achieve well aligned materials include annealing[49], various shear fields[9, 32-34, 37, 47, 50-52], as well as electric and magnetic fields[53]. Several means of orientation have been previously reported for lamellar and cylindrical LC block copolymer systems, including: melt fiber drawing[32], roll casting[51], and oscillatory shear[33].

The interaction of the LC mesophase with the IMDS determines the orientation of the LC mesophase relative to the phase segregated morphology of the block copolymer. Figure 1-10 shows two possible models for the orientation of a LC mesophase confined within a cylindrical domain. In the homogeneous orientation had LC moieties and the smectic layer normal are

parallel to the IMDS and the cylinder axis. The homeotropic orientation has the smectic layer normal perpendicular to the IMDS. These same models could be used when considering a system where the LC mesophase is the matrix and the amorphous block is confined to the cylindrical domains. For the systems studied in this thesis the homogeneous orientation was observed in all cases. The homogeneous orientation is entropically favorable as the siloxane backbone has more conformational freedom than in the homeotropic orientation. Additionally, when the IMDS possesses curvature there is an additional enthalpic penalty for the homeotropic orientation.

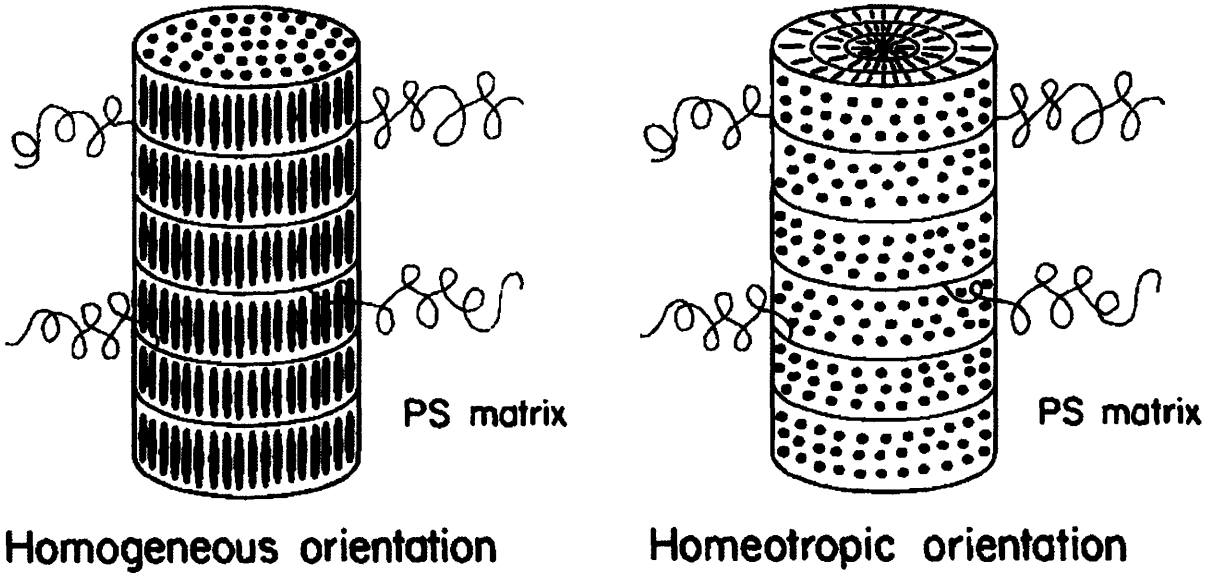

Figure 1-10. Schematic of two possible structures of LC-cylinder in a PS matrix (with a smectic A LC mesophase). Left: homogeneous (mesogen parallel to the IMDS). Right: homeotropic alignment (mesogen perpendicular to the IMDS)[54].

Oscillatory shear alignment of amorphous-amorphous diblock copolymers with a hexagonal close packed cylinder morphology typically results in cylinders parallel to the direction of the shear flow[27]. It has been shown that the incorporation of a LC can have a significant effect upon the orientation of the block copolymer relative to the shear flow[33, 35], see Figure 1-11.

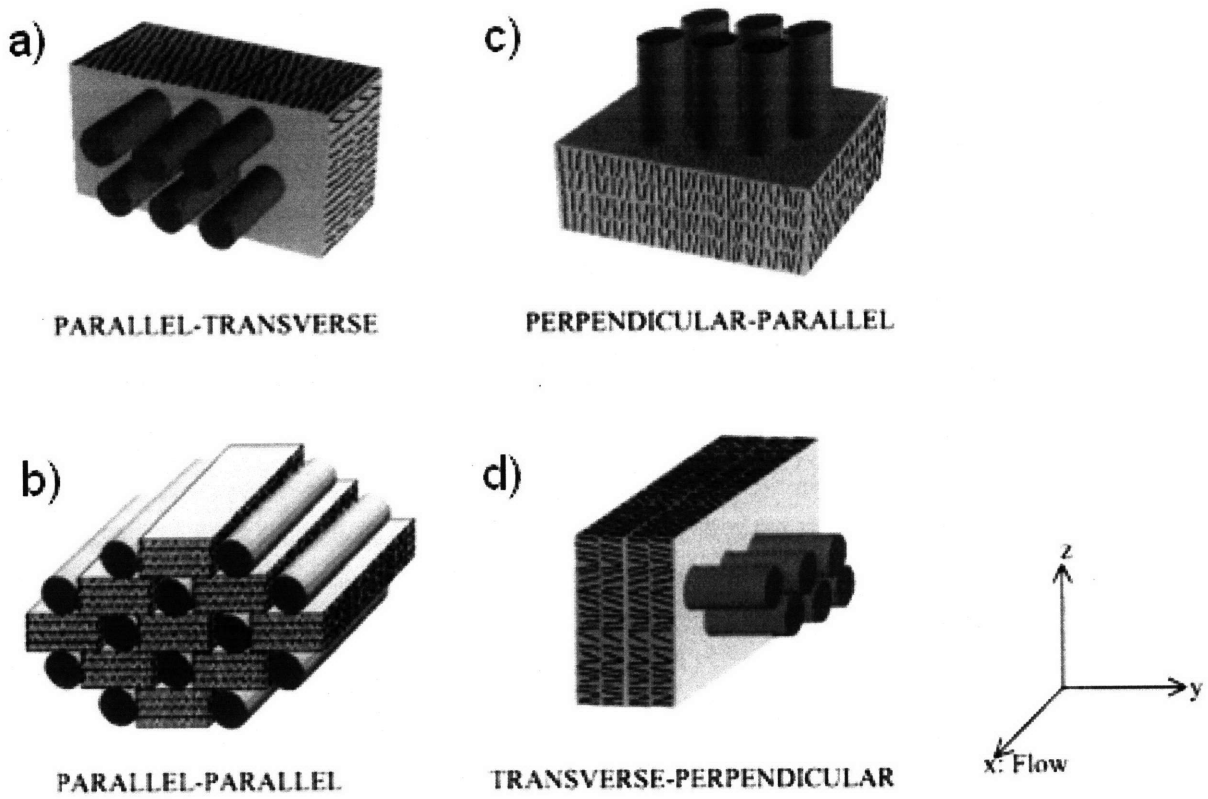

Figure 1-11. Schematic structural models of smectic layers and cylindrical microdomains with various anchoring of the mesogens with respect to the IMDS. Flow is along the *x* direction, *y* is the vorticity direction, and *z* is the gradient direction. (a) Model which places the cylinders in their preferred orientation along the flow direction and with homogeneous anchoring of the mesogens. The smectic layers are in the unfavorable transverse orientation. (b) Model which places the smectic layers in their preferred orientation parallel to the shear flow with homogeneous anchoring. The cylinders are in the unfavorable perpendicular orientation. (c) Model which places both the cylinders and the smectic layers in their preferred orientations, with heterogeneous anchoring. (d) Model which provides a compromise structure in which the cylinders are transverse and the layers are perpendicular but which maintains homogeneous anchoring of the mesogens.[33]

1.3.2 Thin Films

Block copolymer thin films have attracted much recent interest for potential use in nano-patterning applications[55, 56]. It is desired to achieve systems that exhibit long range order as well as gain control over the orientation of the domains. Recently progress has been made in achieving long range order in block copolymer thin films through techniques such as solvent annealing[57, 58], zone casting[59], and optical alignment[60]. Due to the large interfacial area of the thin film, the orientation of the domains depends greatly upon interfacial interactions between the different components and the substrate interfaces[40, 61-63]. The surface morphologies of block copolymer films can be probed with atomic force microscopy (AFM). Additionally, grazing incidence small-angle X-ray scattering (GISAXS) is a powerful non-invasive technique useful for investigating the lateral and transverse structures in the interior of such thin films[61, 64, 65].

The incorporation of a liquid crystalline (LC) component into a block copolymer system can have significant effects upon the self assembly behavior and domain orientation of thin films[40, 66, 67]. Additionally, liquid crystalline polymer thin films are of particular interest as they can allow for the introduction of responsive elements into the system, e.g. thermo-, chemo-, electro-, or photo-responsive. A prime example of a BCP thin film application is utility as lithographic masks[56]. Ordered and oriented layers of microphase domains, deposited onto a suitable substrate are selectively etched to remove one of the block components. Holes in the resulting mask can then be used to transfer the BCP pattern via other etching or deposition steps. More complex multi-component systems can be used to etch and remove one or more of the components allows for holes, pillars, or tubes to be created, examples of this are shown in Figure 1-12.

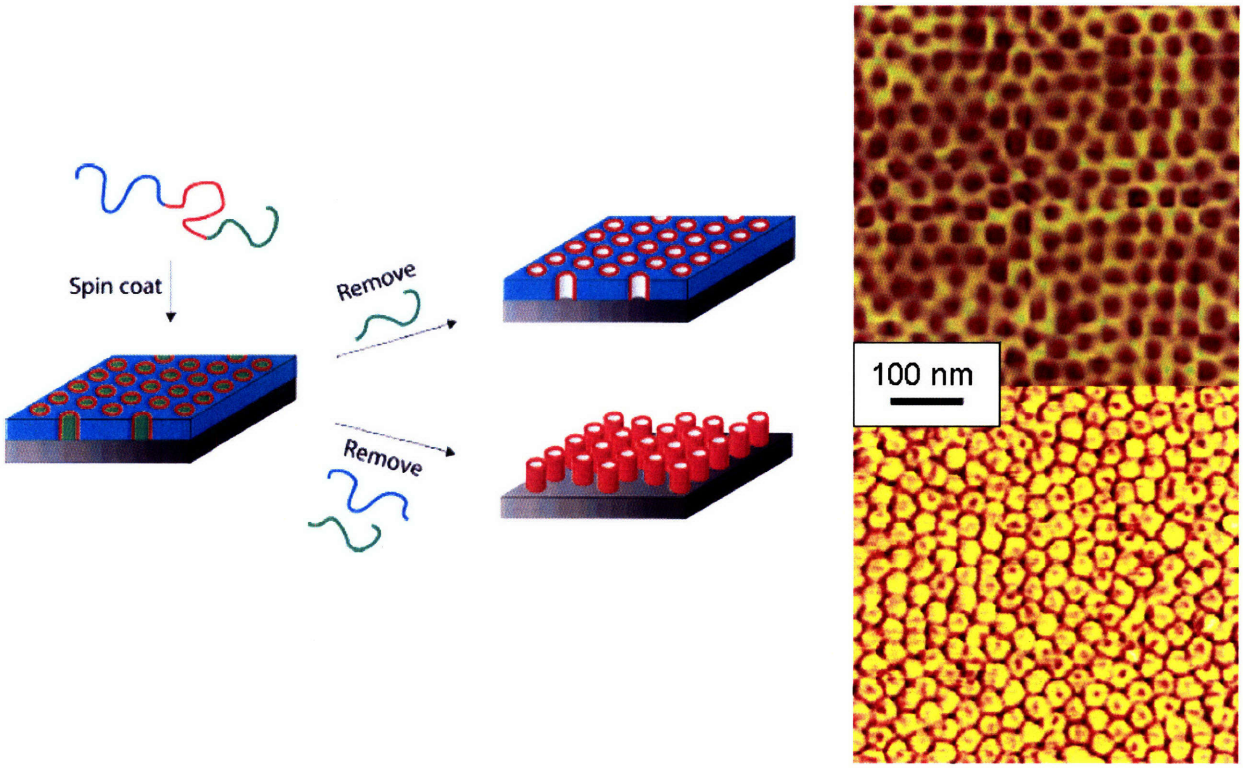

Figure 1-12. Left: schematic representation of the envisioned nanotemplates from thin films of ABC triblock terpolymers. Right Top: AFM phase image of a PI-PS-PLA thin film on a HMDS modified Si substrate after removal of the PLA block. Right Bottom: AFM phase image of a PI-PS-PLA thin film after removal of both the PLA and PI blocks.[68]

Templated self assembly (TSA) is a method of using topographical and/or chemically patterned templates in order to eliminate defects and induce registration and orientation in thin films of materials. In contrast to conventional epitaxy in which the lattice of a thin film bears a well-defined relationship to the lattice of the underlying substrate, templates for TSA are not required to be crystalline materials. For mesoscale templated self-assembly, the topographical and/or chemical pattern is used to guide the organization of the component materials. The

characteristic feature size L_S of templates ranges from the characteristic length scale, L_0, of the self-assembled materials to sizes much larger than L_0, as illustrated in Figure 1-13.

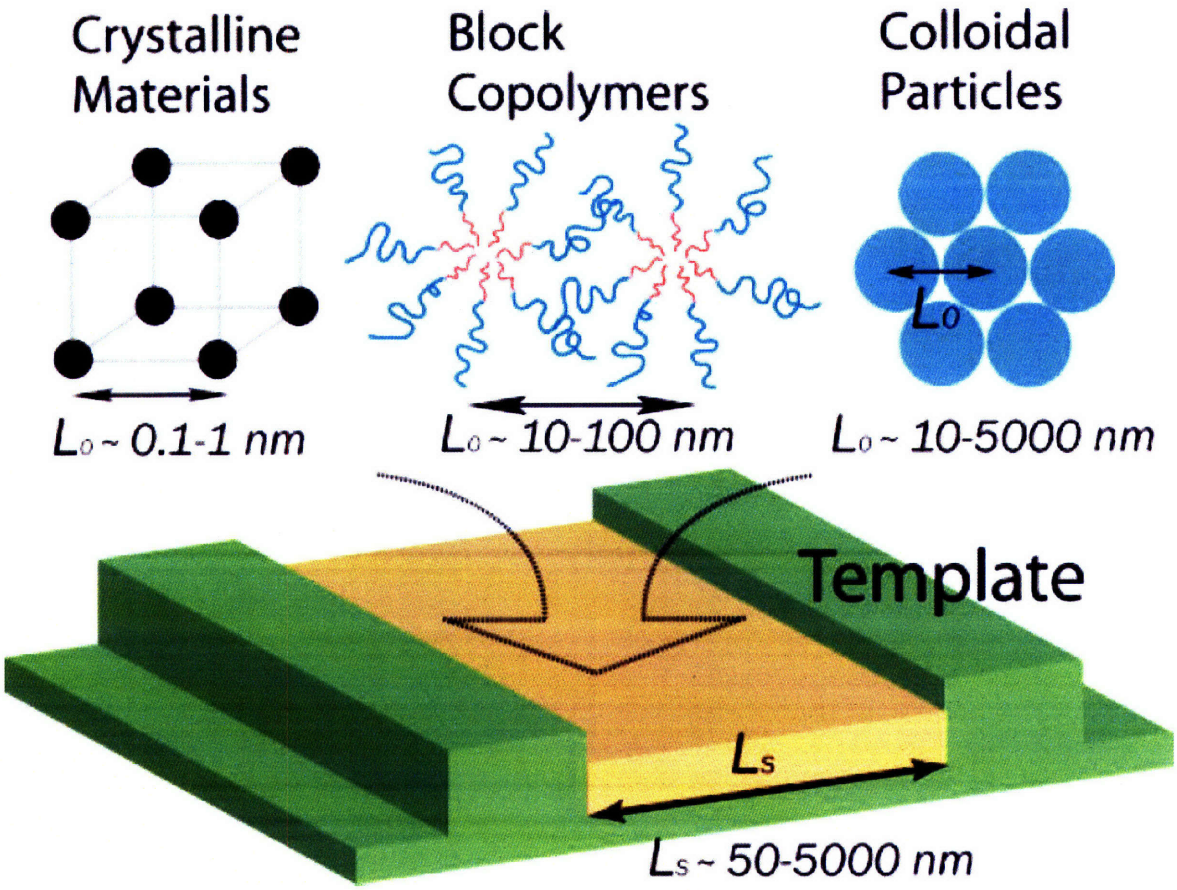

Figure 1-13. Illustration of some types of templated self assembly systems. Characteristic lengths (L_0) of crystalline materials, block copolymers, and colloid assemblies and the characteristic length (L_S) of the template are indicated[69].

A variety of block copolymer systems can be ordered through templated self assembly, including spheres, cylinders and lamellae. Both topographical and chemical pattern templates can be used to create discrete domains (2-D patterning) or channels (1-D patterning). Figure 1-14 shows a 1-D template of a cylindrical diblock copolymer. Increasing annealing times allows for greater registration with the template. For topological templates the edge roughness has an effect on the extent of ordering. Additionally, defects in the self-assembled pattern by can be created and controlled by introducing irregularities into the patterns. In chemical templates the relative interfacial energy contrast between the block copolymer components and the surface template materials affects the driving forces for regular ordering. If the interfacial energy difference is low there is less driving force for ordering, increasing the interfacial energy contrast leads to a greater enthalpic driving force, and increased long range order.

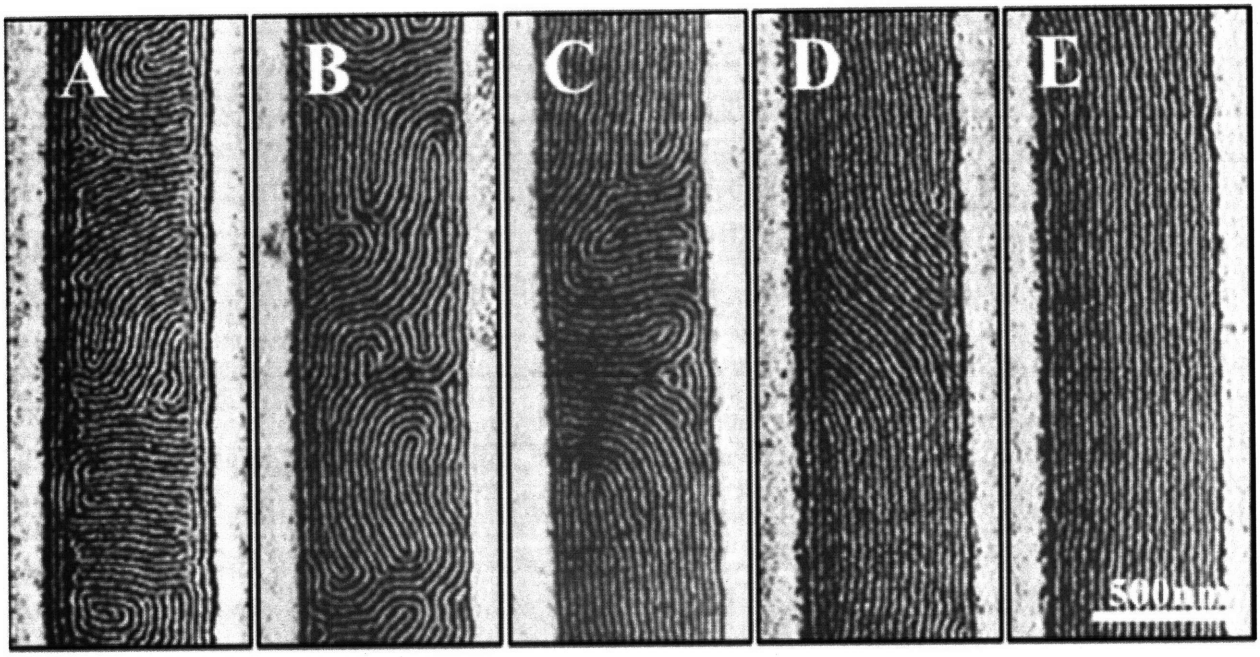

Figure 1-14. AFM images of a cylindrical PS-PEP cylindrical block copolymer in a 95nm deep and 600 nm wide template. Samples were annealed at 130°C for: a) 9, b) 14, c) 19, d) 24, and e) 33 hours[70].

These templating methods can also be applied to liquid crystalline block copolymers; however, the additional influence of the liquid crystalline mesophase must appropriately be taken into account. The liquid crystalline mesophase may have anchoring preferences with the IMDS and/or the substrate affecting the resulting orientation of the block copolymer to the substrate. Additionally, the influence of the LC mesophase will be highly dependent upon the degree of order in the LC mesophase, therefore thermal annealing can have a dramatic effect upon the orientation of such systems (Chapter 5).

1.4 Thesis Outline

Based on the discussion in this Chapter, the goal of this research is to synthesize novel side chain liquid crystalline block copolymers, with a functional low T_g siloxane block, and understand the self-assembly behavior to enable the development of responsive elastomeric systems. Chapter 2 describes the synthesis and characterization of these materials; a schematic of the system is shown in Figure 1-15. The synthetic techniques developed enable precise control over the covalent attachment of the LC moieties to a block copolymer backbone. The influence of variations in LC content significantly affects the morphologies of both the LC mesophase and the self-assembled block copolymer structures. Utilizing this control over the LC attachment, highly tunable morphological, thermal, and mechanical properties are demonstrated. Several techniques for the synthesis of liquid crystalline triblock copolymers are detailed in Chapter 3. These triblock copolymers result in thermoplastic elastomers, and the mechanical properties of the triblock copolymers are compared to the diblock counterparts. Chapter 4 describes the manipulation of the self-assembled morphologies through several mechanical deformation techniques. It is demonstrated that melt fiber drawing, tensile elongation and oscillatory shear can be used to obtain well oriented morphologies, and the physics driving the orientation is studied and understood. Chapters 5 and 6 discuss the thin films morphologies of these liquid crystalline block copolymers. Chapter 5 focuses on the effects of thermal annealing upon the orientation of the self-assembled structures relative to the substrate. Chapter 6 describes the effects of LC content and the film thickness upon the self-assembly of the liquid crystalline block copolymers. These studies provide critical insights in to techniques for manipulating the self-assembly of nanostructured thin films. Finally, this thesis closes with conclusions and recommendations for future work in Chapter 7.

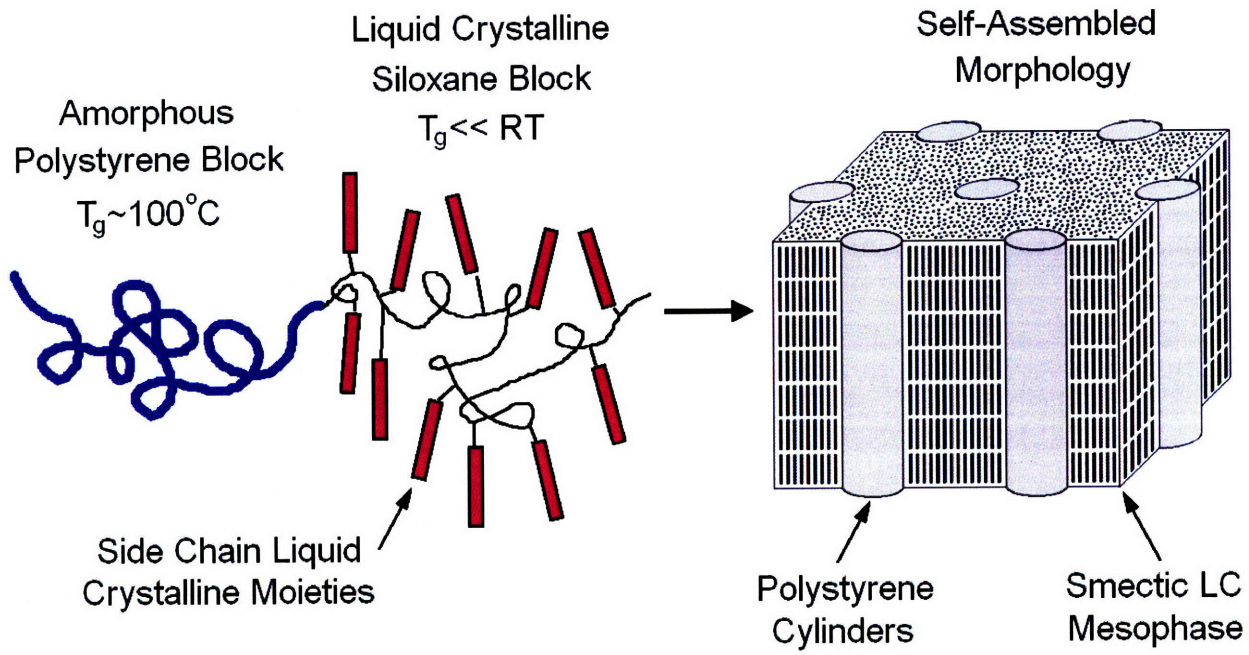

Figure 1-15. Left: Schematic of an amorphous – liquid crystalline block copolymer where polystyrene is the amorphous block and liquid crystals are attached in a side-on manner to a siloxane backbone resulting in the liquid crystalline block. Right: Schematic of self-assembled morphology where the polystyrene domains form hexagonal close packed cylinders and the siloxane based liquid crystalline block forms a smectic LC mesophase that comprises the matrix.

1.4 References

1. Alexander, L. E., *X-ray diffraction methods in polymer science.* John Wiley & Sons, Inc: New York, 1969.

2. Finnigan, B.; Jack, K.; Campbell, K.; Halley, P.; Truss, R.; Casey, P.; Cookson, D.; King, S.; Martin, D. *Macromolecules* **2005,** 38, 7386-7396.

3. Collings, P. J., *Liquid Crystals: Nature's Delicate Phase of Matter.* Princeton Science Library: Princeton, 1990.

4. Mayer, S.; Zentel, R. *Current Opinion in Solid State & Materials Science* **2002,** 6, (6), 545-551.

5. Lehmann, W.; Skupin, H.; Tolksdorf, C.; Gebhard, E.; Zentel, R.; Kruger, P.; Losche, M.; Kremer, F. *Nature* **2001,** 410, (6827), 447-450.

6. Naciri, J.; Srinivasan, A.; Jeon, H.; Nikolov, N.; Keller, P.; Ratna, B. R. *Macromolecules* **2003,** 36, (22), 8499-8505.

7. Rousseau, I. A.; Mather, P. T. *Journal of the American Chemical Society* **2003,** 125, (50), 15300-15301.

8. Thomsen, D. L.; Keller, P.; Naciri, J.; Pink, R.; Jeon, H.; Shenoy, D.; Ratna, B. R. *Macromolecules* **2001,** 34, (17), 5868-5875.

9. Hamley, I. W.; Davidson, P.; Gleeson, A. J. *Polymer* **1999,** 40, (12), 3599-3603.

10. Hiraoka, K.; Uematsu, Y.; Stein, P.; Finkelmann, H. *Macromolecular Chemistry and Physics* **2002,** 203, (15), 2205-2210.

11. Hiraoka, K.; Stein, P.; Finkelmann, H. *Macromolecular Chemistry and Physics* **2004,** 205, (1), 48-54.

12. Lehmann, W.; Hartmann, L.; Kremer, F.; Stein, P.; Finkelmann, H.; Kruth, H.; Diele, S. *Journal of Applied Physics* **1999,** 86, (3), 1647-1652.

13. Kohler, R.; Stannarius, R.; Tolksdorf, C.; Zentel, R. *Applied Physics a-Materials Science & Processing* **2005,** 80, (2), 381-388.

14. de Gennes, P. G. *Phys. Lett. A* **1969,** 28, 725.

15. Lendlein, A.; Jiang, H. Y.; Junger, O.; Langer, R. *Nature* **2005,** 434, (7035), 879-882.

16. Lemieux, R. P. *Soft Matter* **2005,** 1, (5), 348-354.

17. Yu, Y. L.; Ikeda, T. *Macromolecular Chemistry and Physics* **2005,** 206, (17), 1705-1708.

18. Li, M. H.; Keller, P. *Philosophical Transactions of the Royal Society a-Mathematical Physical and Engineering Sciences* **2006,** 364, (1847), 2763-2777.

19. Finkelmann, H.; Nishikawa, E.; Pereira, G. G.; Warner, M. *Physical Review Letters* **2001,** 8701, (1).

20. Beyer, P.; Zentel, R. *Macromolecular Rapid Communications* **2005,** 26, (11), 874-879.

21. Ikeda, T.; Sasaki, T.; Ichimura, K. *Nature* **1993,** 361, (6411), 428-430.

22. Ikeda, T.; Zushi, O.; Sasaki, T.; Ichimura, K.; Takezoe, H.; Fukuda, A.; Skarp, K. A. W. *Molecular Crystals and Liquid Crystals* **1993,** 225, 67.

23. Camacho-Lopez, M.; Finkelmann, H.; Palffy-Muhoray, P.; Shelley, M. *Nature Materials* **2004,** 3, (5), 307-310.

24. Yu, Y. L.; Ikeda, T. *Angewandte Chemie-International Edition* **2006,** 45, (33), 5416-5418.

25. Yu, Y. L.; Nakano, M.; Ikeda, T. *Nature* **2003,** 425, (6954), 145-145.

26. Bates, F. S.; Fredrickson, G. H. *Annual Review of Physical Chemistry* **1990,** 41, 525-557.

27. Hamley, I. W., *The Physics of Block Copolymers*. Oxford University Press: Oxford, 1998.

28. Matsen, M. W.; Bates, F. S. *Macromolecules* **1996,** 29, (23), 7641-7644.

29. Anthamatten, M.; Hammond, P. T. *Journal of Polymer Science Part B-Polymer Physics* **2001,** 39, (21), 2671-2691.

30. Anthamatten, M.; Wu, J. S.; Hammond, P. T. *Macromolecules* **2001,** 34, (24), 8574-8579.

31. Auad, M. L.; Kempe, M. D.; Kornfield, J. A.; Rendon, S.; Burghardt, W. R.; Yoon, K. *Macromolecules* **2005,** 38, (16), 6946-6953.

32. Ferri, D.; Wolff, D.; Springer, J.; Francescangeli, O.; Laus, M.; Angeloni, A. S.; Galli, G.; Chiellini, E. *Journal of Polymer Science Part B-Polymer Physics* **1998,** 36, (1), 21-29.

33. Osuji, C.; Zhang, Y. M.; Mao, G. P.; Ober, C. K.; Thomas, E. L. *Macromolecules* **1999,** 32, (22), 7703-7706.

34. Poser, S.; Fischer, H.; Arnold, M. *Journal of Polymer Science Part a-Polymer Chemistry* **1996,** 34, (9), 1733-1740.

35. Verploegen, E.; McAfee, L. C.; Tian, L. T.; Verploegen, D.; Hammond, P. T. *Macromolecules* **2007,** 40, (4), 777-780.

36. Yamada, M.; Itoh, T.; Hirao, A.; Nakahama, S.; Watanabe, J. *High Performance Polymers* **1998,** 10, (1), 131-138.

37. Hamley, I. W.; Castelletto, V.; Lu, Z. B.; Imrie, C. T.; Itoh, T.; Al-Hussein, M. *Macromolecules* **2004,** 37, (13), 4798-4807.

38. Clark, N. A.; Lagerwall, S. T. *Applied Physics Letters* **1980,** 36, (11), 899-901.

39. Moment, A.; Miranda, R.; Hammond, P. T. *Macromolecular Rapid Communications* **1998,** 19, (11), 573-579.

40. Figueiredo, P.; Geppert, S.; Brandsch, R.; Bar, G.; Thomann, R.; Spontak, R. J.; Gronski, W.; Samlenski, R.; Muller-Buschbaum, P. *Macromolecules* **2001,** 34, (2), 171-180.

41. Sentenac, D.; Demirel, A. L.; Lub, J.; de Jeu, W. H. *Macromolecules* **1999,** 32, (10), 3235-3240.

42. Omenat, A.; Lub, J.; Fischer, H. *Chemistry of Materials* **1998,** 10, (2), 518-523.

43. Merenga, A.; Shilov, S. V.; Kremer, F.; Mao, G.; Ober, C. K.; Brehmer, M. *Macromolecules* **1998,** 31, (25), 9008-9012.

44. Moment, A.; Hammond, P. T. *Polymer* **2001,** 42, (16), 6945-6959.

45. Zheng, W. Y.; Hammond, P. T. *Macromolecules* **1998,** 31, (3), 711-721.

46. Anthamatten, M.; Zheng, W. Y.; Hammond, P. T. *Macromolecules* **1999,** 32, (15), 4838-4848.

47. Galli, G.; Chiellini, E.; Francescangeli, O.; Ferri, D.; Wolff, D.; Springer, J.; Laus, M.; Angeloni, A. S. *Macromolecular Symposia* **1997,** 121, 235-244.

48. Zhou, W. J.; Kornfield, J. A.; Ugaz, V. M.; Burghardt, W. R.; Link, D. R.; Clark, N. A. *Macromolecules* **1999,** 32, (17), 5581-5593.

49. Guarini, K. W.; Black, C. T.; Yeuing, S. H. I. *Advanced Materials* **2002,** 14, (18), 1290.

50. Stein, P.; Assfalg, N.; Finkelmann, H.; Martinoty, P. *European Physical Journal E* **2001,** 4, (3), 255-262.

51. Zheng, W. Y.; Albalak, R. J.; Hammond, P. T. *Macromolecules* **1998,** 31, (8), 2686-2689.

52. Fischer, H.; Poser, S.; Arnold, M.; Frank, W. *Macromolecules* **1994,** 27, (24), 7133-7138.

53. Osuji, C.; Ferreira, P. J.; Mao, G. P.; Ober, C. K.; Vander Sande, J. B.; Thomas, E. L. *Macromolecules* **2004,** 37, (26), 9903-9908.

54. Mao, G. P.; Wang, J. G.; Clingman, S. R.; Ober, C. K.; Chen, J. T.; Thomas, E. L. *Macromolecules* **1997,** 30, (9), 2556-2567.

55. de Jeu, W. H.; Serero, Y.; Al-Hussein, M. *Ordered Polymeric Nanostructures at Surfaces* **2006,** 200, 71-90.

56. Fasolka, M. J.; Mayes, A. M. *Annual Review of Materials Research* **2001,** 31, 323-355.

57. Bang, J.; Kim, S. H.; Drockenmuller, E.; Misner, M. J.; Russell, T. P.; Hawker, C. J. *Journal of the American Chemical Society* **2006,** 128, (23), 7622-7629.

58. Peng, J.; Kim, D. H.; Knoll, W.; Xuan, Y.; Li, B. Y.; Han, Y. C. *Journal of Chemical Physics* **2006,** 125, (6), 064702.

59. Tang, C. B.; Tracz, A.; Kruk, M.; Zhang, R.; Smilgies, D. M.; Matyjaszewski, K.; Kowalewski, T. *Journal of the American Chemical Society* **2005,** 127, (19), 6918-6919.

60. Morikawa, Y.; Nagano, S.; Watanabe, K.; Kamata, K.; Iyoda, T.; Seki, T. *Advanced Materials* **2006,** 18, (7), 883-886.

61. Busch, P.; Krishnan, S.; Paik, M.; Toombes, G. E. S.; Smilgies, D. M.; Gruner, S. M.; Ober, C. K. *Macromolecules* **2007,** 40, (1), 81-89.

62. Cavicchi, K. A.; Russell, T. P. *Macromolecules* **2007,** 40, (4), 1181-1186.

63. Huang, E.; Pruzinsky, S.; Russell, T. P.; Mays, J.; Hawker, C. J. *Macromolecules* **1999,** 32, (16), 5299-5303.

64. Busch, P.; Rauscher, M.; Smilgies, D. M.; Posselt, D.; Papadakis, C. M. *Journal of Applied Crystallography* **2006,** 39, 433-442.

65. Muller-Buschbaum, P. *Analytical and Bioanalytical Chemistry* **2003,** 376, (1), 3-10.

66. Al-Hussein, M.; Serero, Y.; Konovalov, O.; Mourran, A.; Moller, M.; de Jeu, W. H. *Macromolecules* **2005,** 38, (23), 9610-9616.

67. Wu, J. S.; Fasolka, M. J.; Hammond, P. T. *Macromolecules* **2000,** 33, (4), 1108-1110.

68. Guo, S. W.; Rzayev, J.; Bailey, T. S.; Zalusky, A. S.; Olayo-Valles, R.; Hillmyer, M. A. *Chemistry of Materials* **2006,** 18, (7), 1719-1721.

69. Cheng, J. Y.; Ross, C. A.; Smith, H. I.; Thomas, E. L. *Advanced Materials* **2006,** 18, (19), 2505-2521.

70. Sundrani, D.; Darling, S. B.; Sibener, S. J. *Nano Letters* **2004,** 4, (2), 273-276.

Chapter 2 Synthesis and Characterization of Side Chain Liquid Crystalline Block Copolymers: Effects of Liquid Crystal Content

2.1 Introduction

There has been much work done over the past few decades investigating the self-assembly behavior of block copolymers (BCPs)[1-3]. Precise control over anionic and living free radical polymerizations allowed for the design of BCPs with specific compositions and lengths[3]. Additionally, a wide variety of processing techniques have been used to manipulate the microphase separated morphologies of block copolymers, including annealing –thermal[4] or solvent[5]– the application of an electric[6] or magnetic[7] field, and various mechanical deformation techniques[8-12]. This control over the self-assembly behavior allows the structure and properties of such materials to be tailored for specific applications.

The incorporation of a liquid crystalline (LC) component into a BCP has been shown to have significant effects upon the self-assembly behavior[13-19]. In the simple A-B BCP systems, in which two linear amorphous blocks are covalently linked, the morphological phase diagram is typically symmetrical. When a LC component is introduced several factors including conformational asymmetry, structural asymmetry, and the anchoring of the LC mesophase to the (IMDS) can alter the self-assembly behavior. The inter-material dividing surface (IMDS) of the

block copolymer mesophase can be used to orient the liquid crystalline mesophase, as the LCs will preferentially orient with respect to the IMDS due to surface stabilization effects[7, 20]. In this way a well oriented block copolymer mesophase can be used to template order in the LC mesophase. The ability to systematically control the content of covalently attached LC moieties enables a unique tunability, allowing for the structure and properties of the LCBCP system to be tailored for specific applications. Here I will describe a highly tunable LC attachment chemistry, into a low T_g siloxane backbone, enabling the investigation of a very broad range of LC morphologies and properties. This is the first example of a system where the block copolymer self-assembly has been systematically studied specifically as a function of the covalent attachment of LC moieties.

In this Chapter I will discuss a means of controlling the morphologies through variations in the initial composition of the block copolymer as well as the LC content[21]. We have synthesized poly(vinylmethyldisiloxane) (PVMS) homopolymers and poly(styrene)-poly(vinylmethyldisiloxane) (PS-PVMS) block copolymers with varying block lengths. Liquid crystals containing a siloxane tip were added across the vinyl functionalized polymer via hydrosilylation[20, 22-24]. Six different LCs were synthesized with either a butyl ester or fluorinated hexyl ester end group and varying lengths of flexible alkyl spacers connecting the mesogen to the polymer chain. A key advantage of this system is the low glass transition temperature of the siloxane block, which makes a room-temperature elastomer possible[20]. In past studies of liquid crystalline block copolymers it has been difficult to achieve a material with a low LC block glass transition temperature, particularly in combination with tunable functionalization. The thermal properties and self-assembled LC morphologies of these materials were characterized via differential scanning calorimetry (DSC) and small-angle X-ray scattering (SAXS), respectively.

A direct correlation was found between the LC attachment percentage and the properties of the LC mesophase, including the smectic layer spacing and the smectic to isotropic transition temperature (T_{iso})[25, 26].

The morphology can be tailored through variations in the LC attachment percent allowing for a single polymer backbone to yield a range of morphologies. The reaction rate of the liquid crystal attachment is relatively slow, ~1% per minute. Thus, it is possible to remove and quench portions of the reacting solution; enabling a range of attachment percents and morphologies to be obtained from a single synthesis batch. To the best of our knowledge this is the first example in which the morphology of a block copolymer can be systematically controlled by variations in covalently attached side chain liquid crystals. We detail the effects of varying the attachment percent, which include the interaction parameter (χ) between the blocks, as well as the interactions between the LC mesophase and the block copolymer IMDS.

Furthermore, we demonstrate the ability to systematically tune the elastic modulus and thermo-mechanical properties of this system over a broad range, through variations in the LC content. Similar control over mechanical properties has been shown for polymer/inorganic hybrid materials[27], but this is the first example of this nature for a liquid crystalline polymer system. This unique ability to tailor the morphology and thermo-mechanical properties of these hierarchically structured materials enables the design of electro-, magneto-, and photo-responsive systems for use in actuator, sensing, or microfluidics applications.

2.2 Experimental

2.2.1 Instrumentation and Materials

A Waters gel permeation chromatography (GPC) system equipped with 1 Styragel HT3 column (500-30,000 MW range), 1 Styragel HT4 column (5,000-600,000 MW range), 1 Styragel HT5 column (50,000-$4 \cdot 10^6$ MW range), a refractive index detector, and a UV detector (254nm) was used for molecular weight measurement relative to polystyrene standards. Tetrahydrofuran (THF) flowing at 1ml/min was the mobile phase. ^{1}H NMR measurements were made with a Bruker Advance DPX400 400MHz instrument. Samples (~5-10 mg/ml) were dissolved in $CDCl_3$, with TMS as an internal reference. A TA Instruments Q1000 was used for Differential Scanning Calorimetry (DSC), the heating and cooling rate was 10°C min^{-1} in all cases. A TA Instruments Q800 was used for Dynamic Mechanical Analysis (DMA). The heating rate was 3°C min^{-1} and oscillations of amplitude of 25μm were applied to films in 0.02 MPa of tension at a frequency of 1 Hz. A TA Instruments AR 2000 Rheometer using a 5mm aluminum parallel plate geometry in an environmental test chamber was used for rheological analysis. The heating rate was 5°C min^{-1} and 10% oscillatory strain was applied to films ~ 0.5mm in thickness. SAXS studies including temperature dependent SAXS studies were preformed using a Linkam CSS450 shear cell at the X27 beamline at the National Synchrotron Light Source (NSLS) at Brookhaven National Laboratory (BNL). The wavelength of the X-rays was 0.1371nm, and silver behenate was used to calibrate the sample to detector distance with a first order scattering vector of q of 1.076nm^{-1} (with $q = 4\pi \sin\theta/\lambda$ where 2θ is the scattering angle and λ is the wavelength). Fuji CR imaging plates were used to collect scattering data. Additional SAXS experiments were performed at the G1 beamline at the Cornell High Energy Synchrotron Source (CHESS), where the wavelength was 1.239Å. A slow-scan CCD-based X-ray detector, home built by Drs. M.W.

Tate and S.M. Gruner of the Cornell University Physics Department, was used for data collection. All scattering data were processed using the commercially available software Polar. A Reichert-Jung FC4E Ultracut E was used to ultracryomicrotome samples of 50-60nm in thickness. The diamond knife temperature was set at –100°C and the sample temperature set at –105°C. Samples were then observed with a JEOL 200CX electron microscope in bright field mode with accelerating voltages of 160-200kV.

TLC plates (Whatman, AL SIL G/UV), hexane, ethyl acetate, ethanol and methanol were purchased from VWR and used as received. Dichloromethane, toluene and tetrahydrofuran were taken from an Innovative Technology Pure-Solv 400 Solvent Purification System. Cyclohexane was purchased from Aldrich, dried over calcium hydride, degassed and vacuum distilled under nitrogen. Styrene was purchased from Aldrich, washed with 1M sodium hydroxide and dried over magnesium sulfate. Styrene was degassed and vacuum distilled from calcium hydride just prior to use. 1,1,3,3-Tetramethyldisiloxane, N, N-dimethylformamide and N, N-diisopropylcarbodiimide were purchased from Fluka. 4-(Dimethylamino)pyridinium p-toluenesulfonate (DPTS) was prepared in the method of Moore and Stupp[28]. All other chemicals were purchased from Aldrich and used without further purification.

2.2.2 Polymer Synthesis

All manipulation of compounds was performed under nitrogen using standard glovebox techniques. A poly(vinylmethylsiloxane) (PVMS) homopolymer was synthesized via anionic polymerization (Figure 2-1). 0.037 mg of 1,4-Bis(hydroxydimethylsilyl)benzene was dissolved in 30mL of tetrahydrofuran in a 50 mL round bottom flask. 200 μL of n-butyl lithium was then added and stirred for 5 minutes at which point 5 g of the V3 monomer was added and stirred for

12 hours. Termination of the reaction was performed by end capping with an excess (0.3 g) of trimethylchlorosilane, with was added and let stir for 1 hour. The solution was then precipitated into methanol and a viscous oil recovered. The liquid crystal was attached to the resulting homopolymer in the same manner as for the PS-PVMS diblock copolymer. The number-average molecular weight (*M*n) of the PVMS homopolymer was 21,300 g/mol with a polydispersity index (*M*w/*M*n) of 1.14. The substitution percent of the LC onto the homopolymer was similar to that of the PS-PVMS diblock copolymer.

The synthesis of poly(styrene)-poly(vinylmethylsiloxane) (PS-PVMS) block copolymer was previously reported[20, 29]. Several small changes were made to the synthesis previously described. The initiator for the polystyrene polymerization was n-butyl lithium, and the purifications of the monomers and solvents are described in the previous section. The D3 monomer was added to the living styrene and reacted for only 6 hours and the V3 monomer was reacted for 48 hours. All of the anionic polymerizations were carried out in a glovebox in a nitrogen environment. The resulting polymer is technically a triblock copolymer, however considering the small amount of hexamethylcyclotrisiloxane added, for simplicity these polymers will be referred to as PS-PVMS diblock copolymers.

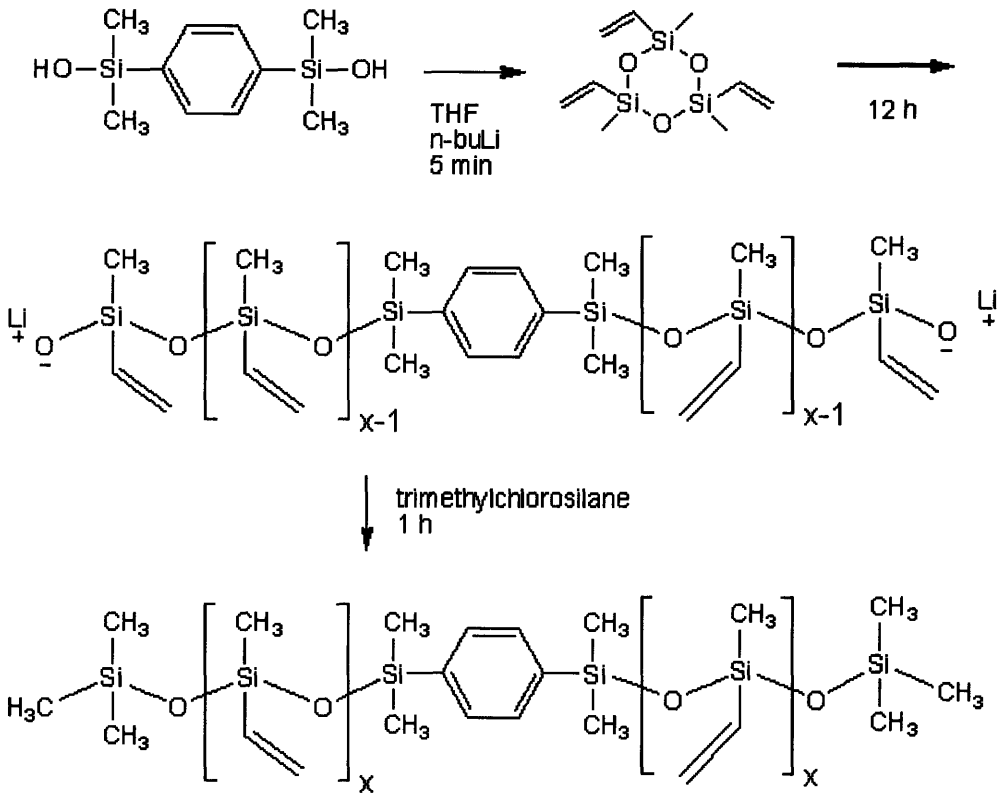

Figure 2-1. Schematic of PVMS homopolymer synthesis.

2.2.3 Liquid Crystal Synthesis

All syntheses were carried out with modifications on the liquid crystal and polyesterification chemistries of Svensson et al.[30] and Moore and Stupp[28]. All manipulations were performed under nitrogen following standard Schlenk procedure. Throughout this paper the **nBPP4** and **nBPP2F4** designation will be used to denote all final, siloxane-containing LC monomers. **P4** denotes the four carbons of the nonfluorinated LC butyl ester end group while **P2F4** denotes fluorination on the last four carbons of the LC hexyl ester group, and **n** is the length of the flexible spacer (4, 6 or 8 carbons). A detailed written procedure is provided for the synthesis of intermediates **1-3** and the product **4BPP4** (Figure 2-2).

Syntheses of the fluorinated compounds **4BPP2F4, 6BPP2F4** and **8BPP2F4** follow identical methods (Figure 2-3) except for the replacement of butanol by fluorinated hexanol. 6-Bromo-1-hexene and 8-bromo-1-octene were the respective precursors in the syntheses of **6BPP4/6BPP2F4** and **8BPP4/6BPP2F4**. All compounds were further purified following the **4BPP4** procedure unless otherwise indicated. All products and intermediates were verified via ^{1}H NMR spectrometry. NMR data were in accordance with the structures for all cases.

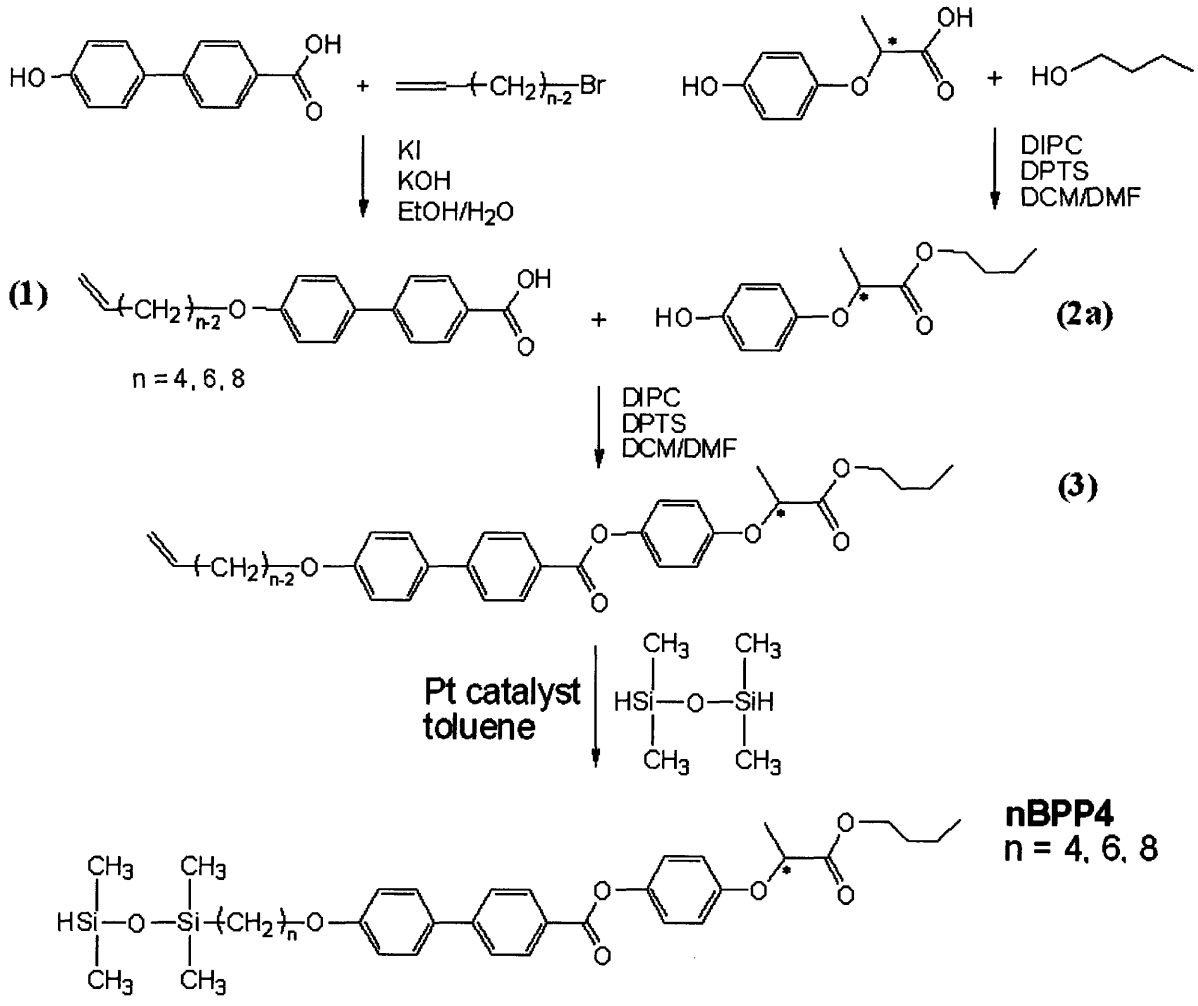

Figure 2-2. Schematic of nonfluorinated LC synthesis.

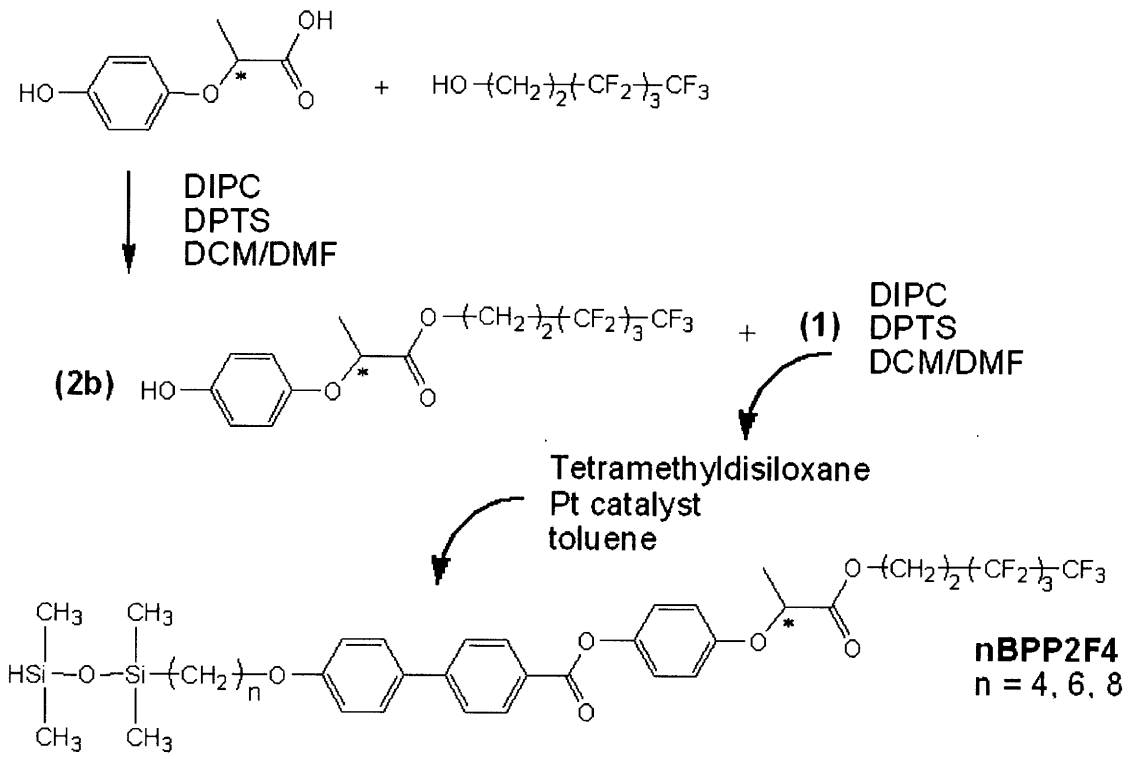

Figure 2-3. Schematic of fluorinated LC synthesis.

4'-(3-Buten-1-yloxy)-[1,1'-biphenyl]-4-carboxylic acid (1) Biphenyl precursor to **4BPP4.** 4'-Hydroxy-4-biphenylcarboxylic acid (6.43 g, 0.030 mol), potassium hydroxide (5.05 g, 0.090 mol) and potassium iodide (1.00 g, 6.0 mmol) were combined with 450 ml ethanol and 25 ml water in a 1 L round bottom flask. The pale yellow mixture was stirred at 50°C. 4-Bromo-1-butene (6.09 ml, 0.060 mol) was added after 1 h and the mixture was refluxed. After 24 h the reaction was cooled to 0°C and 300 ml water added. After stirring at 0°C for 1 h concentrated hydrochloric acid was added slowly (~9 ml, pH ≤). White precipitates were filtered and washed with cold water. Recrystallization was performed from ethanol. Yield: 2.78 g, 0.010 mol, 34.5%. ^{1}H NMR (DMSO) (δ): 2.48 (m, 2H, OCH_2CH_2), 4.05 (t, 2H, OCH_2CH_2), 5.13 (q, 2H,

CH=C*H*$_2$), 5.87 (m, 1H, C*H*=CH$_2$), 7.03 (d, 2H, Ar*H*), 7.66 (d, 2H, Ar*H*), 7.73 (d, 2H, Ar*H*), 7.98 (d, 2H, Ar*H*).

4'-(5-Hexen-1-yloxy)-[1,1'-biphenyl]-4-carboxylic acid Biphenyl precursor for **6BPP4** was synthesized from 4'-hydroxy-4-biphenylcarboxylic acid and 6-bromo-1-hexene (8.02 ml, 0.060 mol). Yield: 8.07 g, 0.027 mol, 90.2%. ^{1}H NMR (DMSO) (δ):1.52 (m, 2H, OCH$_2$CH$_2$C*H*$_2$CH$_2$), 1.73 (m, 2H, OCH$_2$C*H*$_2$CH$_2$CH$_2$), 2.10 (m, 2H, OCH$_2$CH$_2$CH$_2$C*H*$_2$), 4.00 (t, 2H, OC*H*$_2$CH$_2$CH$_2$CH$_2$), 5.02 (q, 2H, CH=C*H*$_2$), 5.83 (m, 1H, C*H*=CH$_2$), 7.04 (d, 2H, Ar*H*), 7.66 (d, 2H, Ar*H*), 7.75 (d, 2H, Ar*H*), 7.97 (d, 2H, Ar*H*).

4'-(7-Octen-1-yloxy)-[1,1'-biphenyl]-4-carboxylic acid Biphenyl precursor for **8BPP4** was synthesized from 4'-hydroxy-4-biphenylcarboxylic acid and 8-bromo-1-octene (10.07 ml, 0.060 mol). Yield: 8.64 g, 0.027 mol, 88.8%. ^{1}H NMR (DMSO) (δ):1.41 (m, 6H, OCH$_2$CH$_2$*(CH$_2$)*$_3$CH$_2$), 1.75 (m, 2H, OCH$_2$C*H*$_2$(CH$_2$)$_3$CH$_2$), 2.05 (m, 2H, OCH$_2$CH$_2$(CH$_2$)$_3$C*H*$_2$), 4.02 (t, 2H, OC*H*$_2$CH$_2$(CH$_2$)$_3$CH$_2$), 5.00 (q, 2H, CH=C*H*$_2$), 5.83 (m, 1H, C*H*=CH$_2$), 7.05 (d, 2H, Ar*H*), 7.67 (d, 2H, Ar*H*), 7.76 (d, 2H, Ar*H*), 8.00 (d, 2H, Ar*H*).

(2R)-2-(4-Hydroxyphenoxy)propionic acid butyl ester (2a) In a 1 L round bottom flask R-(+)-2-(4-hydroxypenoxy) propionic acid (27.3 g, 0.150 mol), butanol (54.9 ml, 0.600 mol) and DPTS (11.74 g, 0.038 mol) were dissolved in 600 ml dichloromethane (DCM) and 60 ml dimethylformamide (DMF). Diisopropylcarbodiimide (DIPC) (27.9 ml, 0.180 mol) was added. The reaction was stirred for 24 h, filtered to remove urea, washed 3 times with 0.1 M hydrochloric acid, 2 times with brine and dried with magnesium sulfate. Rotatory evaporation removed solvent. Further purification was from silica column (4:1 hexane: ethyl acetate). The product (pink-gray oil) was not air and moisture-sensitive and was stored at room temperature for later use. Yield: 25.0 g, 0.104 mol, 69.9%. ^{1}H-NMR ($CDCl_3$) (δ): 0.87 (t, 3H,

$OCH_2CH_2CH_2CH_3$), 1.32 (m, 2H, $OCH_2CH_2CH_2CH_3$), 1.58 (m, 5H, OCH^*CH_3 + $OCH_2CH_2CH_2CH_3$), 4.17 (m, 2H, $OCH_2CH_2CH_2CH_3$), 4.68 (q, 1H, OCH^*CH_3), 6.74 (m, 4H, ArH).

(2R)-2-(4-Hydroxyphenoxy)propionic acid 3,3,4,4,5,5,6,6,6-nonafluoro-1-hexyl ester (2b) The fluorinated hexyl ester derivative was synthesized from R-(+)-2-(4-hydroxypenoxy)propionic acid (1.74 g, 0.0096 mol), fluorinated hexanol (10.1 g, 0.038 mol), DPTS (0.747 g, 0.0024 mol) and DIPC (1.77 ml, 0.011 mol) in 100 ml DCM and 10 ml DMF. The product was washed, dried and further purified through silica column (hexane: ethyl acetate 2:1). Yield: 2.90 g, 0.0068 mol, 70.9%. ^{1}H-NMR ($CDCl_3$) (δ):1.62 (d, 3H, OCH^*CH_3), 2.46 (m, 2H, $OCH_2CH_2CF_2$), 4.48 (t, 2H, $OCH_2CH_2CF_2$), 4.70 (q, 1H, OCH^*CH_3), 6.76 (m, 4H, ArH).

4-[(1R)-2-butoxy-1-methyl-2-oxoethoxy]phenyl 4'-(3-Buten-1-yloxy)-[1,1'-biphenyl]-4-carboxylate (3) Vinyl mesogen precursor for **4BPP4**. Intermediate **(1)** (2.60 g, 0.010 mol), **(2)** (2.48 g, 0.010 mol) and DPTS (0.81 g, 2.60 mmol) were dissolved in 100 ml DCM and 15 ml DMF in a 250 ml round bottom flask. DIPC (1.93 ml, 0.013 mol) was added. The reaction was stirred for 24 h, filtered to remove urea, washed 3 times with 0.1 M hydrochloric acid, 2 times with brine and dried with magnesium sulfate. Rotatory evaporation removed solvent. White to pale yellow solid was obtained from silica column (DCM). Yield: 3.91 g, 8.00 mmol, 76.9%. ^{1}H-NMR ($CDCl_3$) (δ): 0.93 (t, 3H, $OCH_2CH_2CH_2CH_3$), 1.35 (m, 2H, $OCH_2CH_2CH_2CH_3$), 1.65 (m, 5H, OCH^*CH_3 + $OCH_2CH_2CH_2CH_3$), 2.60 (q, 2H, $ArOCH_2CH_2CH{=}CH_2$), 4.09 (t, 2H, $ArOCH_2CH_2CH{=}CH_2$), 4.19 (m, 2H, $OCH_2CH_2CH_2CH_3$), 4.76 (q, 1H, OCH^*CH_3), 5.18 (q, 2H, $CH{=}CH_2$), 5.94 (m, 1H, $CH{=}CH_2$), 6.94 (d, 2H, ArH), 7.02 (d, 2H, ArH), 7.15 (d, 2H, ArH), 7.59 (d, 2H, ArH), 7.68 (d, 2H, ArH), 8.23 (d, 2H, ArH).

4-[(1R)-2-butoxy-1-methyl-2-oxoethoxy]phenyl 4'-(5-Hexen-1-yloxy)-[1,1'-biphenyl]-

4-carboxylate Vinyl precursor to **6BPP4.** Yield: 8.80 g, 0.017 mol, 64.0%. ^{1}H-NMR ($CDCl_3$) (δ): 0.94 (t, 3H, $OCH_2CH_2CH_2CH_3$), 1.35 (m, 2H, $OCH_2CH_2CH_2CH_3$), 1.64 (m, 9H, OCH^*CH_3 + $OCH_2CH_2CH_2CH_3$ + $ArOCH_2CH_2CH_2CH_2CH{=}CH_2$), 1.83 (m, 2H, $ArOCH_2CH_2CH_2CH_2CH{=}CH_2$), 2.17 (q, 2H, $ArOCH_2CH_2CH_2CH_2CH{=}CH_2$), 4.04 (t, 2H, $ArOCH_2CH_2CH_2CH_2CH{=}CH_2$), 4.19 (m, 2H, $OCH_2CH_2CH_2CH_3$), 4.76 (q, 1H, OCH^*CH_3), 5.02 (q, 2H, $CH{=}CH_2$), 5.85 (m, 1H, $CH{=}CH_2$), aryl region same as **4BBP4** vinyl mesogen.

4-[(1R)-2-butoxy-1-methyl-2-oxoethoxy]phenyl 4'-(7-Octen-1-yloxy)-[1,1'-biphenyl]-4-carboxylate Vinyl precursor to **8BPP4.** Yield: 9.16 g, 0.017 mmol, 57.5%. ^{1}H-NMR ($CDCl_3$) (δ): 0.93 (t, 3H, $OCH_2CH_2CH_2CH_3$), 1.46-1.24 (m, 6H, $ArOCH_2CH_2(CH_2)_3CH_2CH{=}CH_2$), 1.52 (m, 2H, $OCH_2CH_2CH_2CH_3$), 1.60 (s, 3H, OCH^*CH_3), 1.64 (m, 2H, $OCH_2CH_2CH_2CH_3$), 1.85 (m, 2H, $ArOCH_2CH_2(CH_2)_3CH_2CH{=}CH_2$), 2.09 (q, 2H, $ArOCH_2CH_2(CH_2)_3CH_2CH{=}CH_2$), 4.03 (t, 2H, $ArOCH_2CH_2(CH_2)_3CH_2CH{=}CH_2$), 4.20 (m, 2H, $OCH_2CH_2CH_2CH_3$), 4.77 (q, 1H, OCH^*CH_3), 5.00 (q, 2H, $CH{=}CH_2$), 5.84 (m, 1H, $CH{=}CH_2$), aryl region same as **4BBP4** vinyl mesogen.

4-[(1R)-2-(3,3,4,4,5,5,6,6,6-nonafluoro-1-hexoxy)-1-methyl-2-oxoethoxy]phenyl 4'-(3-Buten-1-yloxy)-[1,1'-biphenyl]-4-carboxylate Vinyl precursor to **4BPP2F4.** Yield: 3.47 g, 0.0051 mol, 91.6%. Product was used in hydrosilylation without column purification. ^{1}H-NMR ($CDCl_3$) (δ): 1.08 (d, 3H, OCH^*CH_3), 1.55 (m, 2H, $OCH_2CH_2(CF_2)_3CF_3$), 2.50 (m, 2H, $ArOCH_2CH_2CH{=}CH_2$), 4.02 (t, 2H, $ArOCH_2CH_2CH{=}CH_2$), 4.42 (m, 2H, $OCH_2CH_2(CF_2)_3CF_3$), 4.74 (q, 1H, OCH^*CH_3), 5.10 (q, 2H, $CH{=}CH_2$), 5.87 (m, 1H, $CH{=}CH_2$), 6.85 (d, 2H, Ar*H*), 6.94 (d, 2H, Ar*H*), 7.06 (d, 2H, Ar*H*), 7.53 (d, 2H, Ar*H*), 7.62 (d, 2H, Ar*H*), 8.13 (d, 2H, Ar*H*).

4-[(1R)-2-(3,3,4,4,5,5,6,6,6-nonafluoro-1-hexoxy)-1-methyl-2-oxoethoxy]phenyl 4'-(5-Hexen-1-yloxy)-[1,1'-biphenyl]-4-carboxylate Vinyl precursor to **6BPP2F4.** Yield: 13.53 g,

0.020 mol, 100%. Product was used in next hydrosilylation without column purification. ^{1}H-NMR ($CDCl_3$) (δ): 1.03 (d, 3H, OCH*CH_3), 1.55 (m, 2H, $OCH_2CH_2(CF_2)_3CF_3$), 1.75 (m, 2H, $ArOCH_2CH_2CH_2CH_2CH{=}CH_2$), 2.07 (m, 2H, $ArOCH_2CH_2CH_2CH_2CH{=}CH_2$), 2.40 (m, 2H, $ArOCH_2CH_2CH_2CH_2CH{=}CH_2$), 3.95 (t, 2H, $ArOCH_2CH_2CH_2CH_2CH{=}CH_2$), 4.41 (m, 2H, $OCH_2CH_2(CF_2)_3CF_3$), 4.72 (q, 1H, OCH*CH_3), 4.93 (q, 2H, $CH{=}CH_2$), 5.75 (m, 1H, $CH{=}CH_2$), aryl region same as **4BBP2F4** vinyl mesogen.

4-[(1R)-2-(3,3,4,4,5,5,6,6,6-nonafluoro-1-hexoxy)-1-methyl-2-oxoethoxy]phenyl 4'-(3-Buten-1-yloxy)-[1,1'-biphenyl]-4-carboxylate Vinyl precursor to **8BPP2F4**. Product was purified through silica column (hexane: ethyl acetate 4:1). Yield: 5.50 g, 0.0078 mol, 49.9%. ^{1}H NMR: 1.17 (d, 3H, OCH*CH_3), 1.38-1.57 (m, 8H, $ArOCH_2(CH_2)_4CH_2CH{=}CH_2$), 1.84 (m, 2H, $OCH_2CH_2(CF_2)_3CF_3$), 2.12 (m, 2H, $ArOCH_2(CH_2)_4CH_2CH{=}CH_2$), 4.04 (t, 2H, $ArOCH_2(CH_2)_4CH_2CH{=}CH_2$), 4.50 (m, 2H, $OCH_2CH_2(CF_2)_3CF_3$), 4.82 (q, 1H, OCH*CH_3), 5.01 (m, 2H, $CH{=}CH_2$), 5.84 (m, 1H, $CH{=}CH_2$), 6.92 (d, 2H, Ar*H*), 7.03 (d, 2H, Ar*H*), 7.15 (d, 2H, Ar*H*), 7.61 (d, 2H, Ar*H*), 7.70 (d, 2H, Ar*H*), 8.23 (d, 2H, Ar*H*).

4-[(1R)-2-butoxy-1-methyl-2-oxoethoxy]phenyl 4'-[4-(1,1,3,3-tetramethyldisiloxanyl)butoxy]-(1,1'-biphenyl)-4-carboxylate 4BPP4 15 drops (~0.1 ml) of the hydrosilylation catalyst platinum(0)-1,3-divinyl-1,1,3,3-tetramethyldisiloxane complex in xylene (Pt ~2%) was added to a solution containing **(3)** (3.90 g, 8.00 mmol) in 15 ml toluene. The resulting yellow solution was added dropwise to a second, stirring solution of tetramethyldisiloxane (30 ml, 0.170 mol) in 30 ml toluene at 60°C. The reaction was stirred at 60°C for 24 hours and toluene was removed by rotatory evaporation. White to pale yellow solid was obtained from silica column (6:1 hexane: ethyl acetate). Yield: 2.53 g, 4.06 mmol, 50.8%. **6BBP4** was purified through silica column (8:1 hexane: ethyl acetate). Yield: 3.75 g, 0.0058

mol, 33.8%. **8BBP4** was purified through silica column (10:1 hexane: ethyl acetate). Yield: 7.40 g, 0.011 mol, 64.9%. ^{1}H NMR of **4BBP4**, **6BBP4** and **8BBP4** share several identical regions; all differences are indicated in bracket. ^{1}H NMR ($CDCl_3$, n = 1, 3, 5) (δ): 0.09 (s, 6H, Si*Me*$_2$H), 0.17 (s, 6H, Si*Me*$_2$O), 0.61 (t, 2H, C*H*$_2$Si), 0.91 (t, 3H, $OCH_2CH_2CH_2CH_3$), [**4BBP4**: 1.34 (m, 2H, $OCH_2CH_2CH_2CH_2Si$), **6BBP4**: 1.32-1.46 (m, 6H, $OCH_2CH_2(CH_2)_3CH_2Si$), **8BBP4**: 1.32-1.42 (m, 10H, $OCH_2CH_2(CH_2)_5CH_2Si$)], 1.56 (m, 2H, $OCH_2CH_2CH_2CH_3$), 1.64 (m, 5H, OCH^*CH_3 + $OCH_2CH_2CH_2CH_3$), 1.86 (m, 2H, $OCH_2CH_2(CH_2)_nCH_2Si$), 4.03 (t, 2H, $OCH_2CH_2(CH_2)_nCH_2Si$), 4.19 (m, 2H, $OCH_2CH_2CH_2CH_3$), [**4BBP4** and **6BBP4**: 4.72 (m, 1H, OCH^*CH_3), 4.78 (m, 1H, Si*H*), **8BBP4**: 4.70 (m, 1H, OCH^*CH_3), 4.75 (q, 1H, Si*H*)], 6.93 (d, 2H, Ar*H*), 7.03 (d, 2H, Ar*H*), 7.15 (d, 2H, Ar*H*), 7.59 (d, 2H, Ar*H*), 7.70 (d, 2H, Ar*H*), 8.23 (d, 2H, Ar*H*).

All fluorinated compounds were purified through silica column (hexane: ethyl acetate 4: 1). **4BPP2F4** Yield: 2.00 g, 0.0025 mol, 50.9%. **6BPP2F4** Yield: 3.60 g, 0.0043 mol, 22.4%. **6BPP2F4** Yield: 2.50 g, 0.0030 mmol, 20.0%. ^{1}H-NMR ($CDCl_3$, n = 1, 3, 5) (δ): 0.11 (s, 6H, Si*Me*$_2$H), 0.23 (s, 6H, Si*Me*$_2$O), 0.61 (t, 2H, C*H*$_2$Si), [**4BBP2F4**: 1.57 (m, 2H, $OCH_2CH_2CH_2CH_2Si$), **6BBP2F4**: 1.56-1.20 (m, 6H, $OCH_2CH_2(CH_2)_3CH_2Si$), **8BBP2F4**: 1.50 (m, 2H, $OCH_2CH_2CH_2(CH_2)_4CH_2Si$), 1.45-1.23 (m, 8H, $OCH_2CH_2CH_2(CH_2)_4CH_2Si$)], 1.66 (d, 3H, OCH^*CH_3), 1.88 (m, 2H, $OCH_2CH_2(CH_2)_nCH_2Si$), 2.51 (m, 2H, $OCH_2CH_2(CF_2)_3CF_3$), 4.04 (t, 2H, $OCH_2CH_2(CH_2)_nCH_2Si$), 4.51 (t, 2H, $OCH_2CH_2CH_2CH_3$), 4.72 (m, 1H, OCH^*CH_3), 4.82 (m, 1H, Si*H*), 6.95 (d, 2H, Ar*H*), 7.03 (d, 2H, Ar*H*), 7.16 (d, 2H, Ar*H*), 7.61 (d, 2H, Ar*H*), 7.71 (d, 2H, Ar*H*), 8.24 (d, 2H, Ar*H*).

2.2.4 Liquid Crystal-Polymer Attachment

4BPP4 (2.987 g, ~1:2.5 molar ratio of polymer vinyl group to mesogen SiH) was dissolved in 6.5 ml toluene and stirred at 60°C. PS-PVMS polymer (0.464 g, 60/40 molar ratio) and 7 drops (~0.05 ml) of platinum catalyst were dissolved in 3.0 ml toluene. The resulting clear solution was added dropwise to the first mesogen solution. The reaction was stirred continuously at 60°C. 2 to 3 ml of reaction mixture was removed approximately every 12 hours and precipitated into methanol. White precipitate was filtered, redissolved in the initial volume of toluene, and re-precipitated into methanol to allow complete removal of excess, unattached mesogen. White, rubbery solid was isolated by filtering. Rise in LC attachment percent was monitored with NMR. Yield (increases with respect to reaction time): ~0.1-0.3 g. ^{1}H NMR ($CDCl_3$, n = 1, 3, 5) (δ): 0.03-0.24 (m, Si*Me*$_2$OSi*Me*$_2$ + PVMS Si*Me* + $SiCH_2CH_2SiMe_2O$), 0.39 (s, 2H, $SiCH_2CH_2SiMe_2O$), 0.55 (s, 2H, $OCH_2CH_2(CH_2)_nCH_2Si$), 0.88 (t, $OCH_2CH_2CH_2CH_3$), 1.00 (s, 2H, $OCH_2CH_2(CH_2)_nCH_2Si$), [**4BPP4**: 1.23-1.62 (br. m, 11H, styrene $PhCHCH_2Ph$ + $OCH_2CH_2(CH_2)_nCH_2Si$ + OCH^*CH_3 + $OCH_2CH_2CH_2CH_3$), **6BPP4/8BPP4**: 1.25-1.71 (br. m, 13H/15H, styrene $PhCHCH_2Ph$ + $OCH_2CH_2(CH_2)_nCH_2Si$ + OCH^*CH_3 + $OCH_2CH_2CH_2CH_3$)], 1.67-2.10 (br. d, 3H, styrene $PhCHCH_2Ph$ + $OCH_2CH_2(CH_2)_nCH_2Si$), 3.94 (s, 2H, $OCH_2CH_2(CH_2)_nCH_2Si$), 4.13 (s, 2H, $OCH_2CH_2CH_2CH_3$), 4.70 (d, 1H, OCH^*CH_3), 5.70-6.03 (m, 3H, Si-CH=CH_2), 6.26-6.74 (m, 2H, styrene o-Ar*H*), 6.83-7.18 (m, 9H, LC Ar*H* + styrene m, p-Ar*H*), 7.52 (s, 2H, Ar*H*), 7.62 (s, 2H, Ar*H*), 8.16 (s, 2H, Ar*H*).

The same procedure was used in LC attachment to the PVMS homopolymer. Yield (increases with respect to reaction time): ~0.1-1.5 g. ^{1}H NMR ($CDCl_3$, n = 1, 3, 5) (δ): 0.01-0.23 (m, Si*Me*$_2$OSi*Me*$_2$ + PVMS Si*Me* + $SiCH_2CH_2SiMe_2O$), 0.43 (s, 2H, $SiCH_2CH_2SiMe_2O$), 0.54 (s, 2H, $OCH_2CH_2(CH_2)_nCH_2Si$), 0.91 (m, 3H, $OCH_2CH_2CH_2CH_3$), [**4BPP4**: 1.38 (m, 2H,

$OCH_2CH_2CH_2CH_3$), 1.53-1.63 (br. s, 2H, $OCH_2CH_2CH_2CH_2Si$), **6BPP4**: 1.28-1.59 (br. m, 8H, $OCH_2CH_2(CH_2)_3CH_2Si$ + $OCH_2CH_2CH_2CH_3$), **8BPP4**: 1.25-1.55 (t, 12H, $OCH_2CH_2(CH_2)_5CH_2Si$ + $OCH_2CH_2CH_2CH_3$)], 1.63 (m, 5H, OCH^*CH_3 + $OCH_2CH_2CH_2CH_3$), 1.80 (m, 2H, $OCH_2CH_2(CH_2)_nCH_2Si$), 3.99 (t, 2H, $OCH_2CH_2(CH_2)_nCH_2Si$), 4.18 (s, 2H, $OCH_2CH_2CH_2CH_3$), 4.75 (q, 1H, OCH^*CH_3), 5.79 (d, 1H, Si-CH=CH_2), 6.00 (m, 2H, Si-CH=CH_2), 6.97 (m, 4H, Ar*H*), 7.13 (m, 2H, Ar*H*), 7.58 (s, 2H, Ar*H*), 7.67 (s, 2H, Ar*H*), 8.22 (s, 2H, Ar*H*).

2.3 Results and Discussion

2.3.1 LC Attachment

The synthesis of all liquid crystals, polymers, and SCLCBCPs were successfully completed and the structures verified via ^{1}H NMR. Six different liquid crystals (4BPP4, 6BPP4, 8BPP4, 4BPP2F4, 6BPP2F4, 8BPP2F4) were produced and attached onto PVMS homopolymer and PS-PVMS block copolymers. The molecular weight of the polystyrene block was determined via GPC calibrated with polystyrene standards before the addition of the siloxane monomer. The molecular weights of PS-PVMS block copolymers were obtained from ^{1}H NMR integration. Table 2-1 summarizes the polymers used in LC attachment, with molecular weight (M_n), polydispersities (M_n/M_w), and PS/PVMS weight percents. The change in LC attachment percent was monitored via ^{1}H NMR and calculated with modifications of the characterization methods described by Moment et al.[29]. The composition, LC attachment percent, smectic layer spacing, and thermal properties of selected SCLCBCPs are summarized in Table 2-2.

Table 2-1. Summary of number average molecular weights (M_n), polydispersity (M_w/M_n), and polystyrene weight percent (PS wt%) for PVMS homopolymer and PS-PVMS block copolymers.

Polymer	PS M_n (g/mol)	PVMS M_n (g/mol)	Total M_n (g/mol)	M_w/M_n	PS wt%
PVMS15	0	14,800	14,800	1.23	0
PS27-PVMS14	26,900	14,200	41,100	1.14	65.5
PS35-PVMS12	34,700	11,900	46,600	1.34	74.4
PS61-PVMS18	61,100	18,200	79,300	1.21	77.0

Table 2-2. Summary of composition, LC content, and thermal properties for SCLCBCPs.

Sample name	PS wt %	PVMS wt %	LC wt %	attachment %	T_{iso} (°C)	D (nm)	FWHM (nm)
$LCP_{4BPP4}98$	0	15	85	78	81	3.37	0.15
$LCP_{6BPP4}126$	0	12	88	100	113	3.63	0.12
$LCP_{8BPP4}122$	0	12	88	92	153	3.82	0.14
PS27-$LCP_{4BPP4}46$	37	19	44	31	42	3.75	0.47
PS27-$LCP_{4BPP4}57$	32	17	51	41	55	3.53	0.22
PS27-$LCP_{4BPP4}79$	25	15	60	55	67	3.45	0.19
PS27-$LCP_{4BPP4}90$	23	12	65	76	83	3.34	0.17
PS27-$LCP_{4BPP4}115$	19	10	71	100	90	3.32	0.10
PS35-$LCP_{6BPP4}27$	56	19	25	17	-	4.62	2.48
PS35-$LCP_{6BPP4}39$	47	16	37	30	63	4.10	0.40
PS35-$LCP_{6BPP4}47$	42	14	44	40	72	3.85	0.22
PS35-$LCP_{6BPP4}71$	33	11	56	65	115	3.61	0.16
PS35-$LCP_{6BPP4}104$	25	9	66	100	135	3.60	0.16
PS35-$LCP_{8BPP4}26$	57	20	23	15	-	5.23	2.29
PS35-$LCP_{8BPP4}44$	44	15	41	35	-	4.27	0.26
PS35-$LCP_{8BPP4}67$	34	12	54	57	135	3.91	0.19
PS35-$LCP_{8BPP4}93$	27	9	64	88	148	3.85	0.13
PS35-$LCP_{8BPP4}104$	25	8	67	100	160	3.82	0.13
PS27-$LCP_{4BPP2F4}153$	15	8	77	100	120	6.41	0.63
PS35-$LCP_{6BPP2F4}130$	21	7	71	100	132	6.65	0.57
PS27-$LCP_{8BPP2F4}153$	15	8	77	100	140	6.83	0.71

The hydrosilylation reaction adds SiH-tipped mesogens across the vinyl functionalized PVMS backbone. This was seen as the disappearance of the mesogen SiH peak around 4.72 ppm, the appearance of characteristic mesogen peaks in the aromatic region (7.47-8.20 ppm), and the gradual disappearance of Si–C*H*=CH_2 peaks (5.70-6.03 ppm) (Figure 2-4). Six of the twelve mesogenic aryl protons are unobscured while the other six fuse with styrene peaks between 6.30 and 7.25 ppm. This allows calculation of peak area for each LC aryl proton and each styrene

proton by subtracting six LC aryl integrations from the styrene region. The decrease in the areas under the Si–C*H*=CH_2 peaks was used to measure the increase in LC attachment percentage. The LC attachment percentage is calculated as [$Area_{LC\ proton}$ / (A_{LC} + A_{vinyl})] × 100%. LC attachment to the polymer chain is further verified via calculation of the molar fraction of polystyrene within the polymer chain, which is calculated as [$Area_{PS\ proton}$ / (A_{LC} + A_{vinyl} + A_{PS})] × 100%. This fraction is expected to remain constant, because LC attachment to the PVMS block has no effect on the molar fraction of the PS block. Given that ^{1}H NMR does not distinguish between the aryl protons from attached and free, excess LCs, this calculation is necessary to ensure that all liquid crystals present in the final SCLCBCP product are covalently bonded to the polymer chain. A reduction in polystyrene/(vinyl+LC) ratio indicates the presence of free, unattached liquid crystals. To eliminate excess LCs the reaction mixture was precipitated into methanol, the product was filtered, re-dissolved in toluene, and precipitated into methanol for a second time. Although two precipitations were sufficient for most samples, this process can be repeated more often if necessary until the original PS/PVMS ratio from the pure polymer is observed via NMR. Once the PS/PVMS has been brought close to the pure polymer value, further precipitations do not increase the PS molar percent or decrease LC attachment percent. The resulting polymer is shown in Figure 2-5.

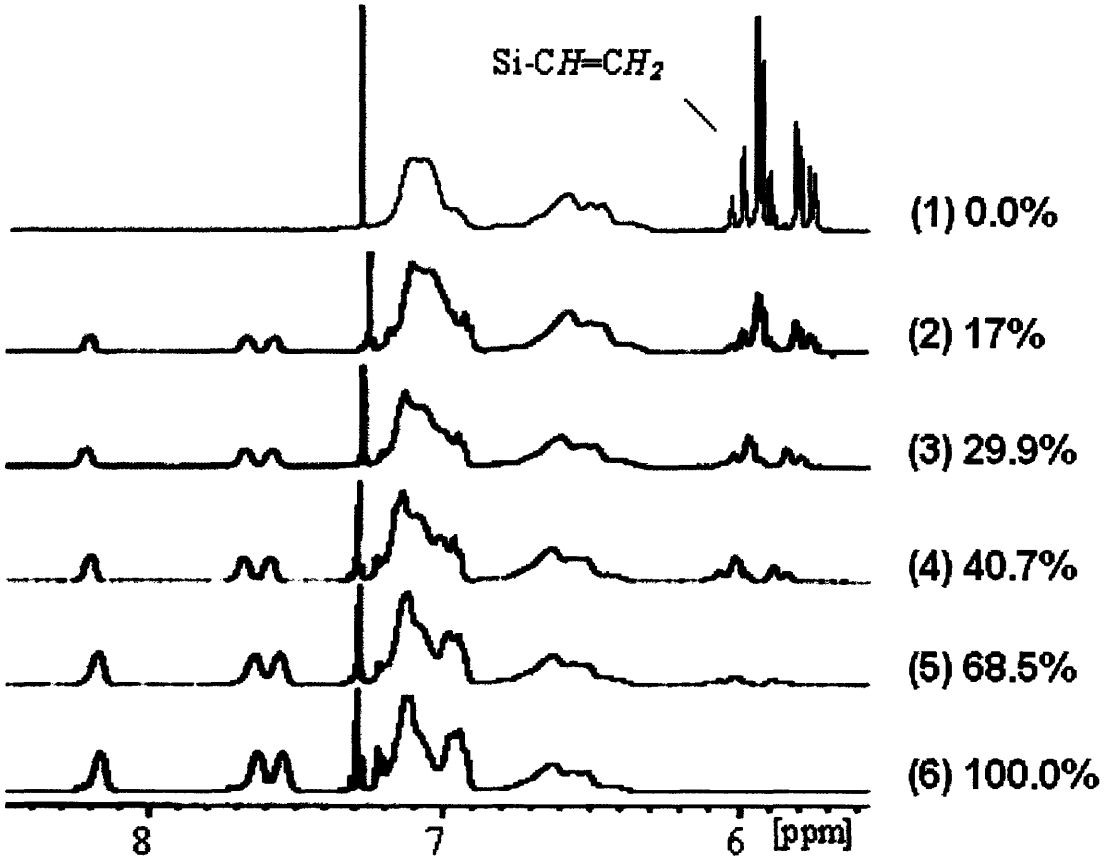

Figure 2-4. NMR of side chain liquid crystalline block copolymers with attachment of 6BPP4 on block copolymers. Increase in LC attachment % is monitored by decrease in area under peaks corresponding to the PVMS vinyl group. LC attachment increases linearly at 1.20%/hr.

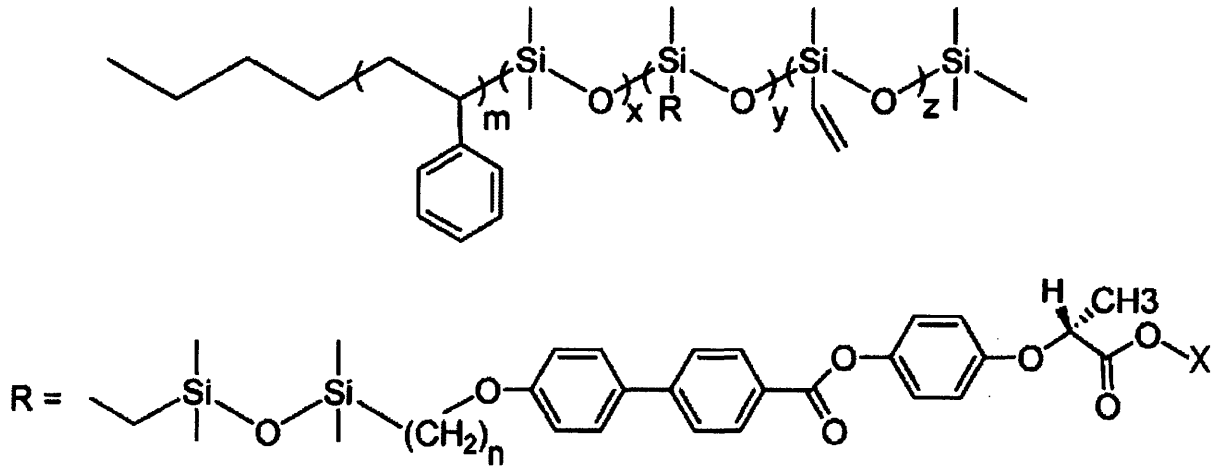

Figure 2-5. Schematic of SCLCBCP where y and z are random, n = 4, 6, or 8, and x is either the nonfluorinated, $-(CH_2)_3-CH_3$, or the fluorinated, $-(CH_2)_2-(CF_2)_3-CF_3$ alkyl ester.

A linear increase in LC attachment percent was observed for the nonfluorinated LCs on both PS-27-PVMS14 and PS35-PVMS12 copolymers (Figure 2-6). Although the rate of LC attachment percent is variable in the presence of different polymer chains and LCs, the increase remains linear for all samples tested. The variability in rate is also affected by small changes in sample concentration and the amount of platinum catalyst added, for which more catalyst and higher concentrations of reaction mixture yield higher reaction rates. In agreement with previous literature, large amounts of platinum catalyst lead to gray solids that easily undergo decomposition when heated.

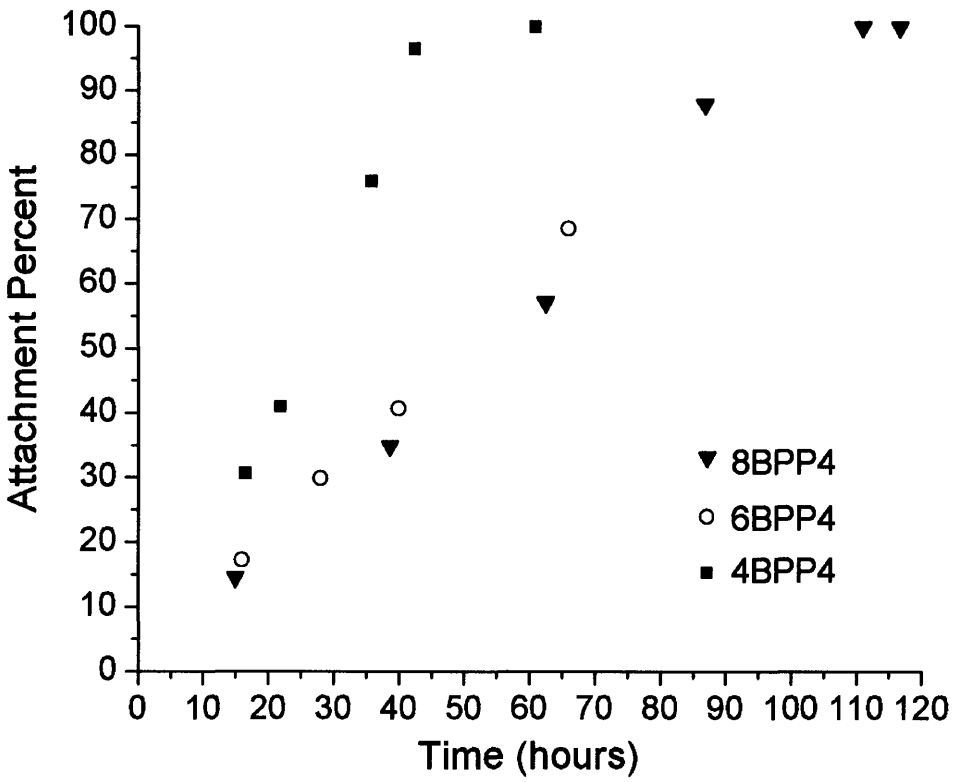

Figure 2-6. Graph of nBPP4 attachment percent with respect to time. In all cases the attachemnt percent increases linearly until 100% attachemnt is reached. For the 4 spacer, 6 spacer, and 8 spacer LC attachments the polymer concentrations were 0.049 g/ml, 0.055 g/ml, and 0.039 g/ml; catalyst concentrations were 0.12 mg/ml, 0.14 mg/ml, and 0.15 mg/ml, respectively.

2.3.2 LC Morphology

The LC morphology was characterized with small angle X-ray scattering (SAXS), where the presence of a smectic polydomain mesophase was confirmed. The d-spacing of the smectic layers (D) was measured with SAXS for all LCs with varying attachment percent to the polymer chain. As expected, larger smectic layer spacings were observed for SCLCBCPs with longer spacer lengths between the LCs and polymer chain. For all SCLCBCPs containing nonfluorinated LCs at 100% attachment, D closely matched LC molecular lengths for fully

extended, all trans conformations (calculated using the Accelrys Materials Studio Molecular Modeling Software). This suggests interdigitation of the liquid crystals from adjacent layers. For all fluorinated LC's, the smectic layer spacings were close to double those of the nonfluorinated values. This is indicative of bilayer formation, and is attributed to the favorable interactions resulting from assembling of the fluorinated LC regions. However, smectic layer spacings for the fluorinated LCs were slightly less than double single smectic layer spacings; from this, it is concluded that partial interdigitation of the fluorinated ester end groups occurs at the interface of LC bilayers. The observed smectic layer spacings (D), calculated molecular lengths, and schematics of LC morphologies can be found in Table 2-3 and Figure 2-7.

Table 2-3. The d-spacing of the smectic layers was measured via SAXS for 100% attachment of LCs onto PS-PVMS block copolymer.

	nBPP4 d-spacing	[a]Calculated nBPP4 molecular length	nBPP2F4 d-spacing	[a]Calculated nBPP2F4 molecular length
4BPPx on polymer	3.4 nm	3.6 nm	6.4 nm	3.8 nm
6BPPx on polymer	3.6 nm	3.8 nm	6.6 nm	4.0 nm
8BPPx on polymer	3.8 nm	4.0 nm	6.8 nm	4.2 nm

[a]Accelrys Materials Studio Molecular Modeling Software was used to calculate maolecular lengths

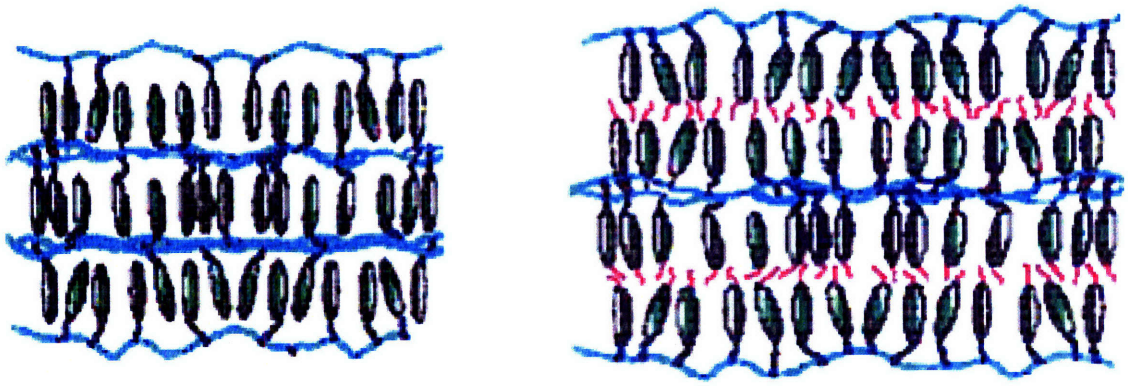

Figure 2-7. Schematic of the observed morphologies of LC smectic layers, showing interdigitated nonfluorinated LCs (left) and partially interdigitated bilayers for the fluorinated LCs (right).

The effects of increasing the LC attachment percent to the block copolymer backbone upon the self-assembled LC morphology were studied for the nBBP4 series. Using SAXS, a decrease in smectic layer spacing was observed as the LC attachment percent increases. At lower LC attachment percent, the low LC density leads to a loosely packed smectic mesophase with poorly defined layer formation. As LC attachment percent increases the greater density of LCs on the siloxane backbone leads to more tightly packed, interdigitated smectic layers. In all cases the decrease in smectic layer spacing is limited by the molecular lengths of the liquid crystals. Consequently, D does not continue to decrease once the LCs become fully interdigitated as attachment approaches 100% (Figure 2-8). This model is confirmed by the increasing sharpness of the SAXS peaks as attachment percent increases. The increase in sharpness can be quantified by looking at the full width at half maximum of the scattering peaks (FWHM). The decrease in the FWHM indicates more well-defined smectic layers at higher attachment percents (Table 2-2).

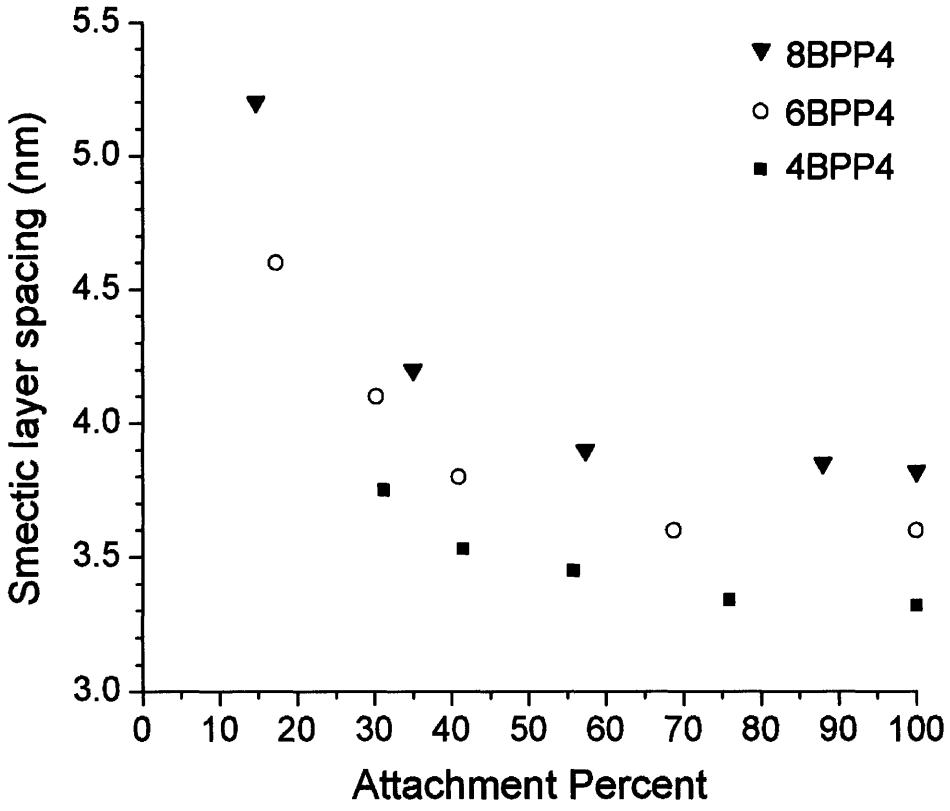

Figure 2-8. Graph of the smectic layer spacing (D) as a function of attachment percent for nonfluorinated LCs on PS-PVMS block copolymers. Increase in LC attachment percent is accompanied by decrease in D. Smectic layer spacing is limited by the molecular lengths of the LCs and remains constant once full interdigitation is achieved. Similar results were seen with attachment of LCs to PVMS homopolymer.

Using DSC, an increase in the T_{iso} of the LCs was also observed with increasing attachment percent, due to the increase in favorable enthalpic interactions among the LCs. A similar increase in T_{iso} with respect to LC attachment has been reported by Martinoty et al.[25]. Previous works involving main-chain mixed-mesogen LCPs have also demonstrated a tunable LC clearing temperature via variations in the chemical composition of the mixed-mesogen blend[31]. Figure 2-9 shows the T_{iso} as a function of LC attachment percent for the attachment of the nBPP4 LC series to block copolymers. No discernible transitions were observed in DSC for several of the SCLCBCPs with lower LC attachment percent. This is consistent with the broad SAXS peaks observed for the same samples. This observation suggests that poorly defined smectic LC mesophases have low enthalpy due to their loose packing. It is also possible that the lack of a clear first order transition is a consequence of the smectic-to-isotropic transition occurring over a broad temperature range. Additionally, it was observed that for longer spacer lengths the T_{iso} was higher for samples having similar attachment percent. The increased conformational space provided by the longer spacer, allows for more efficient packing of mesogens and thus the self-assembly of a more stable smectic mesophase. These results illustrate how variations in the LC structure and content can be used to obtain a range of smectic morphologies. Additionally, the smectic-to-isotropic transition temperature (T_{iso}) can be precisely tuned over a wide range, from room temperature up to 160°C, again through variations in the LC structure and content.

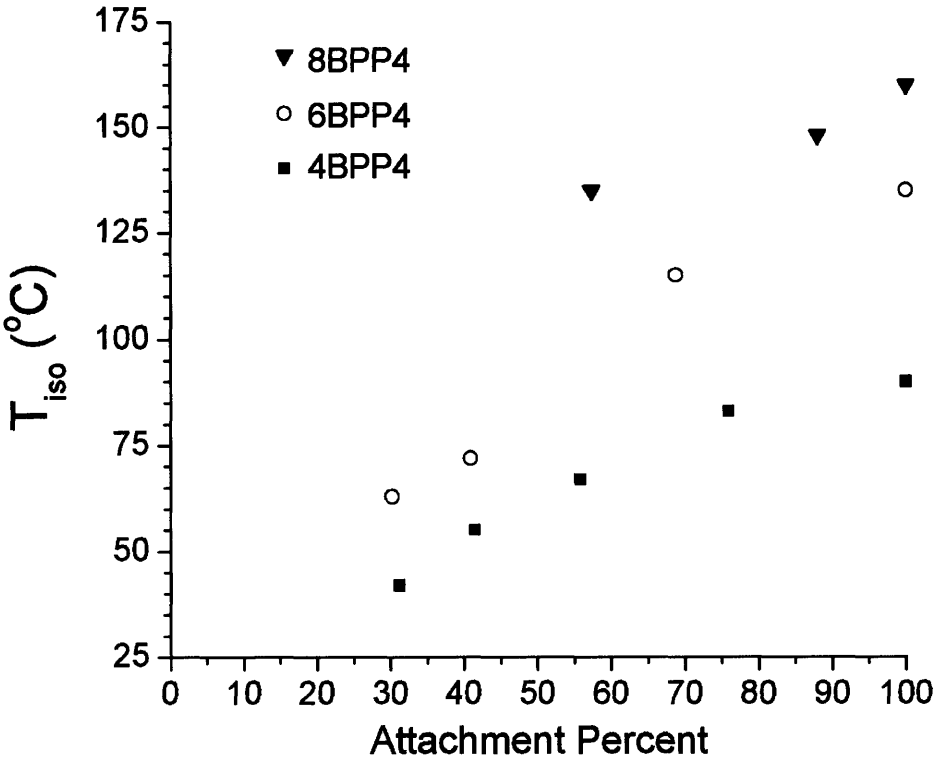

Figure 2-9. Graph of the smectic to isotropic transition temperature (T_{iso}) as a function of attachment percent for nBPP4 mesogens on PS-PVMS block copolymers. No smectic to isotropic transition is observed for lower attachment percentages.

2.3.3 Liquid Crystal Block Copolymer Self-Assembly

We have shown that the morphology and thermal properties of the LC mesophase are significantly and systematically affected by the LC attachment percent to the polymer backbone. The increased stability of the smectic mesophase is resultant from the increased packing density of LCs on the siloxane backbone at higher attachment percents. These changes in LC morphology, in turn, have significant effects upon the self-assembled morphology of the BCP.

The self-assembled morphology of the side chain liquid crystalline block copolymers (SCLCBCPs) were investigated with transmission electron microscopy (TEM) and small-angle X-ray scattering (SAXS). The attachment of LC leads to an increase in the liquid crystalline polymer (LCP) volume fraction and a corresponding decrease in the PS volume fraction. The ability to systematically vary the LC content allows for a range of morphologies to be produced from a single reaction. These morphologies display similar behavior as the morphologies of polystyrene-polyacrylate liquid crystalline block copolymers that were investigated in previous studies[32, 33]. The neat PS-PVMS block copolymer self-assembles with PVMS cylinders in a matrix of PS. At low LCP weight percent LCP cylinders and lamellae coexistence is observed. Further increase in the LC content results in a pure lamellar morphology, coexistence of lamellae and PS cylinders, and a pure PS cylinder morphology (Table 2-4 and Figure 2-10). It is believed that the morphologies that display coexistence of cylinders and lamellae are kinetically trapped metastable states, not equilibrium morphologies. There is further discussion of these transitional morphology is in Chapter 6. These metastable morphologies are observed in as-cast films and upon annealing a pure cylinder morphology is observed.

A second polymer backbone was synthesized with a smaller PS block. The neat PS27-PVMS14 block copolymer also displayed cylinder morphology where the minority PVMS domains form the cylinders. LC was attached to PS27-PVMS14 for a range of attachment percents, all samples displayed a morphology consisting of PS cylinders in a LCP matrix as shown in Table 2-4 and Figure 2-11.

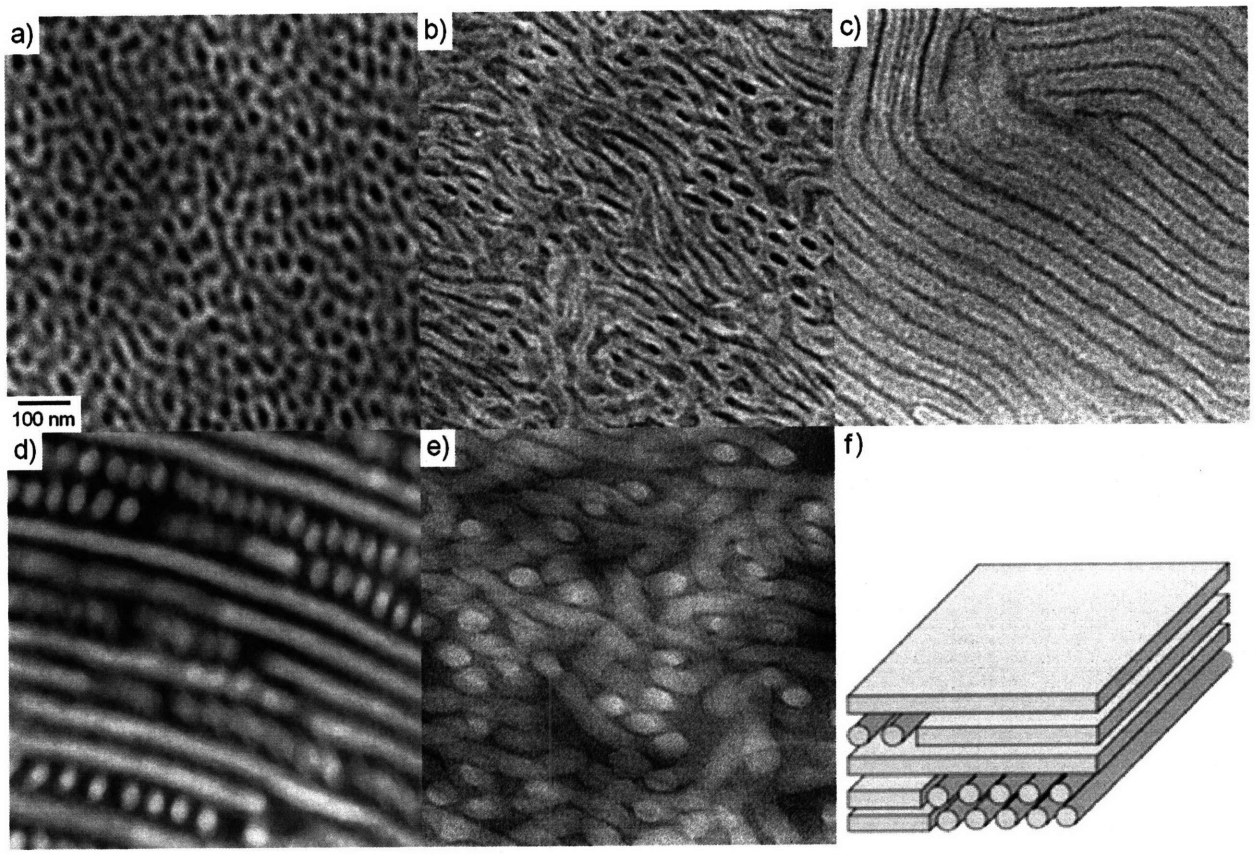

Figure 2-10. TEM images of solvent-cast a) PS61-PVMS18, b) PS61-LCP_{4BPP4}42, c) PS61-LCP_{4BPP4}83, d) PS61-LCP_{4BPP4}135, and e) PS61-LCP_{4BPP4}152. In all cases the PS domains appear light. f) Model of PS cylinders coexisting with lamellae.

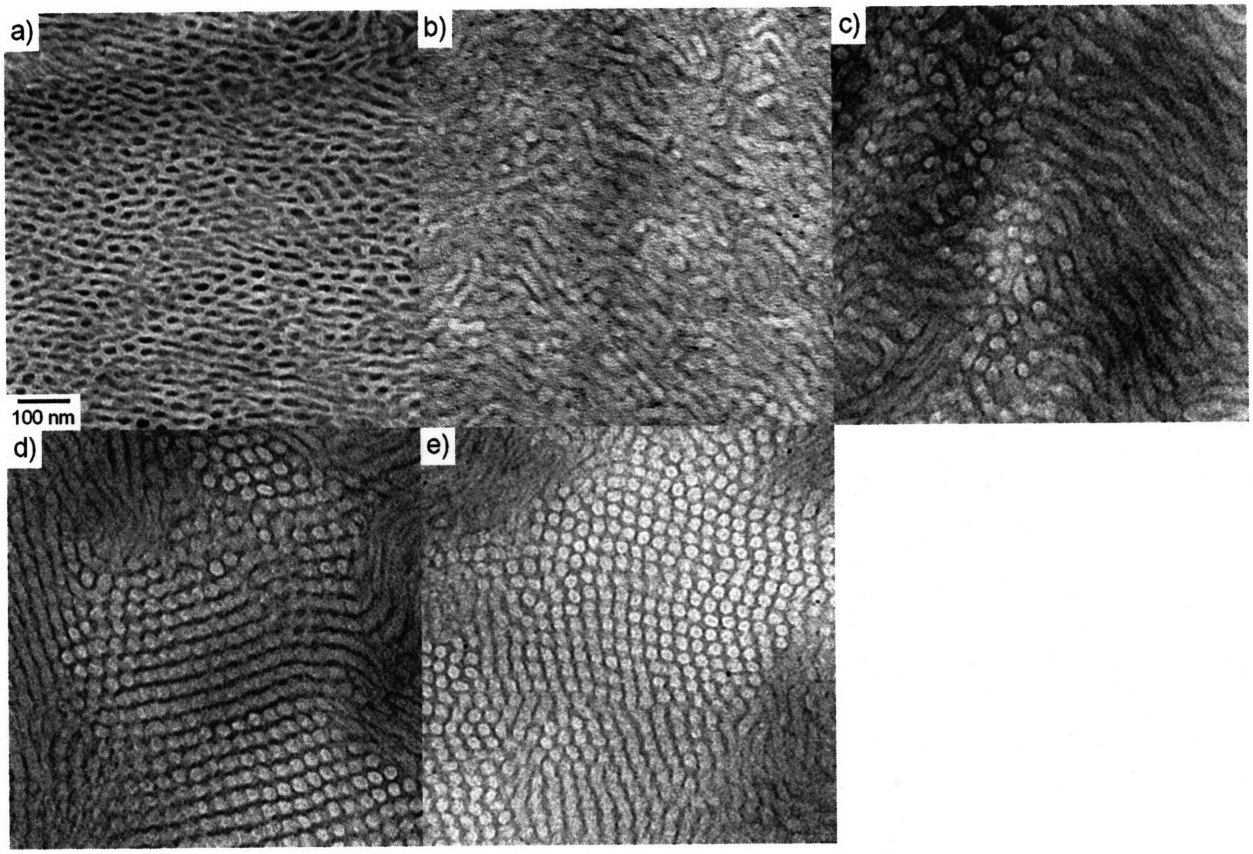

Figure 2-11. TEM images of solvent-cast a) PS27-PVMS14, b) PS27-LCP_{4BPP4}46, c) PS27-LCP_{4BPP4}57, d) PS27-LCP_{4BPP4}90, and e) PS27-LCP_{4BPP4}115. In all cases the PS domains appear light.

Table 2-4. Summary of thermal and mechanical properties*.

Sample name	PS wt %	Attachment %	[1]LCP T_g (°C)	[2]T_{iso} (°C)	T_{ODT} (°C)	[1]G' at -30°C (MPa)	[1]G' at 40°C (MPa)	[5]Morphology
PS61-PVMS18	77	0		-	[3]210			PVMS cylinders
PS61-LCP_{4BPP4}37	62	18	-10	11	[3]120	2220	1540	LCP cylinders/ lamellae
PS61-LCP_{4BPP4}68	49	48	-2	73	[3]180	2240	370	Lamellae
PS61-LCP_{4BPP4}101	38	79	14	81	[3]180	2100	130	lamellae/PS cylinders
PS61-LCP_{4BPP4}123	33	100	20	89	[3]170	2060	30	PS cylinders
PS27-PVMS14	66	0		-	[4]250			PVMS cylinders
PS27-LCP_{4BPP4}46	37	31	0	42	[4]120	2170	270	PS cylinders
PS27-LCP_{4BPP4}57	32	41	7	55	[4]150	1740	16	PS cylinders
PS27-LCP_{4BPP4}90	23	76	14	83	[4]220	1550	6	PS cylinders
PS27-LCP_{4BPP4}115	19	100	16	90	[4]230	1580	1.7	PS cylinders

*The polystyrene weight percent, liquid crystal attachment percent, the glass transition temperature of the liquid crystalline polymer (LCP T_g), the smectic to isotropic transition temperature (T_{iso}), the order-disorder transition temperature (T_{ODT}), G' at -30°C is the value of the elastic modulus in the glassy plateau region, and G' at 40°C is the value of the elastic modulus above the LCP T_g are listed for each sample. Data obtained via [1]dynamic mechanical analysis (DMA), [2]differential scanning calorimetry (DSC), [3]small-angle X-ray scattering (SAXS), [4]rheometry, and [5]transmission electron microscopy (TEM).

Temperature dependent SAXS and rheometry were used in order to identify the order-disorder transition temperature (T_{ODT}) of these materials (details provided in Appendix F). The initial attachment of LC leads to phase mixing at a lower temperature than the neat PS-PVMS block copolymer. The LCP is more chemically similar to the PS block than the pure siloxane block leading to a decrease in the segmental interaction parameter (χ) and the initial decrease in the T_{ODT} upon introduction of the LC moiety. As the LC attachment is further increased a systematic increase in the T_{ODT} is observed (Figure 2-12).

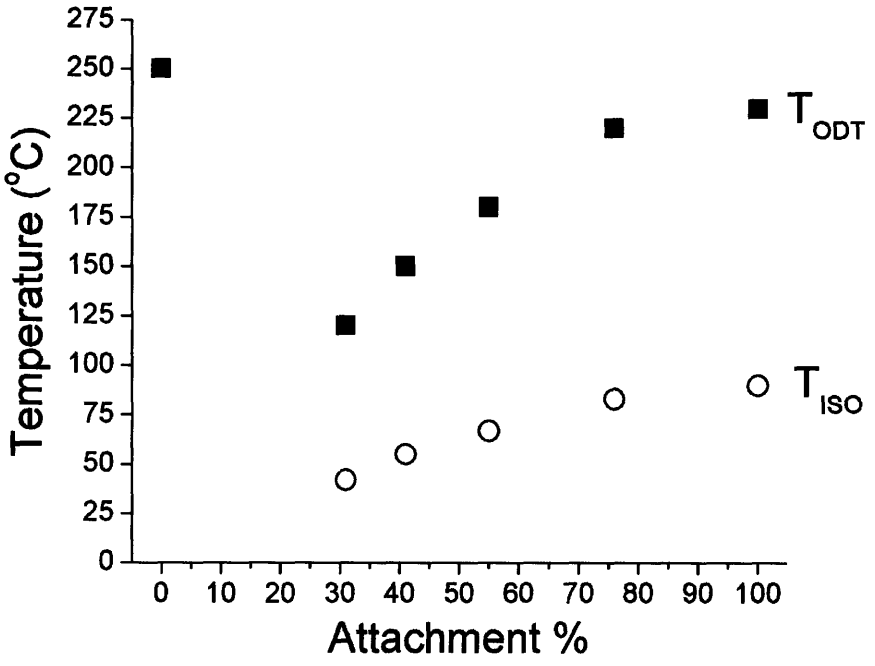

Figure 2-12. Plot of the order-disorder transition temperature (T_{ODT}) and the smectic to isotropic transition temperature (T_{iso}) as a function of attachment percent for PS27-PVMS14, PS27-LCP_{4BPP4}46, PS27-LCP_{4BPP4}57, PS27-LCP_{4BPP4}79*, PS27-LCP_{4BPP4}90, and PS27-LCP_{4BPP4}115. (*PS27-LCP_{4BPP4}79 is material previously studied[20] with the same polymer backbone and LC moiety).

In order to gain insights into the mechanisms driving this phenomena the anchoring of the LC mesophase relative to the IMDS was investigated. Fiber drawing of the SCLCBCPs was performed by heating the samples to 150°C on a hot plate and pulling ~ 500μm fibers from the melt with tweezers. SAXS indicates that for all of the materials investigated the cylinder axis and the smectic layer normal are preferentially oriented parallel to the fiber axis (Figure 2-13). This orientation indicates that the smectic layers are oriented relative to the IMDS consistent

with the homogeneous anchoring condition. Similarly, previous studies utilizing oscillatory shear yielded oriented morphologies that are consistent with the homogeneous anchoring condition when shearing took place above the T_{iso}[20]. This preference for the homogeneous anchoring condition, even in the isotropic LC state, results in stabilization of the block copolymer mesophase. Increased functionalization of the LC onto the siloxane backbone leads to a greater preference for homogeneous anchoring and an increase in T_{ODT}. The effect of increasing the attachment percent is also apparent in the TEM images. The IMDS sharpens and the morphologies become progressively more ordered as the LC content increase. Higher LC attachments result in a more well-defined LC smectic mesophase, which provides greater stabilization of the IMDS due to the preference for homogeneous anchoring. These observations are consistent with the increase in the T_{iso} and T_{ODT} with increasing LC content.

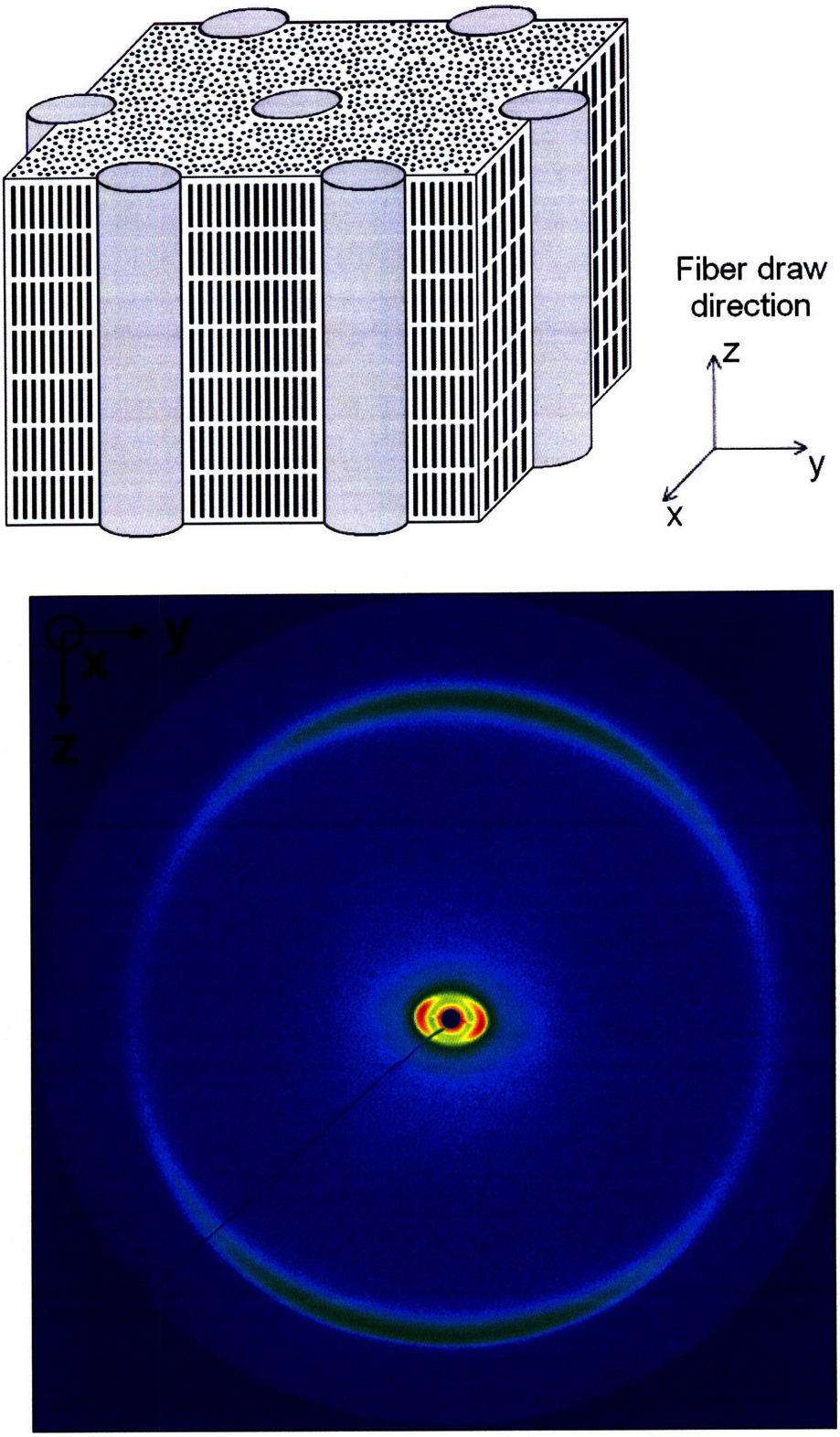

Figure 2-13. a) Cartoon showing observed structure relative to the melt fiber drawn direction, b) SAXS of PS27-LCP_{4BPP4}90 that has been melt fiber drawn.

2.3.4 Mechanical Properties

Dynamic mechanical analysis (DMA) was used in order to study the mechanical properties of these materials, see Figure 2-14. An elastic plateau is observed for all materials below the glass transition temperature (T_g) of both of the components. The attachment of LC moieties to the siloxane backbone results in a systematic increase in the T_g of the liquid crystalline polymer, due to restriction in the flexibility of the backbone from the presence of the bulky LC side groups. While raising the T_g, increasing the LC content results in a more pronounced drop in the elastic modulus. This increase in the magnitude of the transition, at higher LC attachment percents, is due to the greater weight percent of liquid crystalline polymer present in the system. The SCLCBCPs resulting from the attachment of LC to the PS61-PVMS18 block copolymer backbone resulted in a range of morphologies, and subsequently mechanical properties ranging over several orders of magnitude. When PS was the majority component or the PS domains formed lamellar domains, the materials retained their mechanical integrity until temperatures above the PS T_g. However, the materials with cylindrical PS domains failed at lower temperatures, as the majority LCP domains could not provide sufficient mechanical integrity to prevent significant deformation under the test conditions. Increasing LC content leads to failure at lower temperatures for each series of SCLCBCPs.

Here we have demonstrated the ability to tune the mechanical properties, above the LCP T_g over several orders of magnitude through variations in both the morphology and LC content. The combination of a T_g below room temperature with the ability to control the elastic modulus at room temperature, make these materials ideal for custom designing materials for specific applications. Additionally, the ability to incorporate a responsive functionality into these systems enables a diverse range of new functional materials to be developed.

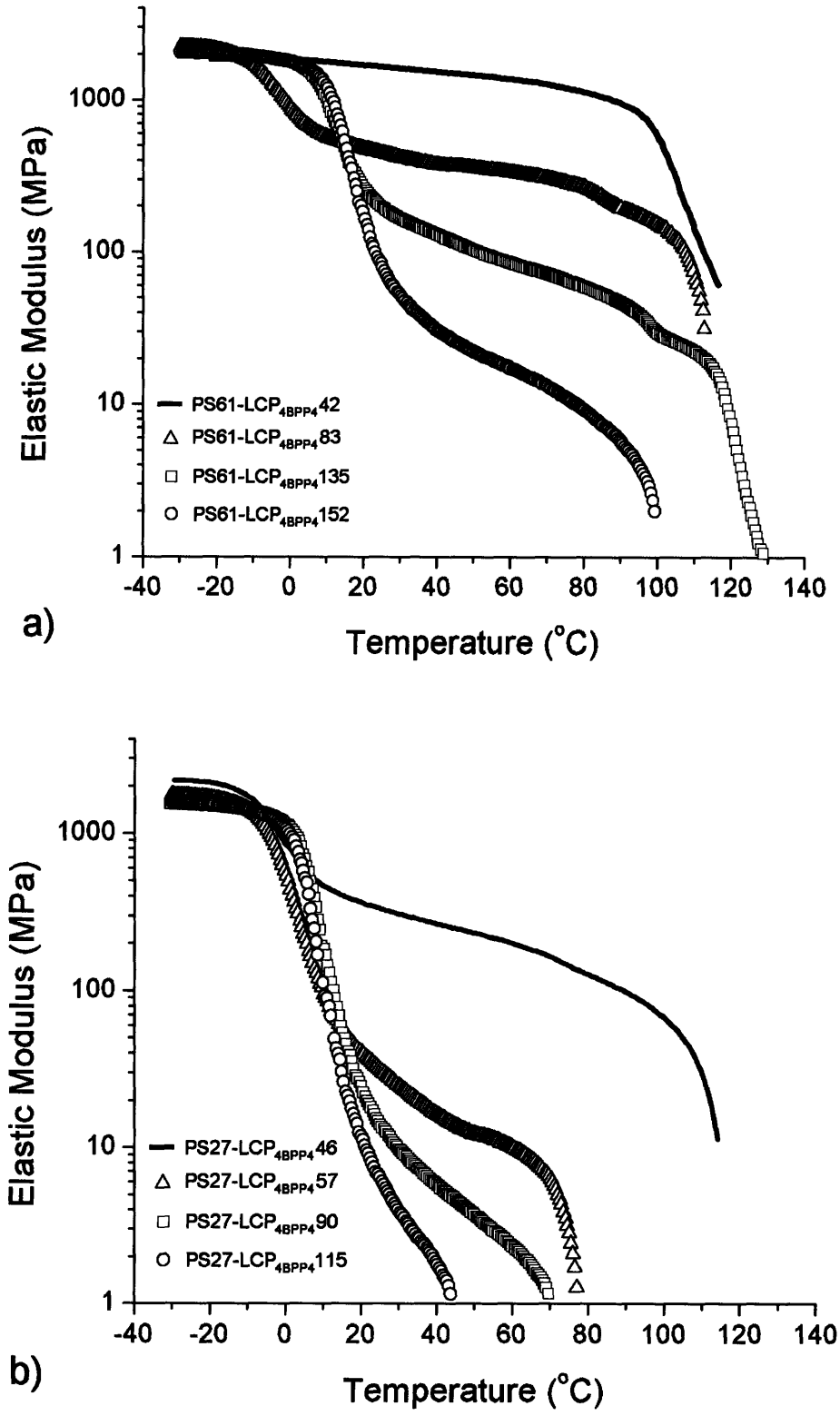

Figure 2-14. Elastic modulus as a function of temperature for a) a range of morphologies and b) materials with a PS cylinder morphology.

2.4 Conclusions

A series of SCLCBCPs has been synthesized via anionic polymerization, esterification, and hydrosilylation chemistries with a high degree of control of both the block copolymer block lengths and the degree of functionalization of the LC along the block copolymer backbone. The chemistries developed provide a simple route for precisely tuning the LC functionalization. The slow linear rate of LC attachment, in combination with the ability to remove and quench portions of the reaction solution to recover products of a specific degree of functionalization, enables a range of LC attachment to be easily obtained from a single synthesis batch.

The LC content significantly affects the morphology and properties of the LC mesophase, as well as, the self-assembled morphology of the block copolymer. Variations in the LC content allow the smectic to isotropic transition temperature to be tuned over a wide range; from room temperature up to 150°C. Furthermore, numerous morphologies, including LCP cylinders, lamellae, PS cylinders, and coexistence of lamellae and cylindrical morphologies were obtained from a single polymer backbone. The tunability enabled through precise control over the self-assembled morphologies of this system allows for the thermal and mechanical properties customized. This work demonstrates the systematic control of the LC fraction of functionalization and the effects upon the resulting self-assembled morphologies.

We have shown that the thermo-mechanical properties of this system can be tailored as a function of both morphology and LC content. The elastic modulus above the T_g of the LCP can be tuned over several orders of magnitude, demonstrating unique control over the mechanical property profile for this system. Furthermore T_g of the siloxane based LCP can be tuned through LC attachment. The combination of functional LC moieties with a T_g below room temperature allows for these polymers to be used as responsive elastomeric materials. The systematic and

precise control over both the thermal and mechanical properties of this system enables the design of responsive materials for specific applications such as electro-mechanical, damping, and mechano-optical devices.

2.5 References

1. Bates, F. S.; Fredrickson, G. H., Block Copolymer Thermodynamics - Theory and Experiment. *Annual Review of Physical Chemistry* **1990,** 41, 525-557.

2. Castelletto, V.; Hamley, I. W., Morphologies of block copolymer melts. *Current Opinion in Solid State & Materials Science* **2004,** 8, (6), 426-438.

3. Lodge, T. P., Block copolymers: Past successes and future challenges. *Macromolecular Chemistry and Physics* **2003,** 204, (2), 265-273.

4. Guarini, K. W.; Black, C. T.; Yeuing, S. H. I., Optimization of diblock copolymer thin film self assembly. *Advanced Materials* **2002,** 14, (18), 1290-+.

5. Pochan, J. M.; Pacansky, T. J.; Hinman, D. F., Effects of Solvent and Thermal Annealing on Dielectric Properties and Morphology of Dimethyl Siloxane-Alpha-Methylstyrene Block Copolymers. *Polymer* **1978,** 19, (4), 431-437.

6. Matsen, M. W., Electric field alignment in thin films of cylinder-forming diblock copolymer. *Macromolecules* **2006,** 39, (16), 5512-5520.

7. Osuji, C.; Ferreira, P. J.; Mao, G. P.; Ober, C. K.; Vander Sande, J. B.; Thomas, E. L., Alignment of self-assembled hierarchical microstructure in liquid crystalline diblock copolymers using high magnetic fields. *Macromolecules* **2004,** 37, (26), 9903-9908.

8. Fischer, H.; Poser, S.; Arnold, M.; Frank, W., On the Influence of the Morphological Structure on the Liquid-Crystalline Behavior of Liquid-Crystalline Side-Chain Block-Copolymers. *Macromolecules* **1994,** 27, (24), 7133-7138.

9. Galli, G.; Chiellini, E.; Francescangeli, O.; Ferri, D.; Wolff, D.; Springer, J.; Laus, M.; Angeloni, A. S., Mesophase structure and alignment under different fields of liquid crystalline main-chain/side-group block copolymers. *Macromolecular Symposia* **1997,** 121, 235-244.

10. Hamley, I. W., Structure and flow behaviour of block copolymers. *Journal of Physics-Condensed Matter* **2001,** 13, (33), R643-R671.

11. Hamley, I. W.; Castelletto, V.; Lu, Z. B.; Imrie, C. T.; Itoh, T.; Al-Hussein, M., Interplay between smectic ordering and microphase separation in a series of side-group liquid-crystal block copolymers. *Macromolecules* **2004,** 37, (13), 4798-4807.

12. Zheng, W. Y.; Albalak, R. J.; Hammond, P. T., Mesogen orientation within smectic C* side chain liquid crystalline diblock copolymers. *Macromolecules* **1998,** 31, (8), 2686-2689.

13. Anthamatten, M.; Hammond, P. T., Free-energy model of asymmetry in side-chain liquid-crystalline diblock copolymers. *Journal of Polymer Science Part B-Polymer Physics* **2001,** 39, (21), 2671-2691.

14. Boyer, S. A. E.; Grolier, J. P. E.; Yoshida, H.; Iyoda, T., Effect of interface on thermodynamic behavior of liquid crystalline type amphiphilic di-block copolymers. *Journal of Polymer Science Part B-Polymer Physics* **2007,** 45, (11), 1354-1364.

15. Figueiredo, P.; Geppert, S.; Brandsch, R.; Bar, G.; Thomann, R.; Spontak, R. J.; Gronski, W.; Samlenski, R.; Muller-Buschbaum, P., Ordering of cylindrical microdomains in thin films of hybrid isotropic/liquid crystalline triblock copolymers. *Macromolecules* **2001,** 34, (2), 171-180.

16. Ivanova, R.; Staneva, R.; Geppert, S.; Heck, B.; Walter, B.; Gronski, W.; Stuhn, B., Interplay between domain microstructure and nematic order in liquid crystalline/isotropic block copolymers. *Colloid and Polymer Science* **2004,** 282, (8), 810-824.

17. Olsen, B. D.; Segalman, R. A., Structure and thermodynamics of weakly segregated rod-coil block copolymers. *Macromolecules* **2005,** 38, (24), 10127-10137.

18. Sentenac, D.; Demirel, A. L.; Lub, J.; de Jeu, W. H., A new lamellar morphology of a hybrid amorphous liquid crystalline block copolymer film. *Macromolecules* **1999,** 32, (10), 3235-3240.

19. Yamada, M.; Itoh, T.; Hirao, A.; Nakahama, S.; Watanabe, J., Side-chain LC block copolymers with well defined structures prepared by living anionic polymerization. 2: Effect of the glass transition temperature of amorphous segments on the phase behaviour and structure of the LC segment. *High Performance Polymers* **1998,** 10, (1), 131-138.

20. Verploegen, E.; McAfee, L. C.; Tian, L. T.; Verploegen, D.; Hammond, P. T., Observation of Transverse Cylinder Morphology in Side Chain Liquid Crystalline Block Copolymers. *Macromolecules* **2007,** 40, (4), 777-780.

21. Verploegen, E.; Zhang, T.; Murlo, N.; Hammond, P. T., Influence of variations of liquid crystalline content upon the self-assembly behavior of siloxane based block copolymers. *Soft Matter* **2008,** Advance Article.

22. Kempe, M. D.; Verduzco, R.; Scruggs, N. R.; Kornfield, J. A., Rheological study of structural transitions in triblock copolymers in a liquid crystal solvent. *Soft Matter* **2006,** 2, (5), 422-431.

23. Lehmann, W.; Skupin, H.; Tolksdorf, C.; Gebhard, E.; Zentel, R.; Kruger, P.; Losche, M.; Kremer, F., Giant lateral electrostriction in ferroelectric liquid-crystalline elastomers. *Nature* **2001,** 410, (6827), 447-450.

24. Finkelmann, H.; Kock, H. J.; Rehage, G., Investigations on Liquid-Crystalline Polysiloxanes.3. Liquid-Crystalline Elastomers - a New Type of Liquid-Crystalline Material. *Makromolekulare Chemie-Rapid Communications* **1981,** 2, (4), 317-322.

25. Martinoty, P.; Hilliou, L.; Mauzac, M.; Benguigui, L.; Collin, D., Side-chain liquid-crystal polymers: Gel-like behavior below their gelation points. *Macromolecules* **1999,** 32, (6), 1746-1752.

26. Rousseau, I. A.; Mather, P. T., Shape memory effect exhibited by smectic-c liquid crystalline elastomers. *Journal of the American Chemical Society* **2003,** 125, (50), 15300-15301.

27. Verploegen, E.; Dworken, B. T.; Faught, M.; Kamperman, M.; Zhang, Y. M.; Wiesner, U., Tuning mechanical properties of block copolymer/aluminosilicate hybrid materials. *Macromolecular Rapid Communications* **2007,** 28, (5), 572-578.

28. Moore, J. S.; Stupp, S. I., Room-Temperature Polyesterification. *Macromolecules* **1990,** 23, (1), 65-70.

29. Moment, A.; Miranda, R.; Hammond, P. T., Synthesis of polystyrene-polysiloxane side-chain liquid crystalline block copolymers. *Macromolecular Rapid Communications* **1998,** 19, (11), 573-579.

30. Svensson, M.; Helgee, B.; Skarp, K.; Andersson, G., Effects of nitro substituents on the properties of a ferroelectric liquid crystalline side chain polysiloxane. *Journal of Materials Chemistry* **1998,** 8, (2), 353-362.

31. Rousseau, I. A.; Qin, H. H.; Mather, P. T., Tailored phase transitions via mixed-mesogen liquid crystalline polymers with silicon-based spacers. *Macromolecules* **2005,** 38, (10), 4103-4113.

32. Anthamatten, M.; Hammond, P. T., A SAXS study of microstructure ordering transitions in liquid crystalline side-chain diblock copolymers. *Macromolecules* **1999,** 32, (24), 8066-8076.

33. Anthamatten, M.; Zheng, W. Y.; Hammond, P. T., A morphological study of well-defined smectic side-chain LC block copolymers. *Macromolecules* **1999,** 32, (15), 4838-4848.

Chapter 3 Synthesis and Characterization of A-B-A Side Chain Liquid Crystalline Triblock Copolymers

3.1 Introduction

Liquid crystal polymers (LCPs) have attracted great interest in recent years due to their combination of small-molecule liquid crystalline properties with the properties of polymers[1, 2]. The combination of a low glass transition temperature (T_g) siloxane-based side chain liquid crystal polymer and an amorphous polymer produces a side chain liquid crystalline block copolymer (SCLCBCP) where the LCs are capable of undergoing switching. LC switching can lead to changes in the electrical, optical, mechanical, and transport properties of the SCLCBCP system[1, 3-6]. Potential new applications, such as electro-mechanical or mechano-optical materials, also benefit from the mechanical integrity that the polymer component provides to this system[1-4].

To achieve optimal field responsive properties, the structures of both the liquid crystal and the polymer need to be carefully designed. Various methods have been employed in recent years for the synthesis of both main chain[7-9] and side chain[10-25] LCPs. LC and polymer components can be synthesized separately before the LCs are linked to the polymer chain covalently[13, 15, 17, 21-23] or via hydrogen bonding[18, 26]. Hydrosilylation chemistry with a platinum catalyst is a common route for covalent LC attachment[11, 13, 17, 21-23, 27]. Side chain LCPs can also be synthesized through living cationic[14] and anionic[10, 24, 25, 28] polymerization, atom transfer

radical polymerization (ATRP)[16], and ring-opening metathesis (ROMP)[12, 16, 20]. Slight crosslinking of the LCP system leads to a liquid crystal elastomer (LCE) that introduces LC properties into a rubbery polymer network[2, 27, 29-32]. This crosslinking can be achieved via direct addition of crosslinker to a mixture of two mesogen monomers[31, 32] or the addition of crosslinker into a hydrosilylation reaction mixture containing LC monomers and polymer backbone[27, 29, 30].

A-B-A triblock copolymers can be used as thermoplastic elastomers, where the outer block has a high glass transition temperature (T_g), above the operating temperature, and the center block has a larger volume fraction and a T_g below the operating temperature. When phase segregation occurs the minority hard domains act as physical crosslinks creating an elastomer[33, 34]. The advantage that this type of elastomer has over a conventional chemically crosslinked elastomer is that it can be remolded and processed by raising the temperature above that of the hard block's T_g.

The advantage of this system is the low glass transition temperature (T_g = -10°C) of the siloxane block, which makes a room-temperature elastomer possible[23]. The intermaterial dividing surface (IMDS) of the block copolymer mesophase can be used to orient the liquid crystalline mesophase as the LC will preferentially orient with respect to the IMDS due to surface stabilization effects[23, 26, 35]. In this way a well oriented block copolymer mesophase can be used to template order in the LC mesophase. The IMDS has also been shown to unwind the pitch in the smectic C* phase via confinement of the liquid crystals[36].

The functional siloxane based triblock copolymers described in this Chapter allows for responsive moieties to be incorporated, allowing for a responsive thermoplastic elastomer to be created. Siloxane based polymers are ideal center blocks for these applications as the low T_g is

necessary for sufficient mobility at room temperature to allow for relatively fast response times at room temperature.

The living diblock copolymer synthesis described in Chapter 2 can be functionalized in a variety of ways instead of termination with trimethylchlorosilane. Coupling of living PS-PVMS diblock via the addition of the difunctional coupling agent, 1,1,3,3-tetramethyl-1,3-dichlorodisiloxane, was attempted with limited success, and the synthesis scheme used is described in Figure 3-1[37, 38]. The main difficulty with this synthesis scheme is that very precise control over the stoichiometry is required. If an excess of the coupling agent is present all of the functional groups will be capped with the coupling agent and there will be no living chains left to react with the silyl chloride functional group. If not enough of the coupling agent is introduced, there will be incomplete coupling. In addition to these stoichiometric issues the kinetics of this scheme reactions are a hindrance and this coupling scheme requires two reactions to give quantitative yields. Designing synthetic schemes that allow for reactants to be used in excess drives the reaction forward allows for higher yields and do not require precise stoichiometry. Coupling of two polymer chain ends presents kinetic challenges, by using a more reactive styryl anion, in comparison with the significantly less reactive siloxy anion, the kinetics limitations can be minimized. The novel triblock synthesis schemes are detailed and discussed. Additionally, the mechanical properties of the resulting triblock SCLCBCPs are compared to their diblock counterparts, and attempts at electro-mechanical actuation are discussed.

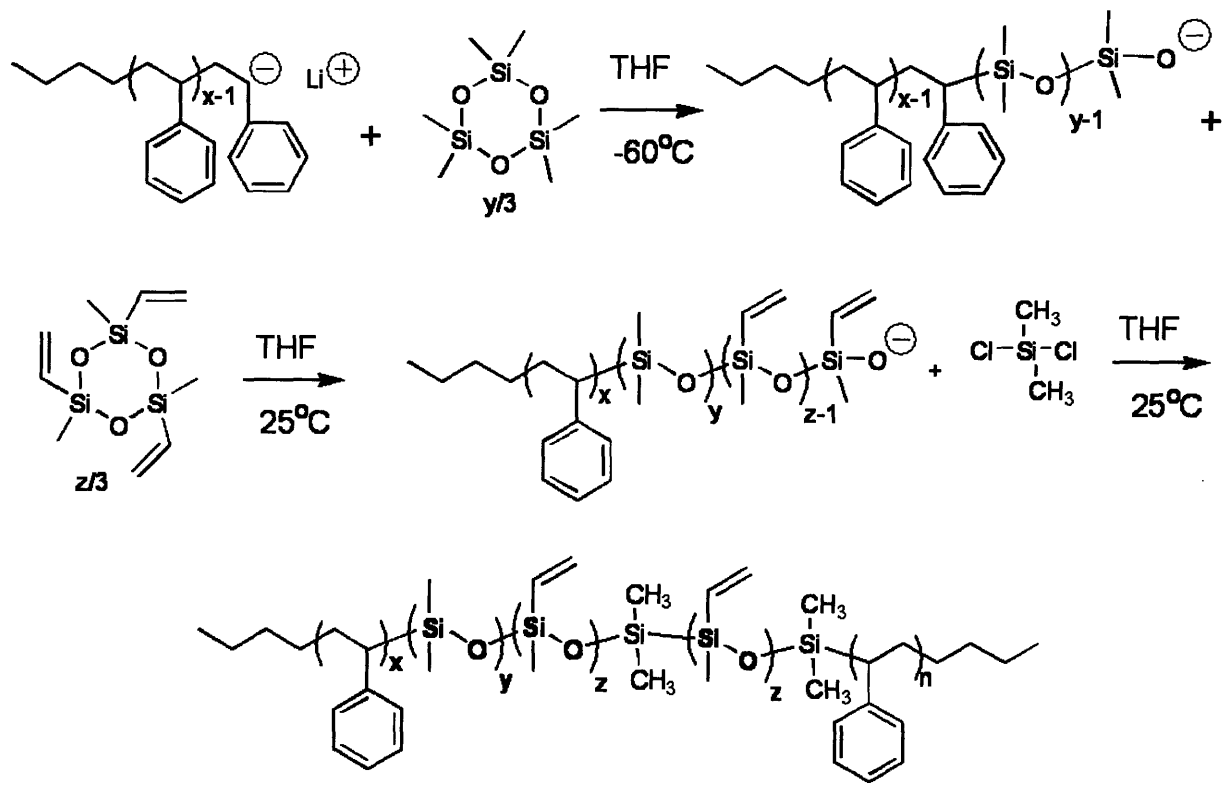

Figure 3-1. Synthetic scheme for triblock copolymers via coupling of two identical living PS-PVMS diblocks.

3.2 Experimental

3.2.1 Synthesis of A-B-A Side Chain Liquid Crystalline Triblock Copolymers

The basis for the synthesis of the A-B-A side chain liquid crystalline block copolymers is the anionic polymerization of poly(vinylmethylsiloxane) (PVMS) homopolymers and poly(styrene)-b-poly(vinylmethylsiloxane) (PS-PVMS) diblock copolymer described in Chapter 2. Instead of terminating the living PVMS or PS-PVMS with trimethylchlorosilane, the propagating anion was functionalized to allow for further synthesis resulting in a triblock copolymer.

3.2.1.1 Living PS Homopolymer Coupling to Difunctional PVMS Homopolymer

This triblock copolymer synthesis scheme involves coupling a difunctional PVMS with living polystyrene is shown in Figure 3-2. In this method the difunctional PVMS is synthesized as described in Chapter 2. However, instead of terminating the reaction with chlorotrimethylsilane, an excess of dichlorodimethylsilane is added to the reaction solution and let stir for 1 hour. The excess dichlorodimethylsilane is then removed by washing in methanol and the product is then dried under vacuum and dissolved in THF. Polystyrene of the desired molecular weight is then synthesized in the typical fashion, and the living PS is combined directly with the difunctional PVMS solution. A stoichiometric excess of living PS is added in order to achieve the highest reaction percent. In order to maintain the reactivity of the styryl anion in THF, the coupling reaction is performed in a -60°C heptane bath within the nitrogen environment of the glovebox and let stir overnight.

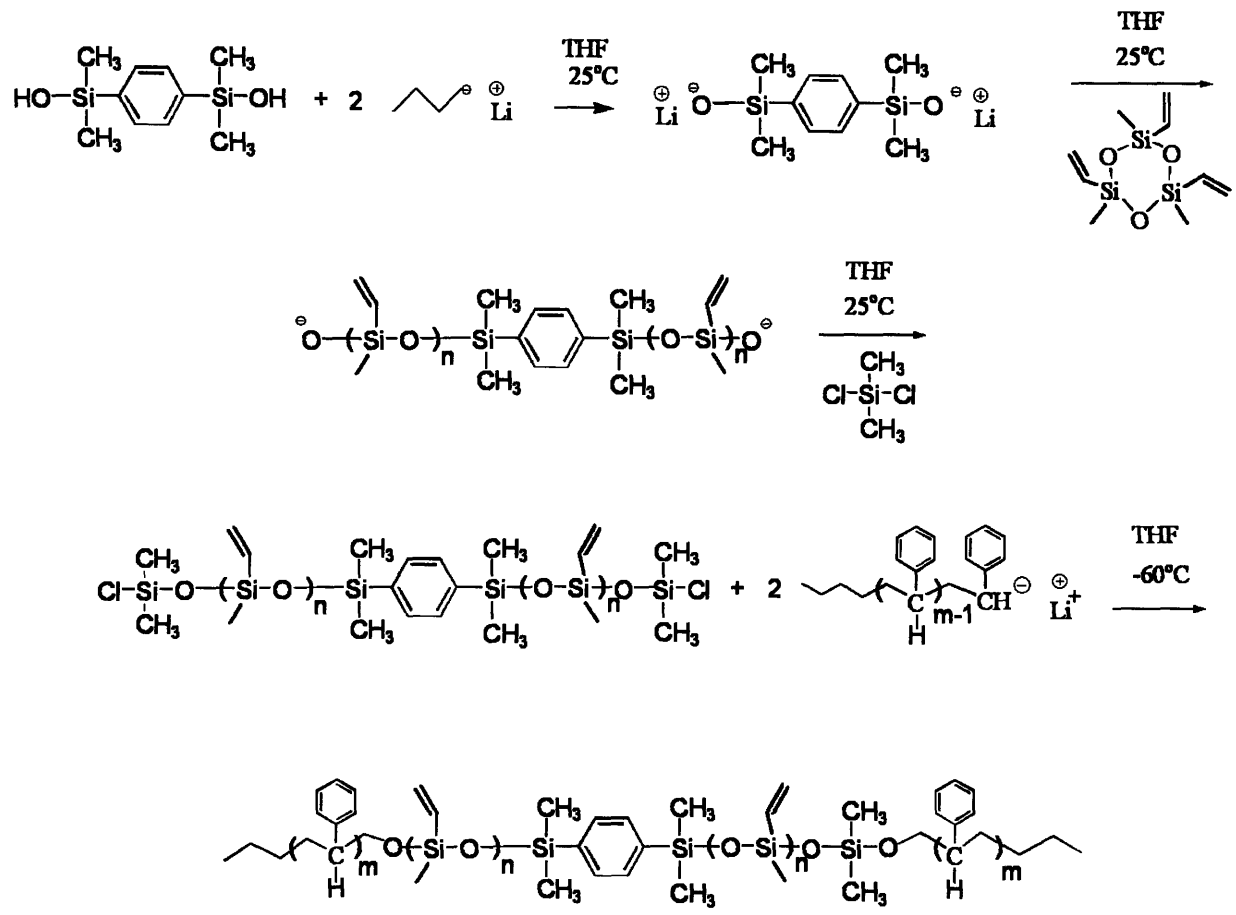

Figure 3-2. Synthetic scheme for triblock copolymers via coupling of living PS with difunctional PVMS.

3.2.1.2 Living PS Homopolymer Coupling to PS-PVMS Diblock

Another similar scheme for creating a triblock copolymer involves the coupling of living PS with a PS-PVMS diblock that has been end capped with dichlorodimethylsilane, and is shown in Figure 3-3. The PS-PVMS diblock is functionalized by adding an excess of dichlorodimethylsilane and let stir for 1 hour. The resulting polymer is washed in methanol to remove the excess dichlorodimethylsilane and then dissolved in THF. The coupling reaction is carried out as described in section 3.2.1.1

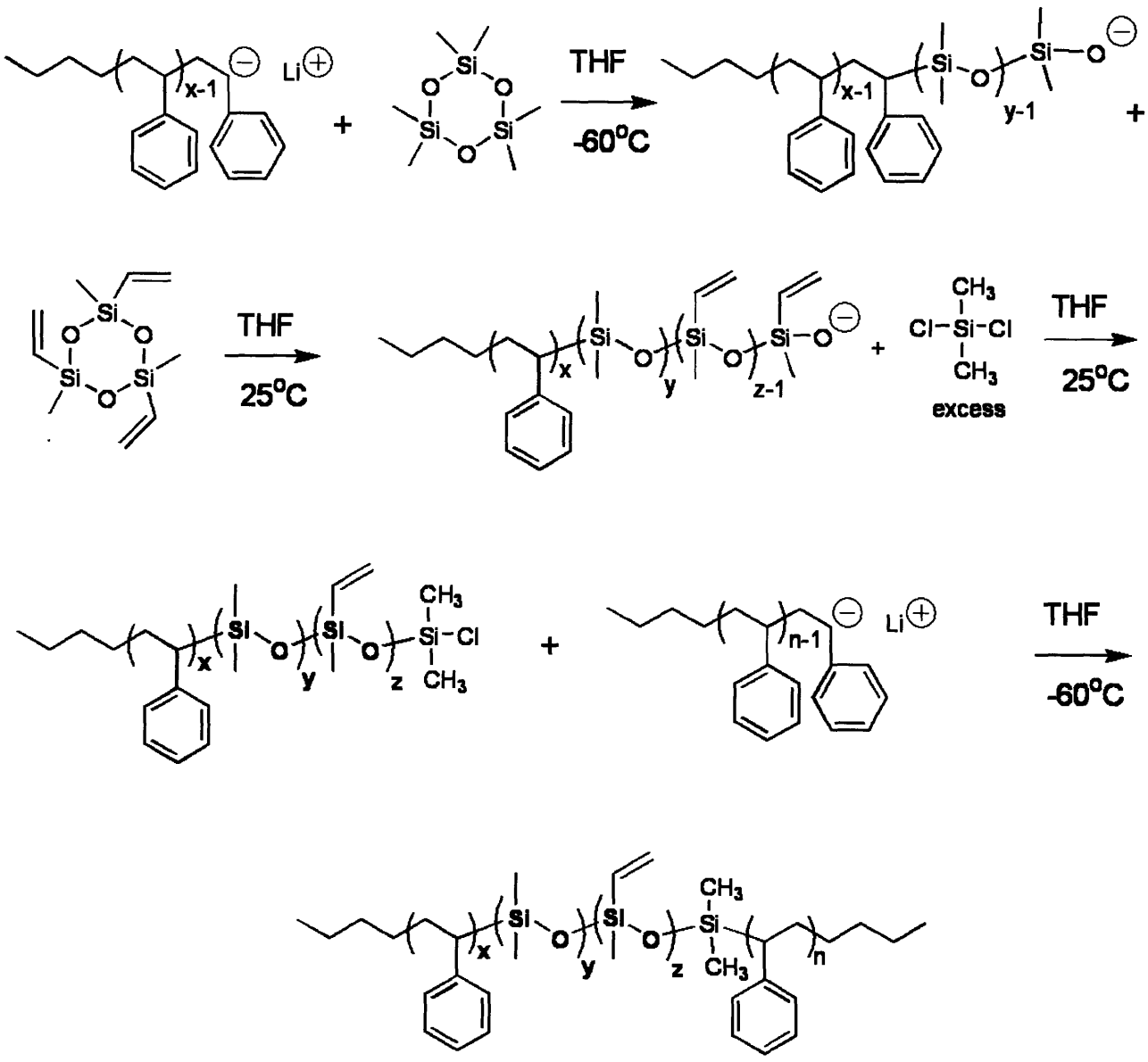

Figure 3-3. Synthetic scheme for triblock copolymers via coupling of living PS with PS-PVMS diblock.

3.2.1.3. Atom Transfer Radical Polymerization (ATRP) Using PS-PVMS as a Macroinitiator

An alternative technique for creating an A-B-A triblock is to use a PS-PVMS diblock as a macroinitiator for atom transfer radical polymerization (ATRP), as shown in Figure 3-4. This is accomplished by functionalizing a PS-PVMS diblock copolymer with an ATRP initiator. An excess of 2-bromopropionyl bromide is added to the living PS-PVMS diblock copolymer and let stir for 4 hours. The polymer is then precipitated into methanol and recovered. Since the radical present during ATRP reaction will attack the vinyl groups on the PVMS block, the siloxane backbone must be fully functionalized. To easily accomplish this the vinyl groups are functionalized with an excess of pentamethyldisiloxane using the hydrosilylation chemistry described in Chapter 2. The resulting polymer was then purified using the same procedure and dried under vacuum overnight. The copper bromide catalyst is placed under vacuum to remove any oxygen present. The macroinitiator and ligand are dissolved in styrene and the copper bromide catalyst is then added to the solution and the polymerization is carried out in bulk polystyrene at 110°C. The reaction is monitored by precipitating aliquots into methanol and analyzing with gel permeation chromatography (GPC). After the desired length is obtained the remaining solution is precipitate into methanol to stop the reaction.

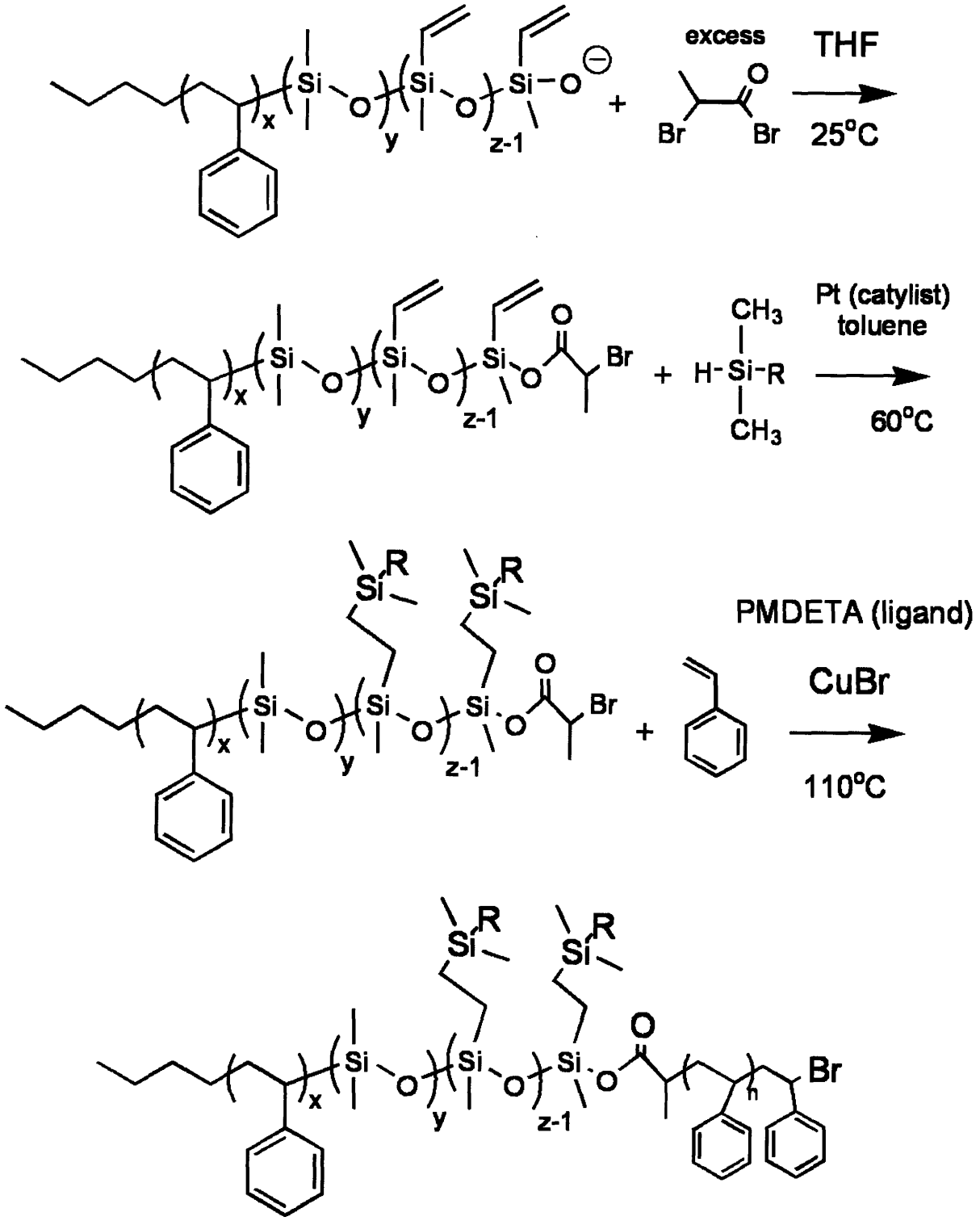

Figure 3-4. Synthetic scheme for triblock copolymers via ATRP, with a PS-PVMS diblock as a macroinitiator.

3.2.2 *Purification of Triblock Copolymers via Fractionation*

Fractionation can be used in order to separate the higher molecular weight species (triblock) from the lower molecular weight species (unreacted diblock and homopolymer). The fractionation method that has been developed here begins with dissolving the polymer in THF and adding ethanol until the higher molecular weight species begin to precipitate out. The solution is then centrifuged and the polymer still dissolved in the THF/ethanol mixture is removed isolating the highest molecular weight polymer that has precipitated out. Repeating this process several times allows for the different species of polymer to be separated by molecular weight. A Waters gel permeation chromatography (GPC) system equipped with 1 Styragel HT3 column (500-30,000 MW range), 1 Styragel HT4 column (5,000-600,000 MW range), 1 Styragel HT5 column (50,000-$4 \cdot 10^6$ MW range), a refractive index detector, and a UV detector (254nm) was used for molecular weight measurement relative to polystyrene standards. Tetrahydrofuran (THF) flowing at 1ml/min was the mobile phase. GPC was used to characterize the molecular weights of the initial polymers, the reaction solution after coupling, and the resulting polymers separated via fractionation.

3.2.3 *Mechanical Properties and Electro-mechanical Response of A-B-A and A-B Block Copolymers*

The mechanical properties of the triblock and diblock copolymers were compared using a TA instruments Q800 for dynamic mechanical analysis (DMA) device. Two different tests were performed, each on a diblock SCLCBCP and a triblock SCLCBCP. The first test was a strain recovery test, where the sample film was elongated to a strain of 5% and held for 5 minutes. The stress was then released and the film was allowed to relax for 20 minutes. Throughout the

experiment a nominal force of 0.001 N was applied to ensure the film was taught. In the second experiment a constant strain rate of 1% per minute was applied, until a strain of 5% was achieved, and the strain was allowed to recover at a rate of 1% per minute. Throughout this experiment the stress was measured. In both cases the stress reached zero before the film fully recovered, indicative of plastic deformation.

The morphological response to an applied electric field was investigated using X-ray scattering at the National Synchrotron Light Source (NSLS) at Brookhaven National Laboratory (BNL) in Upton, NY. The morphology of the SCLCBCP materials was investigated before and after the application of a 2500 volt electric field across the film. The SCLCBCP films were placed in the center of two copper plates and glass spacers were used to control the gap. A caliper mounted on the top of the device was used to apply pressure to the top plate and to precisely measure the gap (Figure 3-5). The gap was typically 250μm resulting in an electric field of 10 MV/m. Insulating blocks were placed below and above the copper blocks to prevent short circuits. Additionally, because of the high voltage and small gap distance, the copper blocks were wrapped in Kapton tape, except for the area in contact with the SCLCBCP films, to prevent arcing.

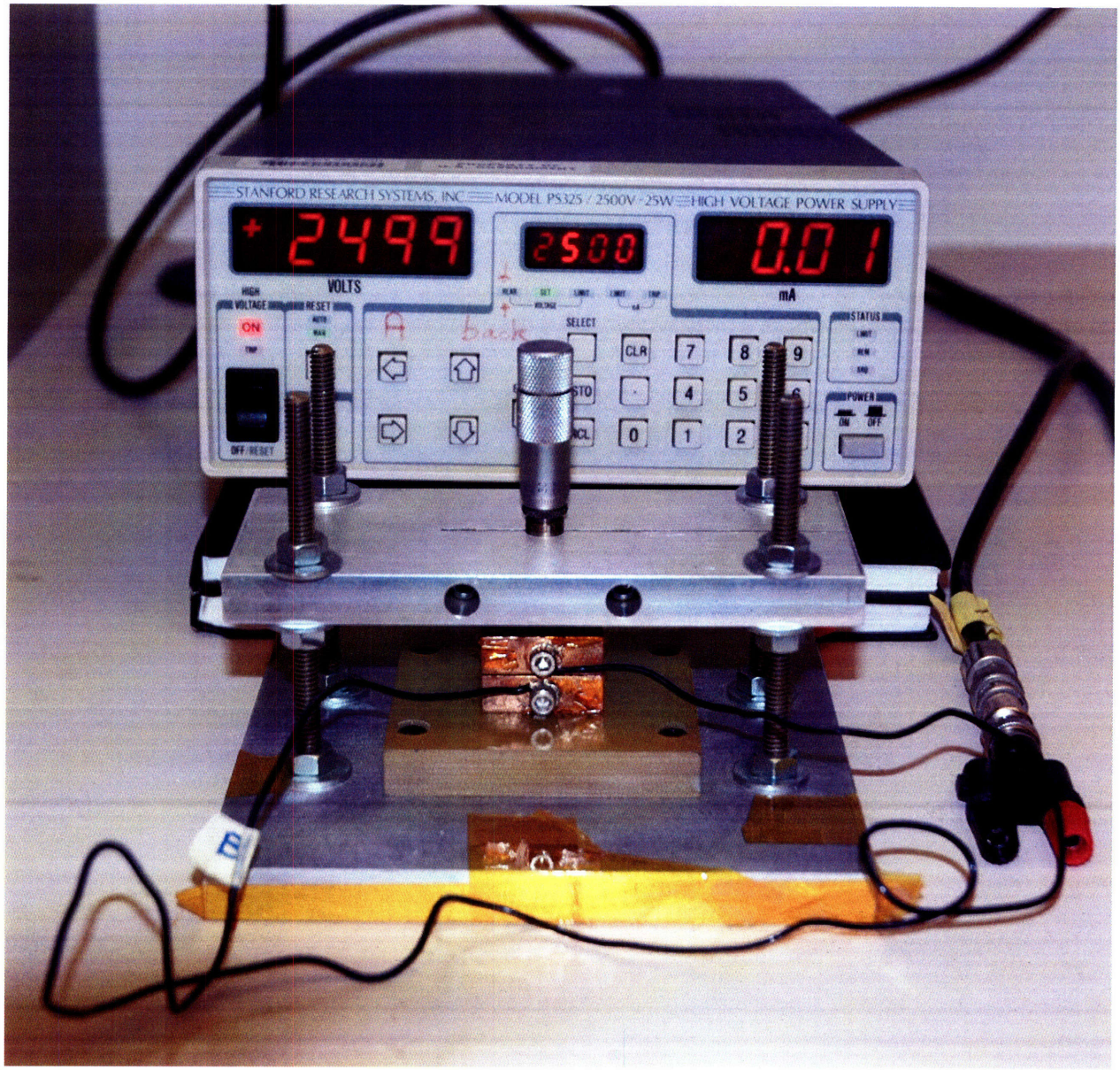

Figure 3-5. Picture of the electro-responsive testing device. The sample is placed between the copper blocks and an electric field of 2500 volts is applied across the gap (the high voltage power source is pictured in the background). Glass spacers are used to control the gap thickness, which is measured with the caliper mounted on the top of the device. This device was placed in the synchrotron X-ray beampath (synchrotron not pictured) and the morphological response to the applied electric field was investigated with X-ray scattering.

The approach for electro-mechanical testing involves applying an electric field across the material while the dimensional change and stress are being monitored in a dynamic mechanical analysis (DMA) device. An electric field is applied across the material under a constant load and the strain is measured as a function of the applied voltage (See Figure 3-6). The SCLCBCP films were coated with a 100nm gold film (deposited by thermal evaporation) on each side and the edges were trimmed so that the gold film is only present two faces of the film. The film was then mounted into a TA instruments Q800 for dynamic mechanical analysis (DMA). using custom insulating grips. A constant force of 0.001 N was applied to the film with and without an applied electric field.

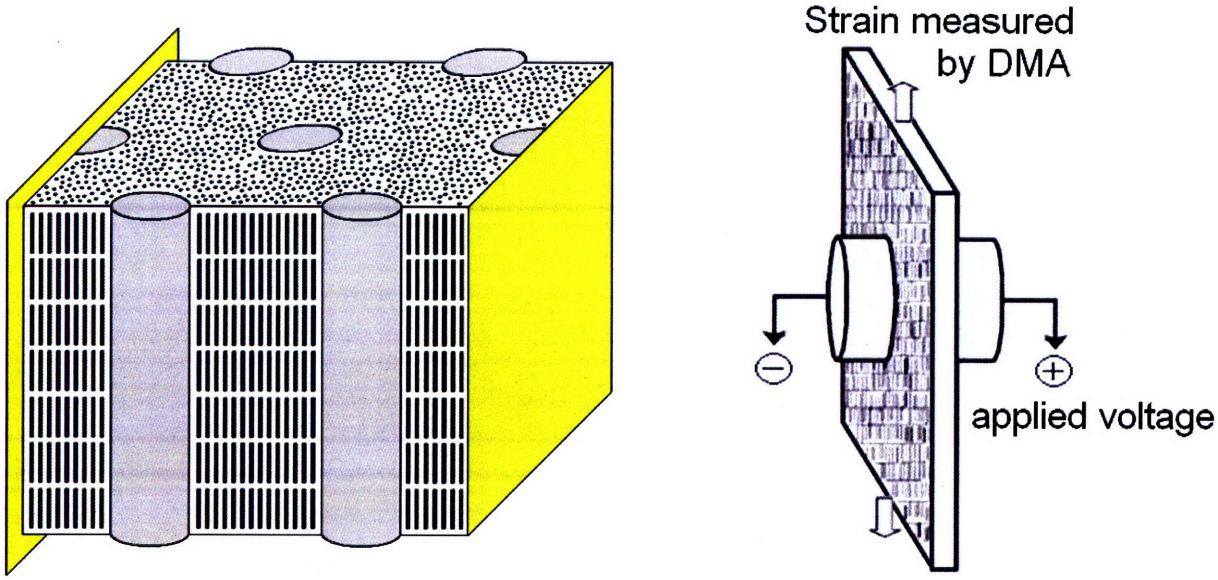

Figure 3-6: Left: Schematic of film preparation, the SCLCBCP film is coated with gold on two faces in order to allow for the application of an electric field (schematic is not to scale for clarity). Right: Schematic of electromechanical testing setup (Modified from Hiraoka, et al. [5])

3.3 Results and Discussion

All three of the synthetic schemes described successfully resulted in the synthesis of PS-PVMS-PS triblock copolymer. The advantages and disadvantages of each synthetic technique will be discussed in this section. The coupling of living PS homopolymer difunctional PVMS homopolymer results in a mixture of triblock, diblock where only one functional group has reacted, unreacted PVMS homopolymer and the excess PS homopolymer. This technique was the most successful in creating PS-PVMS-PS triblock copolymer. Figure 3-7 shows GPC curves for the initial PS homopolymer, difunctional PVMS homopolymer, and the resulting mixture after the coupling reaction.

The PS and PVMS homopolymers were determined to have a weight-average molecular weight (M_w) of 40,000 and 44,000 g/mol, respectively (A summary of the GPC data is provided in Table 3-1). It should be noted that all molecular weight measurements are determined in comparison to PS standards. Therefore, all of the molecular weight measurements are the average coil size of the polymer relative to a polystyrene homopolymer of a given molecular weight that has the same average coil size. The GPC trace of the reaction solution after coupling displayed three primary peaks which are thought to be; 1) triblock copolymer, 2) diblock where only one functional group has reacted, and 3) a combination of excess PS homopolymer and small amounts of unreacted PVMS homopolymer. These peaks occur at elution times of 24.7 min (125,000 g/mol), 25.7 min (73,000 g/mol), and 27.2 min (39,000 g/mol), respectively. The combination of the first and second peaks has a M_w of 127,000 g/mol, and the M_w of the third peak is 40,000 g/mol. The peaks observed at high elution times (greater than 35 minutes) are small molecular weight species such as monomers, initiator, or impurities.

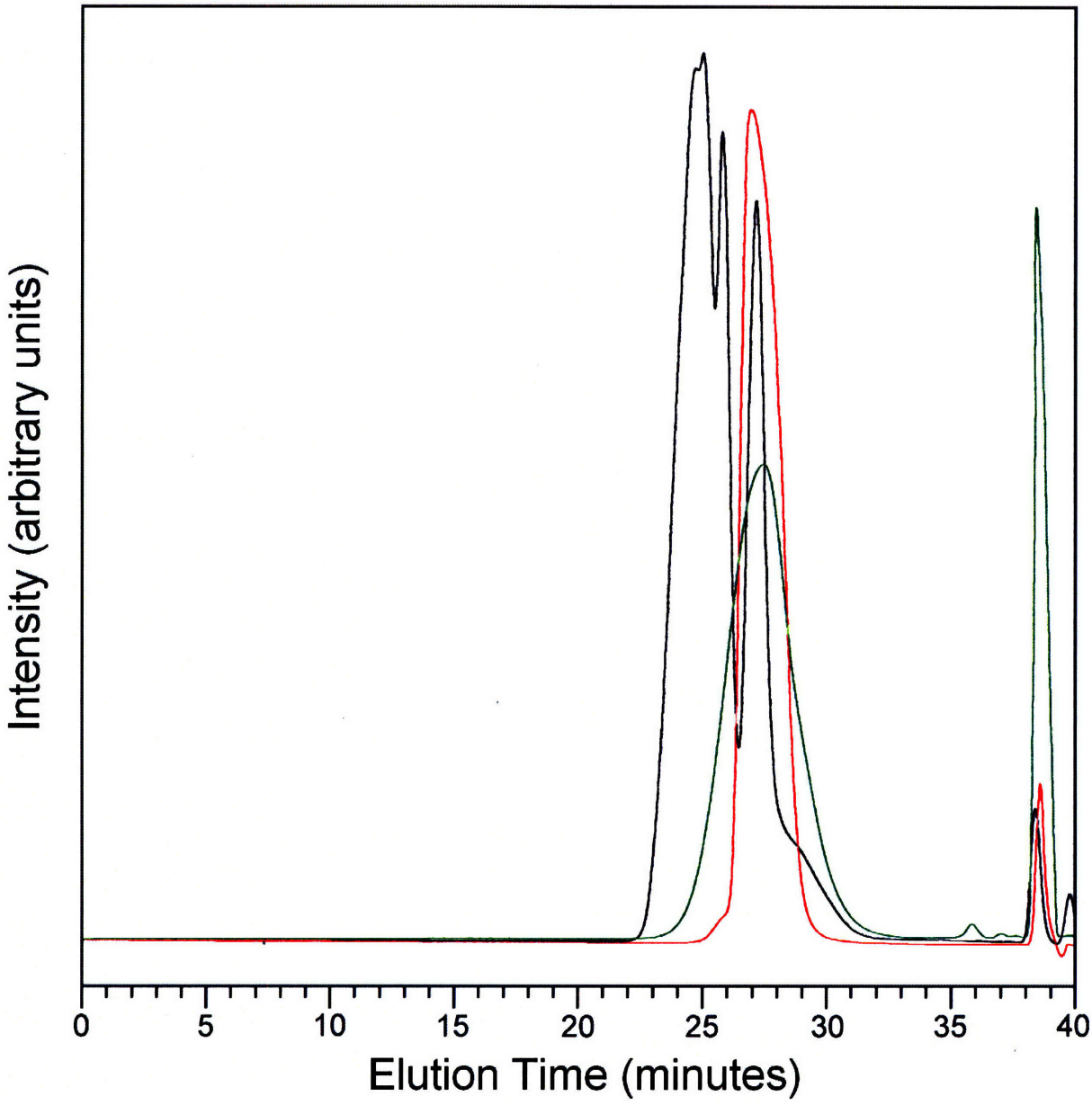

Figure 3-7. GPC curves for the initial PS homopolymer (red), difunctional PVMS (green) homopolymer, and the resulting mixture after the coupling reaction (black).

Table 3-1. Summary of coupling and fractionation results.

Sample name	M_w (primary peak)	PDI	M_w (secondary peak)	PDI
Initial PS	40,000 g/mol	1.09	-	-
Initial PVMS	44,000 g/mol	1.25	-	-
Reaction solution	127,000 g/mol	1.18	40,000 g/mol	1.05
Fractionation 1	158,000 g/mol	1.12	40,000 g/mol	1.09
Fractionation 2	108,000 g/mol	1.11	44,000 g/mol	1.13
Fractionation 3	79,000 g/mol	1.08	39,000 g/mol	1.04

Figure 3-8 displays the GPC trace for the reaction solution (black), and three subsequent fractionations (red, green, and blue respectively). The first fractionation (red) primarily contains triblock copolymer with a M_w of 158,000 g/mol and a small amount of PS homopolymer with a M_w of 40,000 g/mol. It is believed that the low molecular weight peak is only PS as the PVMS homopolymer has a higher solubility in the THF/ethanol mixture, and would not precipitate out. The second fractionation (green) has three peaks that represent a combination of triblock copolymer at elution times of 25.0 min (101,000 g/mol), diblock copolymer 25.5 min (75,000 g/mol), and PS homopolymer 26.8 min (44,000 g/mol). The combination of the first and second peaks has a M_w of 108,000 g/mol, and the M_w of the third peak is 44,000 g/mol. The final fractionation primarily contains PS homopolymer with a M_w of 39,000 g/mol, and a small amount of diblock copolymer with a M_w of 79,000 g/mol. The intensities of the peaks is highly sensitive to the concentration of the polymer in the GPC elution solution, thus the intensities of the curves were scaled for clarity. This displays the ability to effectively separate various species from the reaction solution and isolate the triblock copolymer. The polymer, PS40-PVMS24-PS40, from the first precipitation was functionalized with the 4BBP4 mesogen. A 55% attachment was achieved resulting in the SCLCBCP PS40-LCP_{4BPP4}121-PS40.

The resulting solution was precipitated into methanol and then dissolved in THF (les than 0.1 weight percent solution). Ethanol was then added and mixed until a small amount of precipitate was observed. The solution is then centrifuged and the polymer still dissolved in the THF/ethanol mixture is removed isolating the highest molecular weight polymer that has precipitated out. Typically, the first precipitation occurs when a 1:1 THF:ethanol ratio is approached.

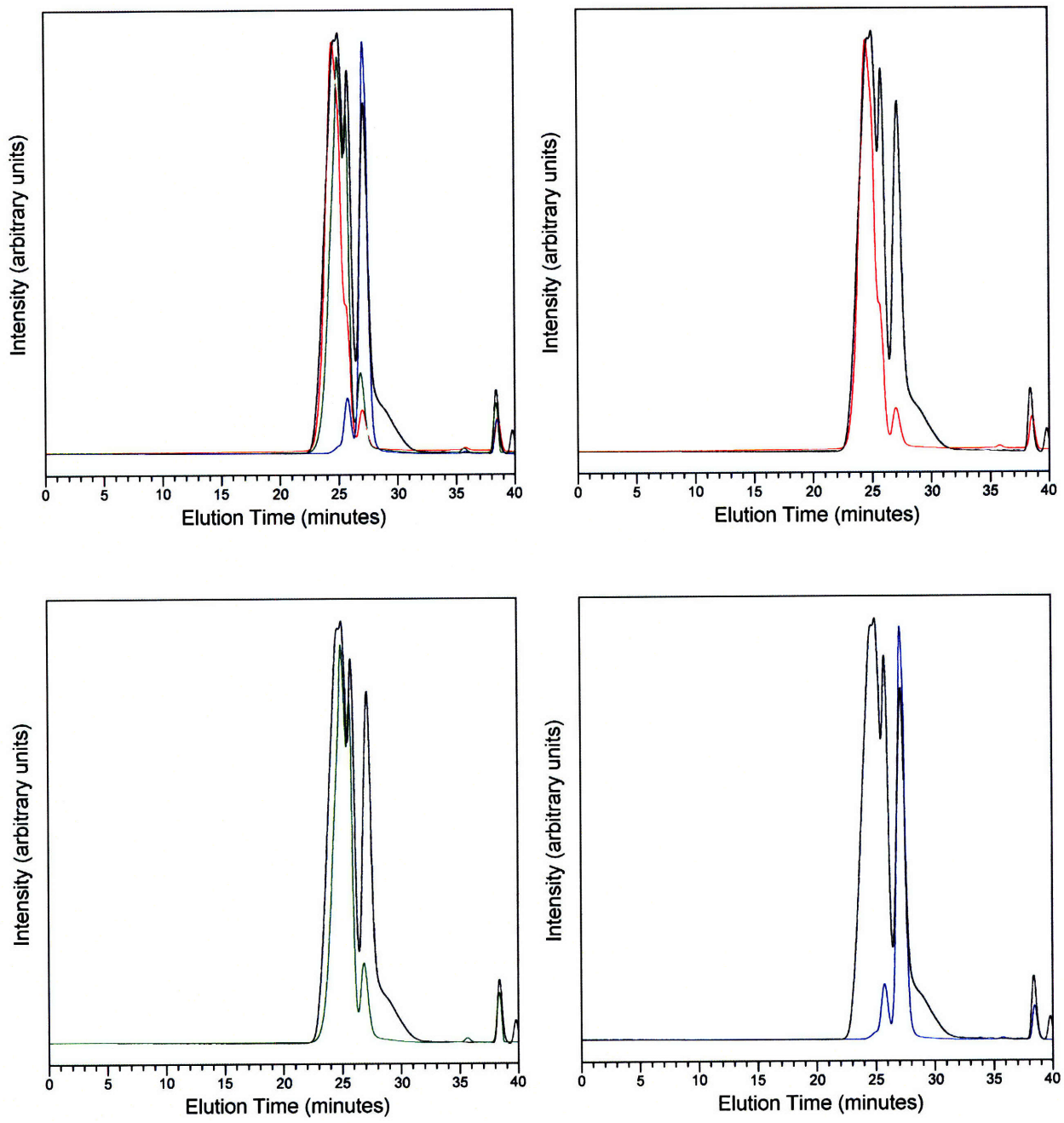

Figure 3-8. GPC curves of a) the reaction solution (black) and three subsequent fractionations (red, green, and blue respectively). b), c), and d) show only the reaction solution and one fractionation for clarity.

The living PS homopolymer coupling to PS-PVMS diblock coupling reaction yielded similar results as the PS homopolymer coupling to difunctional PVMS reaction. Once again a mixture of triblock, unreacted diblock, and excess PS homopolymer was obtained and the same fractionation technique was used to isolate the triblock copolymer. The coupling of PS homopolymer to the PS-PVMS diblock copolymer resulted in lower yields than the coupling of PS homopolymer to the difunctional PVMS. Although the coupling to difunctional PVMS requires two reactions to take place, where the coupling to PS-PVMS diblock only requires one reaction, it is believed that the functionalization of difunctional PVMS is achieved to a higher extent than the functionalization of the PS-PVMS diblock. It appears that the simple procedure for creating the difunctional PVMS homopolymer (initiation, a single propagation step, and functionalization of the living PVMS) results in a well defined and functionalized polymer. However, in the case of the PS-PVMS diblock, there are three separate monomers (styrene, hexamethylcyclotrisiloxane, and 2,4,6-trimethyl-2,4,6-triethynylcyclosiloxane) that must be added before the functionalization can occur. These additional steps possibly lead to the introduction of impurities, thus reducing the final functionalization of the diblock copolymer.

It should be noted that the coupling of PS homopolymer to difunctional PVMS results in a symmetric triblock copolymer. However, the coupling of PS homopolymer to the PS-PVMS diblock is not symmetrical, as the PS ends were each synthesized separately, and there is a small amount of PDMS between the PS and the PVMS of the initial diblock (as noted in Chapter 2). However, the purification of the PS-PVMS diblock is practically easier than the purification of the PVMS homopolymer, as it is easier to remove the methanol from the PS-PVMS diblock than the PVMS homopolymer. Additionally the diblock copolymer is a solid at room temperature allowing for easy handling where the PVMS homopolymer is a viscous oil. The subsequent

attachment of the LC mesogens to each of the triblock copolymers yielded similar results to the attachments to the diblock copolymer described in Chapter 2. Overall, though more tedious, the coupling of PS homopolymer to the difunctional PVMS homopolymer provides better yields and a more well defined triblock copolymer than the coupling of PS homopolymer to the PS-PVMS diblock copolymer, and is the preferred technique.

The PS-PVMS diblock was successfully functionalized for use as a macroinitiator for atom transfer radical polymerization (ATRP). Before the functionalized PS-PVMS diblock copolymer can be used as a macroinitator for ATRP the vinyl functional groups must be protected. The presence of vinyl functional groups will lead to side reactions such as termination, back-biting, or crosslinking of the polymer. The most significant drawback to this method is that the mesogen must be fully attached to the backbone before the reaction takes place. In order to vary the attachment percent of the LC mesogen on the block copolymer backbone the LC must first be attached to the desired functionalization and then a subsequent hydrosilylation reaction is necessary to protect the remaining vinyl functional groups. This second hydrosilylation reaction was achieved using an excess of pentamethyldisiloxane and 100% functionalization was achieved in ~6 hours. Once the macroinitiator is fully functionalized the ATRP reaction can take place. The reaction must be monitored by precipitating into methanol and using GPC analysis to monitor the reaction. The need to monitoring the reaction leads to a significant decrease in the final yield. Additionally, each attachment percent requires two additional steps, the completion of the vinyl functional and the ATRP reaction. This creates a situation where each attachment percent has a slightly different PS block on one end making it difficult to accurately compare the properties as a function of attachment percent. The synthesis of a side chain liquid crystalline block copolymer was successfully synthesized using this

method, however the significant difficulties due to the extra steps required makes this synthetic scheme much less efficient and practical than the other techniques.

The mechanical property studies indicate that the triblock SCLCBCPs have a greater ability to recover an applied strain. After applying a strain of 5% for 5 minutes the triblock copolymer PS40-LCP_{4BPP4}121-PS40 recovered 94% of the applied strain within 20 minutes. In contrast the diblock copolymer, PS61-LCP_{4BPP4}101, only recovered 60% of the applied strain under the same conditions (Figure 3-9a). Similarly, looking at the stress-strain curves from the constant strain rate experiment (Figure 3-9b) the triblock and diblock copolymers recovered 79% and 67% of the applied strain, respectively. These results indicate that there is more elastic recovery in the triblock SCLCBCPs and therefore more plastic deformation in the diblock SCLCBCPs. Each of the materials tested have a similar compositions; polystyrene weight percents of, 40% and 38% for PS40-LCP_{4BPP4}121-PS40 and PS61-LCP_{4BPP4}101, respectively. The only significant difference is the block architecture.

This behavior is expected, as the triblock SCLCBCPs possesses physical crosslinks, that are not present in the diblock SCLCBCPs, due to the A-B-A structure of the triblock copolymer. These physical crosslinks arise from the covalent linkage of the siloxane based liquid crystalline polymer blocks between two PS domains. The diblock SCLCBCP has only one covalent linkage to a PS domain and one free end; thus there is no covalent connectivity between the PS domains. However, in both the diblock and triblock SCLCBCPs the smectic LC mesophase can act as a type of a temporary physical crosslink. Although these crosslinks are not covalent, the side chain liquid crystals, from different polymer backbones, are hindered from moving freely relative to each other when a stress is applied. Once the LC moieties have slipped past each other, the deformation is plastic and not recovered.

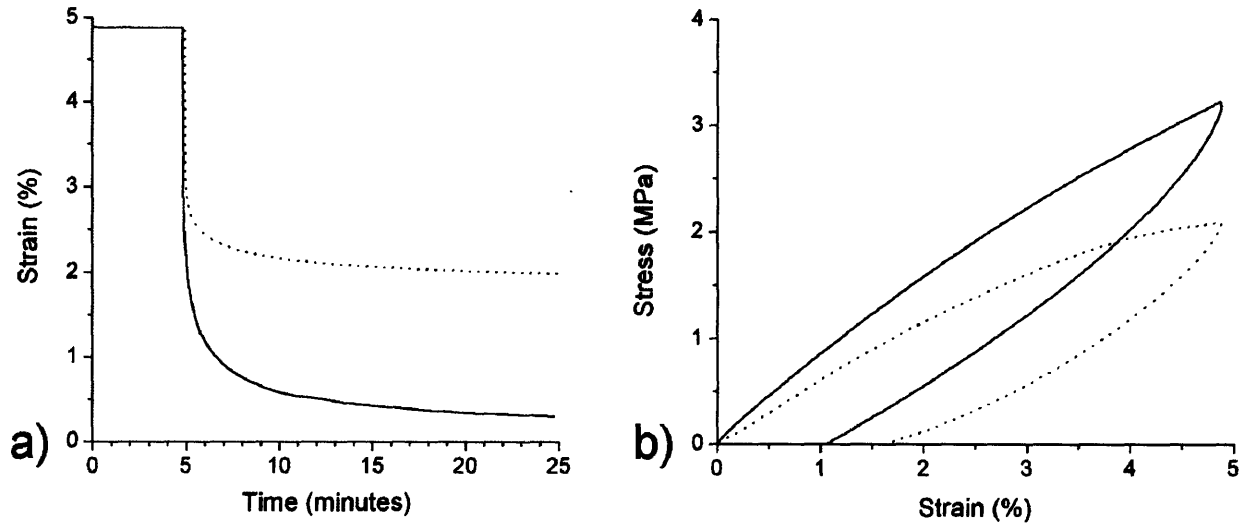

Figure 3-9. Mechanical property comparison of triblock and diblock SCLCBCPs. a) Strain recovery experiment, b) Strain ramp experiment. In both cases the solid line is the triblock SCLCBCP, PS40-LCP_{4BPP4}121-PS40, and the dashed line is the diblock SCLCBP, PS61-LCP_{4BPP4}101.

All of the studies involving the application of an electric field in order to either induce a morphological or mechanical property change were inconclusive. The in-situ electric field experiments were performed at National Synchrotron Light Source (NSLS) in Upton, NY. There was no discernible change in the morphology upon the application of the electric field. The CCD detector provides a resolution of 0.01 nm for experimental setup used (sample to detector distance of 2012 mm) and the feature spacing of interest. This requires the change in smectic layer spacing to be at least 0.3% in order to be detected. In reality, due to the breadth of the peak, the change in the layer spacing must be significantly larger in order to be resolved. Similar work was reported by Kohler et. al., citing changes in layer thickness up to 1% as a result of

electroclinic effects in smectic elastomer films[39]. In this case small angle X-ray reflectivity was used to correlate the observed change in film thickness with a change in the smectic layer thickness. A 0.4% changes in the smectic layer spacing was reported with a 2 MV/m electric field, however the shift in the data presented by Kohler et. al. is subtle and unconvincing (See Figure 3-10). This demonstrates the difficulty in such measurements, even in free-standing films where corresponding lateral extensions are reported. For the desired actuation applications there would most likely be physical constraints on the film and the material would be expected to produce some force, resulting in work. Additionally, the presence of glassy polystyrene domains within this system further hinders any potential electroclinic response. The electro-mechanical response of these materials was investigated where an electric field was applied across the SCLCBCPs while under a constant load. Once again the results were inconclusive, as no changes in the dimensions of the film were observed.

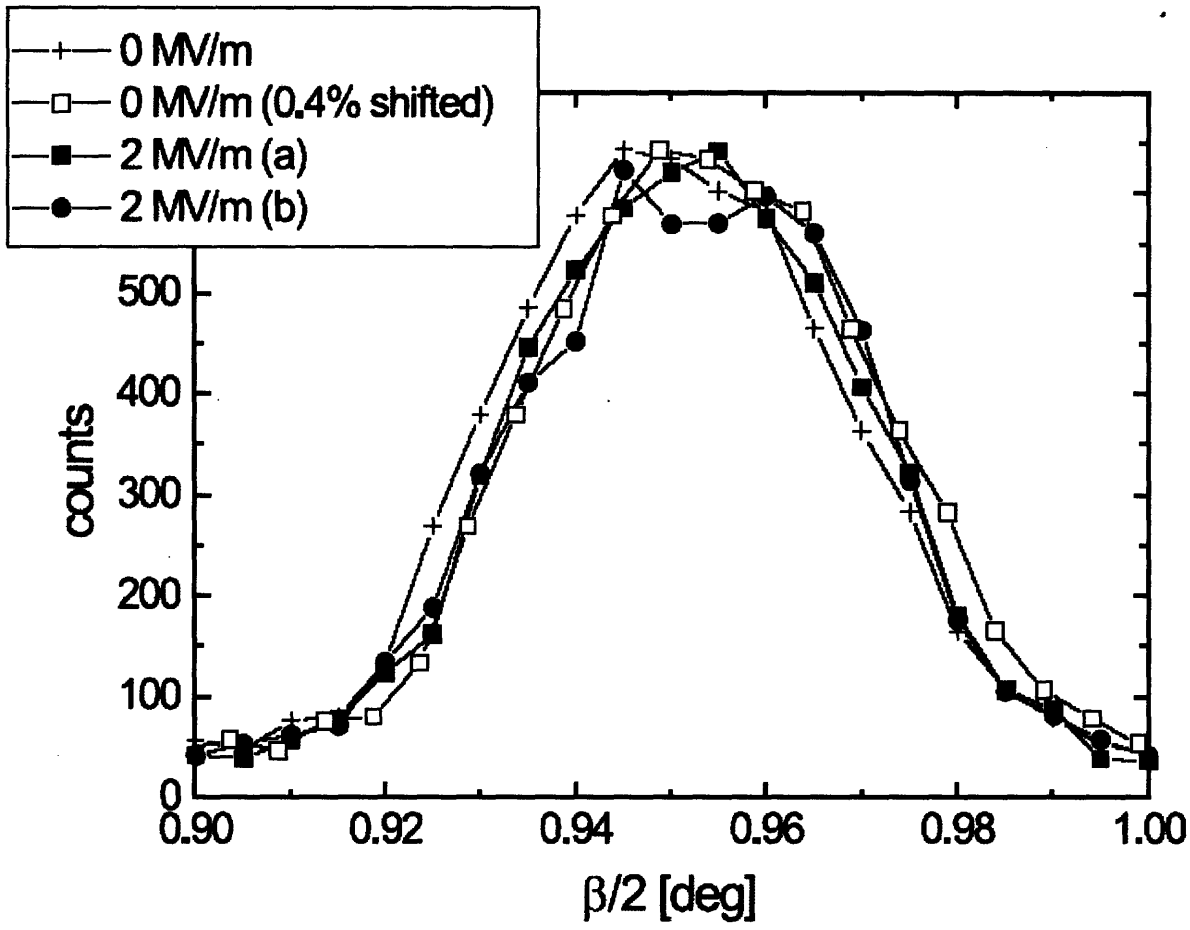

Figure 3-10. X-ray small-angle reflection profile (smectic layer Bragg peak) of a structurally similar material near the smectic A–smectic C* phase transition without electric field (+) and in a 2-MV/m electric field (*filled squares* and *circles* correspond to two independent measurements) vs. reflection angle $\beta/2$. For comparison, the zero-field reflex has been shifted in the angular range by 0.4% to larger angles (*open squares*)[39].

3.4 Conclusions

Several different methods for synthesizing and isolating PS-PVMS-PS triblock block copolymers were developed. Of the three techniques detailed the coupling of PS homopolymer to the difunctional PVMS homopolymer provides the highest yields and the most well defined triblock copolymer and is the preferred technique. Fractionation from THF/ethanol was successfully used to isolate the high molecular weight triblock copolymer. The mechanical properties of the resulting triblock and diblock SCLCBCPs were investigated, primarily to compare the elastic strain recovery as a function of backbone architecture. In both of the studies the triblock SCLCBCPs displayed a greater ability to recover an applied strain, which is attributed to the physical crosslinks resulting for the A-B-A architecture. Attempts to observe either a morphological of mechanical response of these materials upon application of an electric field were inconclusive. It is believed that the electroclinic effect of the smectic liquid crystalline mesophase is not dramatic enough to produce useful morphological or mechanical changes in this class of materials. The inability to achieve the desired results through the electroclinic actuation, leads to the investigation and development of the photo-responsive LC moieties described in Appendix C. It is recommended that more versatile chemistries be developed to increase the triblock copolymer yields. The difunctional siloxane backbone could possibly be the basis and the end groups functionalized for attachment of high T_g blocks. The polystyrene outer blocks could be replaced by another high T_g block, allowing for the advantages of the low T_g of the siloxane center block and the flexible hydrosilylation chemistry to still be utilized. In order to create a system that is more responsive, it is recommended that other actuation mechanisms, such as photo-responsive or chemo-responsive be explored.

3.5 References

1. Liu, C.; Qin, H.; Mather, P. T., Review of progress in shape-memory polymers. *Journal of Materials Chemistry* **2007,** 17, (16), 1543-1558.

2. Mayer, S.; Zentel, R., Liquid crystalline polymers and elastomers. *Current Opinion in Solid State & Materials Science* **2002,** 6, (6), 545-551.

3. Beyer, P.; Zentel, R., Photoswitchable smectic liquid-crystalline elastomers. *Macromolecular Rapid Communications* **2005,** 26, (11), 874-879.

4. Finkelmann, H.; Nishikawa, E.; Pereira, G. G.; Warner, M., A new opto-mechanical effect in solids. *Physical Review Letters* **2001,** 8701, (1)

5. Hiraoka, K.; Stein, P.; Finkelmann, H., Electromechanics of a chiral smectic C elastomer: Measurement of complex piezoelectric constant through successive phase transformations. *Macromolecular Chemistry and Physics* **2004,** 205, (1), 48-54.

6. Lendlein, A.; Jiang, H. Y.; Junger, O.; Langer, R., Light-induced shape-memory polymers. *Nature* **2005,** 434, (7035), 879-882.

7. Hall, E.; Ober, C. K.; Kramer, E. J.; Colby, R. H.; Gillmor, J. R., Diffusion and Melt Viscosity of a Main-Chain Liquid-Crystalline Polyether. *Macromolecules* **1993,** 26, (15), 3764-3771.

8. Percec, V.; Nava, H.; Jonsson, H., The Influence of Molecular-Weight on the Thermotropic Properties of a Random Copolyether Based on 1,5-Dibromopentane,1,7-Dibromoheptane, and 4,4'-Dihydroxy-Alpha-Methylstilbene. *Journal of Polymer Science Part a-Polymer Chemistry* **1987,** 25, (7), 1943-1965.

9. Zhou, W. J.; Kornfield, J. A.; Ugaz, V. M.; Burghardt, W. R.; Link, D. R.; Clark, N. A., Dynamics and shear orientation behavior of a main-chain thermotropic liquid crystalline polymer. *Macromolecules* **1999,** 32, (17), 5581-5593.

10. Bohnert, R.; Finkelmann, H., Liquid-Crystalline Side-Chain Ab Block-Copolymers by Direct Anionic-Polymerization of a Mesogenic Methacrylate. *Macromolecular Chemistry and Physics* **1994,** 195, (2), 689-700.

11. Finkelmann, H.; Kock, H. J.; Rehage, G., Liquid-Crystalline Elastomers - a New Type of Liquid-Crystalline Material. *Makromolekulare Chemie-Rapid Communications* **1981,** 2, (4), 317-322.

12. Gabert, A. J.; Verploegen, E.; Hammond, P. T.; Schrock, R. R., Synthesis and characterization of ABA triblock copolymers containing smectic C* liquid crystal side chains via ring-opening metathesis polymerization using a bimetallic molybdenum initiator. *Macromolecules* **2006,** 39, (12), 3993-4000.

13. Kempe, M. D.; Verduzco, R.; Scruggs, N. R.; Kornfield, J. A., Rheological study of structural transitions in triblock copolymers in a liquid crystal solvent. *Soft Matter* **2006,** 2, (5), 422-431.

14. Laus, M.; Bignozzi, M. C.; Fagnani, M.; Angeloni, A. S.; Galli, G.; Chiellini, E.; Francescangeli, O., Liquid crystalline poly(vinyl ether)s and block copoly(vinyl ether)s by living cationic polymerization. *Macromolecules* **1996,** 29, (15), 5111-5118.

15. Lehmann, W.; Skupin, H.; Tolksdorf, C.; Gebhard, E.; Zentel, R.; Kruger, P.; Losche, M.; Kremer, F., Giant lateral electrostriction in ferroelectric liquid-crystalline elastomers. *Nature* **2001,** 410, (6827), 447-450.

16. Li, M. H.; Keller, P.; Albouy, P. A., Novel liquid crystalline block copolymers by ATRP and ROMP. *Macromolecules* **2003,** 36, (7), 2284-2292.

17. Moment, A.; Miranda, R.; Hammond, P. T., Synthesis of polystyrene-polysiloxane side-chain liquid crystalline block copolymers. *Macromolecular Rapid Communications* **1998,** 19, (11), 573-579.

18. Osuji, C.; Chao, C. Y.; Bita, I.; Ober, C. K.; Thomas, E. L., Temperature-dependent photonic bandgap in a self-assembled hydrogen-bonded liquid-crystalline diblock copolymer. *Advanced Functional Materials* **2002,** 12, (11-12), 753-758.

19. Osuji, C. O.; Chao, C. Y.; Ober, C. K.; Thomas, E. L., Supramolecular microphase separation in a hydrogen-bonded liquid crystalline comb copolymer in the melt state. *Macromolecules* **2006,** 39, (9), 3114-3117.

20. Singh, R.; Verploegen, E.; Hammond, P. T.; Schrock, R. R., Synthesis of ABA triblock copolymers via ring opening metathesis polymerization using a bimetallic initiator: Influence of a flexible spacer in the side chain liquid crystalline block. *Macromolecules* **2006,** 39, (24), 8241-8249.

21. Svensson, M.; Helgee, B.; Skarp, K.; Andersson, G., Effects of nitro substituents on the properties of a ferroelectric liquid crystalline side chain polysiloxane. *Journal of Materials Chemistry* **1998,** 8, (2), 353-362.

22. Verduzco, R.; Scruggs, N. R.; Sprunt, S.; Palffy-Muhoray, P.; Kornfield, J. A., Director dynamics in liquid-crystal physical gels. *Soft Matter* **2007,** 3, (8), 993-1002.

23. Verploegen, E.; McAfee, L. C.; Tian, L. T.; Verploegen, D.; Hammond, P. T., Observation of Transverse Cylinder Morphology in Side Chain Liquid Crystalline Block Copolymers. *Macromolecules* **2007,** 40, (4), 777-780.

24. Yamada, M.; Iguchi, T.; Hirao, A.; Nakahama, S.; Watanabe, J., Synthesis of Side-Chain Liquid-Crystalline Homopolymers and Block Copolymers with Well-Defined Structures by Living Anionic-Polymerization and Their Thermotropic Phase-Behavior. *Macromolecules* **1995,** 28, (1), 50-58.

25. Zheng, W. Y.; Hammond, P. T., Synthesis of new smectic C* liquid-crystalline block copolymers. *Macromolecular Rapid Communications* **1996,** 17, (11), 813-824.

26. Osuji, C.; Ferreira, P. J.; Mao, G. P.; Ober, C. K.; Vander Sande, J. B.; Thomas, E. L., Alignment of self-assembled hierarchical microstructure in liquid crystalline diblock copolymers using high magnetic fields. *Macromolecules* **2004,** 37, (26), 9903-9908.

27. Rousseau, I. A.; Mather, P. T., Shape memory effect exhibited by smectic-c liquid crystalline elastomers. *Journal of the American Chemical Society* **2003,** 125, (50), 15300-15301.

28. Anthamatten, M.; Zheng, W. Y.; Hammond, P. T., A morphological study of well-defined smectic side-chain LC block copolymers. *Macromolecules* **1999,** 32, (15), 4838-4848.

29. Donnio, B.; Wermter, H.; Finkelmann, H., Simple and versatile synthetic route for the preparation of main-chain, liquid-crystalline elastomers. *Macromolecules* **2000,** 33, (21), 7724-7729.

30. Hiraoka, K.; Sagano, W.; Nose, T.; Finkelmann, H., Biaxial shape memory effect exhibited by monodomain chiral smectic C elastomers. *Macromolecules* **2005,** 38, (17), 7352-7357.

31. Shenoy, D. K.; Thomsen, D. L.; Srinivasan, A.; Keller, P.; Ratna, B. R., Carbon coated liquid crystal elastomer film for artificial muscle applications. *Sensors and Actuators a-Physical* **2002,** 96, (2-3), 184-188.

32. Thomsen, D. L.; Keller, P.; Naciri, J.; Pink, R.; Jeon, H.; Shenoy, D.; Ratna, B. R., Liquid crystal elastomers with mechanical properties of a muscle. *Macromolecules* **2001,** 34, (17), 5868-5875.

33. Krause, S.; Lu, Z.; Iskandar, M., Properties of Low-Molecular Weight Block Copolymers.4. Differential Scanning Calorimetry and Refractive-Index Temperature-Measurements on Styrene Butadiene Diblock Copolymers and Styrene Butadiene Styrene Triblock Copolymers. *Macromolecules* **1982,** 15, (4), 1076-1082.

34. Poser, S.; Fischer, H.; Arnold, M., Liquid crystalline side-group block copolymers with triblock structure: Investigations on the influence of the block arrangement on the morphology and the LC-phase behavior. *Journal of Polymer Science Part a-Polymer Chemistry* **1996,** 34, (9), 1733-1740.

35. Osuji, C.; Zhang, Y. M.; Mao, G. P.; Ober, C. K.; Thomas, E. L., Transverse cylindrical microdomain orientation in an LC diblock copolymer under oscillatory shear. *Macromolecules* **1999,** 32, (22), 7703-7706.

36. Clark, N. A.; Lagerwall, S. T., Submicrosecond Bistable Electro-Optic Switching in Liquid-Crystals. *Applied Physics Letters* **1980,** 36, (11), 899-901.

37. McAfee, L. C. Doctoral Thesis. Massachusetts Institute of Technology, Cambridge, MA, 2005.

38. McAfee, L. C.; Hammond, P. T., Synthesis and characterization of elastomeric side-chain liquid crystal block copolymers. *Abstracts of Papers of the American Chemical Society* **2003,** 225, U674-U674.

39. Kohler, R.; Stannarius, R.; Tolksdorf, C.; Zentel, R., Electroclinic effect in free-standing smectic elastomer films. *Applied Physics a-Materials Science & Processing* **2005,** 80, (2), 381-388.

Chapter 4 Effects of Deformation on the Ordering of Side Chain Liquid Crystalline Block Copolymers

4.1 Introduction

Molecular alignment of block copolymers typically involves the orientation of nanoscale domains. Examples of various techniques utilized to achieve well aligned materials include annealing[1], various shear fields[2-10], as well as electric and magnetic fields[11]. Side chain liquid crystalline elastomers (SCLCEs) have attracted recent interest due to their ability to combine the properties of small molecule liquid crystals and polymers[12]. The increased mechanical integrity of attaching a liquid crystalline moiety to a block copolymer backbone can be beneficial for applications such as electromechanical or mechano-optical materials. Additionally, a thermoplastic elastomer can be created utilizing the phase segregation of block copolymers, where the high T_g minority blocks serve as physical crosslinks, allowing the elastomer to be processed by heating above the T_g of the minority block to achieve an oriented liquid crystalline monodomain. The inter-material dividing surface (IMDS) of the block copolymer mesophase can be used to orient the liquid crystalline mesophase, due to surface stabilization effects. In this way a well oriented block copolymer mesophase can be used to template order in the LC mesophase.

In this work the smectic liquid crystals are attached to the functionalized siloxane block of a poly(styrene)-poly(vinylmethylsiloxane) (PS-PVMS) diblock copolymer[13, 14]. Gaining a more complete understanding of the interactions between the block copolymer and the liquid

crystalline mesophases is key for enabling control over the morphologies and thus the properties of these systems; thus, recent research has increased in the area of LC block copolymers[9, 10, 13, 15-24]. The system discussed here has a unique advantage over other liquid crystalline block copolymers - a low T_g siloxane block that makes a room temperature elastomer feasible. Here we investigate the morphologies and the effects of oscillatory shear on the orientation and order of these LC block copolymers, and find that the orientation of the block copolymer domains is heavily influenced by the LC orientation. A few means of orientation have been previously reported for lamellar and cylindrical LC block copolymer systems, including: melt fiber drawing[10], roll casting[3], and oscillatory shear[4]. In this work, the effects of oscillatory shear have been shown to introduce preferential orientation of both block copolymer and liquid crystalline mesophases. Ultimately, transverse orientation of the block copolymer domains is observed in these systems at temperatures above the LC clearing point, which has never been previously observed.

4.2. Results and Discussion

4.2.1 Structural and Thermal Characterization of Side Chain Liquid Crystalline Block Copolymers

PS-PVMS functional diblock copolymer was synthesized with anionic polymerization, LCs were synthesized and attached to the block copolymer backbone via hydrosilylation as described in Chapter 2 (Figure 4-1).

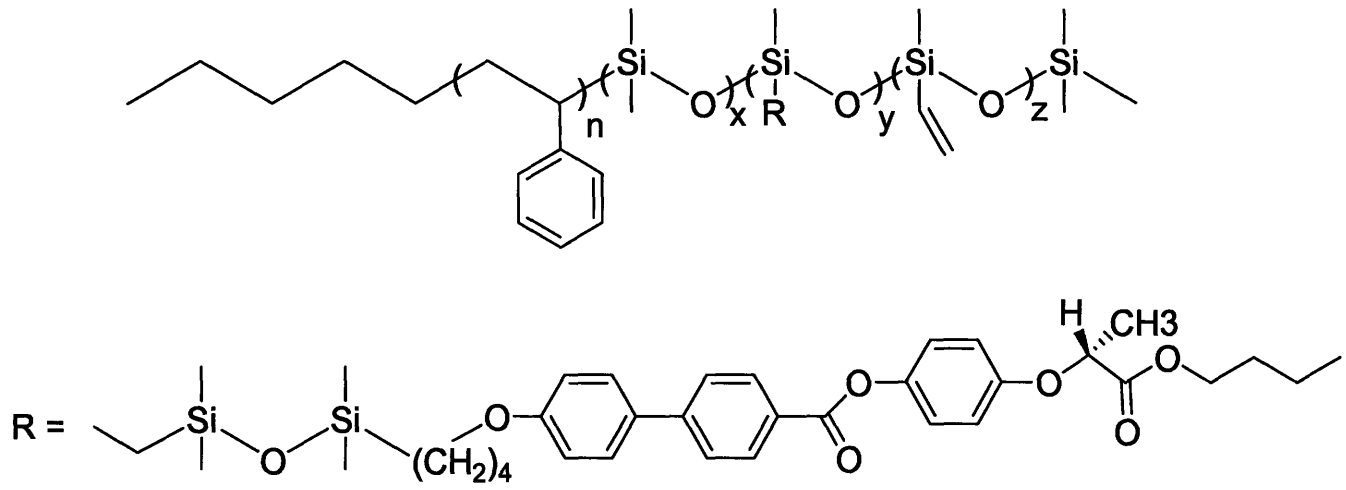

Figure 4-1. Schematic of side chain liquid crystalline block copolymer (with y and z random). The number average molecular weight (M_n) of the polystyrene (PS), liquid crystalline polymer (LCP), and overall block copolymer were determined to be 26,900, 79,400, and 106,300 g/mol, respectively, with a polydispersity index (M_w / M_n) of 1.28. The NMR based mesogen percent substitution was 55%, yielding a weight percent is 75% of the block copolymer[13].

Differential Scanning Calorimetry (DSC) was used in order to determine the thermal transitions of the SCLCBCP. Two glass transition temperature temperatures (T_g) were observed at -14°C and 100°C corresponding to the T_g for the LCP and the styrene, respectively. The smectic to isotropic transition temperature (T_{iso}) of the LC mesophase was observed at 67°C. (Figure 4-2)

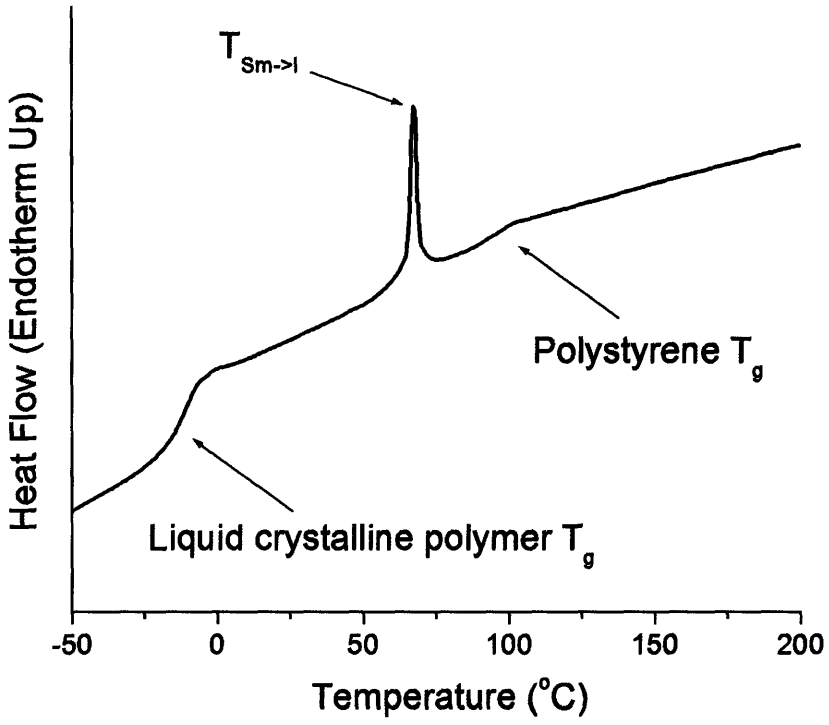

Figure 4-2. DSC heating curve for PS27-LCP_{4BPP4}79.

Polarized Optical Microscopy (POM) was used in order to observe the presence of birefringence in the liquid crystalline polymers from room temperature until the smectic C to isotropic transition temperature of the liquid crystalline phase (Figure 4-3). The focal conic textures observed indicate a smectic liquid crystalline phase is present. The disappearance of birefringence when the samples were heated indicates a transition from a smectic C liquid crystalline phase to the isotropic phase, and in all cases agreed with the DSC data.

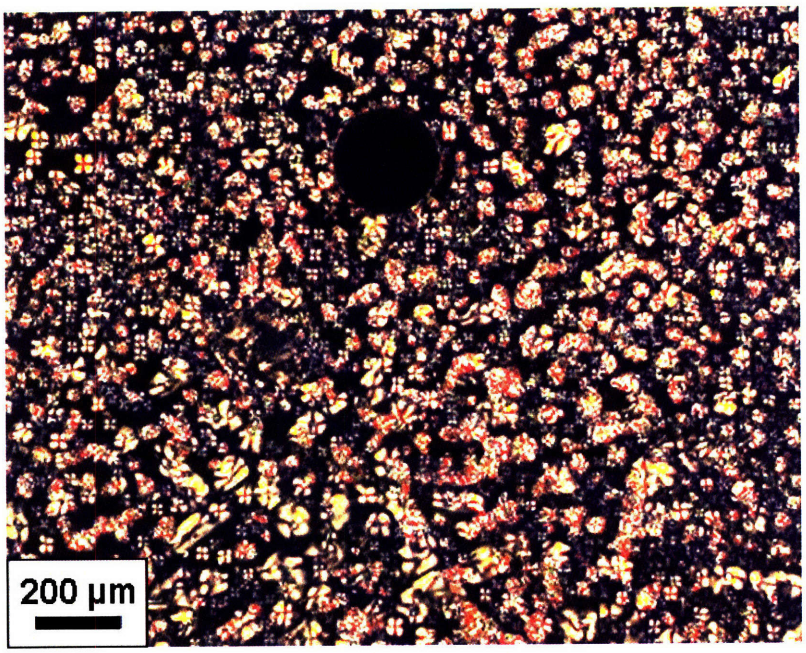

Figure 4-3. POM images displaying typical smectic textures observed below the smectic C to isotropic transition temperature for PS27-LCP_{4BPP4}79.

The presence of a disordered smectic C liquid crystalline phase was confirmed via small-angle X-ray scattering (SAXS). The d-spacings observed are indicative of the presence of smectic layers. Accelrys Materials Studio Molecular Modeling Software was used in order to calculate the molecular lengths of the 4BPP4 mesogen attached to the siloxane backbone. The calculated mesogen length was ~3.6 nm. Comparing the experimentally observed d-spacings

(3.45nm) with the calculated molecular length of the liquid crystalline molecule, it was concluded that the liquid crystals form smectic C single layers with a tilt angle of ~16.6°.

SAXS and TEM were used in order to investigate the morphology of the block copolymer mesophase (Figure 4-4). A TEM of PS27-LCP_{4BPP4}79 indicates a HCP cylinder morphology. The TEM results are corroborated with SAXS, where several higher order reflections were seen for PS27-LCP_{4BPP4}79. The observed higher order peaks correspond to scattering characteristic of a HCP cylinder morphology (Table 4-1).

Table 4-1. Scattering peaks for HCP cylinders as observed in PS27-LCP_{4BPP4}79.

Reflection	Ratio to 1st order peak	q expected (nm^{-1})	q observed (nm^{-1})
1st order	-	-	0.158
2nd order	$\sqrt{3}$	0.273	0.268
3rd order	$\sqrt{4}$	0.316	0.324
4th order	$\sqrt{7}$	0.418	0.414

Temperature dependent SAXS was performed to investigate morphological changes in the block copolymer mesophase as a function of temperature. At elevated temperatures the scattering intensity from the first order peak was observed to decrease. In order to systematically determine the order-disorder transition (ODT), plots of the reciprocal of the maximum scattering intensity ($1/I_{max}$) versus the reciprocal temperature (1/T). Additionally, the wavelength of concentration fluctuations, above T_{iso}, and the d-spacing, below T_{iso}, denoted as (d) was plotted versus reciprocal temperature, similar to the technique used by Anthamatten et al.[24-26]. I_{max} and d are both observed to decrease with increasing temperature (moving from right to left in Figure 4-5), above 80°C, and reach a plateau near 170°C. The smectic to isotropic temperature was

observed at 67°C via DSC (Figure 4-2). It is concluded that there is the order-order transition (OOT) near 80°C related to the smectic to isotropic transition. Additionally, this data along with the disappearance of higher order peaks, leads to the conclusion that the order-disorder transition (ODT) occurs near 170°C.

The interfacial thickness was determined by the method of Hashimoto[25, 26], where the $\ln[I(S)*S^2]$ is plotted versus S^2, where $S = 2\sin(\theta)/\lambda$ and I(S) is the scattering intensity as a function of S. From the slope or this graph the interface thickness (t) can be determined, $t = (|\text{slope}|/2\pi)^{0.5}$ as $I(S)*S^2$ is proportional to $\exp(-2\pi t^2 S^2)$. Using this method interface thicknesses of ~3 nm were calculated.

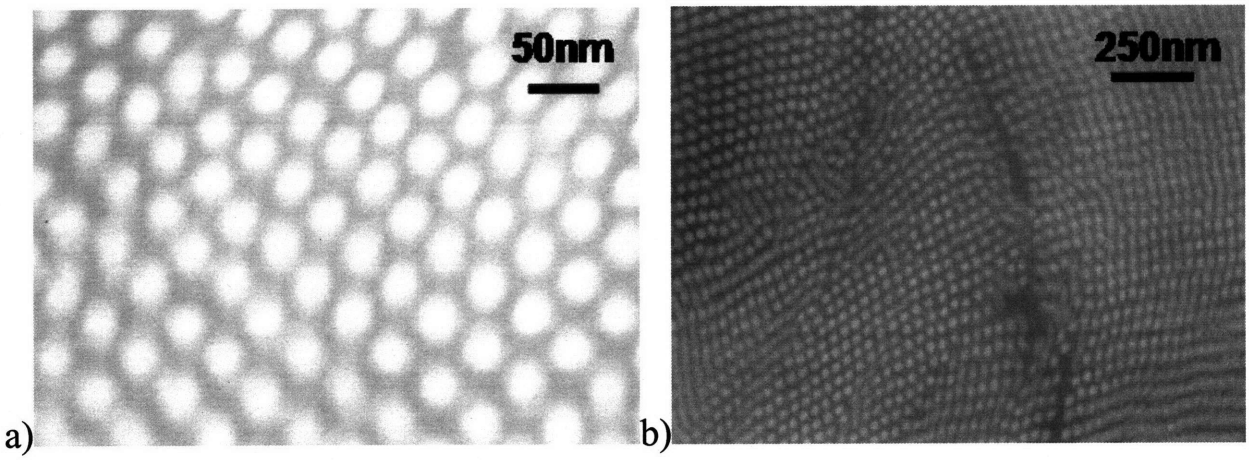

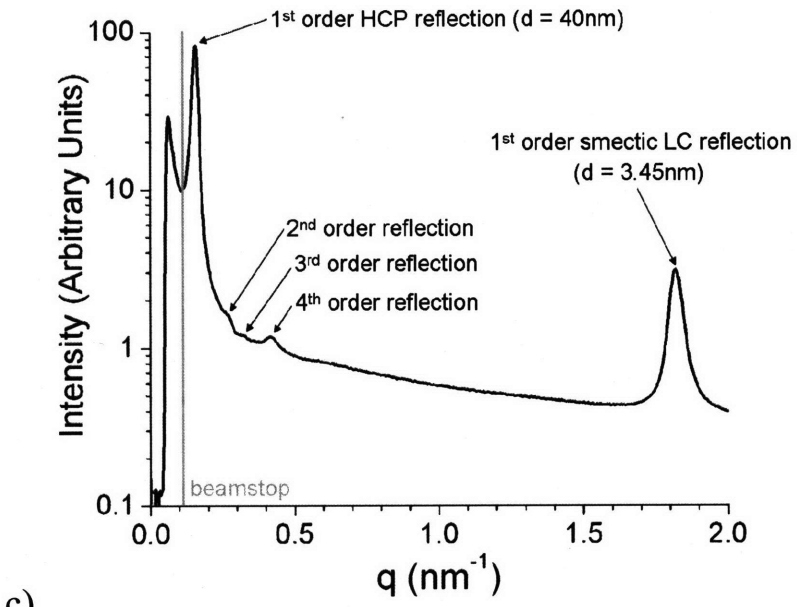

Figure 4-4. a), b) TEM images and c) SAXS of solvent-cast PS27-LCP$_{4BPP4}$79 displaying the HCP cylinder morphology.

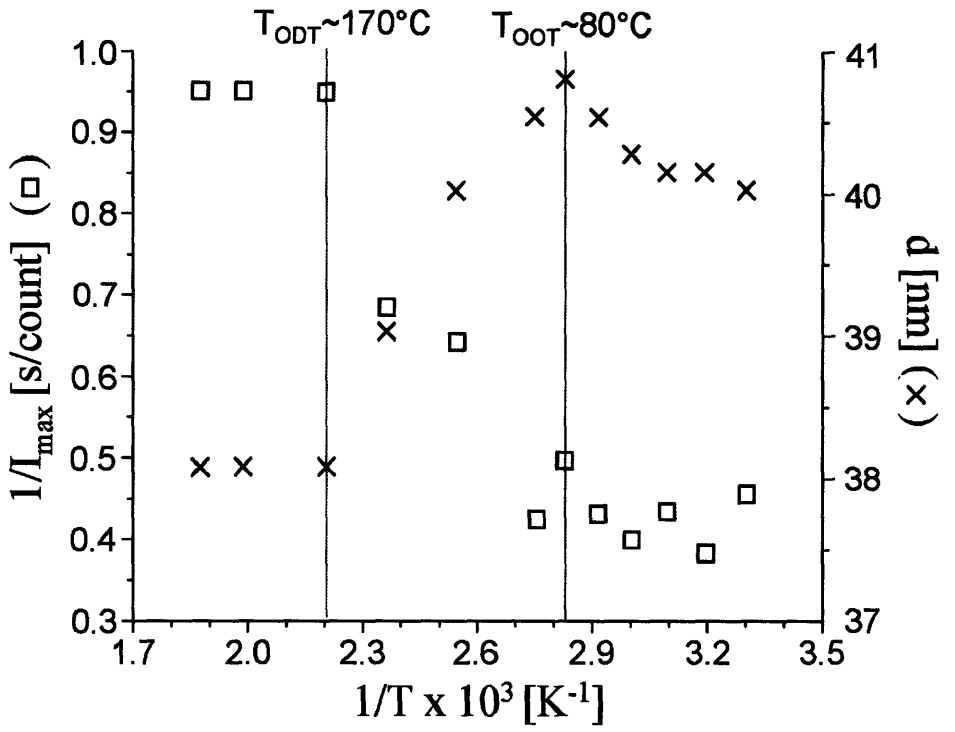

Figure 4-5. Plots of $1/I_{max}$ versus 1/T and d versus 1/T. The smectic to isotropic transition temperature (T_{OOT}) and the order-disorder transition temperature (T_{ODT}) are marked with solid lines. Where I_{max} is the maximum intensity of the scattering in the q range of interest and d is the spacing of the ordered phase below the T_{ODT} and the length scale of concentration fluctuations above the T_{ODT}.

4.2.2 Mechanical Orientation

In-situ SAXS studies were performed by applying oscillatory shear with a Linkam CSS450 shear cell at the NSLS beamline X27C at BNL. Samples were typically films ~6x4 mm with a thickness of 400 μm that were cut to fit the curvature of the channel in the shear cell and placed between thin plates consisting of kapton tape and mica, less than 100 μm, supported by an aluminum frame (not in the beam of the path). The sidewalls of the aluminum frame maintained

the sample shape during shear at high temperatures, and upon cooling the samples were removed for ex-situ analysis (Figure 4-6). Small slices ~1mm were marked and cut in order to investigate the morphology along the vorticity and shear directions. Due to the small sample size aligning the samples parallel to the beam proved difficult.

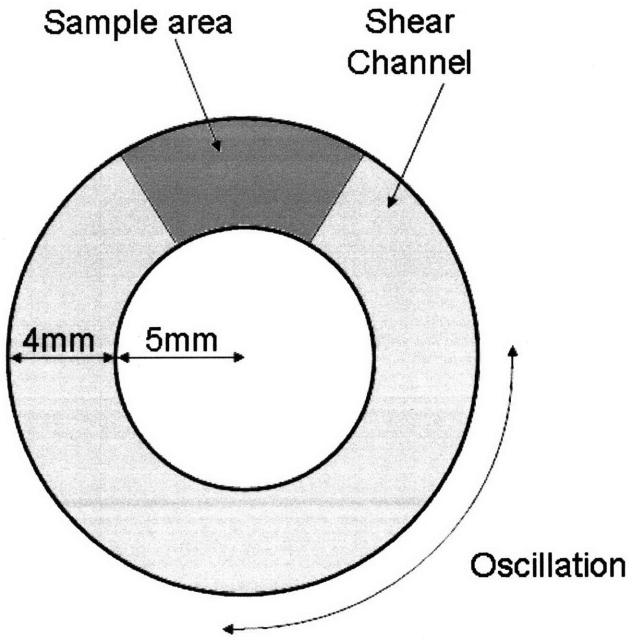

Figure 4-6. Schematic of sample geometry for in-situ shear experiments.

Initial results indicated that shearing must take place above the polystyrene T_g in order for there to be sufficient mobility in the system for orientation of the smectic LC or block copolymer mesophases to occur on the time scales studied (5 min-1 hr). Samples of PS27-LCP_{4BPP4}79 were subjected to 100% shear at a frequency of 1 Hz at 120°C, which is above the smectic to isotropic transition and the order-order transition for this sample. The development of preferential orientation of the HCP cylinders was initially observed within several minutes (in the absence of

scattering from smectic layers), and after approximately 20 minutes no further significant increase in the alignment of the domains was observed.

Upon slow cooling (5°C/min) after the cessation of shear, smectic layers were observed to form preferentially oriented in a manner that is consistent with the homogeneous anchoring relative to the orientation of the HCP cylinder morphology. Both the cylinder axis and the smectic layer normal were preferentially oriented transverse to the shear direction, i.e. parallel to the vorticity direction (Figure 4-7). It was also observed that samples that had been previously deformed could be heated above the smectic LC clearing temperature and the PS T_g, to 120°C and with a cooling rate of 5°C/min the smectic layer preferential orientation was regained. However, when the cooling rate is increased to 20°C/min significantly less preferred orientation was observed in the smectic layers. This result indicates that kinetics play an important role in the formation of the smectic LC mesophase.

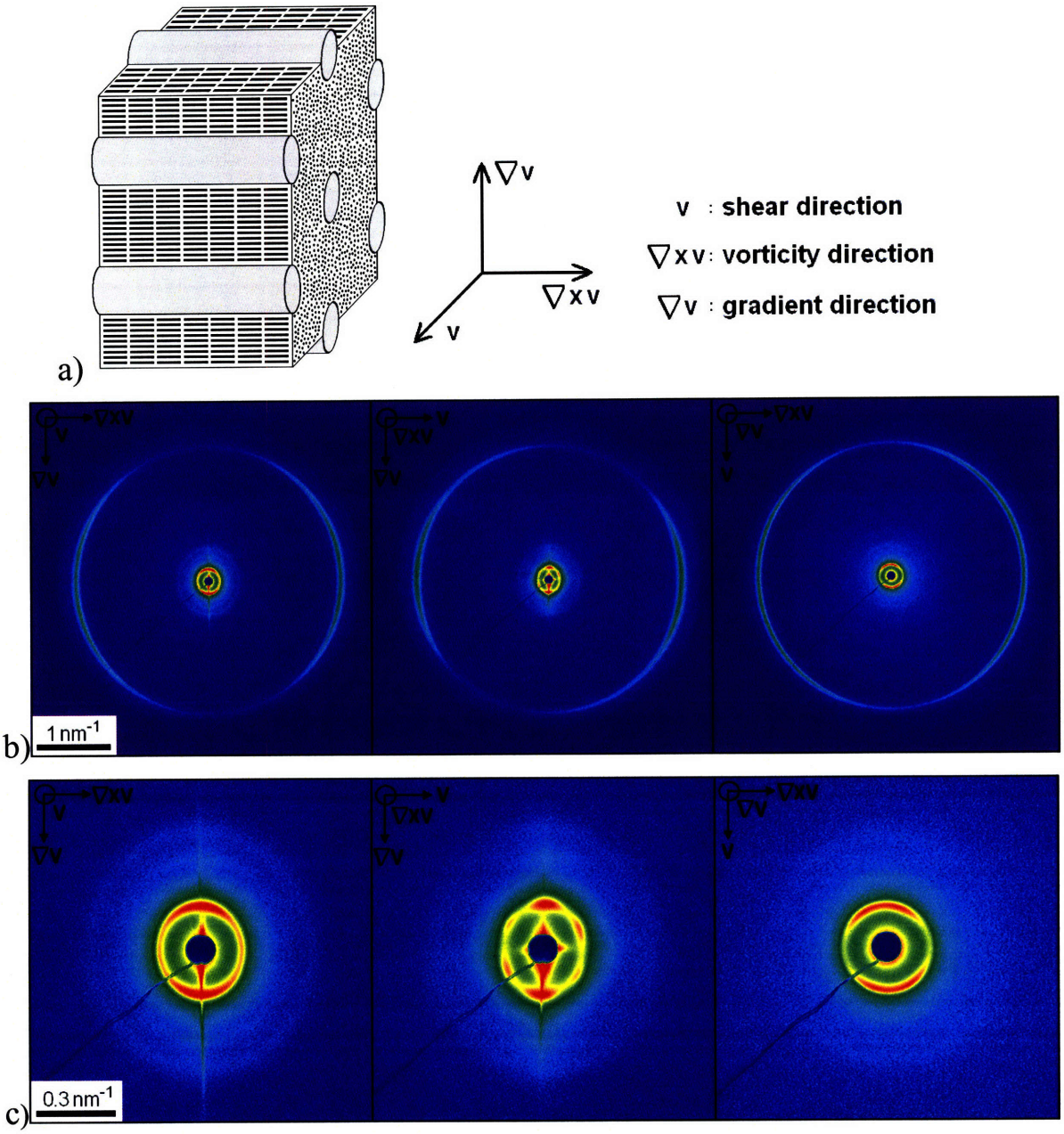

Figure 4-7. a) Cartoon depicting observed predominant structure relative to the direction of shear. b) 2-D SAXS images of sample after shear of 100% at a frequency of 1 Hz took place at 120°C for 1 hour. Moving from left to right, the images were taken with the incident beam parallel to the shear, vorticity and gradient directions, respectively. c) Enlarged views of the 2-D SAXS images, displaying the low angle scattering for each direction, confirming the transverse cylinder orientation.

It is important to note that the cylinders align in the transverse orientation at temperatures where the liquid crystalline mesophase is in the isotropic phase. The lack of smectic ordering is confirmed by the absence of scattering over the relevant q range throughout the in-situ shear experiment. The cylinders would be expected to align in the parallel orientation for an amorphous-amorphous block copolymer[27-29]; however, since the cylinders are observed in the transverse orientation it is clear that even in the isotropic phase, the LC mesophase has an effect upon the physics of the block copolymer orientation (contrary to previous results from other work[4]).

This observation leads to the conclusion that there is residual order in the isotropic LC mesophase, and this anisotropy is the driving force for the transverse orientation of the cylinders. It is generally known that liquid crystals at a surface or interface can retain orientation even when transverse fields or temperatures above the clearing point are introduced. The periodicity of the PS cylinders is only ~40nm, resulting in a situation where surface induced ordering could persist through the entire LC mesophase. Ordering of the LC moieties parallel to the IMDS (i.e. homogeneous anchoring) is consistent with the orientation of the smectic layers observed upon cooling. Additionally, the large size and aspect ratio of the LC moieties in this system could lead to stronger homeotropic anchoring than in other systems, thus having a grater influence upon the orientation of the block copolymer morphology.

The SAXS pattern taken with the beam incident parallel to the vorticity direction clearly shows a hexagonal scattering pattern, indicating that the entire sample is well aligned (the sample and the beam are both ~400μm). This image was taken slightly off axis, leading to the apparent increase in intensity along the gradient direction at low q, and the higher q smectic LC scattering seen along the shear direction. The Herman's orientation parameter (f)[30] was used to quantify the

degree of orientation for the BCP and LC mesophases. This parameter ranges from 1 to -½, with $f = 0$ for a completely random distribution of orientations. When f is 1 or -½ the system is completely aligned parallel or perpendicular, respectively, to the chosen reference direction, which in this case was chosen to be the vorticity direction. The scattering intensity at the relevant scattering vector q was analyzed as a function of angle with respect to the reference direction. An additional method for calculating the orientation parameter, which is more relevant for systems that do not display uniaxial orientation[31] was calculated. This function has a range of 1 to -1 for perfect alignment parallel and perpendicular to the reference direction, respectively. The orientation parameters were calculated, and shown in Table 4-2, for each of the incident bean directions for both the low q (BCP cylinders) and high q scattering (smectic layers). The orientation parameters were not calculated for the low q scattering along the vorticity direction, as in this case a hexagonal pattern was observed, rendering these orientation parameters irrelevant.

Other work has yielded orientation parameters of 0.53 for smectic side chain LC polymers under a steady shear[32] and 0.67 for small molecule LCs oriented using a rubbed polyimide alignment layer[33]. Model block copolymer systems such as PS-PEO have been show to exhibit orientation parameters up to 0.95 under compressive stress and thermal annealing[34]. The lower orientation parameter observed in this system compared to those for model block copolymer systems can be attributed to the larger polydispersity, the PDI in the model systems is typically less than 1.1 and in this system the PDI is 1.28. Additionally, it is likely that the driving force for ordering and orientation in this system is not as strong as that of model systems. Similar materials to those discussed in the main text (a similar mesogen with a higher T_{iso}, ~160°C) were also studied under the same shear conditions (100% strain, 1 Hz, 120°C). The

orientation of the smectic layers for these materials was observed to be stronger, with an orientation parameter of 0.65 for the smectic layers[35]. This is to be expected, as in the case where the shearing takes place in the smectic LC phase, the smectic layers are directly aligned by the oscillatory shear flow. Dissimilarly, for the material described in this paper, the shear takes place above the T_{iso}, and the orientation of the smectic layers is more indirectly resultant from a combination of ordering relative to the IMDS and residual preferential ordering from the isotropic LC phase.

It is important to note that the images taken along the vorticity direction were taken off axis. What is observed is a superposition of the scattering that would be observed for an image taken along the shear direction, with the scattering observed from the image along the vorticity direction. This results in the presence of scattering in the high q regime (which would be isotropic for a sample that was aligned with the vorticity direction exactly parallel to the incident bean. Additionally, there would not be any scattering observed only if the sample had a smectic LC mesophase that was perfectly uniaxially oriented (orientation parameter of 1) *and* aligned exactly parallel to the incident beam.

Table 4-2. Orientation parameter using different functions and different angles.

Sample orientation and relevant q range	Herman's Orientation parameter	Anisotropy factor for biaxial orientation
Shear direction, low q	0.37	0.37
Shear direction, high q	0.51	0.49
Vorticity direction, low q	Not applicable	Not applicable
Vorticity direction, high q	0.43	0.33
Gradient direction, low q	0.28	0.19
Gradient direction, high q	0.31	0.25

Additionally, anisotropy was observed in the d-spacings of the cylinders relative to the direction of the applied shear. This result indicates the HCP lattice has been distorted, such that the cylinder spacings are larger along the shear direction than along the gradient direction (Table 4-3). The hexagonal cylinder lattice appears to be distorted as a result of the oscillatory shear that was used to align the samples. The d-spacing of the block copolymer mesophase was 40 nm at room temperature before the material was subjected to oscillatory shear (Figure 4-4). An increase in the d-spacing was observed along the shear direction, and a corresponding decrease was observed along the gradient direction.

Table 4-3. Block copolymer d-spacing at room temperature after shear.

Direction of incident beam	d-spacing (nm)
Shear direction	38.0 (along gradient direction)
Vorticity direction	37.8 (along gradient direction)
Vorticity direction	42.1 (along shear direction)
Gradient direction	41.6 (along shear direction)

Melt fiber drawing and tensile elongation can also be used to orient liquid crystalline polymers[36] and liquid crystalline block copolymers[10]. Fiber drawing of the side chain liquid crystalline polymers was performed by heating the samples to 150°C on a hot plate and pulling ~ 500μm fibers from the melt with tweezers. SAXS indicates that for all of the materials investigated the cylinder axis and the smectic layer normal are preferentially oriented parallel to the fiber axis (Figure 4-8). This orientation indicates that the smectic layers are oriented relative to the IMDS consistent with the homogeneous anchoring.

Polarized optical microscopy was also used to characterize the orientation of the LC mesophase in these mechanically deformed films (Figure 4-9). The samples were places between orthogonal polarizers. If the sample does not display and birefringence then light will pass through the polarizers. However, if the material possesses birefringence light will pass through as it is reoriented in between the two polarizers, as shown in Figure 4-3 where the material is macroscopically isotropic and displays a local focal conic texture. When the fiber is placed between the orthogonal polarizers the orientation of the fiber relative to the cross polars effects the observed birefringence. When the sample is oriented parallel to one of the polarizers very little birefringence is observed, however when rotated to some angle so that the fiber is not parallel to either of the polarizers birefringence is observed. This observation indicated that the LC mesophase is macroscopically oriented so that polarization of light due to the sample is parallel to the fiber axis. Similar results were observed for samples that were oriented through tensile elongation, as characterized with SAXS and POM. These samples were subjected to a constant stress of 0.1 MPa at 140°C until a strain of 150% was reached.

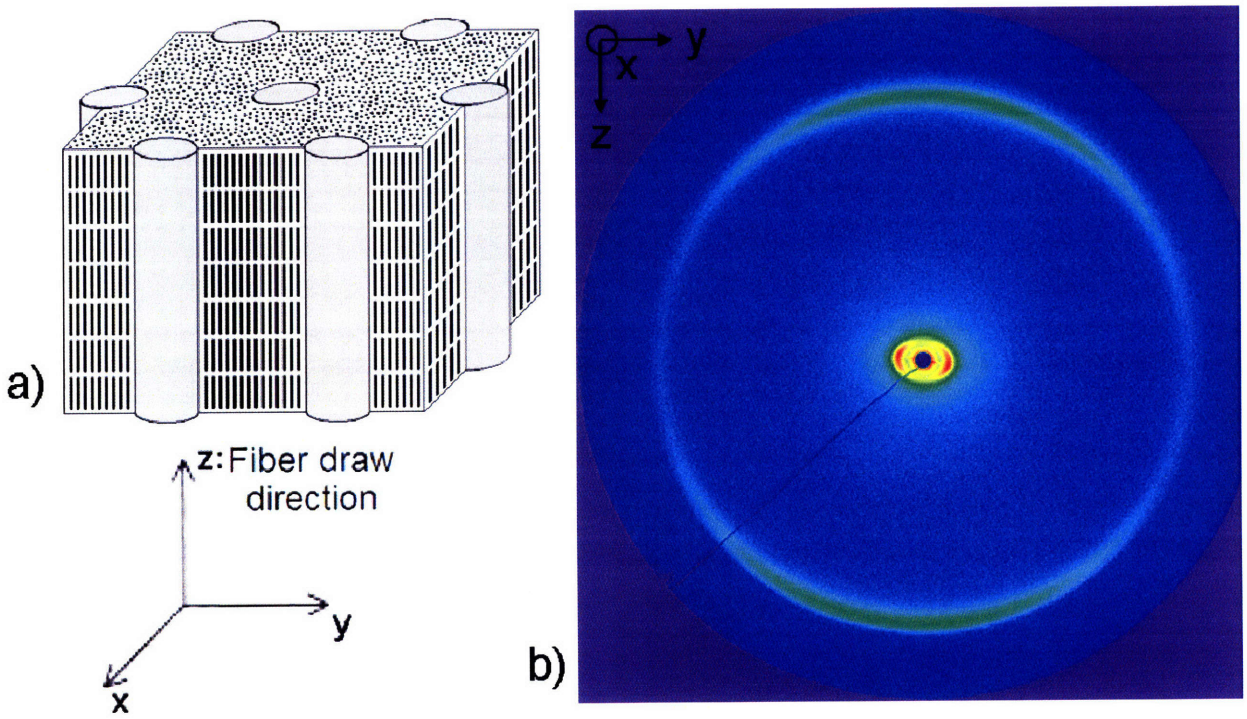

Figure 4-8. a) Cartoon showing observed structure relative to the melt fiber drawn direction, b) SAXS of PS27-LCP$_{4BPP4}$90 that has been melt fiber drawn.

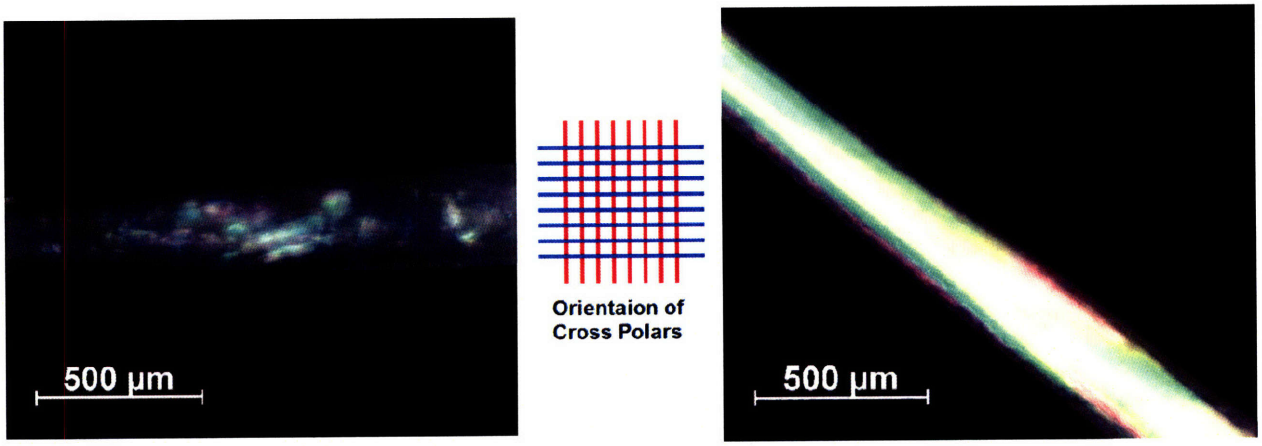

Figure 4-9. POM images of a fiber of PS27-LCP$_{4BPP4}$79 that has been melt drawn, taken under cross polars. The image on the left is with the direction of deformation parallel to the cross polars, the image on the right is the same sample rotated and birefringence is observed.

4.3 Conclusion

A well defined smectic C side chain liquid crystalline block copolymer has been synthesized and characterized. For the side chain liquid crystalline block copolymers studied a cylindrical morphology was observed via TEM and SAXS. When mechanically deformed, the preferential orientation of the smectic LC and the block copolymer mesophases was observed, and homogeneous anchoring between the smectic LC mesophase and the IMDS of the cylindrical block copolymer mesophase was observed.

The transverse HCP cylinders orientation was observed for liquid crystalline block copolymers that experienced oscillatory shear. The transverse orientation was observed while shearing took place above the smectic to isotropic transition temperature. The significance of this result is that it indicates that the presence of the isotropic liquid crystalline phase alters the orientation of the block copolymer morphology in response to shear, which has not been previously reported. PS27-LCP_{4BPP4}79 was deformed using oscillatory shear, resulting in a nearly uniform oriented HCP cylindrical morphology across the thickness of the sample, as observed via SAXS. Achieving macroscopic orientation of the block copolymer and LC morphologies is critical for a material that can be used for electromechanical applications.

Future work in this area includes study and optimization of the effects of the morphology and orientation of the block copolymer and the liquid crystalline polymer mesophases on thermo- and electromechanical response in these liquid crystalline thermoplastic elastomers.

4.4 References

1. Guarini, K. W.; Black, C. T.; Yeuing, S. H. I., Optimization of diblock copolymer thin film self assembly. *Advanced Materials* **2002,** 14, (18), 1290-+.

2. Stein, P.; Assfalg, N.; Finkelmann, H.; Martinoty, P., Shear modulus of polydomain, mono-domain and non-mesomorphic side-chain elastomers: Influence of the nematic order. *European Physical Journal E* **2001,** 4, (3), 255-262.

3. Zheng, W. Y.; Albalak, R. J.; Hammond, P. T., Mesogen orientation within smectic C* side chain liquid crystalline diblock copolymers. *Macromolecules* **1998,** 31, (8), 2686-2689.

4. Osuji, C.; Zhang, Y. M.; Mao, G. P.; Ober, C. K.; Thomas, E. L., Transverse cylindrical microdomain orientation in an LC diblock copolymer under oscillatory shear. *Macromolecules* **1999,** 32, (22), 7703-7706.

5. Fischer, H.; Poser, S.; Arnold, M.; Frank, W., On the Influence of the Morphological Structure on the Liquid-Crystalline Behavior of Liquid-Crystalline Side-Chain Block-Copolymers. *Macromolecules* **1994,** 27, (24), 7133-7138.

6. Poser, S.; Fischer, H.; Arnold, M., Liquid crystalline side-group block copolymers with triblock structure: Investigations on the influence of the block arrangement on the morphology and the LC-phase behavior. *Journal of Polymer Science Part a-Polymer Chemistry* **1996,** 34, (9), 1733-1740.

7. Hamley, I. W.; Davidson, P.; Gleeson, A. J., Shear-induced layer alignment in the smectic phase of a side chain liquid crystal polymer. *Polymer* **1999,** 40, (12), 3599-3603.

8. Hamley, I. W.; Castelletto, V.; Lu, Z. B.; Imrie, C. T.; Itoh, T.; Al-Hussein, M., Interplay between smectic ordering and microphase separation in a series of side-group liquid-crystal block copolymers. *Macromolecules* **2004,** 37, (13), 4798-4807.

9. Galli, G.; Chiellini, E.; Francescangeli, O.; Ferri, D.; Wolff, D.; Springer, J.; Laus, M.; Angeloni, A. S., Mesophase structure and alignment under different fields of liquid crystalline main-chain/side-group block copolymers. *Macromolecular Symposia* **1997,** 121, 235-244.

10. Ferri, D.; Wolff, D.; Springer, J.; Francescangeli, O.; Laus, M.; Angeloni, A. S.; Galli, G.; Chiellini, E., Phase and orientational behaviors in liquid crystalline main-chain/side-group block copolymers. *Journal of Polymer Science Part B-Polymer Physics* **1998,** 36, (1), 21-29.

11. Osuji, C.; Ferreira, P. J.; Mao, G. P.; Ober, C. K.; Vander Sande, J. B.; Thomas, E. L., Alignment of self-assembled hierarchical microstructure in liquid crystalline diblock copolymers using high magnetic fields. *Macromolecules* **2004,** 37, (26), 9903-9908.

12. Mayer, S.; Zentel, R., Liquid crystalline polymers and elastomers. *Current Opinion in Solid State & Materials Science* **2002,** 6, (6), 545-551.

13. Moment, A.; Miranda, R.; Hammond, P. T., Synthesis of polystyrene-polysiloxane side-chain liquid crystalline block copolymers. *Macromolecular Rapid Communications* **1998,** 19, (11), 573-579.

14. Verploegen, E.; McAfee, L. C.; Tian, L.; Verploegen, D.; Hammond, P. T., Observation of transverse cylinder morphology in side chain liquid crystalline block copolymers. *Macromolecules* **2007,** 40, (4), 777-780.

15. Figueiredo, P.; Geppert, S.; Brandsch, R.; Bar, G.; Thomann, R.; Spontak, R. J.; Gronski, W.; Samlenski, R.; Muller-Buschbaum, P., Ordering of cylindrical microdomains in thin films of hybrid isotropic/liquid crystalline triblock copolymers. *Macromolecules* **2001,** 34, (2), 171-180.

16. Yamada, M.; Itoh, T.; Hirao, A.; Nakahama, S.; Watanabe, J., Side-chain LC block copolymers with well defined structures prepared by living anionic polymerization. 2: Effect of the glass transition temperature of amorphous segments on the phase behaviour and structure of the LC segment. *High Performance Polymers* **1998,** 10, (1), 131-138.

17. Sentenac, D.; Demirel, A. L.; Lub, J.; de Jeu, W. H., A new lamellar morphology of a hybrid amorphous liquid crystalline block copolymer film. *Macromolecules* **1999,** 32, (10), 3235-3240.

18. Omenat, A.; Lub, J.; Fischer, H., Liquid-crystalline diblock copolymers produced by living cationic and anionic polymerizations. *Chemistry of Materials* **1998,** 10, (2), 518-523.

19. Merenga, A.; Shilov, S. V.; Kremer, F.; Mao, G.; Ober, C. K.; Brehmer, M., Molecular orientation and dynamics in ferroelectric diblock copolymers monitored by FT-IR spectroscopy. *Macromolecules* **1998,** 31, (25), 9008-9012.

20. Moment, A.; Hammond, P. T., Block copolymers of polystyrene and side-chain liquid crystalline siloxanes: morphology and thermal properties. *Polymer* **2001,** 42, (16), 6945-6959.

21. Zheng, W. Y.; Hammond, P. T., Phase behavior of new side chain smectic C* liquid crystalline block copolymers. *Macromolecules* **1998,** 31, (3), 711-721.

22. Anthamatten, M.; Zheng, W. Y.; Hammond, P. T., A morphological study of well-defined smectic side-chain LC block copolymers. *Macromolecules* **1999,** 32, (15), 4838-4848.

23. Zhou, W. J.; Kornfield, J. A.; Ugaz, V. M.; Burghardt, W. R.; Link, D. R.; Clark, N. A., Dynamics and shear orientation behavior of a main-chain thermotropic liquid crystalline polymer. *Macromolecules* **1999,** 32, (17), 5581-5593.

24. Auad, M. L.; Kempe, M. D.; Kornfield, J. A.; Rendon, S.; Burghardt, W. R.; Yoon, K., Effect of mesophase order on the dynamics of side group liquid crystalline polymers. *Macromolecules* **2005,** 38, (16), 6946-6953.

25. Hashimoto, T.; Shibayama, M.; Kawai, H., Domain-Boundary Structure of Styrene-Isoprene Block Co-Polymer Films Cast from Solution.4. Molecular-Weight Dependence of Lamellar Microdomains. *Macromolecules* **1980,** 13, (5), 1237-1247.

26. Mao, G. P.; Wang, J. G.; Clingman, S. R.; Ober, C. K.; Chen, J. T.; Thomas, E. L., Molecular design, synthesis, and characterization of liquid crystal coil diblock copolymers with azobenzene side groups. *Macromolecules* **1997,** 30, (9), 2556-2567.

27. Honeker, C. C.; Thomas, E. L., Impact of morphological orientation in determining mechanical properties in triblock copolymer systems. *Chemistry of Materials* **1996,** 8, (8), 1702-1714.

28. Chen, Z. R.; Kornfield, J. A.; Smith, S. D.; Grothaus, J. T.; Satkowski, M. M., Pathways to macroscale order in nanostructured block copolymers. *Science* **1997,** 277, (5330), 1248-1253.

29. Tepe, T.; Schulz, M. F.; Zhao, J.; Tirrell, M.; Bates, F. S.; Mortensen, K.; Almdal, K., Variable Shear-Induced Orientation of a Diblock Copolymer Hexagonal Phase. *Macromolecules* **1995,** 28, (8), 3008-3011.

30. Roe, R. J., *Methods of X-ray and Neutron Scattering in Polymer Science.* Oxford University Press: New York, 2000.

31. Cinader, D. K.; Burghardt, W. R., X-ray scattering studies of orientation in channel flows of a thermotropic liquid-crystalline polymer. *Journal of Polymer Science Part B-Polymer Physics* **1999,** 37, (24), 3411-3428.

32. Wiberg, G.; Skytt, M. L.; Gedde, U. W., Shear-induced alignment and relaxation of orientation in smectic side-chain liquid-crystalline polymers. *Polymer* **1998,** 39, (13), 2983-2986.

33. Vanaerle, N. A. J. M.; Tol, A. J. W., Molecular-Orientation in Rubbed Polyimide Alignment Layers Used for Liquid-Crystal Displays. *Macromolecules* **1994,** 27, (22), 6520-6526.

34. Li, Y. J.; Kaito, A., Highly oriented structure formed in a lamella-forming diblock copolymer with high molar mass. *European Polymer Journal* **2006,** 42, (9), 1986-1993.

35. Verploegen, E.; McAfee, L. C.; Tian, L.; Verploegen, D.; Hammond, P. T., Side chain liquid crystalline block copolymers: For use as actuators. *Abstracts of Papers of the American Chemical Society* **2005,** 230, U3673-U3673.

36. Naciri, J.; Srinivasan, A.; Jeon, H.; Nikolov, N.; Keller, P.; Ratna, B. R., Nematic elastomer fiber actuator. *Macromolecules* **2003,** 36, (22), 8499-8505.

Chapter 5 Morphology of Side Chain Liquid Crystalline Block Copolymer Thin Films: Effects of Thermal Annealing

5.1 Introduction

Block copolymer thin films have attracted much recent interest for potential use in nano-patterning applications[1, 2]. It is desired to achieve systems that exhibit long range order as well as gain control over the orientation of the domains. Recently progress has been made in achieving long range order in block copolymer thin films through techniques such as solvent annealing[3, 4], zone casting[5], and optical alignment[6]. Due to the large interfacial area of the thin film, the orientation of the domains depends greatly upon the relative surface energies of the blocks[7-10]. The incorporation of a liquid crystalline (LC) component into a block copolymer system can have significant effects upon the self assembly behavior and domain orientation for both bulk materials[11-18] and thin films[9, 19, 20]. Additionally, liquid crystalline polymers (LCP) are of particular interest as they can allow for the introduction of responsive elements into the system, e.g. thermo-, chemo-, electro-, or photo-responsive[21].

In this work we study the morphology of side chain liquid crystalline block copolymer thin films, the effects of thermal annealing, and the effects of the liquid crystalline mesophase upon the self assembly. We probe the surface morphologies of these films with atomic force microscopy (AFM). Grazing incidence small-angle X-ray scattering (GISAXS) is a powerful non-invasive technique that we used to investigate the both the lateral and transverse structures

in the interior of these thin films[7, 22, 23]. For more details on GISAXS see Appendix E.

5.2 Experimental

The synthesis of the polymer, LC moiety, and attachment were previously developed and described[17, 24]. Spin casting was performed by preparing 3, 5, and 7 wt% homogeneous solutions of the side chain liquid crystalline block copolymer in toluene, and applying a single drop to the silicon substrate rotating at 2500 rpm. The film thicknesses were between 70nm and 250nm, measured via profilometry, with the more dilute solutions resulting in thinner films. Some of the films were then annealed at 170°C under vacuum for 36 hours and cooled to room temperature a 0.5°C/min. A Dimension 3100 AFM by DI Instruments with a Nanoscope 3A Controller in tapping mode was used to investigate the surface morphologies. NCH Pointprobe non-contact mode AFM Cantilevers were purchased from Pacific Nanotechnologies. GISAXS experiments were performed at the G1 beamline at the Cornell High Energy Synchrotron Source (CHESS). The wavelength of the incident beam was 1.239Å, with a sample to detector distance was calibrated with silver behenate (first order scattering vector of q of 1.076nm-1 (with $q = 4\pi \sin(\theta/\lambda)$ where 2θ is the scattering angle and λ is the wavelength). A slow-scan CCD-based x-ray detector, home built by Drs. M.W. Tate and S.M. Gruner of the Cornell University Physics Department, was used for data collection. Incidence angles were chosen between 0.12° and 0.22°, and the final images are an average of ten 1 second exposures.

5.3 Results

The poly(styrene)-poly(vinylmethylsiloxane) (PS-PVMS) functional diblock copolymer was synthesized via anionic polymerization, LCs were synthesized and attached to the block copolymer backbone with a hydrosilylation reaction. The number-average molecular weights (*M*n) of the polystyrene (PS), liquid crystalline polymer (LCP), and overall block copolymer were determined to be 26 900, 79 400, and 106 300 g/mol, respectively, with a polydispersity index (*M*w/*M*n) of 1.28. The NMR-based mesogen percent substitution was 55%, yielding a LCP that is 75% of the overall block copolymer by weight[17, 24].

The relevant thermal transitions of this material in bulk were determined via a combination of differential scanning calorimetry (DSC), and small-angle X-ray scattering (SAXS). Two glass transition temperatures (T_g) were observed at -14°C and 100°C corresponding to the T_g for the LCP and the styrene, respectively. The smectic to isotropic transition temperature (T_{iso}) of the LC mesophase was observed at 67°C and the order-disorder transition (ODT) occurs near 170°C[17].

Figure 5-1 shows AFM phase images of the as-spun and annealed films. In these images the more rigid PS domains appear lighter and the LCP domains appear darker. The as-spun film displays disordered PS cylinders oriented perpendicular to the air interface, as evidenced by the circular bright regions. The annealed films display cylinders parallel to the interface, as evidenced by the observation of bright lines. This image shows less contrast, most likely due to the presence of a layer of LCP on the surface that exists in order to minimize the interfacial energy. A two-dimensional (2D) fast Fourier transform (FFT) of the AFM images measured average *feature spacings* of 47nm and 48nm for the as-spun and annealed films, respectively.

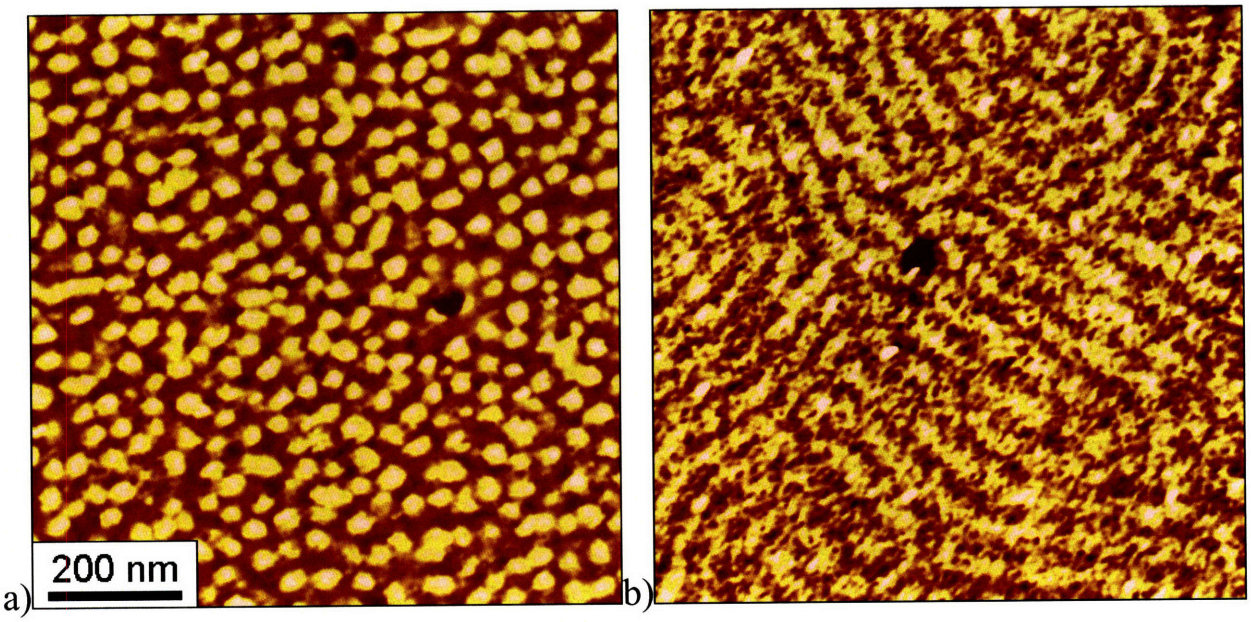

Figure 5-1. AFM phase images of a 250nm SCLCBCP thin film a) as-spun, and b) after annealing at 170°C for 36 hours under vacuum.

2-D GISAXS images of the as-spun and annealed films are shown in Figure 5-2. The as-spun film displays scattering that is indicative of features in the plane of the substrate with a 41.5nm *d-spacing*. The annealed film displays a scattering pattern characteristic of hexagonal cylinders parallel to the substrate with a *d-spacing* of 42nm[8, 25]. It should be noted that the FFT of the AFM image yields a measurement of the center to center distance of the *features* (denoted as L), which in this case are the PS cylinders. In contrast, GISAXS measures the *d-spacing* (denoted as d) between the planes of cylinders. Considering the geometry of cylinders on a hexagonal lattice the d-spacing differs from the feature spacing by a factor of $2/\sqrt{3}$ (Figure 5-3). This accounts for the difference in values obtained between the two techniques. Thus, the d-spacings and orientations observed via GISAXS are consistent with AFM, and additionally confirm that the orientation persists through the thickness of the film.

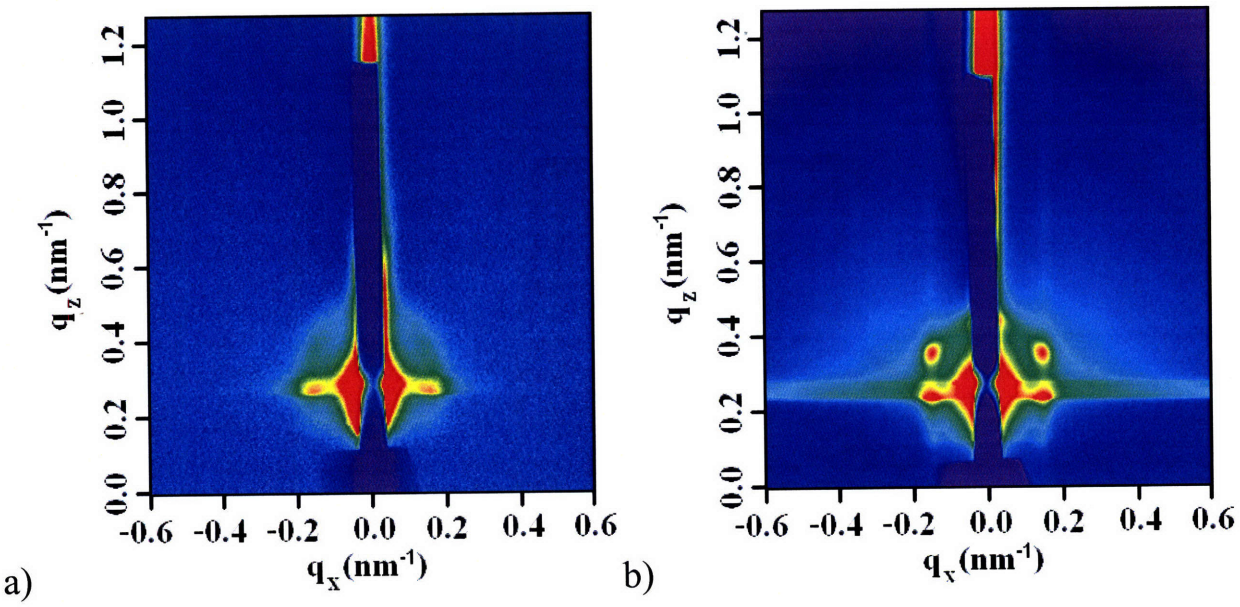

Figure 5-2. 2-D GISAXS images of a 250nm SCLCBCP thin film a) as-spun, and b) after annealing at 170°C for 36 hours under vacuum. Both images were taken with an incidence of α_i = 0.17°, which is larger than the critical angle of the SCLCBCP (α_c = 0.14°) and less than the critical angle of the Si substrate (α_c = 0.2°), allowing the bulk of the film to be investigated.

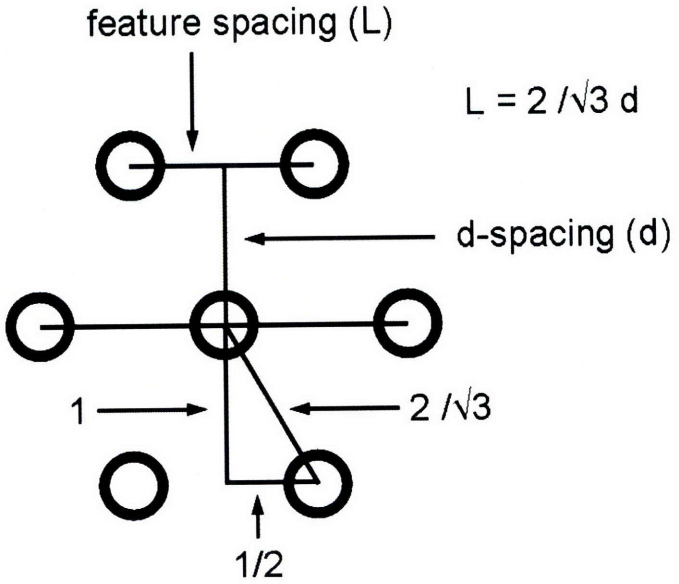

Figure 5-3. Schematic of the geometry of hexagonal close packed cylinders viewed head on.

Additional GISAXS was performed with a sample to detector distance of 444mm in order to capture the scattering from the LC mesophase. The smectic layers were observed parallel and perpendicular to the substrate for the as-spun and annealed films, respectively, as evidenced by GISAXS (Figure 5-4 a,b). These orientations indicate homogeneous anchoring with respect to the curved IMDS with the polystyrene cylinders. Additionally, as-spun liquid crystalline homopolymer displayed smectic layers strongly oriented parallel to the substrate (Figure 5-4 c). The smectic layer spacings observed were 3.6nm and 3.48nm for the SCLCBCP and the LC homopolymer, respectively.

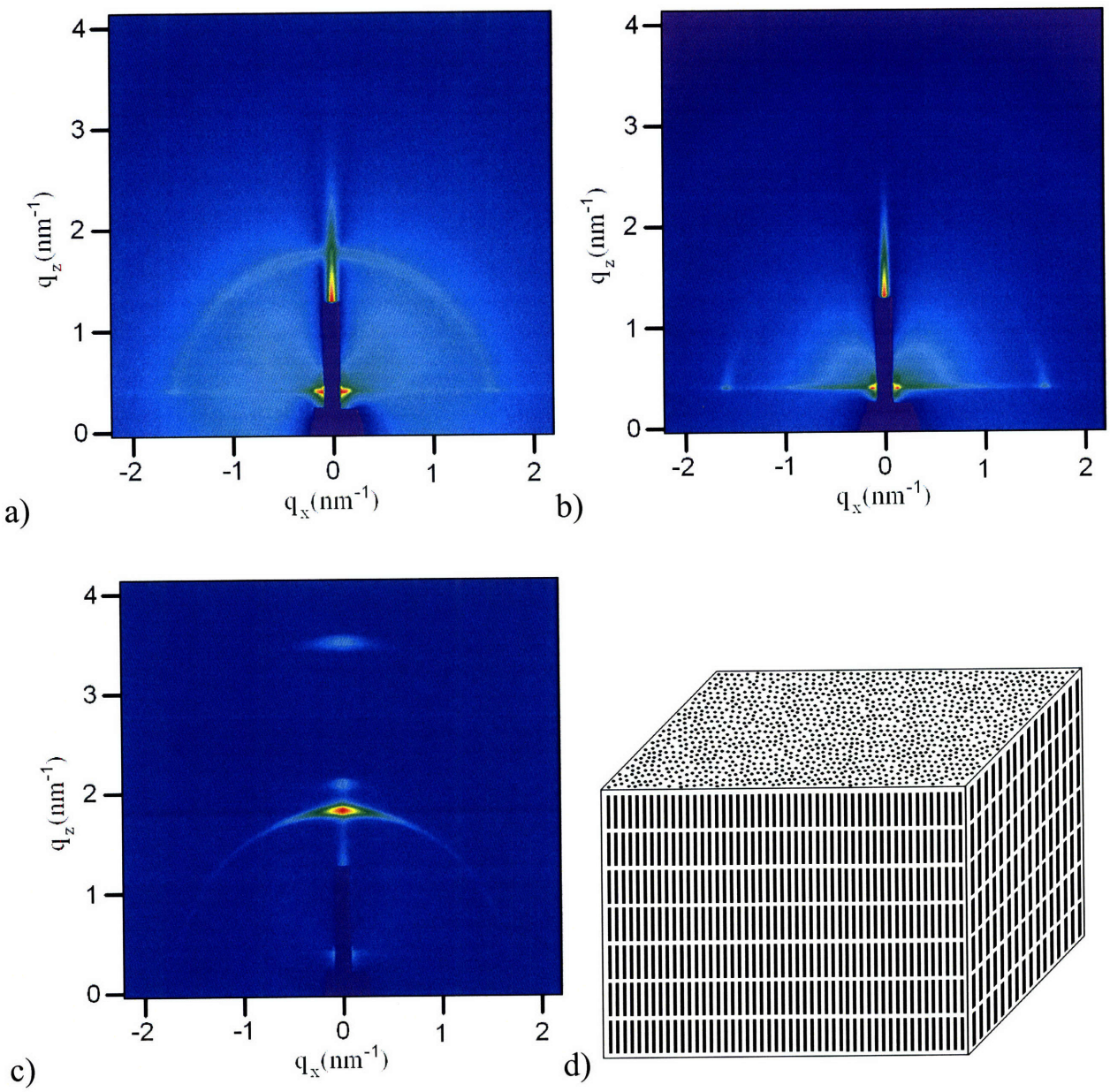

Figure 5-4. GISAXS images of 250nm SCLCBCP thin film a) as-spun, and b) after annealing at 170°C for 36 hours under vacuum. c) GISAXS image of the liquid crystalline homopolymer as-spun. All images were taken with an incidence of $\alpha_i = 0.17°$. d) Schematic of a liquid crystalline homopolymer with the smectic layers oriented parallel to the substrate.

5.4 Discussion

The perpendicular cylinder and parallel cylinder morphologies were observed for all unannealed and annealed samples, respectively, see Figure 5-5. These results were observed for films ranging from 70nm to 250nm in thickness; the 250nm films are shown as they displayed the greatest scattering contrast. The smectic layers were observed parallel to the substrate for the as-spun films and perpendicular to the substrate for the annealed films, as evidenced by GISAXS. Additionally, a homopolymer of PVMS was synthesized, the same liquid crystalline moiety was attached, and spin cast under the same conditions. The smectic layers were strongly oriented parallel to the substrate, with the smectic layer normal perpendicular to the substrate, as evidenced by GISAXS.

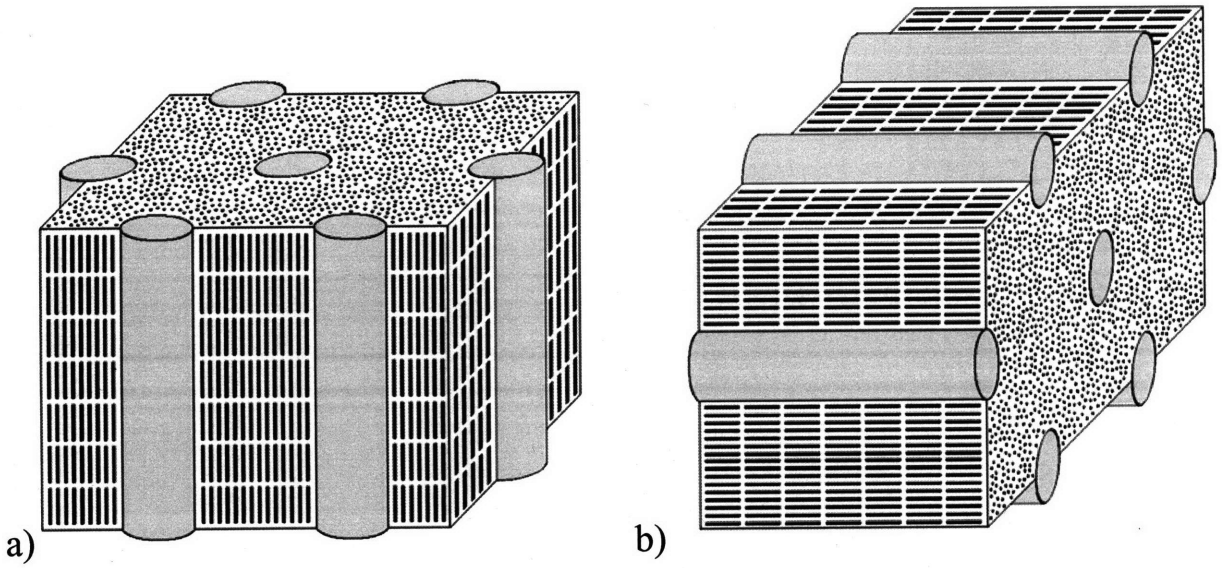

Figure 5-5. Schematics of the morphologies observed a) as-spun and b) after annealing at 170°C for 36 hours under vacuum (schematics are not to scale for clarity).

In bulk this material displayed a hexagonal cylinder morphology with the smectic layer normal oriented parallel to the cylinder axis [15, 17]. This orientation is consistent with the homogeneous anchoring relative to the curved PS/LCP inter-material dividing surface (IMDS). On the time scale of the spin casting process (the solvent evaporates in approximately one second), the smectic LC layers in the side chain liquid crystalline block copolymer orient parallel to the substrate, with the smectic layer normal perpendicular to the substrate. The dominant driving force in the as-spun film is the orientation of the LC mesophase relative to the substrate. The domination of the LC phase in determining the block copolymer orientation suggests that the mesophase appears in the film prior to the evolution of block copolymer domains on solvent removal, enabling the LC orientation to act as a primary influence for morphological development. The PS domains then phase segregate to form cylinders perpendicular to the surface in order to maintain the homogeneous anchoring condition. The as-cast perpendicular cylinder phase appears to have little long range order, as would be expected due to the short time allowed for ordering. It has been shown that perpendicular cylinders can be achieved in an amorphous-amorphous block copolymer by creating a solvent evaporation gradient to orient the cylinders[26]. However, in this study the solvent evaporation rates were several orders of magnitude faster than those where this phenomena has been observed.

Annealing above the T_g of both blocks, the T_{iso}, and near the block copolymer ODT gives increased mobility to the system. Only when the LC phase is removed above the T_{iso}, followed by slow cooling, do we observe the planar arrangement of cylinders typically found with fully amorphous block copolymers. This is particularly true for systems in which one of the two blocks preferentially wets the substrate, as is most often observed experimentally. In this case the minimization of interfacial energies is the dominant driving force, resulting in the hexagonal cylinders oriented parallel to the surface. This morphology allows the siloxane based LCP block

to be in contact with both the substrate and air interfaces, thus avoiding the less favorable PS-air and PS-Si interfaces. Upon cooling, the polystyrene vitrifies, while the LC mesophase is in the isotropic state, kinetically trapping the parallel cylinder morphology. There is significantly more interfacial area between the LC mesophase and the IMDS with the PS than with the substrate. Thus, further cooling below the T_{iso} leads to an orientation of the smectic layers consistent with the homogeneous anchoring condition, such that the smectic layer normal is also parallel to the substrate.

5.5 Conclusion

Grazing incidence small-angle X-ray scattering and atomic force microscopy were used to investigate the morphologies of side chain liquid crystalline block copolymer thin films. The perpendicular cylinder morphology was observed in the as-spun films; however upon thermal annealing the morphology rearranged to yield cylinders parallel to the substrate. The initial morphology is dominated by the ordering of the smectic LC layers relative to the substrate. Annealing results in a reorientation of the morphology such that the surface energy of the film is minimized. Gaining a further understanding of the effects of a LC mesophase upon the morphologies of block copolymer thin films can lead to greater control over the orientation and order for these materials, allowing for advances in the use of block copolymers for nano-patterning.

5.6 References

1. de Jeu, W. H.; Serero, Y.; Al-Hussein, M., Liquid crystallinity in block copolymer films for controlling polymeric nanopatterns. *Ordered Polymeric Nanostructures at Surfaces* 2006, 200, 71-90.

2. Fasolka, M. J.; Mayes, A. M., Block copolymer thin films: Physics and applications. *Annual Review of Materials Research* 2001, 31, 323-355.

3. Bang, J.; Kim, S. H.; Drockenmuller, E.; Misner, M. J.; Russell, T. P.; Hawker, C. J., Defect-free nanoporous thin films from ABC triblock copolymers. *Journal of the American Chemical Society* 2006, 128, (23), 7622-7629.

4. Peng, J.; Kim, D. H.; Knoll, W.; Xuan, Y.; Li, B. Y.; Han, Y. C., Morphologies in solvent-annealed thin films of symmetric diblock copolymer. *Journal of Chemical Physics* 2006, 125, (6), 064702.

5. Tang, C. B.; Tracz, A.; Kruk, M.; Zhang, R.; Smilgies, D. M.; Matyjaszewski, K.; Kowalewski, T., Long-range ordered thin films of block copolymers prepared by zone-casting and their thermal conversion into ordered nanostructured carbon. *Journal of the American Chemical Society* 2005, 127, (19), 6918-6919.

6. Morikawa, Y.; Nagano, S.; Watanabe, K.; Kamata, K.; Iyoda, T.; Seki, T., Optical alignment and patterning of nanoscale microdomains in a block copolymer thin film. *Advanced Materials* 2006, 18, (7), 883-886.

7. Busch, P.; Krishnan, S.; Paik, M.; Toombes, G. E. S.; Smilgies, D. M.; Gruner, S. M.; Ober, C. K., Inner Structure of Thin Films of Lamellar Poly(styrene-b-butadiene) Diblock Copolymers As Revealed by Grazing-Incidence Small-Angle Scattering.

Macromolecules 2007, 40, (1), 81-89.

8. Cavicchi, K. A.; Russell, T. P., Solvent annealed thin films of asymmetric polyisoprene-polylactide diblock copolymers. *Macromolecules* 2007, 40, (4), 1181-1186.

9. Figueiredo, P.; Geppert, S.; Brandsch, R.; Bar, G.; Thomann, R.; Spontak, R. J.; Gronski, W.; Samlenski, R.; Muller-Buschbaum, P., Ordering of cylindrical microdomains in thin films of hybrid isotropic/liquid crystalline triblock copolymers. *Macromolecules* 2001, 34, (2), 171-180.

10. Huang, E.; Pruzinsky, S.; Russell, T. P.; Mays, J.; Hawker, C. J., Neutrality conditions for block copolymer systems on random copolymer brush surfaces. *Macromolecules* 1999, 32, (16), 5299-5303.

11. Anthamatten, M.; Hammond, P. T., Free-energy model of asymmetry in side-chain liquid-crystalline diblock copolymers. *Journal of Polymer Science Part B-Polymer Physics* 2001, 39, (21), 2671-2691.

12. Anthamatten, M.; Wu, J. S.; Hammond, P. T., Direct observation of a smectic bilayer microstructure in side-chain liquid crystalline diblock copolymers. *Macromolecules* 2001, 34, (24), 8574-8579.

13. Auad, M. L.; Kempe, M. D.; Kornfield, J. A.; Rendon, S.; Burghardt, W. R.; Yoon, K., Effect of mesophase order on the dynamics of side group liquid crystalline polymers. *Macromolecules* 2005, 38, (16), 6946-6953.

14. Ferri, D.; Wolff, D.; Springer, J.; Francescangeli, O.; Laus, M.; Angeloni, A. S.; Galli, G.; Chiellini, E., Phase and orientational behaviors in liquid crystalline main-chain/side-group block copolymers. *Journal of Polymer Science Part B-Polymer Physics* 1998, 36,

(1), 21-29.

15. Osuji, C.; Zhang, Y. M.; Mao, G. P.; Ober, C. K.; Thomas, E. L., Transverse cylindrical microdomain orientation in an LC diblock copolymer under oscillatory shear. *Macromolecules* 1999, 32, (22), 7703-7706.

16. Poser, S.; Fischer, H.; Arnold, M., Liquid crystalline side-group block copolymers with triblock structure: Investigations on the influence of the block arrangement on the morphology and the LC-phase behavior. *Journal of Polymer Science Part a-Polymer Chemistry* 1996, 34, (9), 1733-1740.

17. Verploegen, E.; McAfee, L. C.; Tian, L. T.; Verploegen, D.; Hammond, P. T., Observation of Transverse Cylinder Morphology in Side Chain Liquid Crystalline Block Copolymers. *Macromolecules* 2007, 40, (4), 777-780.

18. Yamada, M.; Itoh, T.; Hirao, A.; Nakahama, S.; Watanabe, J., Side-chain LC block copolymers with well defined structures prepared by living anionic polymerization. 2: Effect of the glass transition temperature of amorphous segments on the phase behaviour and structure of the LC segment. *High Performance Polymers* 1998, 10, (1), 131-138.

19. Al-Hussein, M.; Serero, Y.; Konovalov, O.; Mourran, A.; Moller, M.; de Jeu, W. H., Nanoordering of fluorinated side-chain liquid crystalline/amorphous diblock copolymers. *Macromolecules* 2005, 38, (23), 9610-9616.

20. Wu, J. S.; Fasolka, M. J.; Hammond, P. T., Mixed surface morphologies of well-defined smectic diblock copolymer ultrathin films. *Macromolecules* 2000, 33, (4), 1108-1110.

21. Mayer, S.; Zentel, R., Liquid crystalline polymers and elastomers. *Current Opinion in Solid State & Materials Science* 2002, 6, (6), 545-551.

22. Busch, P.; Rauscher, M.; Smilgies, D. M.; Posselt, D.; Papadakis, C. M., Grazing-incidence small-angle X-ray scattering from thin polymer films with lamellar structures-the scattering cross section in the distorted-wave Born approximation. *Journal of Applied Crystallography* 2006, 39, 433-442.

23. Muller-Buschbaum, P., Grazing incidence small-angle X-ray scattering: an advanced scattering technique for the investigation of nanostructured polymer films. *Analytical and Bioanalytical Chemistry* 2003, 376, (1), 3-10.

24. Moment, A.; Miranda, R.; Hammond, P. T., Synthesis of polystyrene-polysiloxane side-chain liquid crystalline block copolymers. *Macromolecular Rapid Communications* 1998, 19, (11), 573-579.

25. Lee, B.; Park, I.; Yoon, J.; Park, S.; Kim, J.; Kim, K. W.; Chang, T.; Ree, M., Structural analysis of block copolymer thin films with grazing incidence small-angle X-ray scattering. *Macromolecules* 2005, 38, (10), 4311-4323.

26. Kim, G.; Libera, M., Morphological development in solvent-cast polystyrene-polybutadiene-polystyrene (SBS) triblock copolymer thin films. *Macromolecules* 1998, 31, (8), 2569-2577.

Chapter 6 Morphology of Side Chain Liquid Crystalline Block Copolymer Thin Films: Effects of Liquid Crystal Content

6.1 Introduction

Recent there has been a great deal of research directed at controlling the self-assembly of block copolymer thin films, specifically obtaining the desired orientation of nanoscale features relative to the substrate[1, 2]. Recently progress has been made in controlling the morphologies of block copolymer thin films through techniques such as solvent annealing[3, 4], zone casting[5], and optical alignment[6]. Due to the large interfacial area of the thin film, the orientation of the domains depends greatly upon the relative surface energies of the blocks[7-10]. The incorporation of a liquid crystalline (LC) component into such systems offers a powerful tool for manipulating the orientation of the self-assembled structures. When a LC component is introduced several factors including conformational asymmetry, structural asymmetry, and the anchoring of the LC mesophase to the inter-material dividing surface (IMDS) can alter the self-assembly behavior[11-16]. The inter-material dividing surface (IMDS) of the block copolymer mesophase can be used to orient the liquid crystalline mesophase, as the LC will preferentially orient with respect to the IMDS due to surface stabilization effects[17-19]. In this way a well oriented block copolymer mesophase can be used to template order in the LC mesophase. Additionally, liquid crystalline

polymers (LCP) are of particular interest as they can allow for the introduction of responsive elements into the system, e.g. thermo-, chemo-, electro-, or photo-responsive[20].

In this Chapter I will describe the effects of varying the LC content upon the self-assembled morphologies of these side chain liquid crystalline block copolymers. The strong preference for homogenous anchoring creates a situation where the orientations of the LC mesophase and the block copolymer nanostructures are linked. Using the LC content as a tool to tune the interfacial interactions of the LC mesophase allows for the orientation and ordering of the morphologies to be manipulated. The synthetic techniques detailed in Chapter 2[21] allow for the systematic control over the covalent attachment of LC moieties to a functional siloxane based block copolymer backbone. The ability to precisely control the content of covalently attached LC moieties enables a unique tunability, allowing for the structure of the thin films to be tailored for specific applications. The surface morphologies of these films are revealed with atomic force microscopy (AFM) and grazing incidence small-angle X-ray scattering (GISAXS) is utilized to probe the interior structures. For more details on GISAXS see Appendix E.

6.2 Experimental

The synthesis of the polymer, LC moiety, and attachment were previously developed and described in Chapter 2[21]. Spin casting was performed by preparing 4, 2, and 1 wt% homogeneous solutions of the side chain liquid crystalline block copolymer in toluene, and applying a single drop to the silicon substrate rotating at 2500 rpm. The film thicknesses were measured with a Tencor P-10 Surface Profilometer. The higher concentration solutions resulted in thicker films, as would be expected. The films were then annealed at 170°C under vacuum for 36 hours and cooled to room temperature a 0.5°C/min. A Dimension 3100 AFM by DI Instruments with a Nanoscope 3A Controller in tapping mode was used to investigate the surface morphologies. NCH Pointprobe non-contact mode AFM Cantilevers were purchased from Pacific Nanotechnologies. GISAXS experiments were performed at the G1 beamline at the Cornell High Energy Synchrotron Source (CHESS). The wavelength of the incident beam was 1.239Å, and silver behenate was used to calibrate the sample to detector distance with a first order scattering vector of q of 1.076nm^{-1} (with $q = 4\pi \sin\theta/\lambda$ where 2θ is the scattering angle and λ is the wavelength). A slow-scan CCD-based x-ray detector, home built by Drs. M.W. Tate and S.M. Gruner of the Cornell University Physics Department, was used for data collection. Incidence angles were chosen between 0.12° and 0.22°, and the final images are an average of two 1 second exposures.

6.3 Results and Discussion

The morphologies and thermal properties of these materials are summarized in Table 1. It was found that increasing the LC content leads to both an increase in the volume fraction of the liquid crystalline polymer block and an increase in the preference for homogeneous anchoring of the LC mesophase. Previously we described techniques for the rearrangement of a liquid crystalline block copolymer through thermal annealing[19]. A metastable morphology was observed in the as-cast film, dominated by interactions of the LC mesophase with the substrate, and a reorientation driven by a minimization of interfacial energies in the annealed film. Here we will investigate and discuss the effects of increasing the preference for LC anchoring upon the thin film morphologies.

Representative grazing incidence small-angle X-ray scattering (GISAXS) images are shown for annealed block copolymers thin films with different LC contents. The polymer with the lowest LC content (PS27-LCP_{4BPP4}46, Figure 6-1a) displays a disordered cylindrical morphology. Polymers with an intermediate LC content exhibit an ordered parallel cylinder morphology (PS27-LCP_{4BPP4}79, Figure 6-1b). Further increase of the LC content, to 100% functionalization, results in the perpendicular cylinder morphology (PS27-LCP_{4BPP4}115, Figure 6-1c). For all of these morphologies homogenous anchoring of the LC mesophase to the IMDS was observed, such that the smectic layer normal is parallel to the cylinder axis.

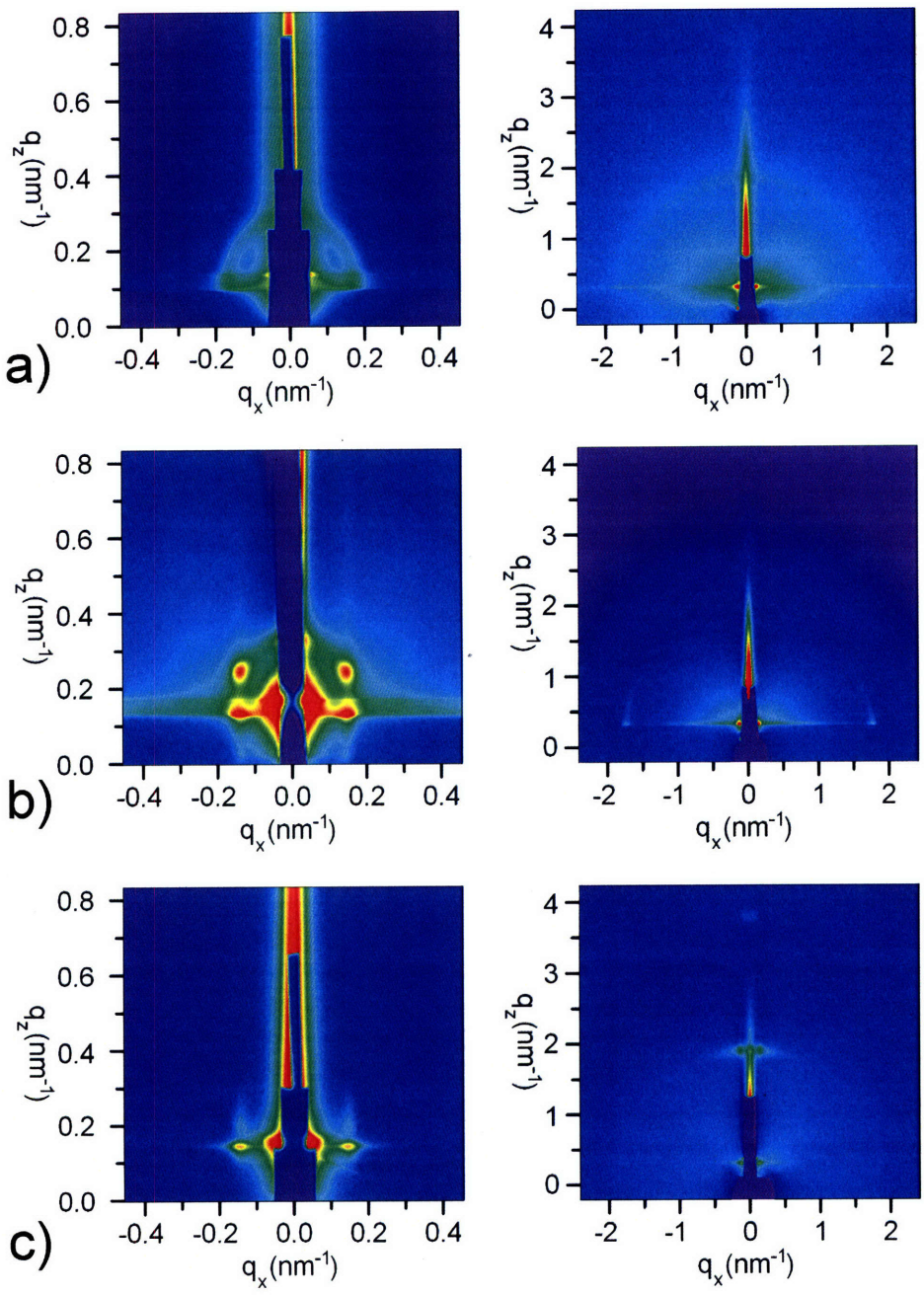

Figure 6-1. Representative grazing incidence small-angle X-ray scattering images of a) PS27-LCP$_{4BPP4}$46, b) PS27-LCP$_{4BPP4}$79, and c) PS27-LCP$_{4BPP4}$115. The images on the left were taken with a sample to detector distance of 2,375mm, and the scattering from the block copolymer mesophase is observed. The images on the right were taken with a sample to detector distance of 442mm and primarily display scattering from the LC mesophase.

For materials with low LC content the poorly defined LC mesophase does not provide a strong of a driving force for orientation, resulting in the disordered morphologies for both the as-cast and annealed films. Increasing the LC content increases the interactions of the LC mesophase and the IMDS, resulting in an ordered cylinder morphology. As-cast films with this intermediate LC content display a metastable perpendicular cylinder morphology as the interactions (i.e. homeotropic anchoring) of the LC mesophase with the substrate are dominant. With the LC normal oriented perpendicular to the substrate, and the requirement of homogeneous anchoring of the LC mesophase to the IMDS, the PS cylinders are forced to orient perpendicular to the substrate. When these films are annealed a reorientation to the parallel cylinder morphology occurs in order minimize the interfacial energies and avoid unfavorable PS-air interactions[19]. The as-cast thin films of the polymers with 100% LC functionalization also display the perpendicular cylinder morphology. However, unlike samples with intermediate LC content annealing does not result in the parallel morphology, as the increased preference for homeotropic anchoring of the LC mesophase to the substrate prevents reorientation. These results are summarized in Table 6-1.

Table 6-1. Summary of thin film morphologies.

Sample name	PS wt %	LC Attachment %	As-cast orientation	Annealed orientation
PS27-LCP$_{4BPP4}$46	37	31	Disordered Cylinder	Disordered Cylinder
PS27-LCP$_{4BPP4}$57	32	41	Disordered Cylinder	Disordered Cylinder
PS27-LCP$_{4BPP4}$79	26	55	Perpendicular Cylinder	Parallel Cylinder
PS27-LCP$_{4BPP4}$90	23	76	Perpendicular Cylinder	Parallel Cylinder
PS27-LCP$_{4BPP4}$115	19	100	Perpendicular Cylinder	Perpendicular Cylinder
PS61-LCP$_{4BPP4}$83	42	62	Perpendicular Lamellar	Parallel Lamellar
PS61-LCP$_{4BPP4}$101	38	79	Perpendicular Transitional	Perpendicular Cylinder
PS61-LCP$_{4BPP4}$123	33	100	Perpendicular Cylinder	Perpendicular Cylinder

AFM images of as-cast and annealed films with 100% LC functionalization are shown in Figure 6-2. Both films exhibit the perpendicular cylinder morphology; however the features appear more clearly in the as-cast film. In order to minimize the interfacial energy of the system the polymer-air interface is wet by as layer of liquid crystalline polymer to avoid unfavorable PS-air interactions. The AFM tip now probes the PS cylinders through the liquid crystalline polymer layer at the air interface, resulting in the lower contract of the features. Additionally, heating above the PS glass transition temperature (T_g) allows the system to further equilibrate, resulting in increased long range order of the cylinders for the annealed film. The unique feature of this system is that the orientation of the PS cylinders is determined by the interactions of the LC mesophase with the IMDS and the substrate, leading to a stable perpendicular morphology for 100% LC functionalization. This ordered perpendicular cylinder morphology is desirable for many nano-patterning applications.

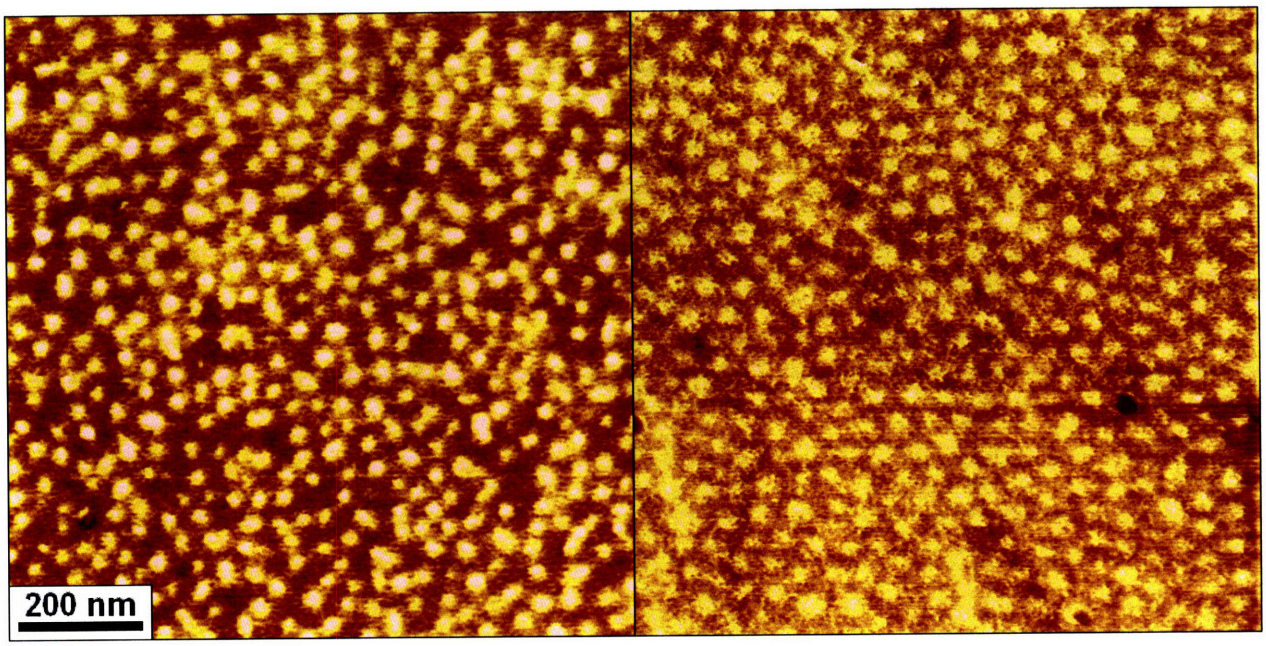

Figure 6-2. Atomic force microscopy phase images of PS27-LCP$_{4BPP4}$115 with 100% LC functionalization displaying the perpendicular cylinder morphology. The left image is as-cast and the right image has been annealed at 170°C for 36 hours.

A higher molecular weight series (PS61-) of side chain liquid crystalline block copolymers was also investigated; these polymers have a significantly larger PS block than the PS27- series, resulting in larger PS volume fractions for comparable LC functionalization. As the molecular weight increases, so does the feature spacing of the self-assembled morphologies. These larger features could not be observed with GISAXS, as the scattering features of interest were obscured by the beamstop and specular reflectance. For these materials increasing the LC functionalization leads to a dramatic change in the PS volume fraction, allowing for a range of morphologies to be obtained from a single polymer backbone.

AFM images are shown in Figure 6-3 a), b), and c) for LC functionalizations of 62, 79, and 100%, respectively. This increase in LC content reduces the PS volume fraction allowing

lamellar, transitional, and cylindrical morphologies to be obtained for PS61-LCP_{4BPP4}83, PS61-LCP_{4BPP4}101, and PS61-LCP_{4BPP4}123, respectively; these results are summarized in Table 6-1. The as-cast films all display these morphologies oriented perpendicular to the substrate (see images on left in Figure 6-3). Upon annealing sample PS61-LCP_{4BPP4}123 remains perpendicular cylinders, exhibiting the same behavior as PS27-LCP_{4BPP4}115 from the lower molecular weight series. Interestingly, annealing of PS61-LCP_{4BPP4}101, which displays a lamellar/cylindrical transitional morphology in the as-cast film and in bulk, results in a perpendicular cylinder morphology, with the typical liquid crystalline polymer wetting layer at the air interface. This result indicates that the cylindrical morphology is stabilized, in favored of the lamellar morphology. This stabilization was not observed in bulk samples of this material that were annealed. It is believed that the relatively small sample thickness of the thin film allows for this rearrangement to the equilibrium morphology to occur more quickly than in bulk.

The perpendicular lamellar morphology observed for PS61-LCP_{4BPP4}83 in the as-cast film and reorients to the parallel lamellar morphology after annealing. This behavior is very similar to that of PS27-LCP_{4BPP4}79 and PS27-LCP_{4BPP4}90 from the lower molecular weight series, which have similar attachment percents to PS61-LCP_{4BPP4}83. In a perfect lamellar morphology there is no curvature of the IMDS, so presumably either the homeotropic or homogeneous orientations are possible. When considering the conformational space of the siloxane backbone it is believed that the homogeneous orientation of the LC moieties relative to the IMDS is more entropically favorable as the siloxane backbone has more conformational freedom than in the homeotropic orientation. Thus it is believed that, one again, the as-cast perpendicular morphology is stabilized by the LC anchoring and upon annealing the morphology reorients in order to minimize the interfacial energy with the air and substrate interfaces.

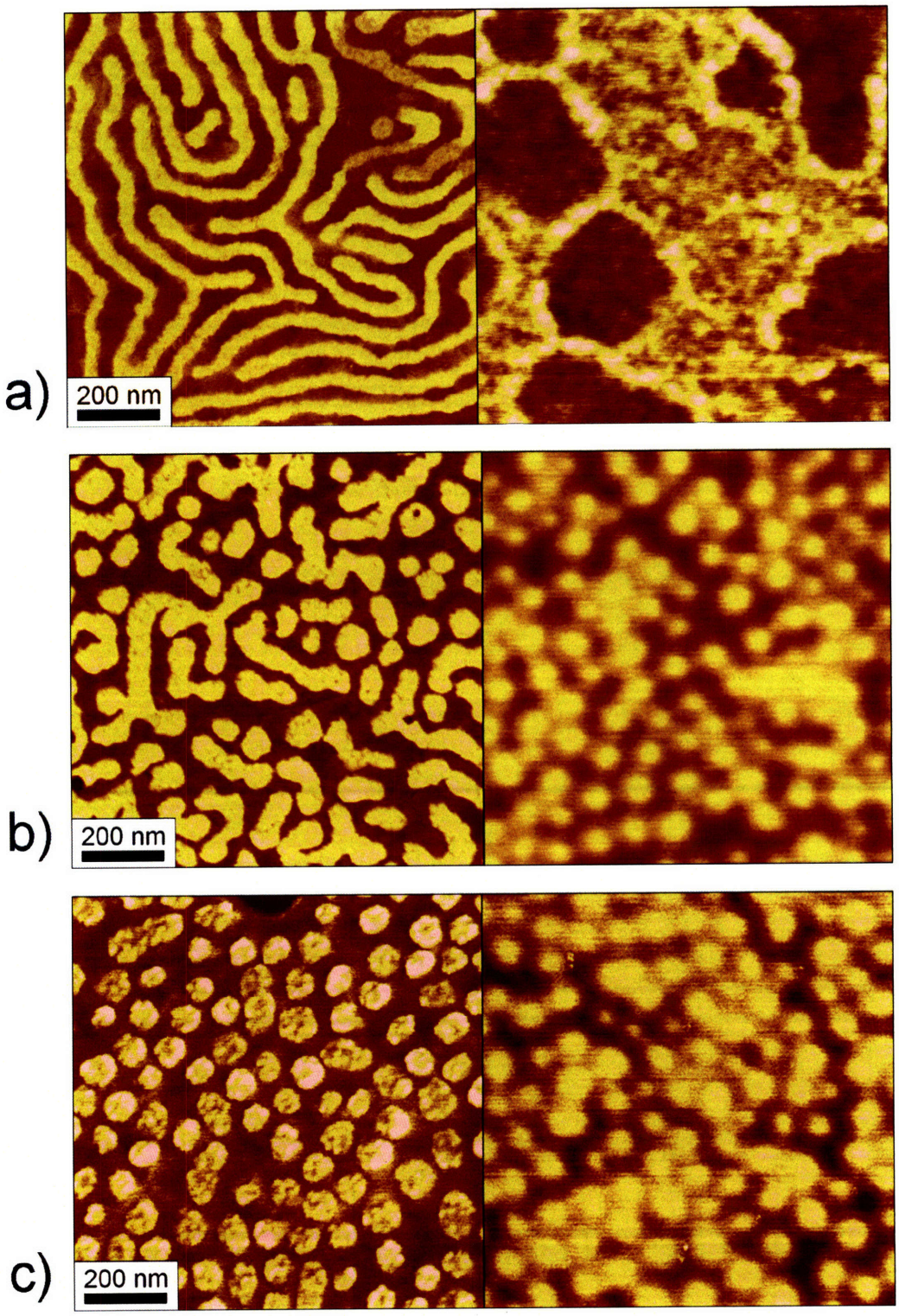

Figure 6-3. Atomic force microscopy phase images of a) PS61-LCP_{4BPP4}83, b) PS61-LCP_{4BPP4}101, and c) PS61-LCP_{4BPP4}123. The images on the left are the as-cast films and the images on the right have been annealed at 170°C for 36 hours.

Additionally, the thickness of the film played a role in the morphology. The films prepared from 2 and 4 wt% solutions displayed the morphologies described above, with film thickness ranging from 70 to 200 nm. The 1 wt% solutions resulted in films ranging form 20 to 30 nm in thickness; which is less than the periodicity of the block copolymer structures (d_o). In this case the system cannot self-assemble into either parallel cylinders or parallel lamellae without significantly exposing the PS interface to either the air or substrate interfaces, or suffering significant energetic penalties for perturbing the polymer chain conformation.

GISAXS of these films indicate that there is some form of periodic structure in the plane of the substrate for the lower molecular weight series. There is no indication of periodic structure normal to the substrate, as would be expected with films less than the characteristic periodicity of the block copolymer. AFM yielded inconsistent results, the features appeared unordered and were not consistent between samples. For this lower molecular weight series of side chain liquid crystalline block copolymers it is believed that the structures are a combination of poorly ordered perpendicular and parallel cylinders. For the higher molecular weight series the film thickness is nearly half of d_o for these materials, and there was no evidence of any self-assembled structures. It is believed that the block copolymer forms a simple wetting layer on the surface, where the liquid crystalline polymer wets the substrate and the PS is exposed to the air interface. Additional studies were performed using variable rate flow casting in order to create a thin film with a thickness gradient, and allow the morphologies as a function of film thickness to be investigate more thoroughly. These samples were prepared at the National Institute for Standards and Technology (NIST) in Gaithersburg, MD, in collaboration with Kirt Page and Michael Fasolka. Initial results indicate that the morphologies reported are observed for all films, until the film thickness approaches d_o and the morphology becomes unclear.

6.4 Conclusion

In summary, we have demonstrated a means of utilizing the covalent attachment of LC moieties to a siloxane based block copolymer backbone as a tool for controlling the thin film morphologies. Increases in LC functionalization lead to stronger preferences for the anchoring of the LC mesophase relative to the substrate and the IMDS. By essentially manipulating the strength of these interactions the morphology of the thin film can be controlled; allowing disordered cylinder, parallel cylinder, and perpendicular cylinder morphologies to be achieved. Additionally, a second series of side chain liquid crystalline polymers were studied, which contained a larger PS block. These materials resulted in perpendicular lamellar, transitional, and cylindrical morphologies with larger feature spacings.

This is the first example of manipulating the morphology and orientation of liquid crystalline block copolymer thin films through variations in LC content. This unique control over the orientation and order of the self-assembled morphologies will allow for the custom design of thin films for specific nano-patterning applications. Future work in with these thin films includes investigation of the effects of variations in the surface energy upon the self-assembly behavior. This work is being conducted in collaboration with Kirt Page and Michael Fasolka from National Institute for Standards and Technology (NIST) in Gaithersburg, MD.

6.5 References

1. de Jeu, W. H.; Serero, Y.; Al-Hussein, M., Liquid crystallinity in block copolymer films for controlling polymeric nanopatterns. *Ordered Polymeric Nanostructures at Surfaces* **2006,** 200, 71-90.

2. Fasolka, M. J.; Mayes, A. M., Block copolymer thin films: Physics and applications. *Annual Review of Materials Research* **2001,** 31, 323-355.

3. Bang, J.; Kim, S. H.; Drockenmuller, E.; Misner, M. J.; Russell, T. P.; Hawker, C. J., Defect-free nanoporous thin films from ABC triblock copolymers. *Journal of the American Chemical Society* **2006,** 128, (23), 7622-7629.

4. Peng, J.; Kim, D. H.; Knoll, W.; Xuan, Y.; Li, B. Y.; Han, Y. C., Morphologies in solvent-annealed thin films of symmetric diblock copolymer. *Journal of Chemical Physics* **2006,** 125, (6), 064702.

5. Tang, C. B.; Tracz, A.; Kruk, M.; Zhang, R.; Smilgies, D. M.; Matyjaszewski, K.; Kowalewski, T., Long-range ordered thin films of block copolymers prepared by zone-casting and their thermal conversion into ordered nanostructured carbon. *Journal of the American Chemical Society* **2005,** 127, (19), 6918-6919.

6. Morikawa, Y.; Nagano, S.; Watanabe, K.; Kamata, K.; Iyoda, T.; Seki, T., Optical alignment and patterning of nanoscale microdomains in a block copolymer thin film. *Advanced Materials* **2006,** 18, (7), 883-886.

7. Busch, P.; Krishnan, S.; Paik, M.; Toombes, G. E. S.; Smilgies, D. M.; Gruner, S. M.; Ober, C. K., Inner Structure of Thin Films of Lamellar Poly(styrene-b-butadiene)

Diblock Copolymers As Revealed by Grazing-Incidence Small-Angle Scattering. *Macromolecules* **2007,** 40, (1), 81-89.

8. Cavicchi, K. A.; Russell, T. P., Solvent annealed thin films of asymmetric polyisoprene-polylactide diblock copolymers. *Macromolecules* **2007,** 40, (4), 1181-1186.

9. Figueiredo, P.; Geppert, S.; Brandsch, R.; Bar, G.; Thomann, R.; Spontak, R. J.; Gronski, W.; Samlenski, R.; Muller-Buschbaum, P., Ordering of cylindrical microdomains in thin films of hybrid isotropic/liquid crystalline triblock copolymers. *Macromolecules* **2001,** 34, (2), 171-180.

10. Huang, E.; Pruzinsky, S.; Russell, T. P.; Mays, J.; Hawker, C. J., Neutrality conditions for block copolymer systems on random copolymer brush surfaces. *Macromolecules* **1999,** 32, (16), 5299-5303.

11. Anthamatten, M.; Hammond, P. T., Free-energy model of asymmetry in side-chain liquid-crystalline diblock copolymers. *Journal of Polymer Science Part B-Polymer Physics* **2001,** 39, (21), 2671-2691.

12. Boyer, S. A. E.; Grolier, J. P. E.; Yoshida, H.; Iyoda, T., Effect of interface on thermodynamic behavior of liquid crystalline type amphiphilic di-block copolymers. *Journal of Polymer Science Part B-Polymer Physics* **2007,** 45, (11), 1354-1364.

13. Ivanova, R.; Staneva, R.; Geppert, S.; Heck, B.; Walter, B.; Gronski, W.; Stuhn, B., Interplay between domain microstructure and nematic order in liquid crystalline/isotropic block copolymers. *Colloid and Polymer Science* **2004,** 282, (8), 810-824.

14. Olsen, B. D.; Segalman, R. A., Structure and thermodynamics of weakly segregated rod-coil block copolymers. *Macromolecules* **2005,** 38, (24), 10127-10137.

15. Sentenac, D.; Demirel, A. L.; Lub, J.; de Jeu, W. H., A new lamellar morphology of a hybrid amorphous liquid crystalline block copolymer film. *Macromolecules* **1999,** 32, (10), 3235-3240.

16. Yamada, M.; Iguchi, T.; Hirao, A.; Nakahama, S.; Watanabe, J., Side-chain liquid crystal block copolymers with well-defined structures prepared by living anionic polymerization I. Thermotropic phase behavior and structures of liquid crystal segment in lamellar type of microphase domain. *Polymer Journal* **1998,** 30, (1), 23-30.

17. Osuji, C.; Ferreira, P. J.; Mao, G. P.; Ober, C. K.; Vander Sande, J. B.; Thomas, E. L., Alignment of self-assembled hierarchical microstructure in liquid crystalline diblock copolymers using high magnetic fields. *Macromolecules* **2004,** 37, (26), 9903-9908.

18. Verploegen, E.; McAfee, L. C.; Tian, L. T.; Verploegen, D.; Hammond, P. T., Observation of Transverse Cylinder Morphology in Side Chain Liquid Crystalline Block Copolymers. *Macromolecules* **2007,** 40, (4), 777-780.

19. Verploegen, E.; Boone, D.; Hammond, P. T., Morphology of side chain liquid crystalline block copolymer thin films and effects of thermal annealing. *Journal of Polymer Science Part B-Polymer Physics* **2007,** 45, (24), 3263-3266.

20. Mayer, S.; Zentel, R., Liquid crystalline polymers and elastomers. *Current Opinion in Solid State & Materials Science* **2002,** 6, (6), 545-551.

21. Verploegen, E.; Zhang, T.; Murlo, N.; Hammond, P. T., Influence of variations of liquid crystalline content upon the self-assembly behavior of siloxane based block copolymers. *Soft Matter* **2008,** Advance Article.

Chapter 7 Conclusions

7.1 Summary of Thesis Contributions

The work presented here details methods for synthesizing a new class of side chain liquid crystalline block copolymers (SCLCBCPs) with a low glass transition temperature (T_g) siloxane backbone. Synthetic methods for controlling the covalent attachment of liquid crystals (LC) to both diblock and triblock polystyrene-polyvinylmethylsiloxane copolymers were developed. Furthermore, the self-assembly behavior of these materials was extensively studied and the driving forces for the resulting morphologies have been detailed for both bulk and thin film systems. This work demonstrates the ability to control and manipulate the self-assembled nanoscale morphologies of these materials through structural modifications, in addition to various processing techniques.

The work presented in Chapter 2 details the synthesis of polystyrene-polyvinylmethylsiloxane (PS-PVMS) diblock copolymers and subsequent attachment of liquid crystalline moieties to the functional siloxane backbone. Exceptional control over the functionalization of the siloxane backbone was demonstrated, allowing for a wide range of LC attachment percents to be achieved. The self-assembly behavior of these materials was investigated as a function of the covalently attached LC content and structure; having a significant impact upon the morphologies of both the liquid crystalline polymer (LCP) and block copolymer mesophases. Variations in the LC content allowed for a wide range of morphologies to be obtained from a single LC attachment reaction, including: LCP cylinders, coexistence of

LCP cylinders and lamellae, lamellae, coexistence of PS cylinders and lamellae, and PS cylinders.

In addition to determining the morphology and thermal properties of the LC mesophase, the LC content was shown to significantly effect the interactions with the inter-material dividing surface (IMDS) with the nanophase segregated polystyrene domains. As a result of a strong preference for homogeneous anchoring of the LC moieties relative to the curved IMDS present in cylindrical morphologies; the order-disorder transition temperature (T_{ODT}) was shown to be highly dependant upon LC functionalization. Furthermore, tunability over the mechanical properties profiles was demonstrated; allowing the elastic modulus to be varied over several orders of magnitude through controlling the LC functionalization.

The work in Chapter 3 describes the several synthesis schemes for creating PS-PVMS-PS triblock copolymers. These materials possess the same functionality as their diblock counterparts allowing for the covalent attachment of LC moieties. The different approaches for triblock copolymer synthesis include, the coupling of living PS homopolymer to either a difunctional PVMS homopolymer or a functional PS-PVMS diblock, and using PS-PVMS diblock copolymer as a macroinitiator for atom transfer polymerization (ATRP) of polystyrene. Fractionation from a tetrahydrofuran (THF) – ethanol mixture was demonstrated as an effective method for isolating the higher molecular weight species resulting from these reactions. This allows for the triblock copolymer to be purified, removing any diblock, homopolymer, or small molecule impurities. Additionally, the mechanical properties of the triblock and diblock SCLCBCPs were compared. The materials based on triblock copolymer backbones displayed greater elasticity than their diblock counterparts, due to the presence of the physical crosslinks resulting form the A-B-A block architecture.

The work presented in Chapter 4 describes the effects of mechanical deformation upon the morphologies of these materials. Mechanical deformations led to the preferential orientation of the smectic LCP and block copolymer mesophases. The preference for homogeneous anchoring of the LC moieties relative to the IMDS of the cylindrical block copolymer mesophase was shown to be a dominant driving force for determining the orientation of the morphologies. In-situ oscillatory shear X-ray experiments enabled the alignment of these materials to be optimized resulting in nearly monodomain morphologies to be achieved. The transverse HCP cylinders orientation was observed for liquid crystalline block copolymers that experienced oscillatory shear. This result reveals that the preference for homogeneous anchoring effects the orientation of the morphology at temperatures above the smectic to isotropic transition temperature (T_{iso}).

The work in Chapter 5 details the effects of thermal annealing upon the thin film morphologies of these SCLCBCPs. Atomic force microscopy (AFM) and grazing incidence small-angle X-ray scattering (GISAXS) enabled the investigation of spin cast SCLCBCP thin films. The perpendicular cylinder morphology was observed in the as-spun films; however upon thermal annealing the morphology rearranged, resulting in cylinders parallel to the substrate. The initial morphology is dominated by the ordering of the smectic LC layers relative to the substrate; as the strong preference for homogenous anchoring results in a perpendicular cylinder morphology. Annealing results in a reorientation of the morphology, to a parallel cylinder morphology, such that the surface energy of the film is minimized.

Finally, Chapter 6 demonstrates the ability to manipulate the self-assembly behavior of SCLCBCP thin films through variations in the covalently attached LC content. Once again, increasing the LC functionalization results in a greater preference for homogeneous anchoring of

the LCs to the IMDS. By essentially manipulating the strength of these interactions the morphology of the thin film can be controlled; allowing disordered cylinder, parallel cylinder, and perpendicular cylinder morphologies to be achieved. Additionally, a second series of side chain liquid crystalline polymers were studied, which contained a larger PS block. These materials resulted in perpendicular lamellar, transitional, and cylindrical morphologies with larger feature spacings.

7.2 Future Work and Recommendations

There are many areas where this work could be expanded upon and further pursued. The hydrosilylation chemistry can be used to attach a wide range of functional liquid crystalline moieties to a siloxane polymer backbone. This could be used to impart desired thermo-, electro-, photo-, or chemo-responsive elements into a polymer system; where the low T_g siloxane provides mobility, allowing the response to occur at room temperature. The ability to precisely control the attachment of these functional groups provides a unique tool for tuning the properties of such a system. When designing such responsive elastomers several issues should be carefully considered: How will the stimuli effect the self-assembly behavior of the system? How do the stimuli affect the morphology and properties of the material? How can these effects be harnessed to provide a useful response? Under what conditions will the material or device be operating and how do these conditions affect the self-assembly and the performance?

In order to achieve the desired results, it is useful to have flexible chemistries or other materials parameters allowing for manipulation of the materials properties. One recommendation regarding this system is that by using the difunctional PVMS as a basis, other chemistries can be explored for attaching a high T_g outer block resulting in a triblock copolymer.

Ideally, this outer block could be easily modified, allowing for further modification of the self-assembly behavior and properties of the system.

The ability to manipulate the thin film morphologies of these systems makes them ideal candidates for use in nanopatterning applications and as responsive membranes. A wide range of issues have yet to be explored. The thin films studied in Chapters 5 and 6 were created using spin casting, however there are many other film preparation techniques that could be used including: flow casting, dipping, and spray deposition. Templated self-assembly could be used to achieve increased long range ordering and to systematically introduce defects. The effects of substrate surface energy upon the resulting morphologies could provide a useful for controlling the orientation of the morphologies. Selective etching can be used to remove one or more of the components in the system allowing for porous materials to be created. Some of these issues are further discussed in Appendix B.

As a result of the inability to achieve useful results from the electroclinic actuation of smectic C liquid crystalline phases, investigations have begun into the development and application of photo-responsive LC moieties. The photoisomerization of LCs containing azo functional groups leads to a significant change in the self-assembly behavior, allowing these materials to be used in actuation applications. These preliminary investigations are further discussed in Appendix C.

Appendix A Incorporation of Nanoparticles into Side Chain Liquid Crystalline Block Copolymers

A.1 Introduction

Recently there has been significant interest, both theoretical[1-3] an experimental[3-11], in the incorporation of nanoparticles into block copolymer systems. Control over the location of nanoparticles within the self-assembled nanostructures of block copolymer mesophase is desirable for many applications including magnetic nanoparticles for data storage, florescence imaging, catalytic surfaces, and molecular electronics such as light emitting diodes and photovoltaic devices[5, 6, 9]. It has been shown that both the size and surface chemistry of the nanoparticles relative to the length scales and the chemistries of the block copolymer matrix both are critical in determining the nature of the incorporation of nanoparticles within the block copolymer mesophase[12]. In this manner variations in the size and surface chemistries of nanoparticles have allowed for the location of nanoparticles within these nanostructures to be controlled[12] (See Figure A-1). Additionally, the block copolymer self-assembly can be manipulated through the resulting changes in volume fraction and interfacial effects resultant from nanoparticle incorporation.

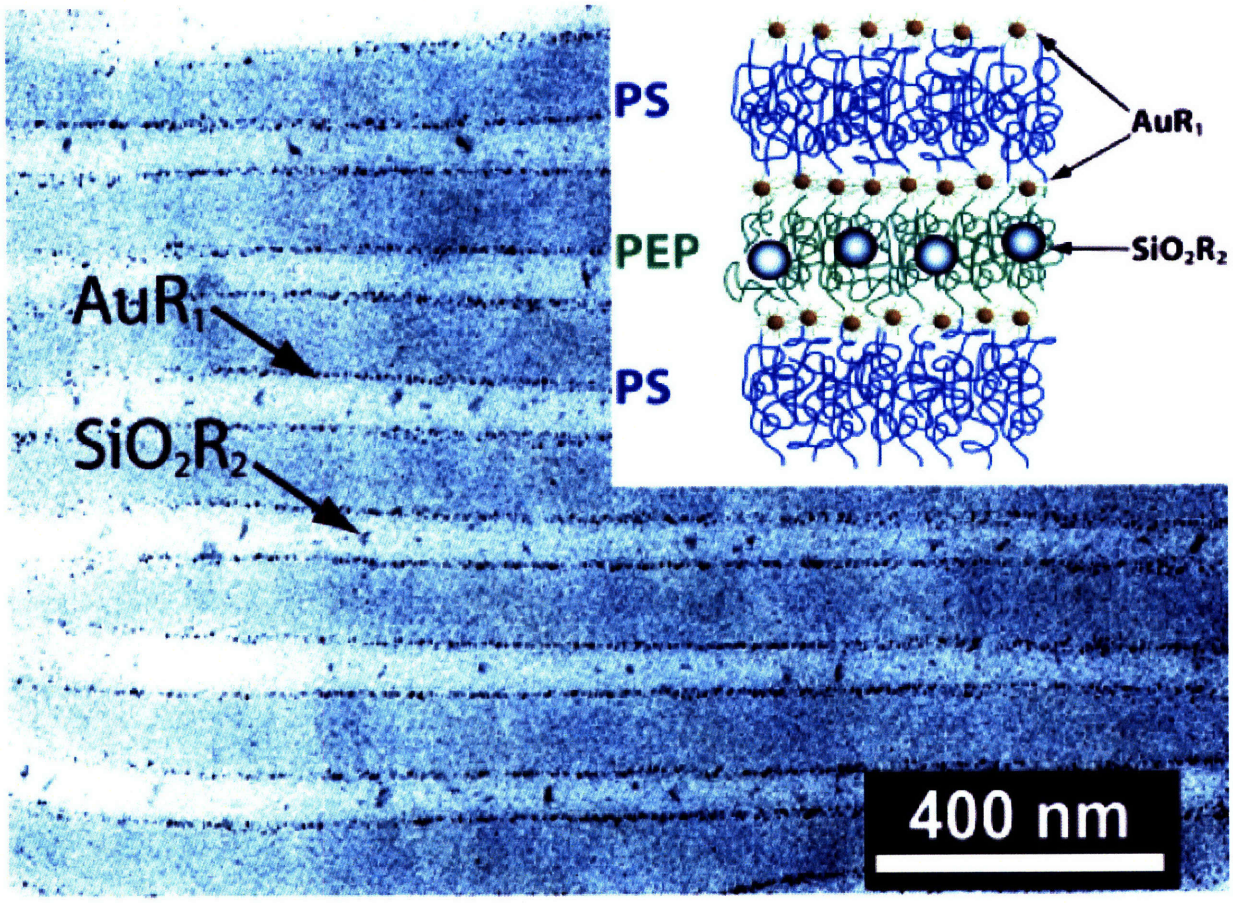

Figure A-1. TEM image of gold and silica nanocrystals self-assembling within a polystyrene-block-poly(ethylenepropylene), PS-PEP, block copolymer. Gold nanocrystals appear as dark spots along the IMDS; silica nanocrystals reside in the center of the PEP domain. Inset: Schematic of the particle distribution (size proportions are changed for clarity)[12].

The ability to actively alter the self-assembly of these systems would allow for the development of materials for a variety of sensing or switching applications[3, 11]. One approach to accomplish this goal is to alter the surface chemistry of the nanoparticle, leading to a change in the equilibrium location of the nanoparticle within the nanophase segregated block copolymer structure. This has been demonstrated by using activated alteration of the nanoparticle surface

chemistry, resulting in a change of the equilibrium location of the nanoparticle with in the block copolymer mesophase[13, 14]. An example of such surface chemistry is shown in Figure A-2.

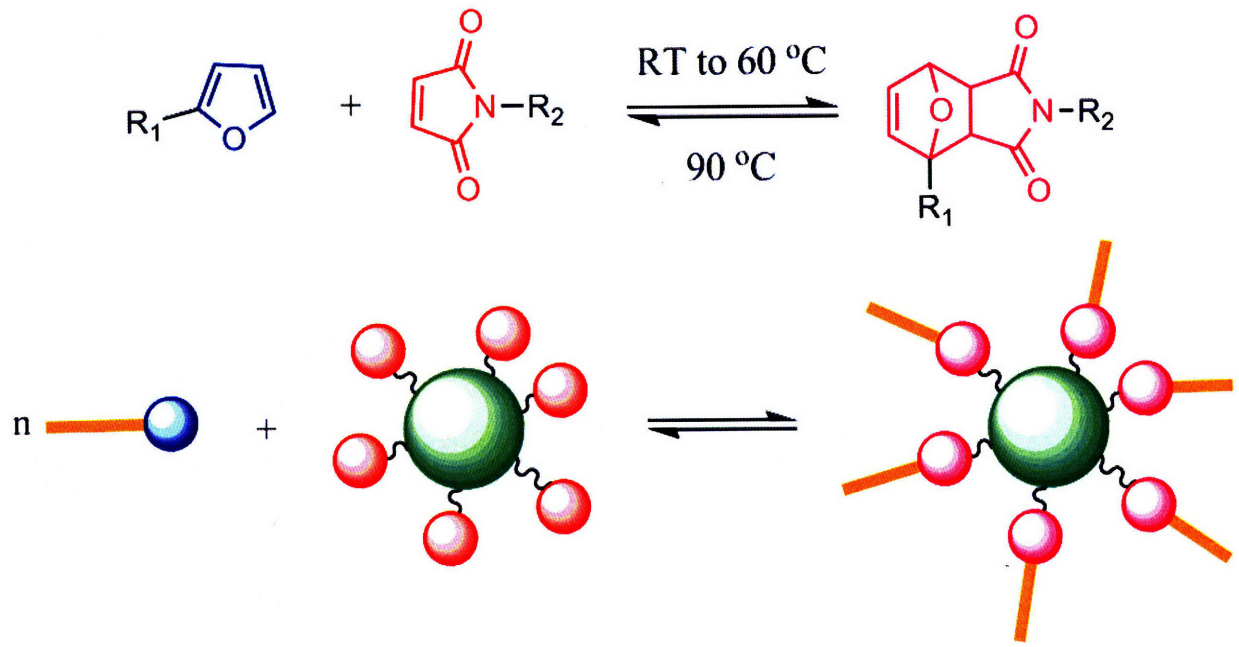

Figure A-2. Top: Reversible Diels-Alder chemistry. Bottom: Schematic of using Diels-Alder chemistry to alter the surface chemistry of a nanoparticle as a function of temperature[15].

However, this method relies on the ability to functionalize nanoparticles with specific functional groups that can respond to stimuli. It would be desirable to design a block copolymer system that can alter the nanoparticle location without modifying the nanoparticle itself. Liquid crystalline block copolymer systems offer a unique capability to achieve this goal. The preference for smectic LC mesophases to avoid interactions with curved interfaces on the length scale of the smectic layer spacing could be utilized to actively control the location of nanoparticles within a liquid crystalline block copolymer. When the LC mesophase is in the isotropic state, the interfacial interactions should dominate the self-assembly behavior. If the

surfaces of the nanoparticle and the block polymer are properly designed the nanoparticles will self-assemble within the siloxane based liquid crystalline domains. However, when the system is cooled into the smectic LC state, the unfavorable steric interactions between the spherical nanoparticles and the smectic layers should lead to exclusion of the nanoparticles and they will be driven to the inter material dividing surface (IMDS). This concept is illustrated in Figure A-3. This novel approach allows for actively manipulating the self-assembly of nanoparticles within a block copolymer without altering the surface chemistry of the nanoparticle, making this approach more versatile for a wide range of nanoparticles.

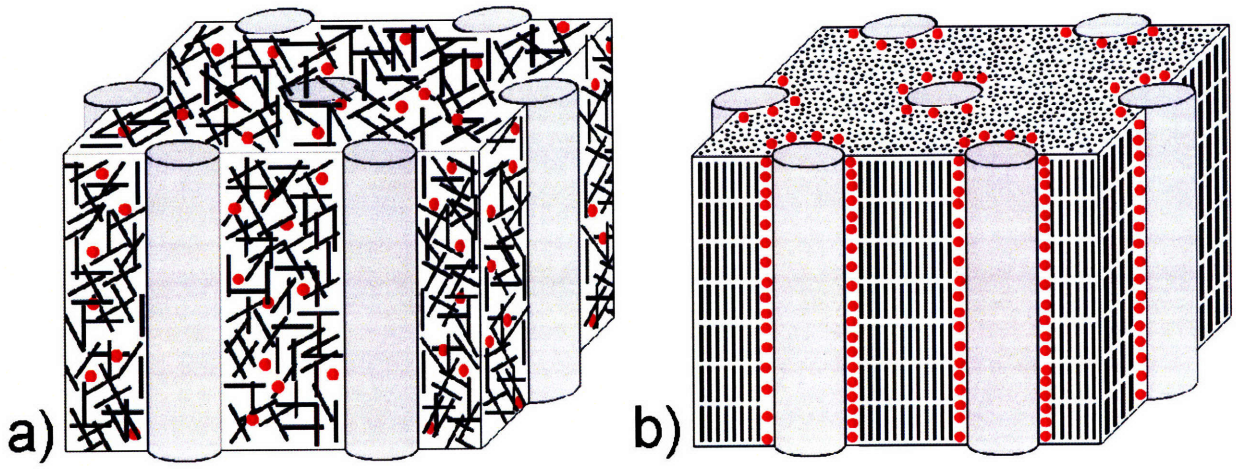

Figure A-3. Schematic of nanoparticle location within a block copolymer as a function of LC morphology. a) When the temperature is above the smectic to isotropic transition temperature the nanoparticles self-assemble within the liquid crystalline polymer domains, as the enthalpic interactions between the surface of the nanoparticle and the siloxane based liquid crystal are favorable. b) When the temperature is lowered the LC mesophase is in the smectic state and the nanoparticles are excluded from the siloxane based liquid crystalline polymer domains and assemble at the interface. In both cases the nanoparticles would not expect to be found within the polystyrene domains due to unfavorable interfacial interactions, and in case b) the polystyrene is below it's T_g before the cooling into the smectic state, thus there is not sufficient kinetic mobility for migration into the PS domains.

A.2 Results and Discussion

The first attempt to alter the self-assembly of nanoparticle containing liquid crystalline block copolymer systems was to synthesize a "soft" nanoparticle with surface chemistry that is tunable as a function of temperature through Diels-Alder chemistry. These nanoparticles were synthesized in collaboration with Rick Beyer and Philip Costanzo from the Army Research Lab (ARL) in Aberdeen, MD. These nanoparticles have a crosslinked siloxane core and PS ligands are attached through Diels-Alder linkages to the outer surface. This allows for the nanoparticles to present a surface of PS at lower temperatures, and a siloxane surface at higher temperatures. A schematic of this system is shown in Figure A-4. These nanoparticles were successfully integrated into the liquid crystalline block copolymer system. However, due to the similarity between the chemistry of the nanoparticles and the block copolymer matrix, it was not possible to image the nanoparticles with TEM due to the lack of electron density contrast.

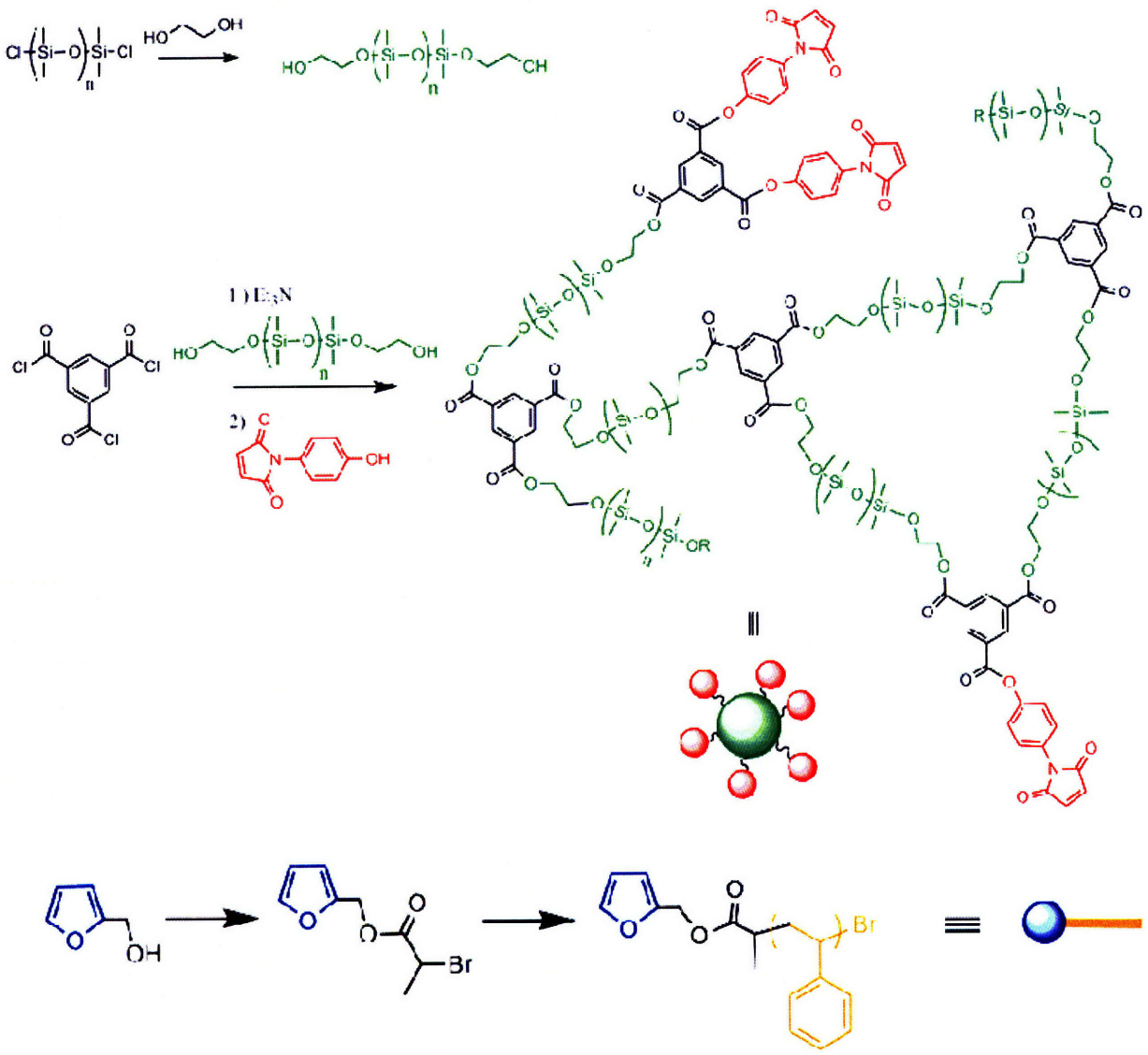

Figure A-4. Schematic of structure of soft nanoparticles with tunable surface chemistry. At lower temperatures the ligands are attached and the nanoparticle has a surface covered in polystyrene. At higher temperatures, the ligands detach from the crosslinked core and the nanoparticles have a siloxane based. Also see Figure A-2.

Two different nanoparticles were designed and synthesized in order to demonstrate the ability to manipulate the self-assembly of a nanoparticle within a liquid crystalline block copolymer, through changes in the morphology of the LC mesophase. The key issues in designing these nanoparticles were the size and surface chemistry of the nanoparticles, as well as a means of imaging the nanoparticle location. The nanoparticles should be between 2 and 10nm in size to allow them to be on the order of the smectic layer spacing, but less than the domain size of the block copolymer mesophase. The surface chemistry should be such that there are favorable enthalpic interactions between the nanoparticles and the siloxane based liquid crystalline polymer. Finally, it must be possible to image the nanoparticle location within the block copolymer.

The first choice was to functionalize gold nanoparticles, using thiol chemistry, with siloxane based ligands. The production of gold nanoparticles of various sizes has been widely studied and they can be purchased commercially. This approach ran in to difficulties when the functionalized surface became unstable during the annealing of the system and the unfunctionalized nanoparticles formed aggregates. I am currently exploring techniques, in collaboration with Rafal Mickiewicz to achieve a siloxane functionalized surface that is stable above 140°C, thus preventing aggregation of the gold nanoparticles. Due to the high electron density of gold atoms, the gold nanoparticles can be easily be imaged when incorporated into the side chain liquid crystalline block copolymer.

The second nanoparticle synthesized was a PAMAM based dendrimer functionalized with siloxane containing ligands. The synthesis was performed similar to the procedure described by Dvornic et. al.[4] using Michael addition of the siloxane groups to the outer amine functional groups of the dendrimer. A schematic of the synthesis and a 3-D model of the

resulting nanoparticle are shown in Figure A-5. The use this type of nanoparticle was designed to facilitate electron energy loss spectroscopy (EELS) of the system. The PS domains only conatin carbon and hydrogen, while the liquid crystalline polymer contains silicon and oxygen atoms, and the PAMAM based nanoparticles are the only species in the system containing nitrogen. It was hoped that the elemental differences in the different species would allow for imaging with EELS. However, while the liquid crystalline polymer could be distinguished from the PS domains, there was not a high enough of a nitrogen signal to detect the PAMAM nanoparticles.

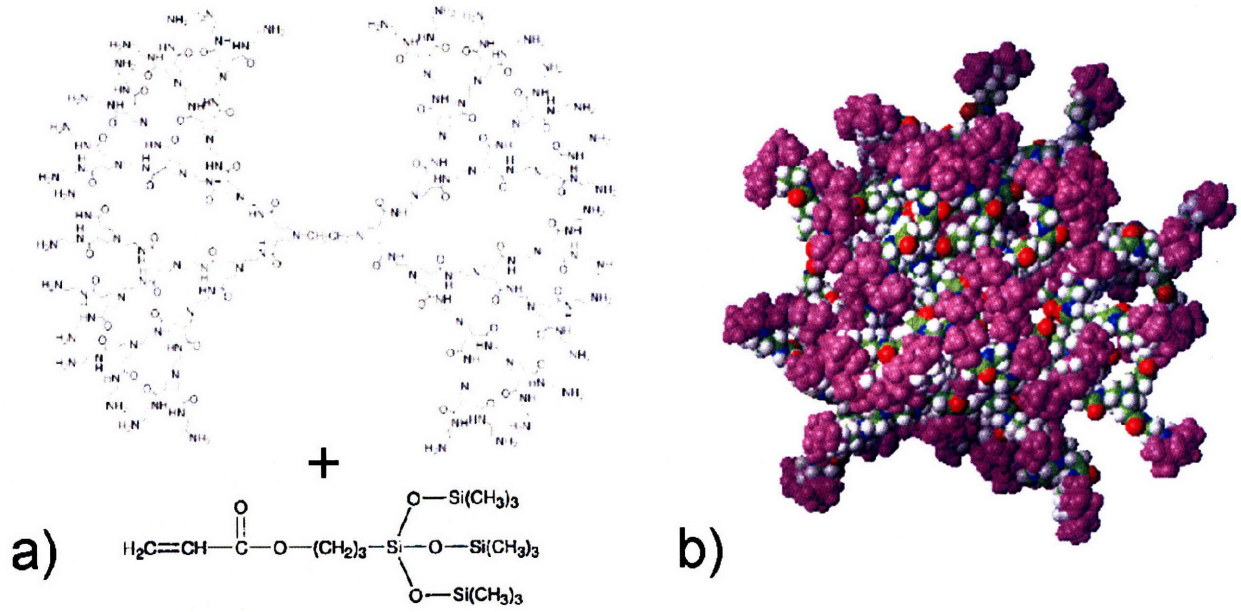

Figure A-5. a) Schematic of the attachment of siloxane based ligands to a PAMAM dendrimers. b) 3-D representation of the resulting nanoparticle, the entire siloxane groups are magenta, while the oxygen, nitrogen, carbon, and hydrogen atoms are represented in red, blue, green, and white, respectively.

A.3 Conclusions

Although none of the techniques described here were successful in demonstrating the tunability of nanoparticle location within a liquid crystalline block copolymer, the concept of utilizing the morphology of the LC mesophase to manipulate the self-assembly behavior of nanoparticle containing block copolymer systems is unique and shows promise. The challenge is to properly design a nanoparticle that can be imaged within the current system. Future work in this area includes the investigation into a siloxane surface functionalization of gold nanoparticles that is stable above the annealing temperatures required. Demonstration of this capability will allow for other more versatile liquid crystalline block copolymer systems to be developed that can be used in conjunction with a wide variety of nanoparticles.

A.4 References

1. Chen, S.; Guo, C.; Hu, G. H.; Liu, H. Z.; Liang, X. F.; Wang, J.; Ma, J. H.; Zheng, L., Dissipative particle dynamics simulation of gold nanoparticles stabilization by PEO-PPO-PEO block copolymer micelles. *Colloid and Polymer Science* **2007,** 285, (14), 1543-1552.

2. Huang, J.; Sun, D., Dynamic Monte Carlo simulation of aggregation of nanoparticles in the presence of diblock copolymer. *Journal of Colloid and Interface Science* **2007,** 315, (1), 355-362.

3. Kamyshny, A.; Magdassi, S., Nanoparticles in confined structures: formation and application. *Colloids and Interface Science Series* **2007,** 40, (6), 207-233.

4. Dvornic, P. R.; de Leuze-Jallouli, A. M.; Owen, M. J.; Perz, S. V., Radially layered poly(amidoamine-organosilicon) dendrimers. *Macromolecules* **2000,** 33, (15), 5366-5378.

5. Garcia, I.; Tercjak, A.; Zafeiropoulos, N. E.; Stamm, M.; Mondragon, I., Self-assembling nanomaterials using magnetic nanoparticles modified with polystyrene brushes. *Macromolecular Rapid Communications* **2007,** 28, (24), 2361-2365.

6. Haryono, A.; Binder, W. H., Controlled arrangement of nanoparticle arrays in block-copolymer domains. *Small* **2006,** 2, (5), 600-611.

7. Kim, B. J.; Bang, J.; Hawker, C. J.; Chiu, J. J.; Pine, D. J.; Jang, S. G.; Yang, S. M.; Kramer, E. J., Creating surfactant nanoparticles for block copolymer composites through surface chemistry. *Langmuir* **2007,** 23, (25), 12693-12703.

8. Lo, C. T.; Lee, B.; Pol, V. G.; Rago, N. L. D.; Seifert, S.; Winans, R. E.; Thiyagarajan, P., Effect of molecular properties of block copolymers and nanoparticles on the morphology of self-assembled bulk nanocomposites. *Macromolecules* **2007,** 40, (23), 8302-8310.

9. Park, S. C.; Kim, B. J.; Hawker, C. J.; Kramer, E. J.; Bang, J.; Ha, J. S., Controlled ordering of block copolymer thin films by the addition of hydrophilic nanoparticles. *Macromolecules* **2007,** 40, (22), 8119-8124.

10. Sanchez-Gaytan, B. L.; Cui, W. H.; Kim, Y. J.; Mendez-Polanco, M. A.; Duncan, T. V.; Fryd, M.; Wayland, B. B.; Park, S. J., Interfacial assembly of nanoparticles in discrete block-copolymer aggregates. *Angewandte Chemie-International Edition* **2007,** 46, (48), 9235-9238.

11. Schmidt, K.; Schoberth, H. G.; Ruppel, M.; Zettl, H.; Haensel, H.; Weiss, T. M.; Urban, V.; Krausch, G.; Boeker, A., Reversible tuning of a block - copolymer nanostructure via electric fields. *Nature Materials* **2008,** 7, (2), 142-145.

12. Bockstaller, M. R.; Lapetnikov, Y.; Margel, S.; Thomas, E. L., Size-selective organization of enthalpic compatibilized nanocrystals in ternary block copolymer/particle mixtures. *Journal of the American Chemical Society* **2003,** 125, (18), 5276-5277.

13. Costanzo, P. J.; Beyer, F. L., Thermoresponsive, optically active films based on Diels-Alder chemistry. *Chemistry of Materials* **2007,** 19, (25), 6168-6173.

14. Costanzo, P. J.; Beyer, F. L., Thermally driven assembly of nanoparticles in polymer matrices. *Macromolecules* **2007,** 40, (11), 3996-4001.

15. Beyer, R., Personal Communication. **2007.**

Appendix B Templated Self-Assembly and Selective Etching of Side Chain Liquid Crystalline Block Copolymer Thin Films

B.1 Introduction

In addition to the thin film studies described in Chapters 5 and 6, I initiated preliminary investigations into the templated self-assembly and selective etching of side chain liquid crystalline block copolymers in collaboration with Yeon-Sik Jung and Prof. Caroline Ross in the Department of Materials Science and Engineering at MIT.

A prime example of a block copolymer thin film application is their demonstrated utility as lithographic masks[1]. Ordered and oriented layers of microphase domains deposited onto a suitable substrate can be selectively etched via plasma, ozone, or wet chemical means, to remove one of the block components. Holes in the resulting mask can then be used to transfer the BCP motif pattern, via other etching or deposition steps, onto the substrate. More complex multi-component systems can be used to etch and remove one or more of the components allows for holes, pillars, or tubes to be created, examples of this are shown in Figure B-1.

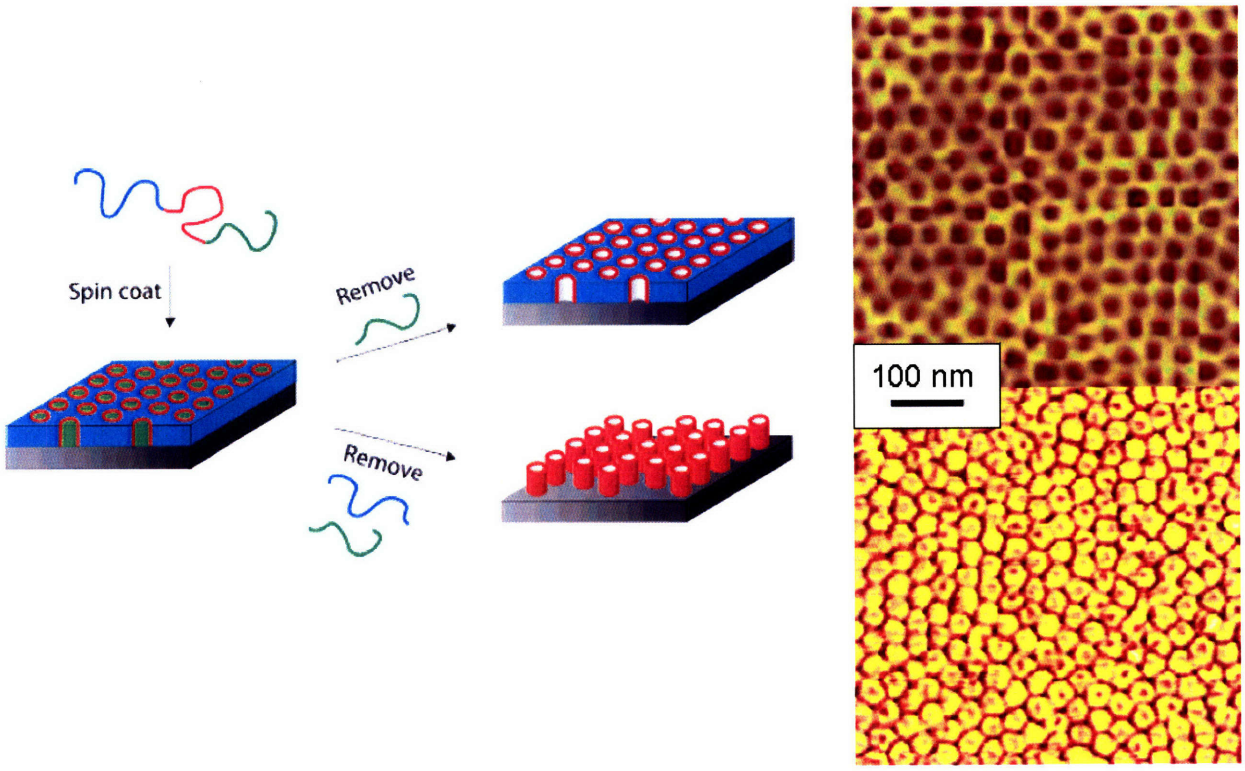

Figure B-1. Left: schematic representation of the envisioned nanotemplates from thin films of ABC triblock terpolymers. Right Top: AFM phase image of a polyisoprene-block-polysyrene-block-polylactic acid (PI-PS-PLA) thin film on a HMDS modified Si substrate after removal of the PLA block. Right Bottom: AFM phase image of a PI-PS-PLA thin film after removal of both the PLA and PI blocks.[2]

Templated self assembly (TSA) is a method of eliminating defects and inducing registration and orientation in thin films of materials using artificial topographical and/or chemically patterned templates. In contrast to conventional epitaxy in which the lattice of a thin film bears a well-defined relationship to the lattice of the underlying substrate, templates for TSA are not required to be crystalline materials. In the concept of templated self-assembly, the

topography and/or chemical pattern of the templates instead of the atomic lattice of the substrate are used to guide the organization of the component materials.

A variety of block copolymer systems can be ordered through templated self assembly, including spheres, cylinders and lamellae. Both topographical and chemical pattern templates can be used to create discrete domains (2-D patterning) or channels (1-D patterning). Figure B-2 shows a 1-D template of a cylindrical diblock copolymer. Increasing annealing times allow for greater register with the template. For topological templates the edge roughness has an effect on the extent of ordering. Defects in the self-assembled pattern by can be created and controlled by introducing irregularities into the patterns. In chemical templates the relative interfacial energy contrast between the block copolymer components and the surface template materials affects the driving forces for regular ordering. If the interfacial energy difference is low there is less driving force for ordering, increasing the interfacial energy contrast leads to a greater enthalpic driving force, and increased long range order. These templating methods can be applied to liquid crystalline block copolymers, however, the additional influence of the liquid crystalline mesophase must appropriately be taken into account. The liquid crystalline mesophase may have anchoring preferences with the IMDS and/or the substrate affecting the resulting orientation of the block copolymer to the substrate.

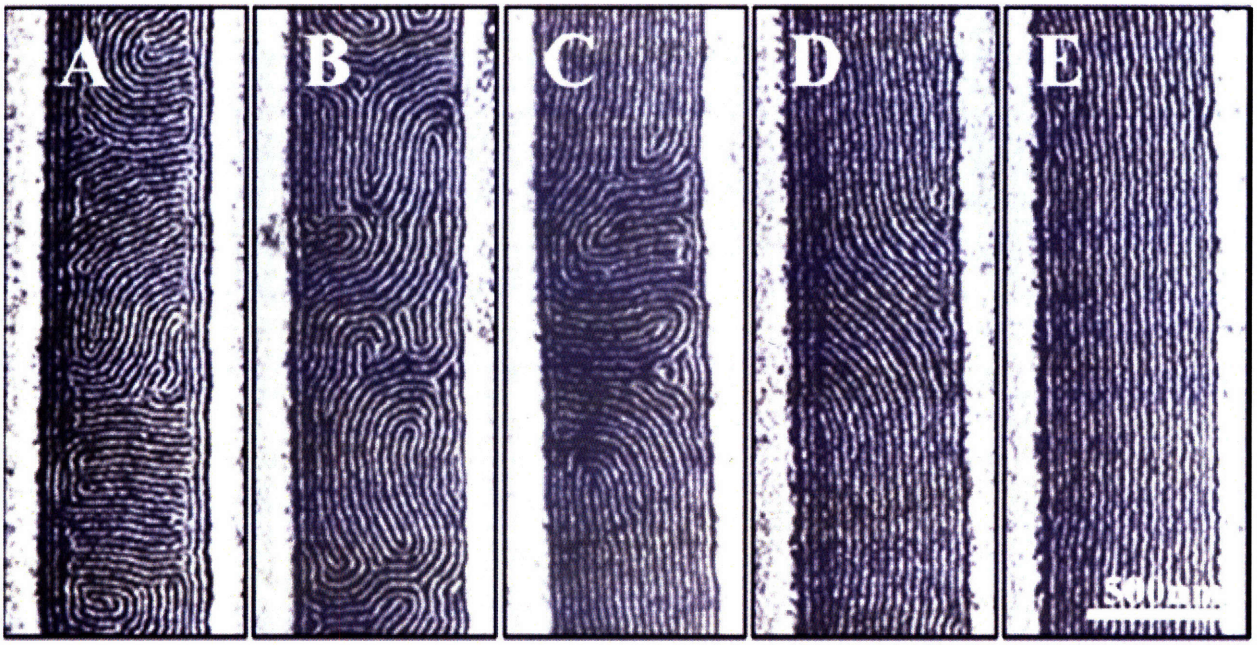

Figure B-2. AFM images of a cylindrical polystyrene-block-poly(ethylenepropylene) block copolymer in a 95nm deep and 600 nm wide template. Samples were annealed at 130°C for: a) 9, b) 14, c) 19, d) 24, and e) 33 hours[3].

B.2 Results and Discussion

Initial studies were performed by using a 10 minute O_2 reactive ion etch (RIE) to selectively remove the PS domains of the side chain liquid crystalline block copolymer thin films. The first thin film sample investigated was not annealed and display a perpendicular cylinder morphology. These films were chosen for their presence of PS domains at the air interface, this allows the O_2 reactive ion etch direct access to the PS without having to first penetrate a liquid crystalline polymer layer, as would be the case for an annealed thin film. The etch ratio is approximately 10:1 for PS and poly(dimethylsiloxane) PDMS, and the siloxane based liquid crystalline polymers in this study are expected to have similar properties in response

to the O_2 reactive ion etch. Figure B-3a shows an AFM phase image of a side chain liquid crystalline block copolymer thin film displaying PS cylinders perpendicular the substrate. After the O_2 RIE scanning electron microscopy (SEM) reveals a porous surface on the thin film. The selectively removal of the PS domains resulting in the pores and pits observed in the film; however, it is important to note that some of the liquid crystalline polymer has been degraded. Additionally, due to the lack of regular ordering in these as-cast films, the features are not well defined. The depth of the pores is not known, but due to the moderate etch selectivity and the poor ordering, it is not expected that all of the PS domains have been removed.

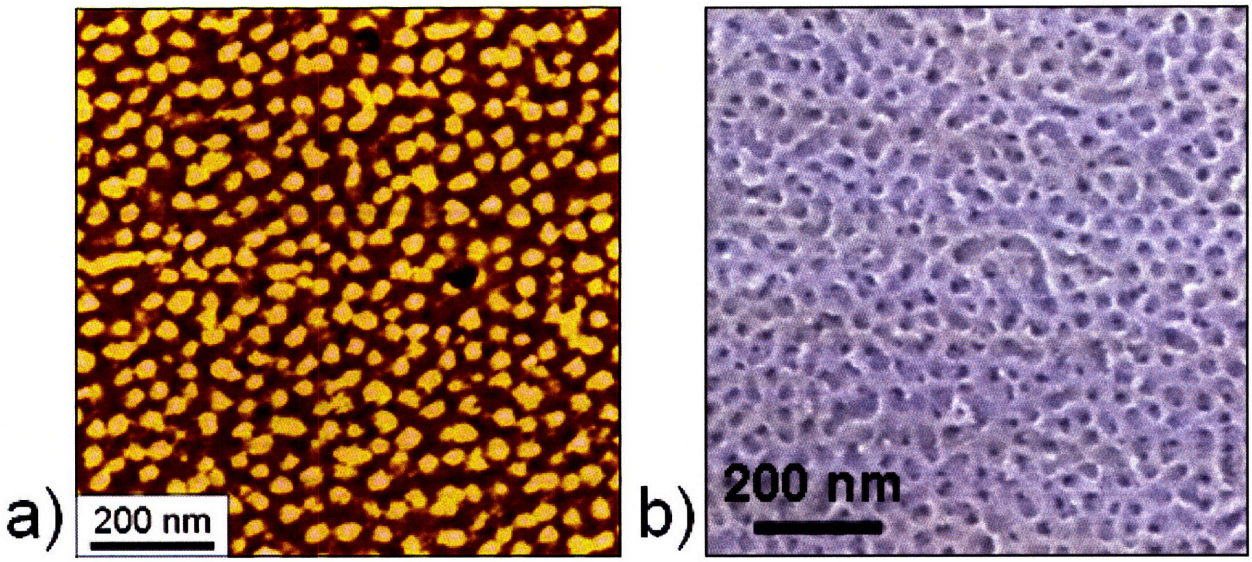

Figure B-3. a) AFM phase image of as-cast PS27-LCP_{4BPP4}79 displaying PS cylinders perpendicular the substrate. b) SEM image of the same film after O_2 reactive ion etch (RIE). The O_2 RIE selectively removes the PS domains, resulting in the porous film.

In order to obtain more well defined structures a two step etch process was used[4]. The first step is a very short CF_4 reactive ion etch (RIE) that removes the top siloxane segregation layer and another O_2 reactive ion etch step to remove PS domains. The removal of the top siloxane liquid crystalline polymer (LCP) layer allows the second O_2 RIE to have more direct access to the PS domains, and thus enhances the final etch quality. Figures B-4, B-5, and B-6 display a) AFM phase images of films before etching and b) SEM images of the same films after the two step etch. The samples shown in Figures B-4 and B-5 are as-cast films and the sample in Figure B-6 was annealed at 170°C for 36 hours. The need for the CF_4 RIE is particularly important for the films that have been annealed as the siloxane LCP layer at the air interface is more significant.

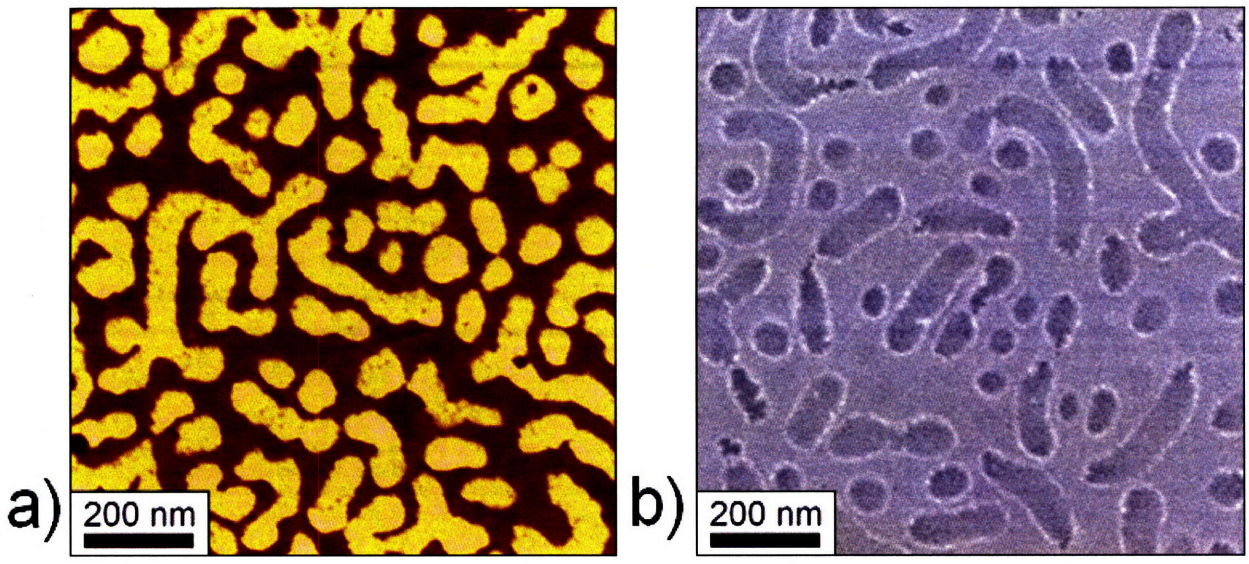

Figure B-4. a) AFM phase image of as-cast PS61-LCP_{4BPP4}101 which displays a lamellar/cylindrical transitional morphology in the as-cast film, this lamellar/cylindrical transitional morphology was also observed with TEM in bulk samples. b) SEM image of the same film after the two-step etch process, resulting in the porous film.

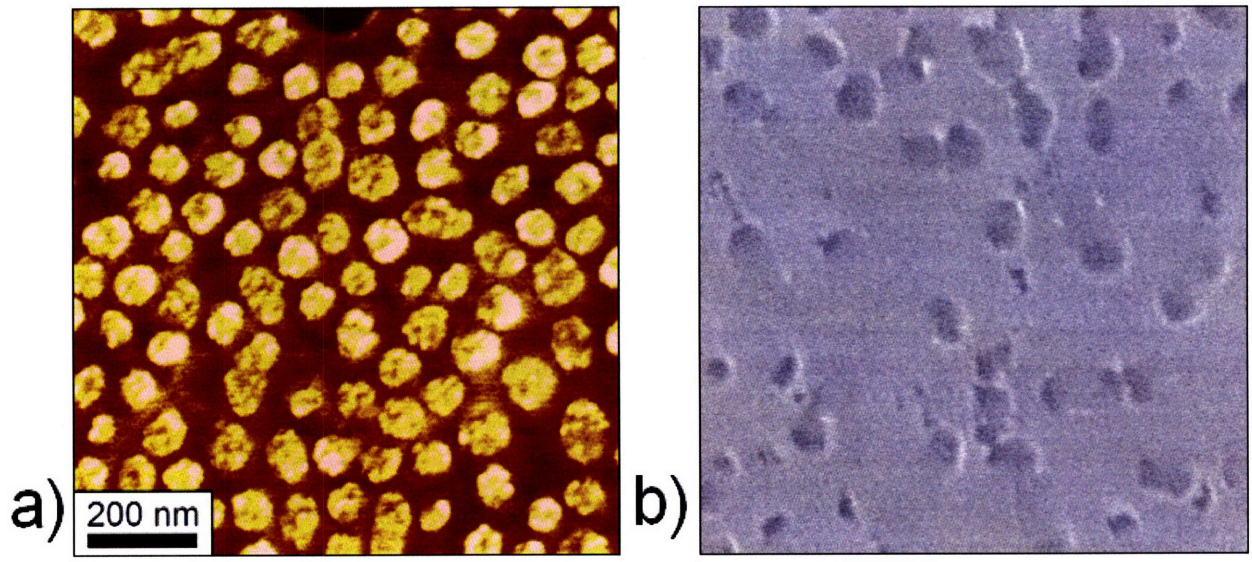

Figure B-5. a) AFM phase image of as-cast PS61-LCP$_{4BPP4}$123 thin film displaying PS cylinders perpendicular the substrate. b) SEM image of the same film after the two-step etch process, resulting in the porous film.

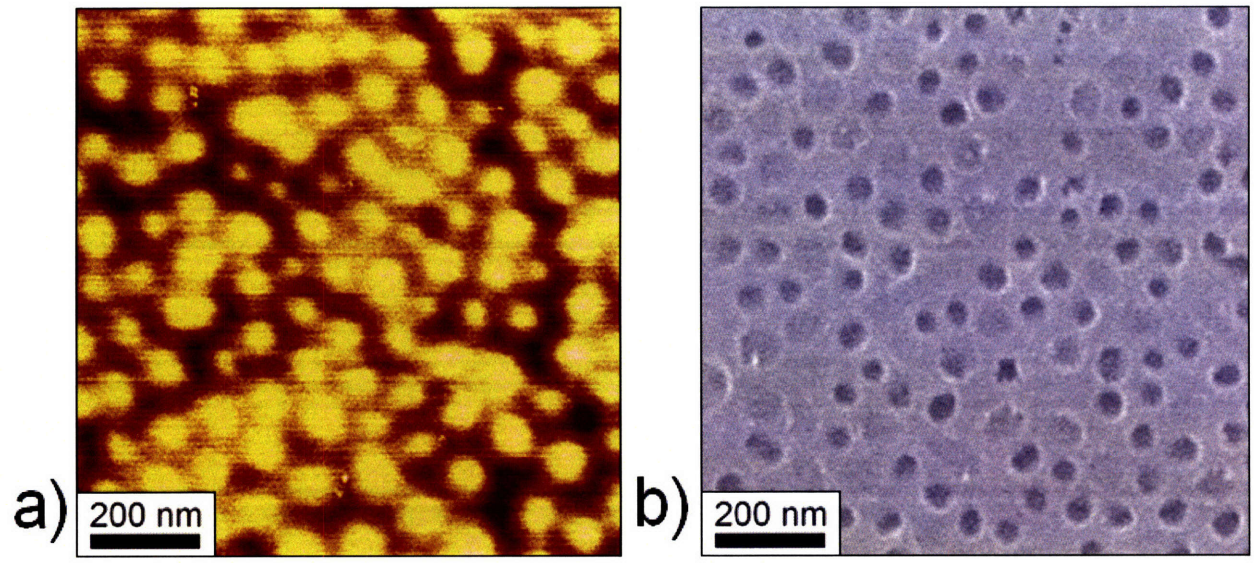

Figure B-6. a) AFM phase image of a PS61-LCP$_{4BPP4}$123 thin film that has been annealed for 36 hours at 170°C and displays PS cylinders perpendicular the substrate. b) SEM image of the same film after the two-step etch process, resulting in the porous film.

B.3 Conclusions

These initial results demonstrate the ability to selectively remove the PS domains in this system. Future work in this area includes etching of thin films that display lamellar morphologies and more regular ordering. Additionally, a more selective etch or the incorporation of an amorphous block that is easier to etch would be desirable. An investigation into the templated self-assembly of these side chain liquid crystalline polymers is currently underway.

B.4 References

1. Fasolka, M. J.; Mayes, A. M., Block copolymer thin films: Physics and applications. *Annual Review of Materials Research* **2001,** 31, 323-355.

2. Guo, S. W.; Rzayev, J.; Bailey, T. S.; Zalusky, A. S.; Olayo-Valles, R.; Hillmyer, M. A., Nanopore and nanobushing Arrays from ABC triblock thin films containing two etchable blocks. *Chemistry of Materials* **2006,** 18, (7), 1719-1721.

3. Sundrani, D.; Darling, S. B.; Sibener, S. J., Guiding polymers to perfection: Macroscopic alignment of nanoscale domains. *Nano Letters* **2004,** 4, (2), 273-276.

4. Jung, Y. S.; Ross, C. A., Orientation-Controlled Self-Assembled Nanolithography Using a Polystyrene-Polydimethylsiloxane Block Copolymer. *Nanoletters* **2007,** 7, (7), 2046-2050.

Appendix C Photoresponsive Side Chain Liquid Crystalline Block Copolymers

C.1 Introduction

Liquid crystalline (LCP) polymers have attracted recent interest due to their ability to combine the properties of small molecule liquid crystals and those of a polymer [1]. LC polymeric materials benefit over their small molecule LC counterparts from the mechanical integrity that the polymer component provides to the system. Additionally, by lightly crosslinking the polymer a liquid crystalline elastomer (LCE) can be created, allowing for the combination of the rubber elasticity of a polymer network with the properties of LC phases. Siloxane based LCEs present specific advantages associated with the very low T_g of the siloxane backbone, including a nearly ideal elastometric response and a low glass transition temperature, allowing for the materials to retain their properties over a wide temperature range, particularly at very low temperatures[2-4]. This class of materials can be designed to exhibit a conformational change on the molecular level in response to thermal, electrical or optical stimulation. The molecular conformational change can lead to a change in the mechanical properties or the dimensions of the materials, making them candidates for electromechanical, actuator, and shape memory applications. By incorporating a photoresponsive liquid crystalline moiety into a siloxane based polymer a new class of photo-responsive liquid crystalline polymers can be created that exhibit unique dynamic properties.

Photoresponsive LCEs present several potential advantages compared with LCEs that rely on thermotropic phase transitions or application of electric field. The utilization of photoisomerization of LC moieties in order to produce actuator materials was first proposed by deGennes[5]. This class of materials can be stimulated by exposure to particular wavelengths of electromagnetic radiation (light), resulting in molecular rearrangements that manifest the desired effects. For example, this class of materials has been used to create photoresponsive shape memory polymers [6]. The photoisomerization of incorporated azo moieties has been shown to disrupt the stability of nematic[7] and smectic[8] LC phases. There are several examples of molecules that have garnered great interest for their abilities to photoisomerize to generate useful properties in polymers [9-11].

Azobenzene moieties have been found to undergo a *trans* to *cis* photoisomerization upon exposure to 366nm light (see Figure C-1). The *trans* state is the equilibrium state and the moiety relaxes to the *trans* state with time. The return to the *trans* state can be accelerated with either heat, or stimulation with light > 540nm. If properly designed the azobenzene moiety in the *trans* state can be incorporate into a smectic LC phase, with little effect upon its stability. However, upon photoisomerization the azobenzene moiety in the *cis* state has been shown to significantly disrupt the smectic LC phase, leading to a change in the smectic to isotropic transition temperature (T_{iso}) [9, 12, 13]. An isothermal smectic to isotropic transition can be achieved when the T_{iso} is above operating temperature when the azo moiety in the *trans* state and the T_{iso} is lowered below the operating temperature when the azo moiety is switched to the *cis* state. By inducing a smectic to isotropic transition, significant molecular conformational changes can be achieved, leading to a change in the properties of the material (diffusivity, mechanical, and dimensional).

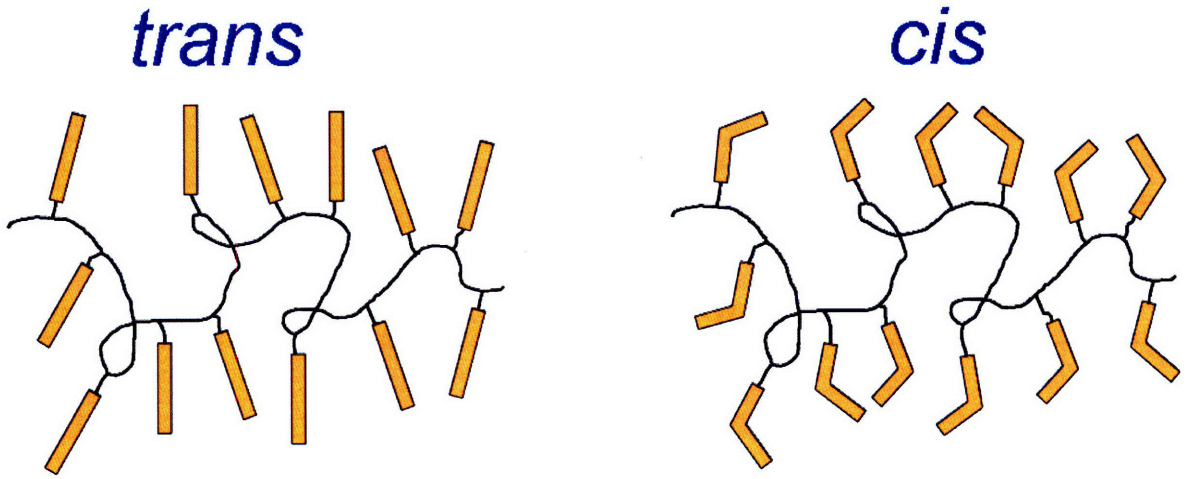

Figure C-1. A schematic of a side-chain liquid crystalline polymer in the *trans* and *cis* conformations.

Recently, photoisomerization of azo moieties has been utilized to create materials that exhibit a bending actuation due to the contraction or expansion of a material that has had one surface exposed to light [14-16]. This contraction of the surface of the material exposed to light results in internal stress in the material that leads to bending of the film (Figures C-2 and C-3).

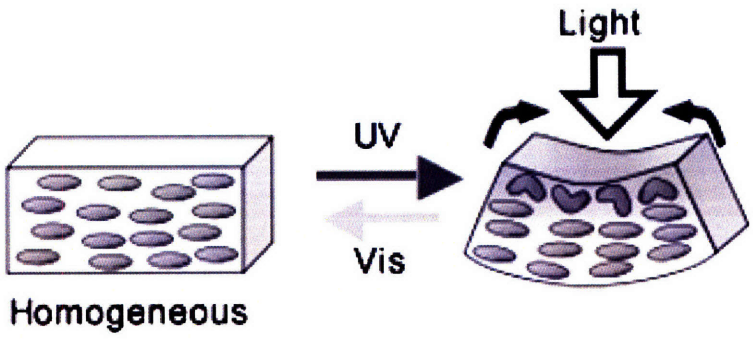

Figure C-2. A schematic of the bending actuation driven by exposure to UV light (366 nm) and return to upon exposure to visible light (>540 nm) [15].

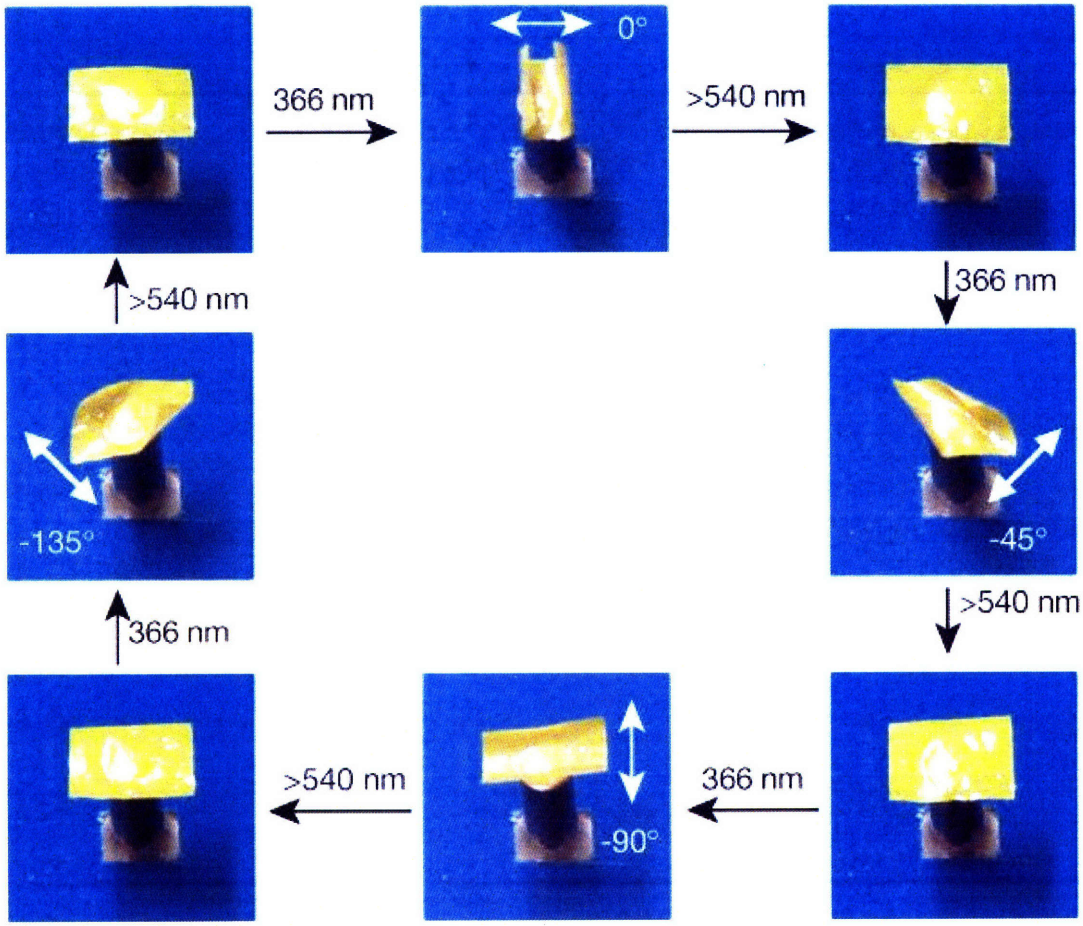

Figure C-3. An example of a LCE photoresponsive film that utilizes the photoisomerization of an azo moiety to create an actuation effect. Photographic frames of the film bending in different directions in response to irradiation by linearly polarized light of different angles of polarization (white arrows) at 366 nm, and being flattened again by visible light longer than 540 nm. The flat film (4.5 mm ×3 mm ×7 μm) lay on a copper stick fixed to a copper plate; a stage under the plate was set at 85 °C to control the temperature of the film, which was covered by a piece of blue paper. The bending time for the four different bending directions was within 10s, when the light intensity of 366-nm linearly polarized light was 3.5 mW cm^{-2} after exposure to visible light longer than 540 nm (547 nm, 24.2 mW cm^{-2}; 577 nm, 26.8 mW cm^{-2}), the bent film reverted to the flat state in about 10s [16].

Incorporation of these photoresponsive azo moieties, into the side chain liquid system previously developed, allows for the creation of a unique novel class of photoresponsive actuators, where the morphology and properties can be manipulated though stimulation with UV light. In this Chapter I will detail the synthesis of these materials and discuss the effects of UV photostimulation upon the morphology and mechanical properties of these materials. Additionally, by utilizing a liquid crystalline block copolymer system, nanotemplating of a thin film liquid crystalline mesophase can be achieved. This allows for the potential to selectively etch a liquid crystalline block copolymer thin film, leaving behind the nanotemplated liquid crystalline polymer mesophase. If the remaining liquid crystalline mesophase is crosslinked, a nanoporous LCE that can be photostimulated to create a tunable porosity membrane can be created. Further discussion of selective etching of thin films can be found in Appendix B.

C.2 Experimental

C.2.1 Instrumentation and Materials

400 MHz ^{1}H NMR spectra were obtained from a Bruker Avance-DPX400 NMR spectrometer and processed using Topspin 1.3. Molecular weights (MW) of polymers were made relative to a polystyrene standard on a Waters gel permeation chromatography (GPC) system equipped with 1 Styragel HT3 column (500-30,000 MW range), 1 Styragel HT4 column (5,000-600,000 MW range), 1 Styragel HT5 column (50,000-4·10^{6} MW range), a refractive index detector, and a UV detector (254 nm). Tetrahydrofuran (1 ml/min) was the mobile phase. A Thermal Advantage Instruments Q1000 was used for differential scanning calorimetry (DSC), the heating and cooling rate was 10°C min^{-1} in all cases. A Carl Zeiss Axioskop polarized light microscope was used in order to observe the presence of birefringence in the liquid crystalline

polymer. A Dymax Blue Wave 200 light source with a Thorlabs, Inc. FGUV W53199 ultraviolet (UV) filter in order to induce a *trans* to *cis* isomerization in the azo containing LC moieties. I would like to note an important safety precaution regarding the UV light source: **NEVER** look into the binoculars of the light microscope when the UV light is on. Any reflected UV light off of the sample (which is then magnified) could cause seriously damage to one's eyesight. Only use a camera to take images of samples in this case.

SAXS experiments were performed at the G1 beamline at the Cornell High Energy Synchrotron Source (CHESS). The wavelength of the X-rays was 1.239Å, and silver behenate was used to calibrate the sample to detector distance with a first order scattering vector of q of $1.076nm^{-1}$ (with $q = 4\pi \sin\theta/\lambda$ where 2θ is the scattering angle and λ is the wavelength). A slow-scan CCD-based X-ray detector, home built by Drs. M.W. Tate and S.M. Gruner of the Cornell University Physics Department, was used for data collection. All scattering data were processed using the commercially available software Polar. For the polarized light microscopy and small-angle X-ray scattering experiments a Linkam CSS450 shear cell was used to heat the samples. Rheological analysis was performed using an Advanced Rheometric Expansion System (ARES) at the Hatsopoulos Microfluids Laboratory at the Massachusetts Institute for Technology (MIT).

TLC plates (Whatman, AL SIL G/UV), hexanes, ethyl acetate, and methanol were purchased from VWR and used as received. Dichloromethane (DCM), toluene and tetrahydrofuran were taken from an Innovative Technology Pure-Solv 400 Solvent Purification System. Cyclohexane was purchased from Aldrich, dried over calcium hydride, degassed and vacuum distilled under nitrogen. Styrene was purchased from Aldrich, washed with 1M sodium hydroxide and dried over magnesium sulfate. Styrene was degassed and vacuum distilled from calcium hydride just prior to use. 1,1,3,3-Tetramethyldisiloxane, N, N-dimethylformamide

(DMF) and N, N-diisopropylcarbodiimide (DIPC) were purchased from Fluka. 4-Butoxyaniline was purchased from TCI America. 4-Hydroxy-4'-methoxyazobenzene was purchased from SJPC Fine Chemicals. 4-(Dimethylamino)pyridinium p-toluenesulfonate (DPTS) was prepared in the method of Moore and Stupp[17]. All other chemicals were purchased from Aldrich and used without further purification.

C.2.2. Synthesis of Photoresponsive Liquid Crystalline Block Copolymers

All polymer syntheses were performed under nitrogen following standard glovebox techniques. Syntheses of poly(styrene)-poly(vinylmethylsiloxane) homopolymer has been previously reported[18, 19]. All mesogen synthesis and mesogen-polymer attachment reactions were performed under nitrogen following standard Schlenk techniques. A detailed schematic of these reactions is provided in Figure C-4.

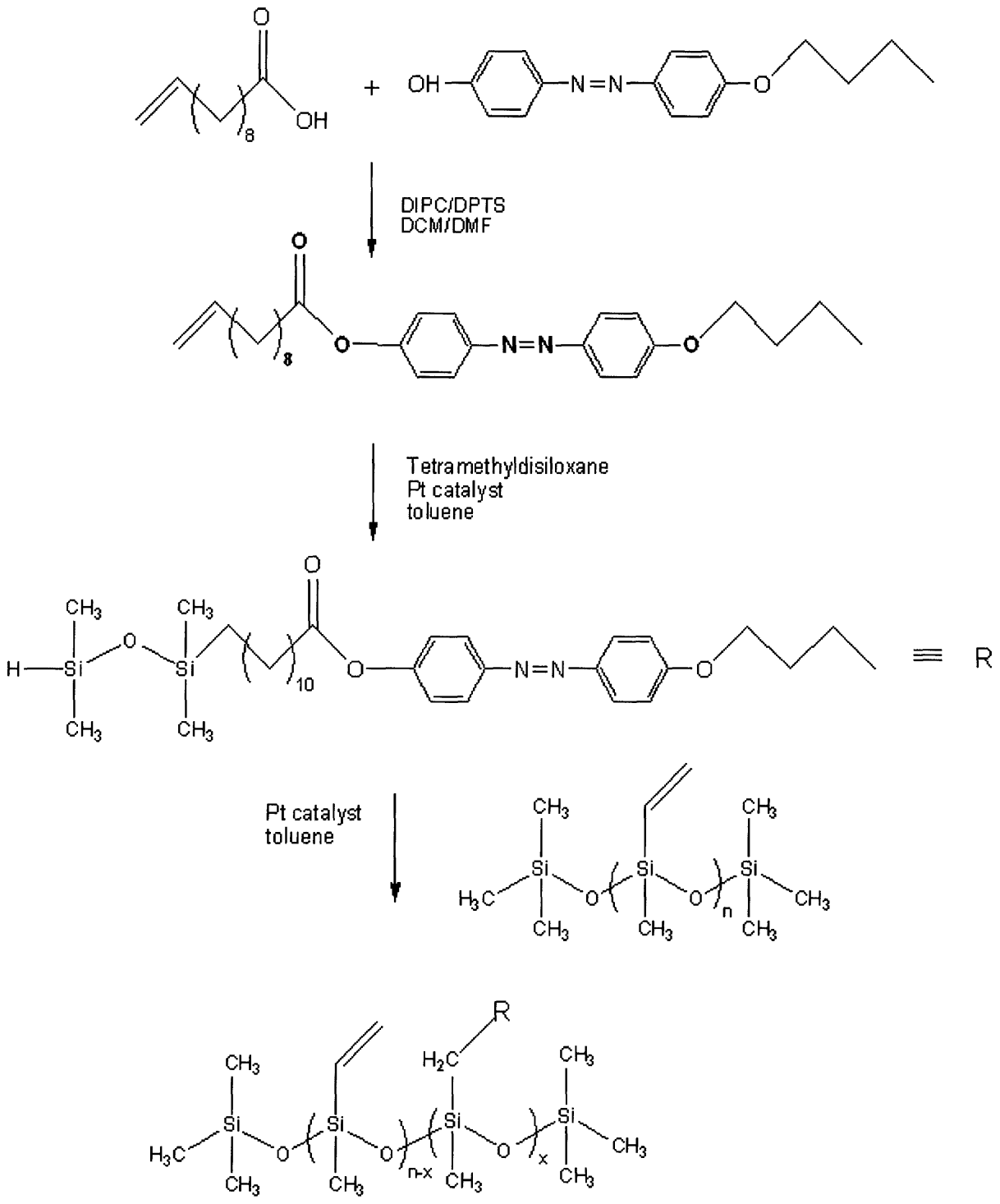

Figure C-4. Synthesis of a side chain liquid crystalline polymer with an azobenzene moiety, where: (x/n) 100% is the attachment percent.

4-Butoxy-4'-hydroxyazobenzene (1) was synthesized following the exact procedure detailed by Vanoppen et al, with 4-butoxyaniline as starting material[20]. No recrystallization was necessary. Yield: 15.68 g, 58.00 mmol, 100.0%. ^{1}H NMR ($CDCl_3$) (δ): 0.91 (t, 3H, –$OCH_2CH_2CH_2CH_3$), 1.45 (m, 2H, –$OCH_2CH_2CH_2CH_3$), 1.71 (m, 2H, –$OCH_2CH_2CH_2CH_3$), 4.02 (t, 2H, –$OCH_2CH_2CH_2CH_3$), 6.93 (d, 2H, –$ArH_2O(CH_2)_3CH_3$) 7.08 (d, 2H, –ArH_2OH), 7.75 (q, 4H, –$ArH_2N{=}NArH_2$–).

4-[(4-butoxyphenyl)azo]phenyl ester 4-pentenoic acid (2) In a 250 ml round bottle pentenoic acid (2.55 ml, 25.0 mmol), 4-butoxy-4'-hydroxyazobenzene **(1)** (6.76 g, 25.0 mmol), and 4-(dimethylamino)pyridinium p-toluenesulfonate (DPTS) (1.84 g, 6.3 mmol) were dissolved in 90 ml DCM and 14 ml DMF. N, N-diisopropylcarbodiimide (DIPC) (4.65 ml, 30.0 mmol) was added to the resulting dark brown solution. The reaction was stirred at room temperature under nitrogen for 24 h, filtered to remove urea, washed 3 times with 0.1 M hydrochloric acid, twice with brine, and dried with magnesium sulfate. Solvent was removed via rotatory evaporation. The resulting dark brown solid was further purified via column chromatography on silica gel (7:1 hexanes: ethyl acetate). Bright orange solid was obtained as final product. Yield: 5.19 g, 14.70 mmol, 80.0%. ^{1}H NMR ($CDCl_3$) (δ): 0.97 (t, 3H, –$OCH_2CH_2CH_2CH_3$), 1.49 (m, 2H, –$OCH_2CH_2CH_2CH_3$), 1.77 (m, 2H, –$OCH_2CH_2CH_2CH_3$), 2.50 (m, 2H, –$COOCH_2CH_2$–), 2.68 (t, 2H, –$COOCH_2CH_2$–), 4.02 (t, 2H, –$OCH_2CH_2CH_2CH_3$), 5.10 (q, 2H, –$CH{=}CH_2$), 5.89 (m, 1H, –$CH{=}CH_2$), 6.97 (d, 2H, –$ArH_2O(CH_2)_3CH_3$), 7.19 (d, 2H, –ArH_2COO–), 7.87 (t, 4H, –$ArH_2N{=}NArH_2$–).

4-[(4-butoxyphenyl)azo]phenyl ester 5-(1,1,3,3-tetramethyldisiloxanyl)valeric acid (3) In a 200 ml round bottle a mixture of tetramethyldisilane (22.2 ml, 125.7 mmol) and toluene

(32 ml) was stirred under nitrogen at 60°C. In a separate batch vinyl mesogen intermediate **(2)** (2.22 g, 6.3 mmol) was dissolved in 15 ml toluene. 12 drops (~0.08 ml) of the hydrosilylation catalyst platinum(0)-1,3-divinyl-1,1,3,3-tetramethyldisiloxane complex in xylene (Pt ~2%) was added to the mesogen solution, and the resulting orange solution added dropwise to the stirring silane/toluene mixture. The entire reaction mixture was stirred under nitrogen at 60°C for 24 h. Solvent was removed via rotatory evaporation. Bright orange solids were obtained after column chromatography (9:1 hexanes: ethyl acetate). Yield: 2.00 g, 5.69 mmol, 90.3%. ^{1}H NMR ($CDCl_3$) (δ): 0.08 (s, 6H, $-CH_2Si(CH_3)_2OSi(CH_3)_2H$), 0.17 (s, 6H, $-CH_2Si(CH_3)_2OSi(CH_3)_2H$), 0.60 (t, 2H, $-CH_2Si-$), 0.98 (t, 3H, $-OCH_2CH_2CH_2CH_3$), 1.49 (m, 4H, $-OCH_2CH_2CH_2CH_3$ + $-COO(CH_2)_2CH_2CH_2-$), 1.79 (m, 4H, $-OCH_2CH_2CH_2CH_3$ + $-COOCH_2CH_2(CH_2)_2-$), 2.58 (t, 2H, $-COOCH_2(CH_2)_3-$), 4.03 (t, 2H, $-OCH_2CH_2CH_2CH_3$), 4.69 (m, 1H, Si*H*), 6.99 (d, 2H, $-ArH_2O(CH_2)_3CH_3$), 7.20 (d, 2H, $-ArH_2COO-$), 7.89 (t, 4H, $-ArH_2N{=}NArH_2-$).

4-[(4-butoxyphenyl)azo]phenyl ester 10-undecenoic acid (4) was synthesized following exact procedure as **(2)**, with 4-butoxy-4'hydroxyazobenzene and 10-undecenoic acid as major starting materials. Bright orange solids were obtained from column chromatography on silica gel (8:1 hexane: ethyl acetate). Yield: 3.71 g, 8.50 mmol, 50.1%. ^{1}H NMR ($CDCl_3$) (δ): 0.98 (m, 2H, $-OCH_2CH_2CH_2CH_3$), 1.21-1.56 (m, 12H, $-COOCH_2CH_2(CH_2)_6-$) 1.78 (m, 4H, $-OCH_2CH_2CH_2CH_3$ + $-COOCH_2CH_2(CH_2)_6-$), 2.03 (m, 2H, $-OCH_2CH_2CH_2CH_3$), 2.56 (t, 2H, $-COOCH_2(CH_2)_7-$), 4.02 (t, 2H, $-OCH_2CH_2CH_2CH_3$), 4.95 (q, 2H, $-CH{=}CH_2$), 5.80 (m, 1H, $-CH{=}CH_2$), 6.98 (d, 2H, $-ArH_2O(CH_2)_3CH_3$), 7.20 (d, 2H, $-ArH_2COO-$), 7.88 (t, 4H, $-ArH_2N{=}NArH_2-$).

4-[(4-butoxyphenyl)azo]phenyl ester 11-(1,1,3,3-tetramethyldisiloxanyl)undecanoic acid (5) was synthesized following the exact procedure as **(3)**, with vinyl intermediate **(4)** as the

major starting material. Bright orange solids were obtained from column chromatography on silica gel (9:1 hexane: ethyl acetate). Yield: 2.83 g, 5.00 mmol, 58.3%. ^{1}H NMR ($CDCl_3$) (δ): 0.04 (s, 6H, –Si(CH_3)$_2$OSi(CH_3)$_2$H), 0.14 (s, 6H, –Si(CH_3)$_2$OSi(CH_3)$_2$H), 0.51 (t, 2H, –COO(CH_2)$_9$CH_2–), 0.97 (t, 3H, –OCH_2CH_2CH_2CH_3), 1.21-1.45 (m, 14H, –COOCH_2CH_2(CH_2)$_7$CH_2–), 1.50 (m, 2H, –OCH_2CH_2CH_2CH_3), 1.77 (m, 4H, –OCH_2CH_2CH_2CH_3 + –COOCH_2CH_2(CH_2)$_8$–), 2.56 (t, 2H, –COOCH_2(CH_2)$_9$–), 4.03 (t, 2H, –OCH_2CH_2CH_2CH_3), 4.65 (m, 1H, –SiH), 6.98 (d, 2H, –ArH_2O(CH_2)$_3$CH_3), 7.19 (d, 2H, –ArH_2COO–), 7.88 (t, 4H, –ArH_2N=NArH_2–).

4-[(4-methoxyphenyl)azo]phenyl ester 10-undecenoic acid (6) was synthesized following the same procedure as **(2)**, with 10-undecenoic acid and 4-hydroxy-4'-methoxyazobenzene as major starting materials. Bright orange solids were obtained from column chromatography on silica gel (dichloromethane). Yield: 17.16 g, 43.50 mmol, 87.0%. ^{1}H NMR ($CDCl_3$) (δ): 1.03-1.47 (m, 10H, –COOCH_2CH_2(CH_2)$_5$CH_2–), 1.75 (m, 2H, –COOCH_2CH_2(CH_2)$_6$–), 2.03 (m, 2H, –COO(CH_2)$_7$CH_2–), 2.56 (t, 2H, –COOCH_2(CH_2)$_7$–), 3.87 (s, 3H, –OCH_3), 4.96 (q, 2H, –CH=CH_2), 5.80 (m, 1H, –CH=CH_2), 7.00 (d, 2H, –ArH_2OCH_3), 7.20 (d, 2H, –ArH_2COO–), 7.90 (d, 4H, –ArH_2N=NArH_2–).

4-[(4-methoxyphenyl)azo]phenyl ester 11-(1,1,3,3-tetramethyldisiloxanyl) undecanoic acid (7) was synthesized following exact procedure as **(3)**, with vinyl intermediate **(6)** as the major starting material. Bright orange solids were obtained from column chromatography on silica gel (7:1 hexane: ethyl acetate). Yield: 3.23 g, 6.12 mmol, 48.2%. ^{1}H NMR ($CDCl_3$) (δ): 0.06 (s, 6H, –Si(CH_3)$_2$OSi(CH_3)$_2$H), 0.16 (s, 6H, –Si(CH_3)$_2$OSi(CH_3)$_2$H), 1.23-1.47 (m, 16H, –COOCH_2CH_2(CH_2)$_8$Si–), 1.75 (m, 2H, –COOCH_2CH_2(CH_2)$_8$Si–), 2.57 (t,

2H, –COOCH_2(CH_2)$_9$Si–), 3.86 (s, 3H, –OCH_3), 4.68 (m, 1H, Si*H*), 7.00 (d, 2H, –ArH_2OCH$_3$), 7.21 (d, 2H, –ArH_2COO–), 7.90 (d, 4H, –ArH_2N=NArH_2–).

All attachment of SiH-tipped liquid crystals to PS-PVMS diblock copolymers and PVMS homopolymers follow identical hydrosilylation and workup procedures. The attachment of mesogen **(7)** to 70:30 molar ratio PS-PVMS diblock copolymer is provided as example.

In a 50 ml round bottle SiH-tipped mesogen **(7)** (2.011 g, 3.80 mmol) is dissolved in 6 ml toluene. The resulting bright orange solution is stirred under nitrogen at 60°C. In a separate 20 ml vial the PS-PVMS diblock copolymer (0.500 g) is dissolved in 3 ml toluene. To the polymer solution 7 drops (~0.04 ml) of the previously mentioned Pt catalyst was added, and the clear polymer/Pt solution added dropwise to the stirring mesogen solution. The reaction was stirred constantly under nitrogen at 60°C. A portion of the reaction (~0.2 ml) was pulled approximately every 24 h and precipitated into stirring, room temperature methanol. The resulting white solids were filtered, re-dissolved in toluene, re-precipitated into methanol and filtered again to remove all excess mesogen. % attachment of mesogen onto polymer increases linearly with time (~1%/h) and has been confirmed via ^{1}H NMR. Attachment rate is highly dependent upon reaction concentration and amount of Pt catalyst used. ^{1}H NMR data correspond to previous attachment reactions and have all been previously reported[18].

C.3 Results and Discussion

The polymer that will be discussed in this section is a PVMS homopolymer with a number average molecular weight (M_n) of 14,800 g/mol and a LC attachment percent of 67%, yielding a polymer with a total molecular weight of 80,700 g/mol, and will be referred to for the

rest of this section as: $LCP_{azo}81$. Differential scanning calorimetry (DSC) was used in order to identify the smectic to isotropic transition temperature (T_{iso}) of the liquid crystalline polymer. The T_{ISO} for $LCP_{azo}81$ measured via DSC was 124°C. Polarized light microscopy was used to confirm the T_{iso} and to investigate the morphological response to UV stimulation. A room temperature, focal conic textures were observed, indicating the presence of a smectic liquid crystalline phase. The liquid crystalline polymers were then heated until birefringence was no longer observed, indicating a transition from a smectic liquid crystalline phase to the isotropic phase. In all cases agreed this temperature corresponded to the T_{iso} determined with DSC.

The response to UV light was investigated by heating the samples to temperatures a few degrees below the T_{iso}. The samples were then exposed to UV light from a Dymax Blue Wave 200 light source with a Thorlabs, Inc. FGUV W53199 filter. In most cases, full or partial disappearance of birefringence was observed upon stimulation with UV light. The UV light was subsequently removed and the birefringence returned indicating reversibility of the system. It should be noted that these experiments are less than ideal, as the incident white light used to investigate the birefringence of the materials includes wavelengths > 540 nm, which are know to accelerate the relaxation from the *cis* to the equilibrium *trans* conformation. Thus, when the materials are stimulated with UV light they are also exposed to the white light from the microscope. As a reminder, to avoid possible damage to the eyes never look into the binoculars when performing experiments with UV light, always use the camera to take images and monitor the transitions.

Small-angle X-ray scattering (SAXS) was used in order to further characterize the morphological response of the liquid crystalline polymers to UV stimulation. SAXS provides information regarding the periodicity of the smectic layers, and has the additional advantage of

not requiring light with a wavelength > 540 nm, that can hinder the *trans* to *cis* isomerization. With no UV light, each liquid crystal film was heated using a Linkam CSS450 shear cell to a temperature immediately below the smectic to isotropic transition temperature, 120°C, and POM. Then UV light was applied while the temperature is held constant for 15 minutes. A decrease in the scattering corresponding to the smectic layer spacing was observed upon exposure to UV light (see Figure C-5). The *trans* to *cis* isomerization, upon exposure to UV light, destabilizes the smectic mesophase, which accounts for the observed decrease in scattering.

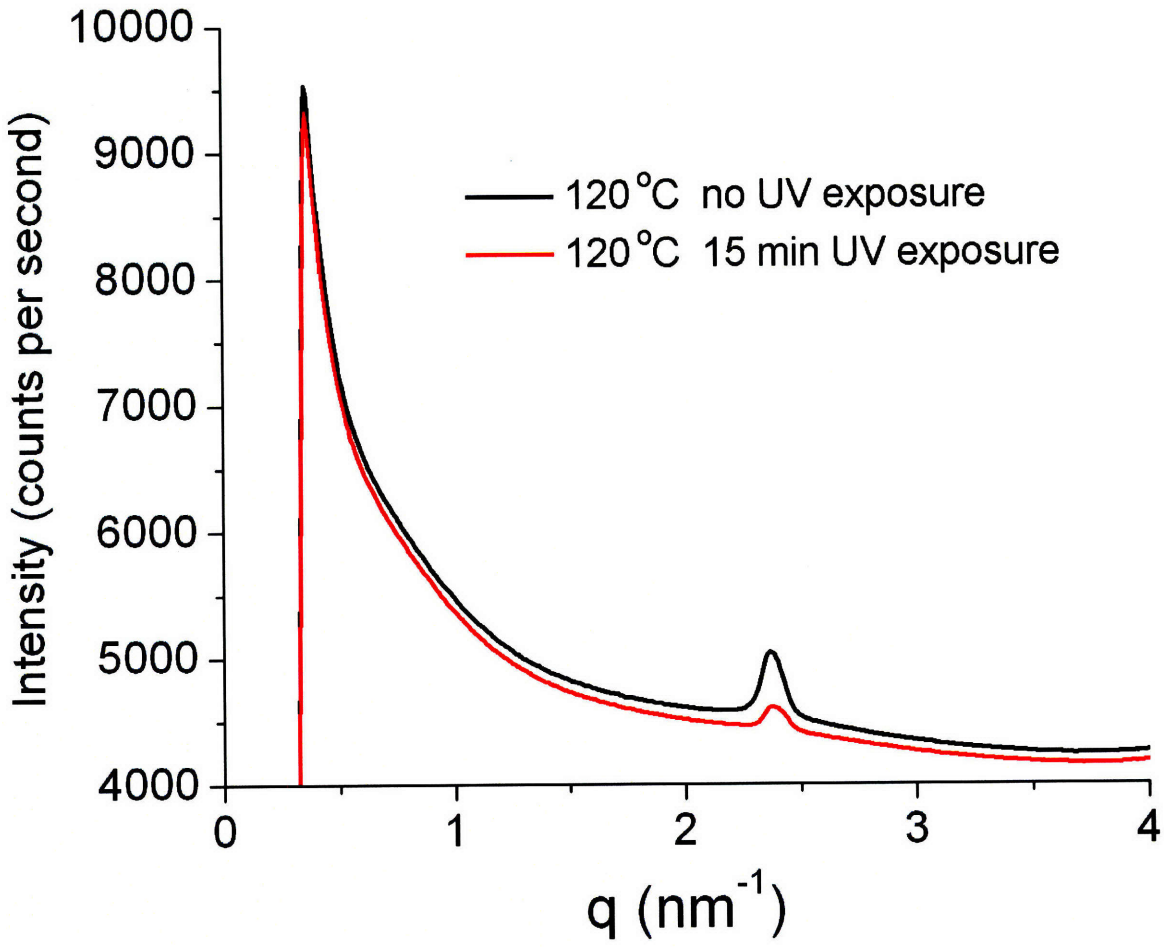

Figure C-5. 1-D Small-angle X-ray scattering profile of $LCP_{azo}81$. The sample was heated to 120°C for 15 minutes with no exposure to UV light (black). The sample was then exposed to UV light at 120°C for 15 minutes (red).

UV light rheometery experiments were performed around the optimal transition temperatures observed in the SAXS experiments. In these experiments, the sample was allowed to equilibrate during an oscillatory shear experiment, the UV light was then applied inducing a decrease in the shear modulus (G'). Once the system reached a steady state the UV light was then removed and the experiment was continued until the system stabilized once again. A significant decrease in the shear modulus of the material was observed upon exposure to UV light (see Figure C-6). This property change is highly reversible as the shear modulus sharply increases upon removal of the UV light, and nearly reaches it's original value. For the sample tested in this experiment the sample area was smaller that the area of the parallel plates, therefore the magnitude of the shear modulus could not be calculated. Further studies are currently underway to systematically evaluate the response of these materials as a function of LC attachment percent and temperature. Initial results indicate that the response is diminished when the LC attachment or temperature are decreased.

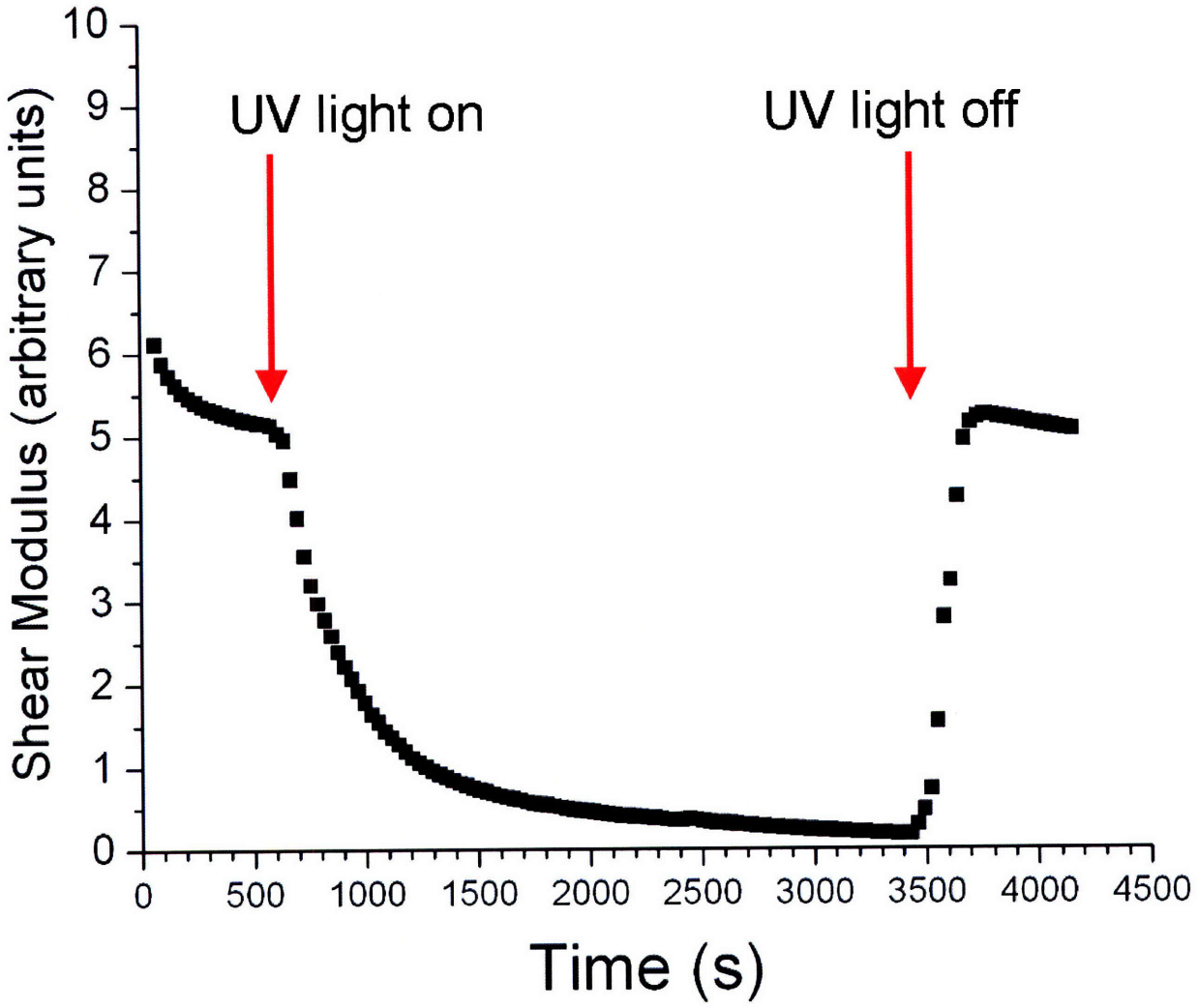

Figure C-6. Plot of the shear modulus as a function of time and stimulation with UV light. The shear modulus decreases by nearly an order of magnitude when exposed to UV light within ~ 15 minutes. Upon removal of the UV light the shear modulus returns to it's original value within 5 minutes. This experiment was preformed at 100°C.

C.4 Conclusions

This initial study demonstrates the ability to reversibly alter the morphology of side chain liquid crystalline polymers containing azo moieties through stimulation with UV light. The UV light induces a *trans* to *cis* isomerization, which disrupts the smectic LC mesophase. This morphological rearrangement can be used to manipulate the mechanical properties of the material. In this study we demonstrated a drop in the shear modulus of an order of magnitude. Future work includes investigating the effects of LC architecture and attachment percentage upon the responsive properties of this class of materials as well as the temperature dependence of the response. The low T_g siloxane backbone is an important component of these materials, enabling for elastomeric response at or near room temperature.

C.5 References

1. Mayer, S.; Zentel, R., Liquid crystalline polymers and elastomers. *Current Opinion in Solid State & Materials Science* **2002,** 6, (6), 545-551.

2. Lehmann, W.; Skupin, H.; Tolksdorf, C.; Gebhard, E.; Zentel, R.; Kruger, P.; Losche, M.; Kremer, F., Giant lateral electrostriction in ferroelectric liquid-crystalline elastomers. *Nature* **2001,** 410, (6827), 447-450.

3. Naciri, J.; Srinivasan, A.; Jeon, H.; Nikolov, N.; Keller, P.; Ratna, B. R., Nematic elastomer fiber actuator. *Macromolecules* **2003,** 36, (22), 8499-8505.

4. Rousseau, I. A.; Mather, P. T., Shape memory effect exhibited by smectic-c liquid crystalline elastomers. *Journal of the American Chemical Society* **2003,** 125, (50), 15300-15301.

5. de Gennes, P. G., Possibilities allowed by polymer reticulation in the presence of a liquid crystal. *Phys. Lett. A* **1969,** 28, 725.

6. Lendlein, A.; Jiang, H. Y.; Junger, O.; Langer, R., Light-induced shape-memory polymers. *Nature* **2005,** 434, (7035), 879-882.

7. Finkelmann, H.; Nishikawa, E.; Pereira, G. G.; Warner, M., A new opto-mechanical effect in solids. *Physical Review Letters* **2001,** 8701, (1), -.

8. Beyer, P.; Zentel, R., Photoswitchable smectic liquid-crystalline elastomers. *Macromolecular Rapid Communications* **2005,** 26, (11), 874-879.

9. Lemieux, R. P., Photoswitching of ferroelectric liquid crystals using photochromic dopants. *Soft Matter* **2005,** 1, (5), 348-354.

10. Yu, Y. L.; Ikeda, T., Photodeformable polymers: A new kind of promising smart material for micro- and nano-applications. *Macromolecular Chemistry and Physics* **2005,** 206, (17), 1705-1708.

11. Li, M. H.; Keller, P., Artificial muscles based on liquid crystal elastomers. *Philosophical Transactions of the Royal Society a-Mathematical Physical and Engineering Sciences* **2006,** 364, (1847), 2763-2777.

12. Ikeda, T.; Sasaki, T.; Ichimura, K., Photochemical Switching of Polarization in Ferroelectric Liquid-Crystal Films. *Nature* **1993,** 361, (6411), 428-430.

13. Ikeda, T.; Zushi, O.; Sasaki, T.; Ichimura, K.; Takezoe, H.; Fukuda, A.; Skarp, K. A. W., Photochemical Control of Switching Behaviors of Ferroelectric Polymer Liquid-Crystals - Poly(2-Methylbutyl 4'-(10-Acryloyloxydecyloxy)Biphenyl-4-Carboxylate). *Molecular Crystals and Liquid Crystals* **1993,** 225, 67-&.

14. Camacho-Lopez, M.; Finkelmann, H.; Palffy-Muhoray, P.; Shelley, M., Fast liquid-crystal elastomer swims into the dark. *Nature Materials* **2004,** 3, (5), 307-310.

15. Yu, Y. L.; Ikeda, T., Soft actuators based on liquid-crystalline elastomers. *Angewandte Chemie-International Edition* **2006,** 45, (33), 5416-5418.

16. Yu, Y. L.; Nakano, M.; Ikeda, T., Directed bending of a polymer film by light - Miniaturizing a simple photomechanical system could expand its range of applications. *Nature* **2003,** 425, (6954), 145-145.

17. Moore, J. S.; Stupp, S. I., Room-Temperature Polyesterification. *Macromolecules* **1990,** 23, (1), 65-70.

18. Verploegen, E.; Zhang, T.; Murlo, N.; Hammond, P. T., Influence of variations of liquid crystalline content upon the self-assembly behavior of siloxane based block copolymers. *Soft Matter* **2008,** Advance Article.

19. Verploegen, E.; Boone, D.; Hammond, P. T., Morphology of side chain liquid crystalline block copolymer thin films and effects of thermal annealing. *Journal of Polymer Science Part B-Polymer Physics* **2007,** 45, (24), 3263-3266.

20. Vanoppen, P.; Grim, P. C. M.; Rucker, M.; DeFeyter, S.; Moessner, G.; Valiyaveettil, S.; Mullen, K.; DeSchryver, F. C., Solvent codeposition and cis-trans isomerization of isophthalic acid derivatives studied by STM. *Journal of Physical Chemistry* **1996,** 100, (50), 19636-19641.

Appendix D Quantitative Characterization of Carbon Nanotubes Forests with X-ray Scattering

D.1 Introduction

In the course of performing synchrotron X-ray studies for my core thesis work and through conversations with Ben Wang we realized the utility of X-ray scattering for investigating the morphologies of carbon nanotube forests. In collaboration with Ben, John Hart, Ryan Bennett, and Prof. Robert Cohen we have developed methods for the quantitative characterization of vertically aligned multi-wall carbon nanotube (MWCNT) forests[1, 2].

Films of carbon nanotubes (CNTs), grown by chemical vapor deposition (CVD) processes, have shown promise for use in nanoelectronics[3], energy absorbing foams[4], superhydrophobic surfaces[5], and power applications[6]. The bulk morphology of these films, as well as the CNT dimensions, can be tailored through careful selection of catalyst and growth conditions.[7, 8] A significant amount of tortuosity and CNT entanglement can be present despite efforts to create vertically aligned films.[9, 10] This entanglement can decrease the performance in certain applications and enhance suitability in others. Therefore it is important to understand the bulk morphology of CNT films to determine the appropriate choice of applications, as well as to relate this morphology to the reaction conditions.

Scanning electron microscopy (SEM) and transmission electron microscopy (TEM) have been the methods of choice to characterize the structure and arrangement of MWCNTs that make up these films.[8, 9] TEM is a powerful tool that gives direct visualization of CNT dimensions and internal structure with resolution down to the angstrom scale; however it is inherently a local measurement. To obtain average CNT diameters using TEM requires many individual measurements from multiple micrographs, making the analysis of the macroscopic films tedious. In addition it is difficult to maintain the spatial correspondence between the location of the film and the TEM sample. SEM provides a mesoscopic view of MWCNT film morphology, but subjective image analysis is required to compare order and alignment and the resolution of SEM is typically insufficient to measure CNT diameters, see Figure D-1.

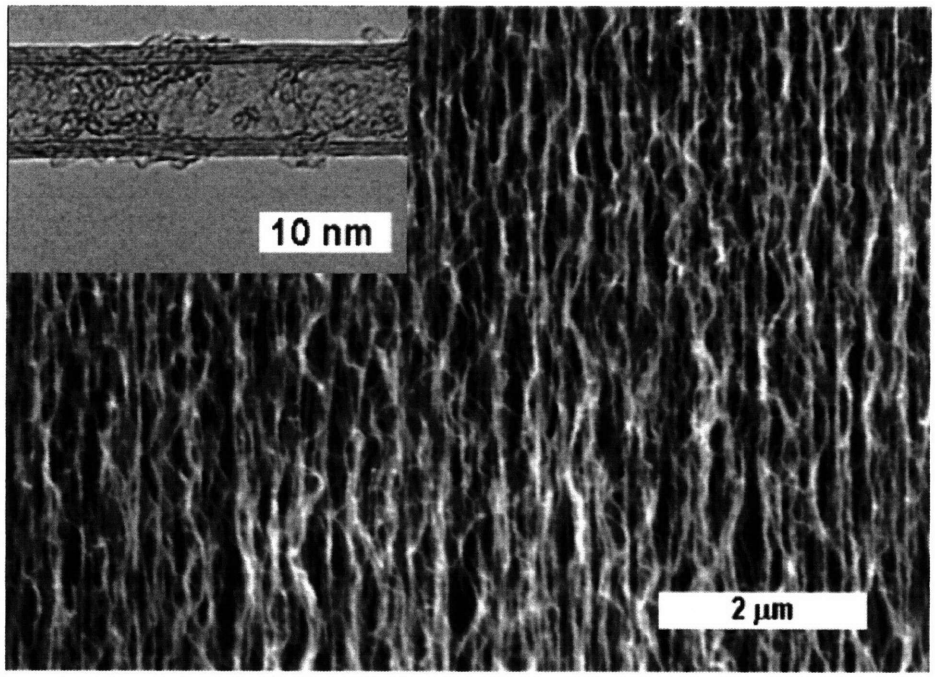

Figure D-1. Scanning electron microscopy (SEM) image of a vertically aligned multiwall carbon nanotube forest. Inset: transmission electron microscopy image of a single multiwall carbon nanotube.

Scattering methods, such as small-angle X-ray scattering (SAXS) are useful for investigating features on the order of 1 – 100 nm. Though SAXS is not a direct visualization technique, it provides a Fourier transform of real space information. For a typical SAXS setup with a beam spot size on the order of a few hundred microns, the resulting data samples over millions of CNTs and can reflect a "locally averaged" measurement of CNT morphology, see Figure D-2.

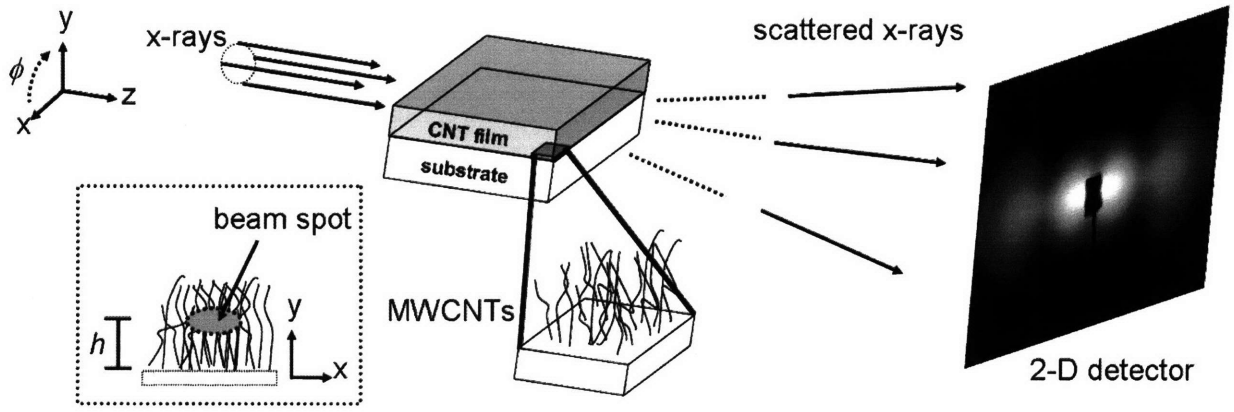

Figure D-2. Schematic of the experimental setup for small-angle X-ray scattering of multiwall carbon nanotube forests. A motorized stage provides spatial resolution allowing for the morphology to be investigated as a function of position within the film.

D.2 Experimental

Small-angle X-ray studies were performed at the G1 beamline station at the Cornell High Energy Synchrotron Source (CHESS). The wavelength of the X-rays was 0.1239 nm, and the sample to detector distance was calibrated with silver behenate (first order scattering vector of q

of 1.076nm^{-1} (with $q = 4\pi \sin(\theta/\lambda)$ where 2θ is the scattering angle and λ is the wavelength). A slow-scan CCD-based X-ray detector, home built by Drs. M.W. Tate and S.M. Gruner of the Cornell University Physics Department, was used for data collection. Additional studies were performed at the X27C beamline at the National Synchrotron Light Source (NSLS) at Brookhaven National Laboratory (BNL). The wavelength of the X-rays was 0.1371 nm. Data were collected on a MarCCD X-ray detector with a pixel width of 0.158 mm. Both systems use motors connected to the sample fixture, which allowed fine control of the positioning of the sample, relative to the incident X-ray beam, to study the local CNT morphology at various locations in the film.

D.3 Results and Discussion

We have that shown small-angle X-ray scattering (SAXS) is a powerful tool for investigating the morphologies of multiwall carbon nanotube (MWCNT) films[1, 2]. By fitting the SAXS data to a model for cylindrical form factor, the average CNT diameter and an estimate of the standard deviation can be determined. The diameters determined through SAXS correspond well to high resolution transmission electron microscopy (HRTEM) data. SAXS provides the advantage of sampling millions of CNTs in a single image, and additionally provides spatial resolution not accessible through HRTEM. The ability to characterize the CNTs as a function of position within the film allows us to create a morphological map of both the orientation and diameter, see Figure 3.

We observed and quantified a change in morphology from entangled to vertically aligned growth through the thickness of a film. We also noted a widening in the average CNT diameters through the height of the CNT forest. We speculate that this observation can correspond to

preferential growth of wider CNTs. For film morphologies that are dictated by base-growth mechanism we include the possibility that the CNTs narrow as they grow from the substrate, with the widest portion of an individual CNT located at the top of the film.

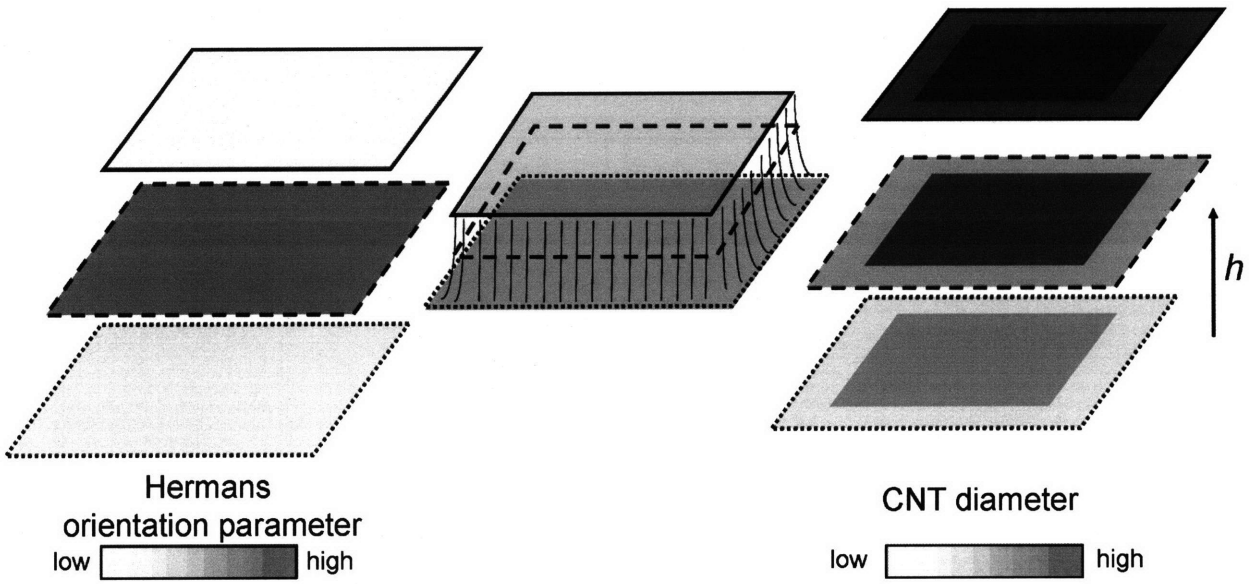

Figure D-3. Morphological map of the CNT forests. The alignment is highest in the center of the film and the diameter is largest at the top and center of the forest.

Systematic studies of the morphologies of the CNT forests as a function of variations in the growth conditions are underway and will provide insights into the fundamental mechanisms of the CNT growth process. We have recently developed instrumentation that allows for in-situ investigation of the CNT growth process. By monitoring this process in real time we are able to directly correlate the growth conditions to the morphology of the CNT forest. Gaining a complete understanding of this process is critical for enabling materials structure and properties to be optimized and customized for specific applications.

We have also investigated the effects of mechanical manipulations upon the morphologies of these MWCNT forests[1], including uniaxially compression and densification through solvent evaporation. A low angle scattering feature in the data, corresponding to the interparticle structure factor, allows us to extract information about the packing density of the CNTs. We have recently performed ultra small-angle X-ray scattering (USAXS) measurements which confirm this result and additionally reveal the presence of CNT aggregates in these films. This analysis allows for determination of the average spacing between the CNTs which varies significantly with mechanical manipulation. Additionally, we have used wide-angle X-ray scattering (WAXS) to determine the number of grapheme sheets present in the nanotube walls, i.e. the number of walls in the multi-wall carbon nanotubes.

D.4 Conclusions

X-ray scattering can be used to provide rich morphological information that is not accessible through conventional microscopy techniques. By using a combination of ultra small-angle, small-angle, and wide-angle X-ray scattering, (USAXS), (SAXS), and (WAXS) respectively, we have demonstrated the ability to characterize the morphologies of carbon nanotube films over a wide range of length scales. USAXS enables the characterization of the average spacing and aggregation of the nanotubes. SAXS allows for quantitative characterization of both the diameter and orientation of CNTs. WAXS can allow the number of average walls in the multi-wall nanotubes to be determined. All three of these techniques provide locally averaged information allowing for spatial resolution of the morphologies within the films. These techniques and analysis can easily be applied to single wall CNTs, zinc oxide nanowires, and a variety of other similar systems.

D.5 References

1. Wang, B. N.; Bennett, R. D.; Verploegen, E.; Hart, A. J.; Cohen, R. E., Characterizing the morphologies of mechanically manipulated multiwall carbon nanotube films by small-angle X-ray scattering. *Journal of Physical Chemistry C* **2007,** 111, (48), 17933-17940.

2. Wang, B. N.; Bennett, R. D.; Verploegen, E.; Hart, A. J.; Cohen, R. E., Quantitative characterization of the morphology of multiwall carbon nanotube films by small-angle X-ray scattering. *Journal of Physical Chemistry C* **2007,** 111, (16), 5859-5865.

3. Snow, E. S.; Novak, J. P.; Campbell, P. M.; Park, D., Random networks of carbon nanotubes as an electronic material. *Applied Physics Letters* **2003,** 82, (13), 2145-2147.

4. Chakrapani, N.; Wei, B.; Carrillo, A.; Ajayan, P. M.; Kane, R. S., Capillarity-driven assembly of two-dimensional celluar carbon nanotube foams. *Proceedings of the National Academy of Sciences* **2004,** 101, (12), 4009 - 4012.

5. Lau, K. K. S.; Bico, J.; Teo, K. B. K.; Chhowalla, M.; Amaratunga, G. A. J.; Milne, W. I.; McKinley, G. H.; Gleason, K. K., Superhydrophobic Carbon Nanotube Forests. *Nano Letters* **2003,** 3, (12), 1701 - 1705.

6. Raffaelle, R. P.; Landi, B. J.; Harris, J. D.; Bailey, S. G.; Hepp, A. F., Carbon nanotubes for power applications. *Materials Science and Engineering B* **2005,** 116, 233-243.

7. Hart, A. J.; Slocum, A. H.; Royer, L., Growth of conformal single-walled carbon nanotube films from Mo/Fe/Al2O3 deposited by electron beam evaporation. *Carbon* **2006,** 44, (348 - 359).

8. Hart, A. J.; Slocum, A. H., Rapid growth and flow-mediated nucleation of millimeter-scale aligned carbon nanotube structures from a thin-film catalyst. *Journal of Physical Chemistry B* **2006,** 110, 8250-8257.

9. Bennett, R. D.; Hart, A. J.; Cohen, R. E., Controlling the morphology of carbon nanotube films by varying the areal density of catalyst nanoclusters using block copolymer micellar thin films. *Advanced Materials* **2006,** 18, (17), 2274.

10. Zhang, L.; Li, Z.; Tan, Y.; Lolli, G.; Sakulchaicharoen, N.; Requejo, F. G.; Mun, B. S.; Resasco, D. E., Influence of a top crust of entangled nanotubes on the structure of vertically aligned forests of single-walled carbon nanotubes. *Chemistry of Materials* **2006,** 18, (23), 5624-5629.

Appendix E Applications of Grazing Incidence Small-Angle X-ray Scattering for the Characterization of Thin Films

E.1 Introduction and Experimental

I initially utilized grazing incidence small-angle X-ray scattering (GISAXS) for the study of the side chain liquid crystalline block copolymer thin films, described in Chapters 5 and 6. As I became more familiar with this technique I discovered, what I believe to be, the untapped utility of this powerful technique for the characterization of a wide range of nanostructured thin film systems. GISAXS is a powerful non-invasive technique that we used to investigate the both the lateral and transverse structures in the interior of these thin films[1-3]. In this section I will describe several examples of my work where GISAXS proved to be a valuable tool for revealing the structure and dynamics of various thin films. Among the systems studied with GISAXS are; layer-by-layer films containing nanoscale clay platelets and amphiphilic micelles, nanoparticles templated via amphiphilic block copolymers, and the in-situ study of the dynamics of the coalescence of nanoparticles as a function of temperature. None of this work would have been possible without the guidance and support of Arthur Woll at the G1 beamline at the Cornell High Energy Synchrotron Source (CHESS).

The typical GISAXS setup includes a stepper motor that enables precise control over the y and z position and the horizontal tilt of the sample. The thin film sample, usually on a silicon substrate is placed on the sample stage and the position and tilt of the sample is calibrated using

an ion chamber. The ion chamber detects the intensity of the incoming beam and by moving the sample in front of the beam allowing its position relative to the X-ray beam to be found. It is critical for GISAXS to precisely know the angle of the incident beam relative to the substrate. In order to achieve the maximum scattering contrast an incident angle (α_i) is chosen below the critical angle (α_c) of the substrate and above the critical angle of the thin film. Silicon has a critical angle of 0.20°, where the beam is reflected and there is negligible X-ray transmission through the silicon. Typical polymer films have critical angles ~0.14°. When the incident angle is between the α_c of the substrate and the α_c of the film, the beam probes the entire thickness of the film. In this case there are four primary modes of scattering:

1) Scattering of the incident beam upon entry to the film.
2) Transmission through the film, followed by reflection by the silicon substrate, and scattering from the film.
3) Scattering of the incident beam upon entry to the film and subsequent reflection by the substrate.
4) Transmission through the film, followed by reflection by the silicon substrate, scattering from the film, and reflection once again by the substrate.

Each of these scattering modes results in a different scattering angle from the sample. The first two scattering modes are the most intense and subsequently dominate the resulting scattering pattern. However, if the incident angle is less than the α_c of the thin film, and the film has sufficiently low surface roughness, then the incident beam is reflected by the sample and only penetrates ~10nm into the film. Thus for films significantly thicker than the penetration depth, only the top surface of the film is probed and only the first scattering mode is observed.

The wavelength of the incident beam at CHESS is 1.239Å, and silver behenate was used to calibrate the sample to detector distance with a first order scattering vector of q of 1.076nm^{-1} (with $q = 4\pi \sin\theta/\lambda$ where 2θ is the scattering angle and λ is the wavelength). A slow-scan CCD-based x-ray detector, home built by Drs. M.W. Tate and S.M. Gruner of the Cornell University Physics Department, was used for data collection. Incidence angles were typically chosen between 0.12° and 0.22°, and the final images are an average of two 1 second exposures. The sample detector distance is chosen to best capture the scattering over the desired q range, between 100mm and 2000mm for features ranging from 0.5 nm to 100nm, respectively. A typical experimental setup is shown in Figure E-1. In the next section I will briefly describe a few of the thin film systems that I have characterized with GISAXS. As a note grazing incidence diffraction (GID) is a similar technique, there is no fundamental difference between GISAXS and GID, except the typical length scale of interest. The technique is typically referred to as GISAXS when studying materials with larger feature sizes, from a few nanometers up to a micron, and GID when the feature size is less than a few nanometers.

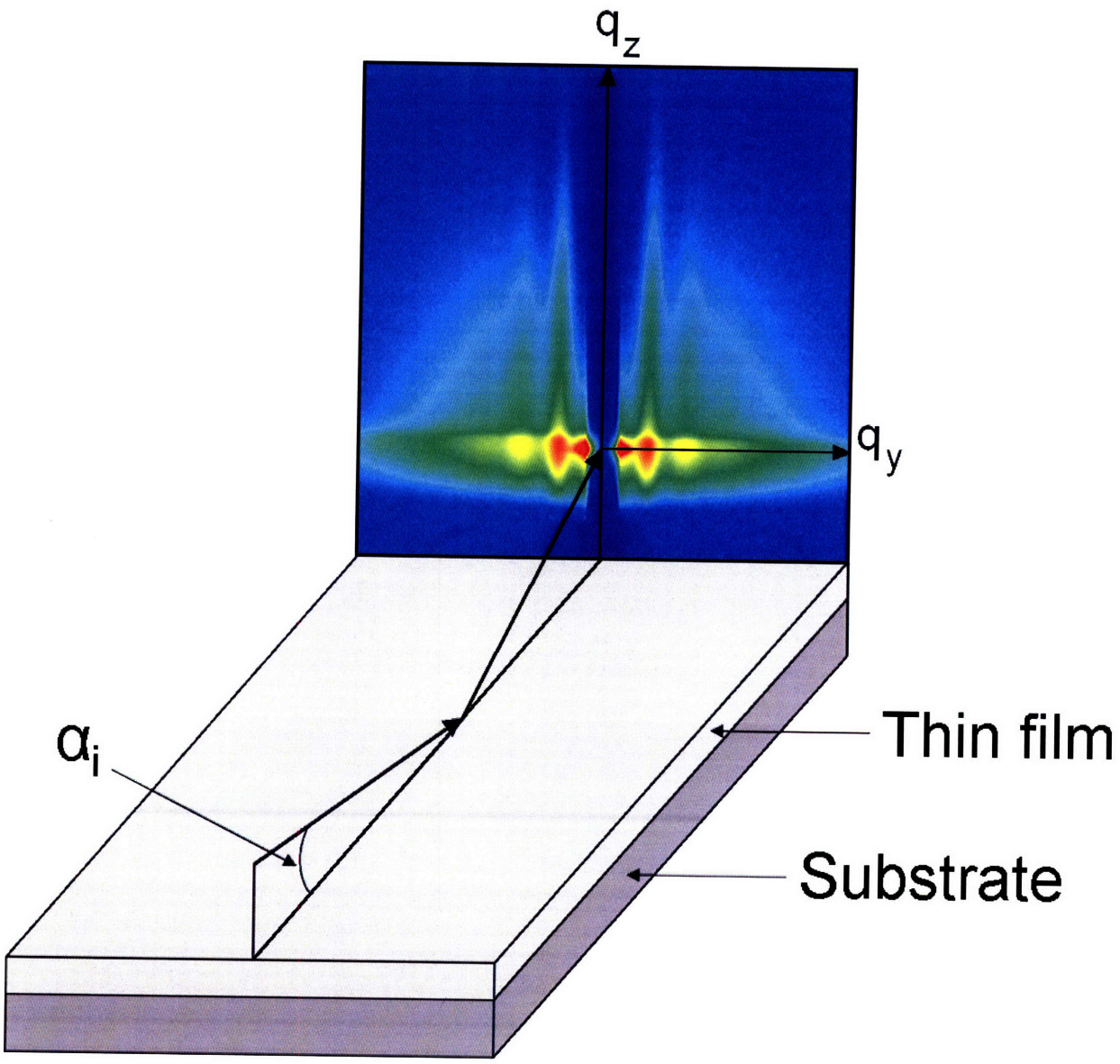

Figure E-1. A schematic of a typical grazing incidence small-angle X-ray scattering (GISAXS) setup. Scattering along the q_y direction is resultant from structures in the plane of the film, scattering along the q_z direction is resultant from structures parallel to the substrate.

E.2 Results and Discussion

E.2.1 GISAXS of layer-by-layer thin films containing nanostructured clay

Using the layer-by-layer (LbL) assembly technique, a polymer-clay structure can be created from a combination of LbL materials: poly(ethylene imine), laponite clay, and poly(ethylene oxide)[4]. This trilayer LbL structure is assembled using a combination of hydrogen bonding and electrostatic interactions. A layered anisotropic structure was observed with GISAXS, which resulted in in-plane ion transport 100 times faster than cross-plane at 0% relative humidity as measured by electrochemical impedance spectroscopy (EIS). The GISAXS characterization (see Figure E-2) was critical for understanding the structure property relationship of these materials.

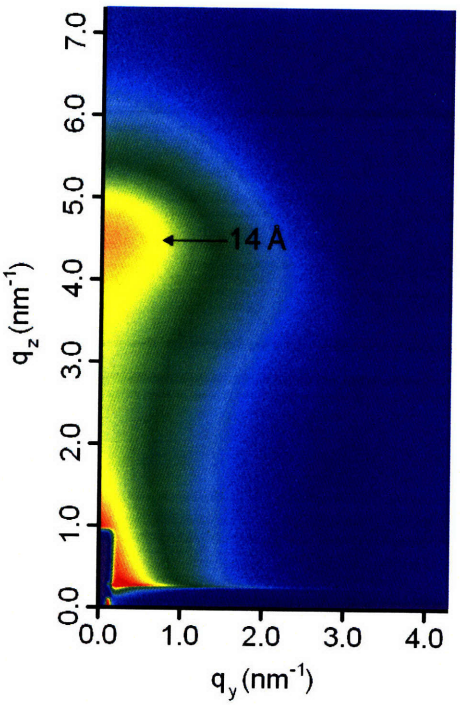

Figure E-2. GISAXS scattering data of a PEI/Li-clay/PEO LbL film. Scattering reveals there is regular 14 Å spacing in the direction perpendicular to the substrate. This data indicates the clay platelets are oriented parallel to the substrate surface.

E.2.2 GISAXS of layer-by-layer thin films containing amphiphilic micelles

To confirm the presence of micelles in the LbL films, GISAXS was performed on LbL films composed of PPO-PAMAM and PAA[5]. The films contained either empty micelles or micelles encapsulating triclosan. Figure F-3 displays a GISAXS spectrum with strong scattering seen in the q_y direction (q_y) at 0.6 nm^{-1}. From the GISAXS data, it was established that there was regular spacing of 10.5 nm and 11.7 nm in the plane parallel to the substrate for the films with no drug and with drug, respectively. Additionally, for the film containing drug, scattering in the Angstrom length scales indicate the presence of triclosan, which has crystallized within the micelles. As reported in earlier work, the triclosan loading is unusually large in the linear-dendritic block copolymer micelles, yielding stabilized nanoparticles containing bulk drug within the core of the micelle. There is also evidence of regular spacing on the nanometer length scale of the same order of magnitude in the direction normal to the substrate, which would correspond to the spacing of the micelles in the q_z direction. However, the scattering is less intense and inconclusive due to interference of the beam stop and specular reflectance. The spacing in the LbL films revealed by GISAXS is of the same order of magnitude as the size of the micelles experimentally determined by dynamic light scattering and TEM.

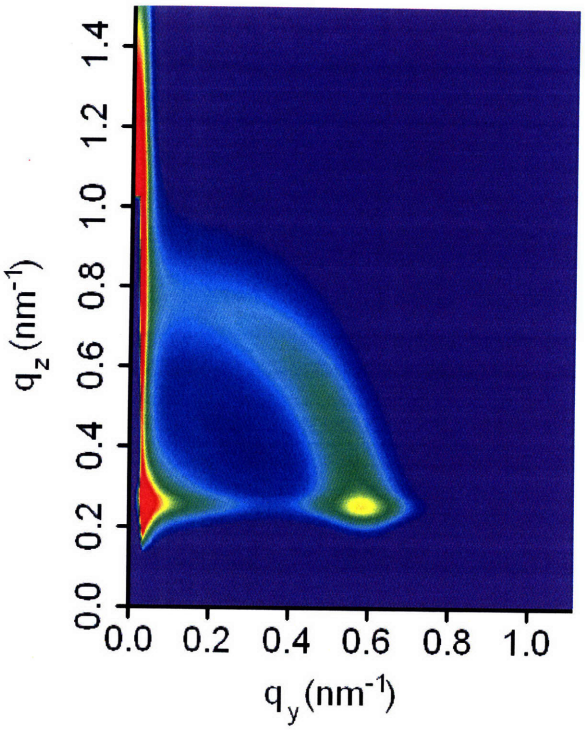

Figure E-3. GISAXS scattering data of a 10 bilayer LbL film composed of PPO-PAMAM micelles and PAA. Scattering reveals there is regular spacing of 10.5 nm spacing in the direction parallel to the substrate. There is some evidence of scattering in the plane perpendicular to the substrate but is inconclusive.

E.2.3 GISAXS of block copolymer templated nanoparticles

Iron nanoparticles can be templated using a PS-*b*-PAA micellar film onto an Al_2O_3-coated Si substrate[6]. The amphiphilic block copolymer poly(styrene-*block*-acrylic acid) (PS-*b*-PAA) forms micelles in solution which are capable of self-organizing into ordered structures on surfaces. By spin-coating these solutions onto a variety of substrates a quasihexagonal arrays of PAA spheres within a PS matrix can be created. The carboxylic acids groups in the PAA domains can be utilized in an ion-exchange protocol to selectively sequester iron ions, which results in iron nanoparticles that are nearly monodisperse in size. Using an oxygen plasma etch

the PS-PAA block copolymer can be removed leaving behind only the iron nanoparticles. These nanoparticles can then be used to catalyze the growth of CNTs in a thermal chemical vapor deposition (CVD) process. For the sample shown in Figure E-4, GISAXS revealed an average nanoparticle spacing of 33 nm. Similar systems using polystyrene-b-poly(4-vinylpyridine), PS-P4VP, can be used to template gold nanoparticles.

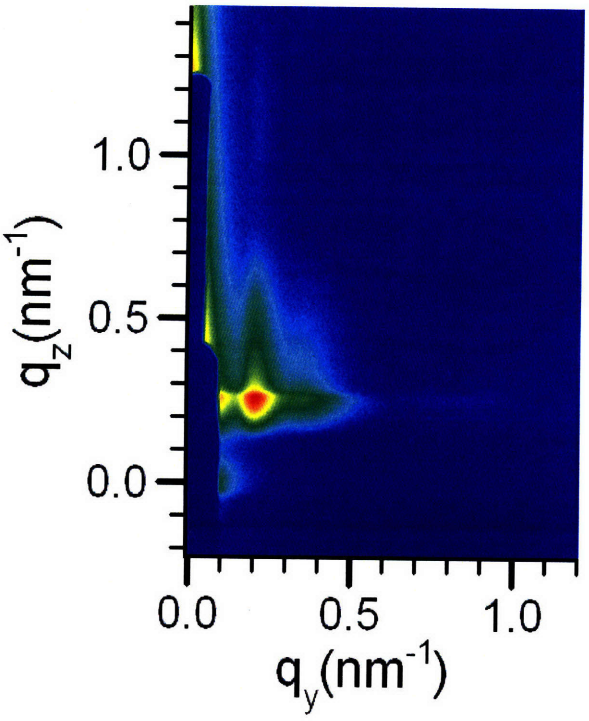

Figure E-4. GISAXS scattering data from an iron nanoparticle array indicating a hexagonal array of particles with an average spacing of 33 nm.

E.2.4 In-situ GISAXS of the kinetics of nanoparticle coalescence

By heating a 2 nm iron film on an Al_2O_3-coated silicon substrate to 820°C in a reducing hydrogen-helium environment, the iron film coalesces forming iron nanoparticles. In-situ GISAXS can be used to monitor this process the dynamics of the nanoparticle coalescence can be

studied[7]. Using a custom built furnace the temperature and annealing environment can be controlled while the collecting GISAXS data. No coalescence was observed in a pure helium environment indicating that hydrogen is necessary for the process to occur. In the hydrogen-helium environment the initial coalescence begins to occur at ~650°C and further develops with increasing time and temperature. These iron nanoparticles can be used for the growth of carbon nanotubes, and understanding the nanoparticle formation process can enable the control over nanoparticle size and subsequently the size of the carbon nanotubes.

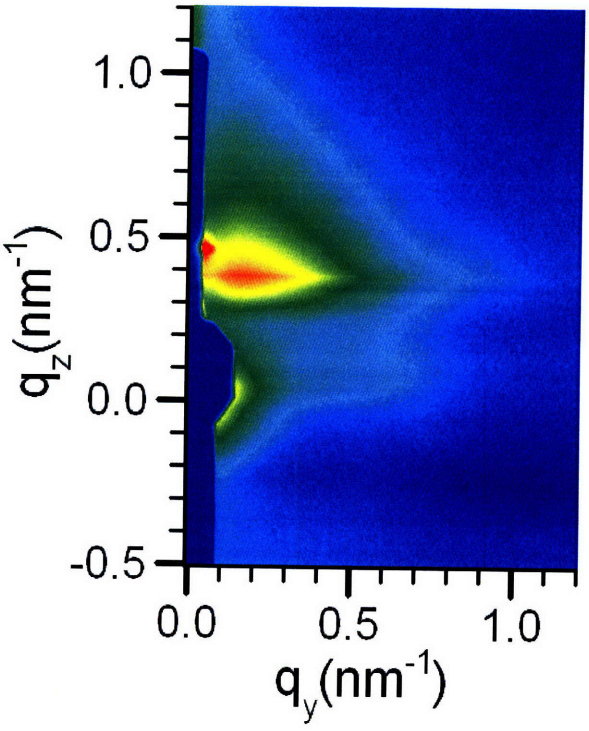

Figure E-5. GISAXS scattering data from an iron film on an Al_2O_3-coated Si substrate that has formed nanoparticles due to coalescence of the iron film at 820°C. The average nanoparticle spacing is 42 nm.

E.3 Conclusions

Grazing incidence small-angle X-ray scattering (GISAXS) can be used to investigate a wide range of nanostructured thin films. This technique allows for the nanostructured morphology both parallel and perpendicular to the substrate to be investigated. GISAXS can also be used for in-situ monitoring of physical phenomena, providing insights that cannot be accessed through conventional microscopy techniques.

E.4 References

1. Busch, P.; Rauscher, M.; Smilgies, D. M.; Posselt, D.; Papadakis, C. M., Grazing-incidence small-angle X-ray scattering from thin polymer films with lamellar structures-the scattering cross section in the distorted-wave Born approximation. *Journal of Applied Crystallography* **2006,** 39, 433-442.

2. Muller-Buschbaum, P., Grazing incidence small-angle X-ray scattering: an advanced scattering technique for the investigation of nanostructured polymer films. *Analytical and Bioanalytical Chemistry* **2003,** 376, (1), 3-10.

3. Busch, P.; Krishnan, S.; Paik, M.; Toombes, G. E. S.; Smilgies, D. M.; Gruner, S. M.; Ober, C. K., Inner Structure of Thin Films of Lamellar Poly(styrene-b-butadiene) Diblock Copolymers As Revealed by Grazing-Incidence Small-Angle Scattering. *Macromolecules* **2007,** 40, (1), 81-89.

4. Lutkenhaus, J. L.; Olivetti, E. A.; Verploegen, E. A.; Cord, B. M.; Sadoway, D. R.; Hammond, P. T., Anisotropic structure and transport in self-assembled layered polymer-clay nanocomposites. *Langmuir* **2007,** 23, (16), 8515-8521.

5. Nguyen, P. M.; Zacharia, N. S.; Verploegen, E.; Hammond, P. T., Extended release antibacterial layer-by-layer films incorporating linear-dendritic block copolymer micelles. *Chemistry of Materials* **2007,** 19, (23), 5524-5530.

6. Wang, B. N.; Bennett, R. D.; Verploegen, E.; Hart, A. J.; Cohen, R. E., Quantitative characterization of the morphology of multiwall carbon nanotube films by small-angle X-ray scattering. *Journal of Physical Chemistry C* **2007,** 111, (16), 5859-5865.

7. Hart, A. J.; Verploegen, E.; Meshot, E. R.; Han, S., Eludicating the Dynamics of Carbon Nanotube Film Growth by In Situ X-Ray Scattering. **2008,** In Preperation.

Appendix F Measurement of Order-Disorder Transition Temperatures (T_{ODT})

F.1 Small-angle X-ray Scattering and Rheology

Temperature dependent small-angle X-ray scattering (SAXS) was used to investigate the effects of increasing LC content upon the self-assembly behavior. Analyzing the reciprocal of the maximum scattering intensity ($1/I_{max}$) as a function of the reciprocal temperature (1/T) allows for systematic determination of the order-disorder transition temperature (T_{ODT}). Additionally, the wavelength of concentration fluctuations, above T_{ODT}, and the d-spacing, below T_{ODT}, denoted as (d) was plotted versus reciprocal temperature[1, 2]. An example of this type of analysis is shown in Figure F1.

Additionally, rheometry was used to confirm the order-disorder transition temperatures that were determined via temperature dependant SAXS. The T_{ODT} is characterized by a maxima in tan delta, which is the ratio of the loss modulus (G") and the storage modulus (G'), as shown in Figure F2. The values for the T_{ODT} obtained via rheometry were consistent with those from SAXS, however due to the faster ramp rate, 5°C/min for rheometry compared to 30 min equilibration for SAXS, the values were typically ~20°C higher than those from SAXS. Some samples were not investigated via SAXS or rheometry as they had not yet been synthesized or there was not sufficient material available, respectively.

It is difficult to compare the T_{ODT} for the samples resulting in the attachment of LC to the PS61-PVMS18 backbone to the samples synthesized with PS27-PVMS14 for several reasons.

Both the molecular weight and the polydispersity of these polymers differ, and this has an effect upon the T_{ODT}. Additionally, while homogeneous anchoring of the LC mesophase with the inter-material dividing surface (IMDS) is exclusively observed in this system where the PS domains form cylinders, it is expected that either homogeneous or heterogeneous anchoring could exist for lamellar morphologies[3]. As the LC anchoring is a significant driving force for the self assembly of these materials it is expected that the anchoring will influence the T_{ODT}. In depth studies into the lamellar and transitional morphologies are currently underway.

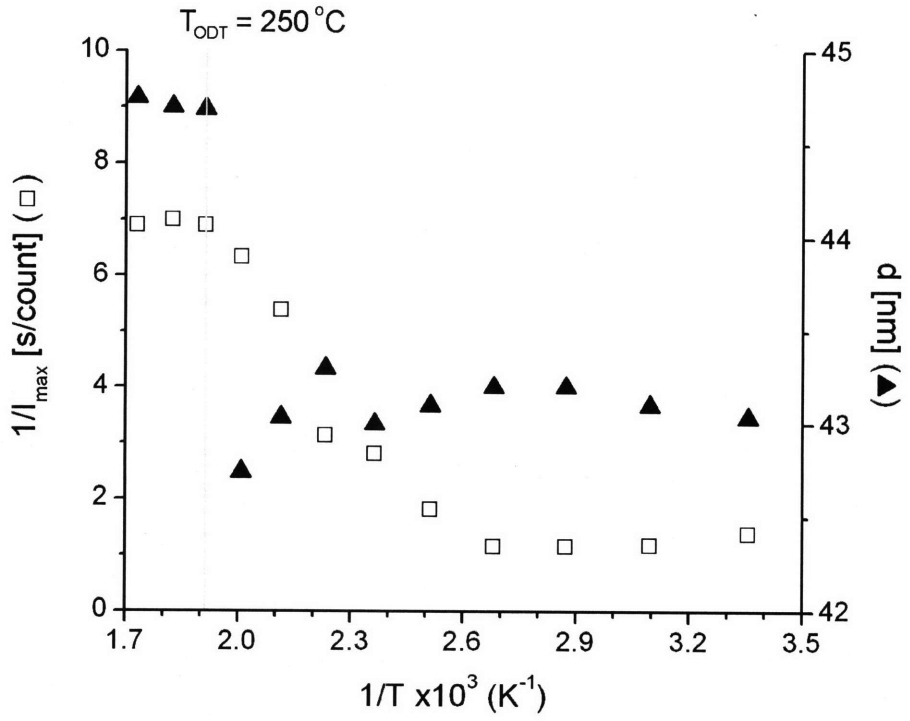

Figure F1. Plot of $1/I_{max}$ versus 1/T and d versus 1/T for sample PS27-PVMS14. Where I_{max} is the maximum intensity of the scattering in the q range of interest and d is the spacing of the ordered phase below the T_{ODT} and the length scale of concentration fluctuations above the T_{ODT}.

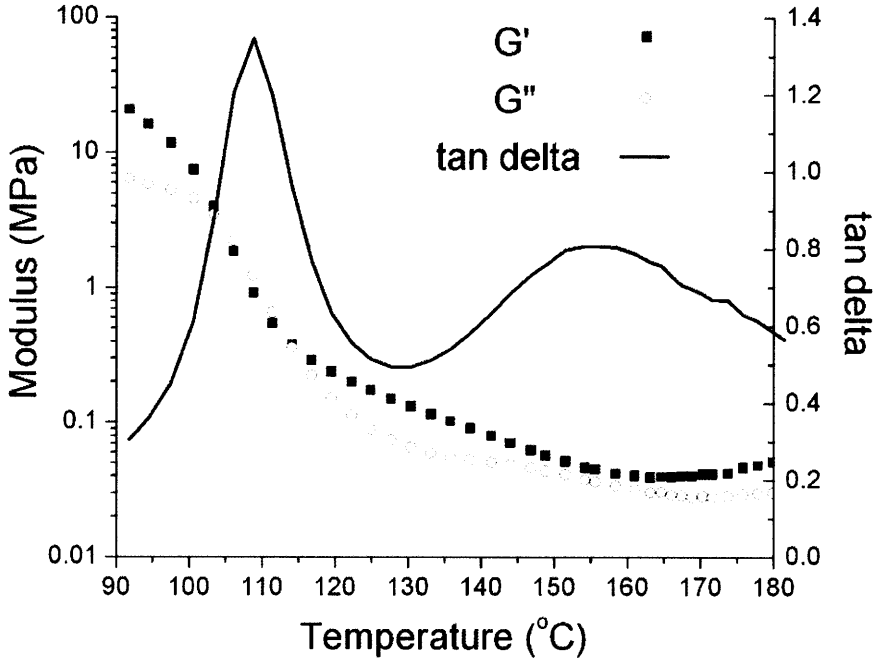

Figure F2. Rheometry for sample PS27-LCP$_{4BPP4}$46. G' is the storage modulus, G" is loss modulus, and tan delta = G'/G". The polystyrene T_g is observed at 110°C and the T_{ODT} is observed at 155°C.

F.2 References

1. Hashimoto, T.; Shibayama, M.; Kawai, H., Domain-Boundary Structure of Styrene-Isoprene Block Co-Polymer Films Cast from Solution.4. Molecular-Weight Dependence of Lamellar Microdomains. *Macromolecules* **1980,** 13, (5), 1237-1247.

2. Mao, G. P.; Wang, J. G.; Clingman, S. R.; Ober, C. K.; Chen, J. T.; Thomas, E. L., Molecular design, synthesis, and characterization of liquid crystal coil diblock copolymers with azobenzene side groups. *Macromolecules* **1997,** 30, (9), 2556-2567.

3. Anthamatten, M.; Zheng, W. Y.; Hammond, P. T., A morphological study of well-defined smectic side-chain LC block copolymers. *Macromolecules* **1999,** 32, (15), 4838-4848.